

CHALLENGES IN MOLECULAR MODELING
ENGAGED FROM TWO DISTINCT THEORETICAL PERSPECTIVES

A Dissertation

Submitted to the Faculty

of

Purdue University

by

Carlos Hernán Borca Paredes

In Partial Fulfillment of the

Requirements for the Degree

of

Doctor of Philosophy

May 2017

Purdue University

West Lafayette, Indiana

**THE PURDUE UNIVERSITY GRADUATE SCHOOL
STATEMENT OF DISSERTATION APPROVAL**

Prof. Lyudmila V. Slipchenko, Chair

Department of Chemistry

Prof. Adam Wasserman

Department of Chemistry and Department of Physics and Astronomy

Prof. David R. McMillin

Department of Chemistry

Prof. Sabre Kais

Department of Chemistry

Approved by:

Prof. Timothy Zwier

Head of the Department Graduate Program

A Laura Isabel, Stella y Néstor Pedro.

ACKNOWLEDGMENTS

I would like to start thanking my family. Stella Paredes Rodríguez and Néstor Pedro Borca Taboada, who could not have been better parents, always giving their best, so that I would have the best opportunities. My uncle Manuel Víctor Borca and aunt Consuelo Carrillo, who have guided me here in so many ways; and all the members of my family who are not living close to me now, but always were there when I needed them.

I am deeply thankful to my wife, and lifetime collaborator, Laura I. Mosquera-Giraldo for being my endless support regardless of the situation. For the uncountable number of constructive discussions we have had. For her patience, understanding, and wisdom, I will always be grateful.

I want to especially thank Dr. Martín A. Mosquera, for sharing almost five years of science, friendship, and homesickness. Also, José F. Rivera and Yuan Jiang with whom I have shared wonderful moments.

I am very grateful to my fellow group members: Dr. Ben T. Nebgen, Dr. Ilya A. Kaliman, Yen H. Bui, Yongbim Kim, Sungmin Hong, and Jennifer Werner. I want to especially acknowledge, Pradeep K. Gurunathan, with whom I shared so many valuable thoughts and moments since 2012, and Claudia I. Viquez-Rojas, with whom for better or for worse, I shared the same workspace in the last few years.

I want to thank Dr. Xavier I. Andrade and Dr. Alfredo A. Correa, for offering me the opportunity to work in the implementation of Tkatchenko-Scheffler density functional for van der Waals interactions, for their guidance and support, and for making my stay at the Lawrence Livermore National Laboratory one of the best experiences of my academic life.

I am thankful to the following faculty members of Purdue University: Lynne S. Taylor, Paul B. Shepson, David R. McMillin; and Northwestern University: Mark A. Ratner and George C. Schatz.

I am deeply grateful to have worked with Prof. Adam Wasserman. I want to thank him for his support and for helping me develop personally, academically, and professionally. I cherish what I learned following him as an example of sharpness, clarity, and prudence.

Finally, I am greatly indebted and truly grateful to my adviser Prof. Lyudmila V. Slipchenko for showing me a clear path through the hardest parts of my research (until a year ago), for her motivation to keep me moving forward and avoiding the frustration, for the knowledge she transmitted to me during our discussions, and for the support given to me.

This research was funded by the Office of Basic Energy Sciences, U.S. Department of Energy, under grant No.DEFG02-10ER16196, by the National Science Foundation, grant No.CHE-1465154, by the Lawrence Livermore National Laboratory¹ through the Computational Chemistry and Materials Science Summer Institute of 2015, and by Purdue University. This research was supported in part through computational resources provided by Information Technology at Purdue University.

¹Lawrence Livermore National Laboratory is operated by Lawrence Livermore National Security, LLC, for the U.S. Department of Energy, National Nuclear Security Administration under Contract DE-AC52-07NA27344.

TABLE OF CONTENTS

	Page
LIST OF FIGURES	x
ABBREVIATIONS	xiv
ABSTRACT	xvii
1. INTRODUCTION	1
PART ONE	
2. GROUND-STATE CHARGE TRANSFER IN DENSITY FUNCTIONAL THEORY	4
2.1 Introduction	4
2.1.1 Motivation	5
2.1.2 Theory	6
2.1.3 Background	9
2.2 Computational Methods	10
2.3 Results and Discussion	14
2.3.1 Charge Distributions	14
2.3.2 Frontier Molecular Orbitals	18
2.3.3 State-crossing	24
2.3.4 Excited-state Calculations	27
2.3.5 Interaction Energy	29
2.4 Summary	32
3. MODULAR IMPLEMENTATION OF TKATCHENKO-SCHEFFLER FUNCTIONAL MODEL FOR VAN DER WAALS INTERACTION	33
3.1 Introduction	33
3.1.1 Motivation	33
3.1.2 Background	34
3.2 The Model of Tkatchenko and Scheffler for van der Waals Interactions .	37
3.2.1 van der Waals Energy	37
3.2.2 Electronic Potential	41
3.2.3 Atomic Forces	43
3.3 Implementation	46

	Page
3.3.1 Octopus	46
3.3.2 Overview of the TS-vdW Library	47
3.3.3 Features	48
3.4 Simple Tests	49
3.4.1 Validation of the Implementation	49
3.4.2 van der Waals-induced Shifts in Optical Spectra	52
3.5 Summary	54
4. STANDARD AND LONG-RANGE-CORRECTED HYBRID FUNCTIONALS FOR EXCITATION ENERGIES	56
4.1 Introduction	56
4.1.1 Motivation	56
4.1.2 Background	57
4.1.2.1 Local Density Approximation	58
4.1.2.2 Generalized Gradient Approximations	59
4.1.2.3 Hybrid Approximations	61
4.1.2.4 Linear-response TD-DFT Properties	62
4.2 Theory	62
4.2.1 LDA-based, Hybrid Approximations	63
4.2.2 LDA-based, Range-separated-hybrid Approximations	64
4.3 Computational Details	65
4.4 Results	67
4.5 Summary	70
PART TWO	
5. THE EFFECTIVE FRAGMENT POTENTIAL METHOD	72
5.1 Introduction	72
5.2 Background	72
5.2.1 The Origins	73
5.2.2 The EFP1 Model	73
5.2.3 The EFP2 Model	75
5.3 The Effective Fragment Potential Method	75
5.3.1 Electrostatics	77
5.3.2 Polarization	81
5.3.3 Dispersion	86
5.3.4 Exchange Repulsion	89
5.4 Preparation of EFP Fragment Parameters	100
5.4.1 Protocol of Parametrization Implemented in MAKEFP	100
5.4.2 MAKEFP Control Options	101
5.4.3 Library of Precomputed Fragments	103
5.5 Range of Applicability of the EFP Method in Classical Simulations . .	104

	Page
6. THE MELTING TEMPERATURE OF WATER WITH THE EFFECTIVE FRAGMENT POTENTIAL	105
6.1 Introduction	105
6.1.1 Motivation	105
6.1.2 Background	106
6.2 Theory	108
6.2.1 The Solid-liquid Equilibrium in Water	108
6.2.2 The Direct Coexistence Method	109
6.3 Computational Details	112
6.4 Results	117
6.4.1 Time-evolution of the Total Energy	117
6.4.2 Visual Analysis	119
6.4.3 Radial Distribution Functions	121
6.4.4 Density as a Function of Temperature	122
6.5 Summary	124
7. COMPUTATIONAL EFFICIENCY OF MOLECULAR DYNAMICS WITH THE EFFECTIVE FRAGMENT POTENTIAL METHOD	126
7.1 Introduction	126
7.1.1 Motivation	126
7.1.2 Background	127
7.2 Theory	128
7.3 Computational Details	129
7.4 Results	131
7.5 Summary	135
8. EXPLOITING THE TIMESCALE SEPARATION OF ENERGY CONTRIBUTIONS TO ACCELERATE MOLECULAR DYNAMICS IN THE EFFECTIVE FRAGMENT POTENTIAL METHOD	137
8.1 Introduction	137
8.1.1 Motivation	137
8.1.2 Background	138
8.2 Theory Development	138
8.3 Computational Details	141
8.4 Results	142
8.5 Implementation	146
8.6 Summary	148
9. SUMMARY	150
REFERENCES	157

	Page
APPENDICES	
A. PORTABLE C LIBRARY OF THE TKATCHENKO-SCHEFFLER VAN DER WAALS MODEL	176
B. OCTOPUS SAMPLE INPUT: TS-VDW GROUND-STATE CALCULATION	182
C. OCTOPUS SAMPLE INPUT: TS-VDW EXCITED-STATES CALCULATION	184
D. OCTOPUS SAMPLE OUTPUT: TS-VDW GROUND-STATE CALCULATION	185
E. QUANTUM ESPRESSO SAMPLE INPUT: TS-VDW LIBRARY VALIDATION	205
F. NWCHEM SAMPLE INPUT: CAM-LDA0 TD-DFT CALCUALTION	207
G. CALCULATED EXCITATION ENERGIES FOR SEVERAL HYBRID FUNCTIONALS	208
H. GAMESS SAMPLE INPUT: BASIC MAKEFP RUN	209
I. EFPMD SAMPLE INPUT: BASIC EFP-MD RUN	210
VITA	211
PUBLICATIONS	213

LIST OF FIGURES

Figure	Page
2.1 Graphical description of the Delocalization Error. Adapted from Reference [27].	9
2.2 Lithium-benzene complex. The lithium atom is displaced along the z -axis towards the center of the benzene ring.	11
2.3 Contribution of E_X^{HF} to the total E_X , as a function of the electronic coordinates (r_{12}), for the density-functional approximations employed in this work.	13
2.4 Charge accumulated over the lithium atom as a function of the separation between fragments in the lithium-benzene complex. Noteworthy, charge-distribution schemes produce diverse results. By admixing HF exchange, the description of the charge transfer changes.	15
2.5 Frontier MO energies, as a function of the separation between fragments, for each density functional approximation applied to the lithium-benzene complex. When the HF character of the exchange functional increases, the occupied MOs are stabilized, while unoccupied MOs are destabilized.	20
2.6 Evolution of the lithium-benzene HOMO as a function of the separation between fragments, for HF, PBE0, and PBE. The HOMO adopts one character at long separation and another one at short separation in HF and PBE0, whereas in PBE it exhibits three different characters. Interestingly, at separations shorter than 1.3 Å the HOMO is exclusively localized over the benzene molecule in all cases.	21
2.7 Contributions from s atomic orbitals on lithium to the HOMO of lithium-benzene as a function of the separation between fragments, for each functional applied to the complex.	22
2.8 Contributions from p_z atomic orbitals on lithium to the HOMO of lithium-benzene as a function of the separation between fragments, for each functional applied to the complex.	23

Figure	Page
2.9 Energy of the electronic states as a function of the separation between the plane of benzene and the lithium atom, obtained by the maximum overlap method. The neutral state is plotted with a blue line. The CT state is depicted in green.	25
2.10 Energy of the electronic states as a function of the separation between the plane of benzene and the lithium atom, obtained by the EOM-EA-CCSD method. The ground state (GS) is plotted with a continuous black line. Dotted lines represent the first nine excited states (ES). SOMOs corresponding to the leading configuration of each state are shown at several separations. A crossing between the long-separation ground state, in which the SOMO is mainly localized over lithium, and a CT state, in which the SOMO localizes exclusively over the benzene molecule, occurs at 1.5 Å. . .	28
2.11 Interaction energy of the lithium-benzene complex computed by different methods. The black dotted horizontal line corresponds to the most accurate interaction energy in lithium-benzene found in the literature [43]. The black dotted vertical line indicates the most accurate equilibrium distance [42]. All results of the present work are obtained in 6-31G* basis. . .	30
3.1 Damping function of Equation (3.3). Plotted using a fixed $R_{AB}^{(0)}[n] = 1$, $d = 20$, and $s_R = 0.96$	38
3.2 Parameters of the TS-vdW model as a function of atomic number. Values in atomic units are retrieved from Reference [106].	40
3.3 Visual representation of the change in effective volume of two non-interacting atoms (top) vs. two interacting atoms (bottom). This is the principle through which interactions are modeled in the TS-vdW scheme.	41
3.4 Benzene dimer in the sandwich conformation.	50
3.5 Comparison of the TS-vdW energy computed with two different implementations: Octopus and Quantum Espresso.	51
3.6 Comparison of the interaction energy computed with LDA vs. TS-vdW corrected LDA.	52
3.7 The hydrogen fluoride dimer in anti-parallel conformation.	53
3.8 Absorption cross section spectrum of the hydrogen fluoride dimer with and without van der Waals effects.	54
4.1 Testing set for excitation energies with the LDA-based hybrids.	66
4.2 Comparison of the mean absolute error in eV of the excitation energies computed on the set shown in Figure 4.1.	68

Figure	Page
5.1 Schematic representation of fragments of water. A and B denote the positions of the COM of each fragment, the coordinates of a and b are points on fragments A and B, respectively; and $\mathbf{R} = \mathbf{B} - \mathbf{A}$ is the separation vector between the COM of the fragments.	76
6.1 Schematic representation of the direct coexistence method.	110
6.2 Schematic representation of the methodology of this study. Colors correspond to simulation steps involving the liquid (red), the ice (blue), and both (purple).	113
6.3 Unitary cell of the system after joining the ice and liquid water boxes. . .	116
6.4 Time evolution of the total energy of the system along the trajectory. .	118
6.5 Representative snapshots sampling the time evolution of the configuration of the system along the trajectory.	120
6.6 Oxygen-oxygen RDF of the EFP water model at the simulated temperature and comparison with the reference.	122
6.7 Schematic representation of the statistical analysis.	123
6.8 Statistical analysis of the density at different simulation temperatures. .	124
7.1 Spherical water cluster including 128 fragments.	130
7.2 Execution times comparison for small water clusters of several sizes: all energy contributions scale with the square of the number of fragments. .	132
7.3 Execution times in logarithmic axes: exchange repulsion is the most computationally expensive component of EFP-MD, followed by polarization, electrostatics, and dispersion, respectively.	133
7.4 Relative cost of each energy component with respect to the full calculation. Exchange repulsion proportional cost decays with the size of the system, but it is always at least three times that of polarization.	134
8.1 Illustration representing the idea of the multiple time-step theory of timescale separation. In the example of (b), by separating the time evolution in multiple time-steps polarization (green) is calculated at every step, whereas the exchange repulsion (red) is calculated every five steps and estimated in all other steps	140
8.2 Small cluster of water including 8 fragments.	141
8.3 Comparison of the time-evolution of electrostatics (orange) and polarization (green). The fastest period elapses about 5 to 10 fs.	142

Figure	Page
8.4 The hydrogen bond <i>vibration</i> is the fastest motion determining fluctuations in the electrostatics and polarization potentials.	144
8.5 Comparison of the time-evolution of dispersion (blue) and the exchange repulsion (red). The fastest period elapses about 15 to 20 <i>fs</i>	145
8.6 Comparison of the contributions of each energy term to the total energy. The shaded area represents each of the contributions to the total EFP potential energy. The black line shows the total energy along the trajectory. Features of the electrostatics energy are clearly visible in the total energy. Electrostatics is the main driver in EFP water dynamics.	147

ABBREVIATIONS

BJ	Becke-Johnson
BLYP	Becke88-exchange and Lee-Yang-Parr-correlation
C	Correlation
CAM	Coulomb Attenuated Method
CASPT2	Complete Active Space with Second-order Perturbation Theory
CBS	Complete Basis Set
CCSD	Coupled-cluster with Single and Double excitations
CC2	Second-order Approximate Coupled-cluster
ChElPG	Chemical Electrostatic Potentials using a Grid
COM	Center of Mass
CPU	Central Processing Unit
CT	Charge-transfer
DMABN	4-(N,N-dimethylamino) benzonitrile
DCACP	Dispersion Corrected Atom-centered Potentials
DFT	Density Functional Theory
DMA	Distributed Multipole Analysis
DNA	Deoxyribonucleic Acid
EA	Electron-attachment
EES	Electric Energy Storage
EF	Effective Fragment
EFP	Effective Fragment Potential
EOM	Equation of Motion
ES	Excited-states

ETRS	Enforced Time-reversal Symmetry
FHI-aims	Fritz Haber Institute <i>Ab Initio</i> Molecular Simulations
GGA	Generalized Gradient Approximation
GPL	General Public License
GS	Ground-state
H	Hartree
HF	Hartree-Fock
HOMO	Highest Occupied Molecular Orbital
HXC	Hartree-exchange-correlation
L-BFGS	Limited-memory Broyden-Fletcher-Goldfarb-Shanno
LAP	Local Atomic Potentials
LDA	Local Density Approximation
LMO	Localized Molecular Orbital
LRC	Long-range Correction
LSDA	Local Spin-Density Approximation
LUMO	Lowest Unoccupied Molecular Orbital
MAE	Mean Absolute Error
MBD	Many-body Dispersion
MCDHO	Mobile Charge Densities in Harmonic Oscillators
MCQDPT	Multi-configurational Quasi-degenerate Perturbation Theory
MCSCF	Multi-configurational Self-consistent Field
MD	Molecular Dynamics
MO	Molecular Orbital
MOM	Maximum Overlap Method
MP	Møller-Plesset perturbation theory
MP2	Second-order Møller-Plesset perturbation theory
MP4	Fourth-order Møller-Plesset perturbation theory
MPA	Mulliken Population Analysis
MRPT	Multi-reference Perturbation Theory

MRCI	Multi-reference Configuration Interaction
NBO	Natural Bond Orbital
NPT	Isobaric-Isothermal Ensemble
NVE	Microcanonical Ensemble
NVT	Canonical Ensemble
PA	Polyacetylene
PBC	Periodic Boundary Conditions
PBE	Perdew-Burke-Ernzerhof
PDB	Protein Data Bank
PES	Potential Energy Surface
PP	1-Phenylpyrrole
QM/MM	Quantum-Mechanics/Molecular-Mechanics
RDF	Radial Distribution Function
RPA	Random Phase Approximation
SAPT	Symmetry-adapted Perturbation Theory
SGO	Spherical Gaussian Overlap
SOMO	Singly Occupied Molecular Orbital
TD	Time-dependent
TS-vdW	Tkatchenko-Scheffler van der Waals
VVO	Valence Virtual Orbitals
VWN5	Fifth parametrization of the Vosko-Wilk-Nusair correlation
X	Exchange
XC	Exchange-correlation
XR	Exchange-repulsion

ABSTRACT

Borca, Carlos H. Ph.D., Purdue University, May 2017. Challenges in Molecular Modeling Engaged from Two Distinct Theoretical Perspectives. Major Professor: Lyudmila V. Slipchenko.

My doctoral research has been focused on how to approach intermolecular interactions from two different perspectives: the Effective Fragment Potential (EFP) method and Density Functional Theory (DFT). This dissertation essentially presents a summary of my work on these two fields. The document consists of two parts, each organized in chronological order. Important problems in DFT, such as the accurate description of charge transfer, dispersion, and excited states, are addressed in the first part. The purpose of the second part is two-fold. First, to provide an inclusive, fully-detailed, and up-to-date description of EFP. Hopefully, it will serve as an accessible guide to the theory behind the method, which to the best of my knowledge is still missing in the literature. And second, to engage important challenges in the vastly unexplored field of molecular dynamics (MD) with the EFP method: the determination of the melting point of the EFP water model, analysis of the computational cost of MD simulations with the EFP method, and alternatives to achieve better efficiency when performing these simulations. Additionally, the information compiled in this document intends to be complete enough to guarantee that my work can be reproduced, and to serve as a base for the generation of new ideas in both fields.

1. INTRODUCTION

This thesis consists essentially of two parts: three chapters addressing various topics in the field of Density Functional Theory (DFT), and four chapters engaging challenges in the Effective Fragment Potential (EFP) method. A brief description of each chapter is provided in the following paragraphs.

Starting with the DFT part, Chapter 2 is an exploration of how various approximate functionals and charge-distribution schemes describe ground-state atomic-charge distributions. To understand the trends, comparisons with Hartree-Fock (HF) and correlated post-HF calculations are carried out, confirming that the frontier-molecular-orbitals gap is narrower in semi-local functionals, but wider in hybrid functionals with large fractions of HF exchange. In this project, we analyze and explain why this happens, discuss implications, and conclude that hybrid functionals with an admixture of about one-fourth of HF exchange, such as PBE0 or B3LYP, are particularly useful in describing charge transfer in the lithium-benzene model. These findings have been recently reported in the Journal of Physical Chemistry A [1].

In Chapter 3, the derivation of the equations of the Tkatchenko-Scheffler van der Waals (TS-vdW) method is explained in detail, and a portable implementation of the TS-vdW scheme is presented. In particular, the expressions for the force and the exchange-correlation (XC) potential are derived. The portable *C* library is designed to allow for modular interfacing with codes that use various basis set representations. A pilot implementation in the Octopus code is tested and its results validated with other codes for internal consistency. Exploratory results for both ground- and excited-states properties are presented.

In Chapter 4, a brief review of the theory of hybrid functionals is initially presented, leading to a discussion on why the inclusion of HF exchange, and its long-range-corrected form, dominate over the generalized gradient corrections in the improvement of the quality of the fundamental gap and the enhancement excitation-energy estimations. As an illustration, the CAM-LDA0 method is introduced: a three-parameter functional, with 1/4 global and 1/2 long-range HF interaction, respectively; a range separation factor of 1/3; and pure LDA exchange and correlation. It is shown that CAM-LDA0 works for electronic excitations as well as the CAM-B3LYP functional, with the advantage of reduced computational cost due to the omission of the convoluted generalized gradient corrections. These findings have also been recently reported in the Journal of Physical Chemistry A [2].

Chapter 5 transitions to the EFP method. It serves as an introduction to the topic and provides basic information about its working mechanism. It intends to provide an accessible guide to EFP. The chapter starts with a quick historical perspective. Subsequently, the most common derivations for each energy term of the purely-classical method are described. Finally, it concludes with a short explanation of the basic steps required to run an EFP calculation.

In Chapter 6, the thermodynamic equilibrium between water and ice is explored using molecular dynamics (MD) with the EFP method. Important characteristics of the EFP water model are discussed based on the time evolution of the energy, and average properties, such as the radial distribution functions (RDF) and the density. The melting point of the EFP ice is calculated based on the analysis of the evolution of the total energy along simulations in the isothermal-isobaric ensemble at different temperatures. Unfortunately, a similar investigation [3] was published before this study could be submitted for peer-review consideration. Notwithstanding, this chapter summarizes the results obtained in the effort, which coincide with what was reported in the aforementioned article.

Chapter 7 presents an exploration of the computational efficiency of MD simulations with the EFP method. Using EFP-MD simulations on small clusters of water,

the computational demands of each of the energy terms of the EFP method are analyzed. A discussion on the computational scaling and cost pre-factor of each term is presented, leading to the conclusion that the exchange-repulsion (XR) term is the most demanding. Being at least three times more expensive than polarization, XR is the bottleneck interaction in EFP-MD.

Chapter 8 explores how to exploit the inherent timescale separation between energy contributions to accelerate MD simulations with the EFP method. It is shown that XR interactions are mildly dependent on molecular orientation and evolve slowly with respect to the other types of interactions in the EFP method. Therefore, a Taylor expansion, updated intermittently, allows for an estimation of the XR term offering the possibility to improve the efficiency of EFP-MD simulations in small- and medium-sized systems.

Finally, a short summary of the most important messages of each project and perspectives for future research derived from this work, are presented in Chapter 9. Concluding this thesis, the summary chapter also mentions briefly other projects in which I have been involved throughout my doctoral studies.

PART ONE

2. GROUND-STATE CHARGE TRANSFER IN DENSITY FUNCTIONAL THEORY

2.1 Introduction

Kohn-Sham DFT is one of the most popular electronic structure methods applied throughout science and engineering [4]. However, most density-functional approximations have intrinsic problems related to delocalization and self-interaction errors, which undermine the description of charge transfer.

An accurate description of these phenomena is essential in modeling of novel electric energy storage systems such as supercapacitors, which are becoming increasingly used in the development of clean and renewable energy technology.

In this chapter, I present an exploration of how various approximate functionals and charge-distribution schemes describe ground-state atomic-charge distributions in the lithium-benzene complex, a model system of relevance to carbon-based supercapacitors [1].

To understand the trends, HF and correlated post-HF calculations are used for comparison, confirming that the approximated fundamental gap is narrower in semi-local functionals, but widened by hybrid functionals with large fractions of HF exchange.

For semi-local functionals, natural bond orbital (NBO) and Mulliken schemes yield opposite pictures of how charge transfer occurs. Furthermore, the partial charges in conjugated materials depend on the interplay between the charge-distribution scheme employed and the underlying XC functional, being critically sensitive to the admixture of HF exchange. An analysis and explanation of why this happens is presented, implications are discussed, and it is concluded that hybrid functionals with an admix-

ture of about one-fourth of HF exchange are particularly useful in describing charge transfer in the lithium-benzene model.

2.1.1 Motivation

Climate change and the increasing demand of limited fossil fuels are concerning for both the scientific community and society at large [5,6]. Around the world, efforts to produce renewable and clean energy are supported by governments and private sectors [7]. The creation of more powerful electric energy storage (EES) systems is one of the main challenges in the area, and porous carbon materials have great potential for the construction of novel EES devices such as supercapacitors [8,9].

Due to experimental limitations, high costs of nanotechnology research, and importance of quantum effects, computational-aided fabrication of carbon materials for supercapacitors is promising [10–13]. Often, classical force fields provide useful data for calculations of chemical stability, adsorption and desorption dynamics, and other properties of these materials [14]. Yet, the exploration of quantum phenomena such as charge transfer, which is at the heart of the working mechanism of supercapacitors, requires *ab initio* treatment.

The goal of this study is to investigate whether standard approximations in Kohn-Sham DFT [15,16], when used in combination with popular charge-distribution schemes [17], provide an adequate description of the ground-state charge transfer that occurs in a very simple model system: the lithium-benzene complex. Some of the key features observed in this system are due to the interaction between a lithium atom that can be easily ionized and a benzene ring whose valence electrons are delocalized due to aromaticity, so these observations are relevant to the much more complex simulations of carbon nanoporous electrodes in supercapacitors [18], where such interactions are ubiquitous. More generally, the question is how different charge-distribution schemes perform for various families of approximate XC functionals, and understand the trends.

2.1.2 Theory

In Kohn-Sham DFT, the time-independent Schrödinger equation of a fictitious system of non-interacting electrons that generates the same density as a given system of interacting electrons, is solved. This is known as the Kohn-Sham equation. Using atomic units:

$$\left\{ -\frac{1}{2} \nabla_i^2 + v_s(\mathbf{r}) \right\} \phi_i(\mathbf{r}) = \varepsilon_i \phi_i(\mathbf{r}), \quad (2.1)$$

where \mathbf{r} is the electronic coordinate, ε_i is the energy of the Kohn-Sham orbital, $\phi_i(\mathbf{r})$, and $v_s(\mathbf{r})$, is the effective potential acting on the system, known as the Kohn-Sham potential, and it consist of the external potential and electron-electron interactions.

Given that electrons do not interact explicitly, the density for this N -electron system, $n(\mathbf{r})$, can be defined as the sum of the squares of the Kohn-Sham orbitals:

$$n(\mathbf{r}) = \sum_{i=1}^N |\phi_i(\mathbf{r})|^2; \quad (2.2)$$

then, the ground-state energy of the system is defined as

$$E[n] = F[n] + \int d^3\mathbf{r} v_{\text{ext}}(\mathbf{r}) n(\mathbf{r}), \quad (2.3)$$

where $v_{\text{ext}}(\mathbf{r})$ is the non-universal external potential that is unique for each system. $F[n]$ is known as the universal functional¹ from Levy's constraint search [19,20] which can be decomposed as the kinetic energy of the non-interacting electron gas, $T[n]$, and the Hartree-exchange-correlation (HXC) energy, $E_{\text{HXC}}[n]$, a functional that represents the interactions between electrons,

$$F[n] = T[n] + E_{\text{HXC}}[n]. \quad (2.4)$$

In Kohn-Sham DFT the kinetic-energy term is conveniently approximated by taking the sum of the kinetic energies of the Kohn-Sham orbitals:

$$T_S[n] = \min_{\Phi_s \rightarrow n} \langle \Phi_s | \hat{T} | \Phi_s \rangle = -\frac{1}{2} \sum_{i=1}^N \int d^3\mathbf{r} \phi_i^*(\mathbf{r}) \nabla^2 \phi_i(\mathbf{r}), \quad (2.5)$$

¹Squared-bracket functional notation is employed throughout. Dependence on \mathbf{r} is left implicit in functional notation.

where Φ_s is the Slater determinant that corresponds to the density $n(\mathbf{r})$. In addition, the $E_{\text{HXC}}[n]$ can be further decomposed in a Coulomb-repulsion (H) term and an XC term,

$$E_{\text{HXC}}[n] = E_{\text{H}}[n] + E_{\text{XC}}[n]. \quad (2.6)$$

The repulsion term, $E_{\text{H}}[n]$, is generally known as the Hartree-energy functional, and is defined in a way similar to wave-function methods:

$$E_{\text{H}}[n] = \frac{1}{2} \int d^3\mathbf{r} \int d^3\mathbf{r}' \frac{n(\mathbf{r}) n(\mathbf{r}')}{|\mathbf{r} - \mathbf{r}'|}. \quad (2.7)$$

The exact form of the exchange-correlation-energy functional, $E_{\text{XC}}[n]$, is unknown. Hence approximations are required. Usually $E_{\text{XC}}[n]$ is split in the exchange-energy functional, $E_{\text{X}}[n]$, and the correlation-energy functional, $E_{\text{C}}[n]$,

$$E_{\text{XC}}[n] = E_{\text{X}}[n] + E_{\text{C}}[n]. \quad (2.8)$$

The main idea behind rational density-functional development is to find approximations to $E_{\text{XC}}[n]$ that satisfy the simple exact conditions known for the limit behavior of the universal functional and that, at the same time, reach high chemical accuracy.

One of those conditions, known for one-electron systems, is that $E_{\text{HXC}}[n]$ must vanish,

$$E_{\text{HXC}}[n] = E_{\text{H}}[n] + E_{\text{X}}[n] + E_{\text{C}}[n] = 0. \quad (2.9)$$

If the requirement of Equation (2.9) is not met, there is a case of what is called the self-interaction error [21–25], meaning that the density of one electron is interacting with itself producing a spurious $E_{\text{HXC}}[n]$.

Additionally, in one-electron systems, $E_{\text{C}}[n]$ must be equal to zero because there is only one electron, thus the $E_{\text{H}}[n]$ must be equal to minus $E_{\text{X}}[n]$,

$$E_{\text{H}}[n] = -E_{\text{X}}[n]. \quad (2.10)$$

As is well known, however, approximate DFT calculations suffer from problems that need to be addressed [26]. For instance, most standard approximations to the

XC functional underestimate charge-transfer (CT) excitation energies and overestimate binding energies of CT complexes [27, 28]. Mori-Sanchez et al. [29] and Cohen et al. [30] demonstrated that this problem can be traced back to the delocalization error of approximate functionals: their tendency to minimize the energy by unrealistically spreading-out the electronic density, especially at large separations between the fragments involved in the charge transfer. As discussed by Cohen et al. [27], this inaccuracy is closely related to the self-interaction error, and it is caused by the unphysical convex behavior of the energy as a function of fractional charge.

For example, standard functionals work well around the equilibrium separation in H_2^+ , but they fail as the molecule is stretched. In an ensemble representation, at infinite separation, there should be two H atoms with half an electron each. Then, the exact energy of an atom, as a function of the charge, is a straight-line interpolation between integers [31], because of the discrete nature of electrons. However, functionals incorrectly convex the energy between the charge integers yielding incorrect energies in cases where there are atoms with fractional charges [32], as depicted in Figure 2.1.

Rational design of functionals is based on improvements gained by considering universal constraints, rather than using empirical parameters, in order to create more universally useful functionals. Perdew and Schmidt have proposed a hierarchy, the Jacob's ladder for functional sophistication [33]. It starts with HF on the ground level, considering no correlation. The first three rungs are the local density approximation (LDA), the generalized gradient approximation (GGA), and the meta-GGA. Local and semi-local approximations are useful, given their computational efficiency and non-empirical nature. They are followed by the hybrid functionals, which are the most used functionals in chemistry, and tend to be more accurate for equilibrium properties. Generally, this rung of functionals includes some fitted parameters, and many of them include a HF-exchange term, E_X^{HF} , to better capture the long-range interactions. Currently, the ladder ends up with the random-phase approximations (RPA), though it is intended to eventually lead to the universally-exact density functional.

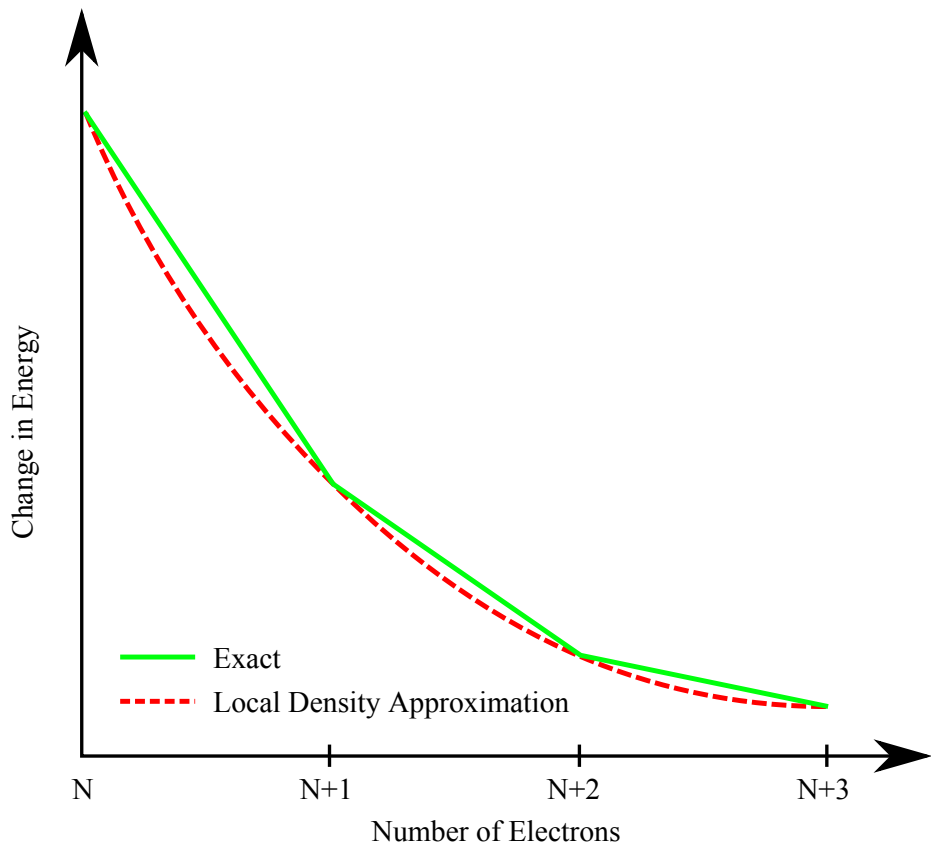


Figure 2.1. Graphical description of the Delocalization Error.
Adapted from Reference [27].

2.1.3 Background

Properties of alkali-conjugated complexes have been explored in several computational studies [34–40]. For instance, studying the conformation of complexes of lithium and C₆₀ fullerenes, Varganov et al. found a strong ionic interaction between the atom and the fullerene [41]. The structures and dissociation energies of lithium and benzene sandwich complexes were researched by Vollmer et al. using several quantum-mechanical methods [35]. Kang studied the formation of neutral lithium-aromatic complexes and found that it originates in the charge transfer from the lithium atom to the aromatic rings [36]. An emerging discussion about the existence of charge transfer between lithium and aromatic carbon compounds motivated Ferre-Vilaplana [37] and Martinez et al. [38] to look into the lithium-benzene

complex. Marshall et al. explored cation- π interactions, modeling the approach of alkali-cations to a benzene ring from different angles and inclinations pointing out that non-perpendicular interactions in cation-benzene complexes are attractive [39].

In response to the controversy about charge transfer, Baker and Head-Gordon [42] studied a set of polyaromatic carbon systems with lithium, which included the lithium-benzene complex, and suggested that some density-functional approximations may produce artificial charge transfer due to the self-interaction error, whereas HF underestimates the amount of charge transfer as a result of overlocalization. Inspired by that work, Denis and Iribarne [43] used the lithium-benzene complex as a prototype system to understand the interaction in lithium-doped carbon compounds, focusing on the relationship between its symmetry and stability. Employing highly sophisticated techniques, they concluded that charge transfer does indeed occur.

Two questions that are relevant in this context are asked here: (1) What do popular charge-distribution schemes tell about ground-state charge transfer in the lithium-benzene complex; (2) How does the answer to the first question depend on the approximation employed for the XC functional? As will be made clear, the admixture of HF exchange in the functional plays a critical role. Resorting to HF and post-HF multi-state calculations, I explain why. First, a summary of the computational methods employed is presented in the next section.

2.2 Computational Methods

Ground-state electron transfer is studied as a function of the separation between a lithium atom and the center of a benzene ring. A potential energy surface (PES) rigid scan is performed along the coordinate of separation between the center of mass (COM) of the benzene molecule and the lithium atom, perpendicular to the plane of benzene (see Figure 2.2). This is done in a series of unrestricted single-point calculations [44], where the lithium atom advances towards the benzene molecule along the main symmetry axis, while the geometry of the benzene molecule, optimized with B3LYP/6-31G*, is kept fixed. The atom starts its path towards the ring at 7.0 Å,

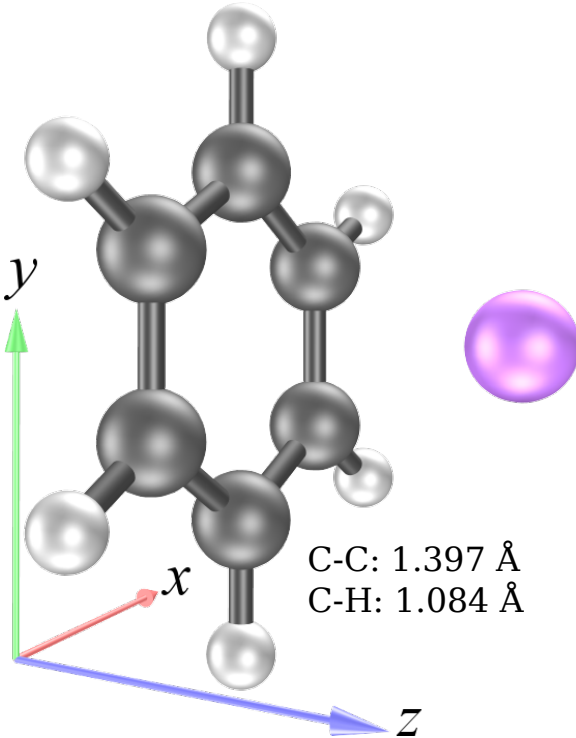


Figure 2.2. Lithium-benzene complex. The lithium atom is displaced along the z -axis towards the center of the benzene ring.

moving at 0.1 \AA steps, and totaling 71 points. Initial separation of 7.0 \AA guarantees minimal interaction between the two fragments. The electronic structure and the atomic charge on lithium are analyzed as a function of separation. For consistency, all calculations are carried out with the same basis set, 6-31G*, in the computational chemistry package Q-Chem 4.3 [45–47]. The self-consistent field convergence criteria are chosen such that the direct inversion in the iterative subspace error is below 1.0×10^{-9} . For each geometry, the lowest energy solution was found by employing the maximum overlap method (MOM) [48] when necessary.

Two sets of approximate functionals are employed (Table 2.1). Each set has functionals from different rungs in Perdew’s Jacob’s ladder of approximations [4] or levels of sophistication.

On the one hand, PES calculations are performed with PBE [49], PBE0 [50, 51], PBE50 [52], and LRC- ω PBEPBE [53] functionals. PBE is a non-empirical GGA with

Table 2.1.
Composition of exchange and correlation functionals of the PBE and BLYP families.

Functional	Exchange	Correlation
PBE	E_X^{PBE}	E_C^{PBE}
PBE0	$0.75E_X^{\text{PBE}} + 0.25E_X^{\text{HF}}$	E_C^{PBE}
PBE50	$0.50E_X^{\text{PBE}} + 0.50E_X^{\text{HF}}$	E_C^{PBE}
BLYP	E_X^{B88}	E_C^{LYP}
B3LYP	$0.08E_X^{\text{Slater}} + 0.72E_X^{\text{B88}} + 0.20E_X^{\text{HF}}$	$0.19E_C^{\text{VWN5}} + 0.81E_C^{\text{LYP}}$

exchange and correlation expressions derived from physical constraints. The hybrids PBE0 and PBE50 are prepared by admixing 25% and 50% of E_X^{HF} , respectively, as this inclusion is believed to improve atomization energies, energy barriers, and energy gaps in materials without impacting computational performance [54, 55]. A different way of including a fraction of E_X^{HF} in hybrids is through the Long-Range Correction (LRC), as in LRC- ω PBEPBE. In LRC functionals the $1/r_{12}$ dependence of the exchange potential is decomposed into an error function of ωr_{12} , which accounts for the amount of E_X^{HF} and governs the long-range behavior, and its complementary, which corresponds to pure-DFT exchange, E_X^{DFT} , and rules short-range interactions, as shown in Figure 2.3. ω is a range-separation parameter that adjusts the distance at which the E_X^{DFT} vanishes.

On the other hand, BLYP [56], B3LYP [57], and CAM-B3LYP [58] were used. BLYP is a simple GGA constructed by putting together the pure-DFT Becke88 exchange [59] and the Lee-Yang-Par correlation [60] functionals. Replacing the exchange with a mixture of Slater [15, 16, 61], Becke88, and HF exchange, and combining VWN5 [62] and LYP correlation, produces the highly popular B3LYP hybrid. CAM-B3LYP is another LRC hybrid prepared by using an attenuated Coulomb interaction to correct the long-range exchange. The decomposition of $1/r_{12}$ in the calculation of

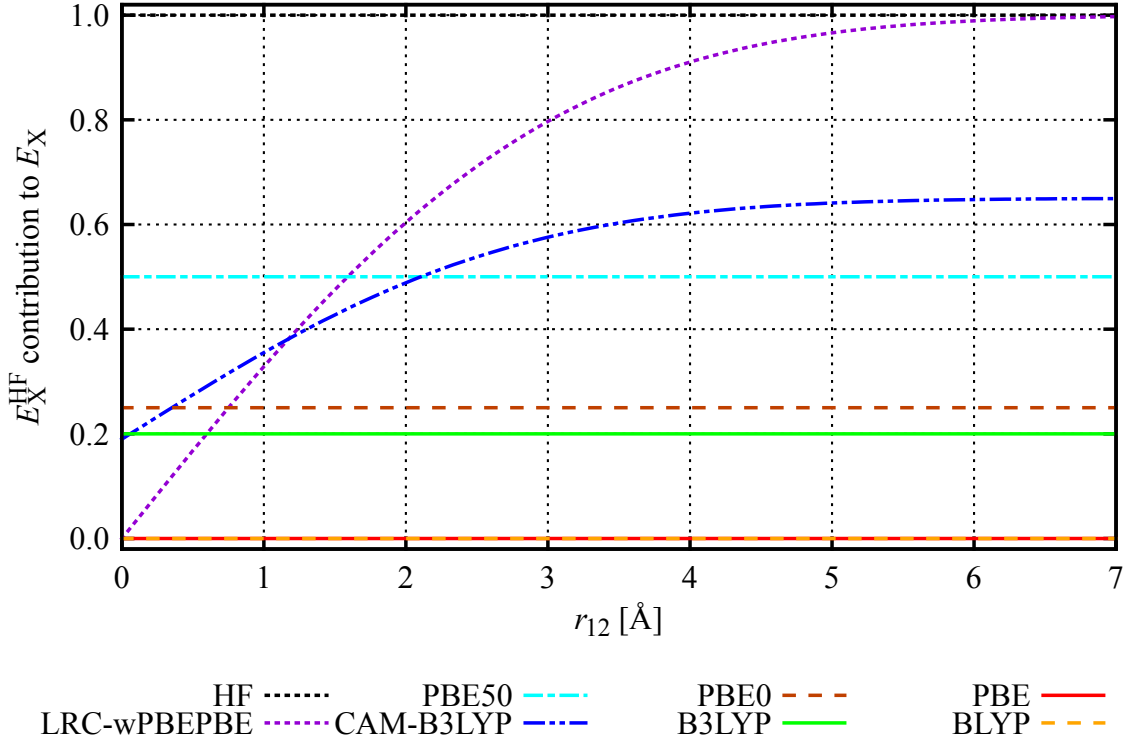


Figure 2.3. Contribution of E_X^{HF} to the total E_X , as a function of the electronic coordinates (r_{12}), for the density-functional approximations employed in this work.

E_X is done by including two parameters. The second parameter avoids vanishing of E_X^{HF} at short distances and of E_X^{DFT} at long distances. Notably, CAM-B3LYP does not include Slater exchange, as opposed to B3LYP.

In addition to the DFT calculations, lithium-benzene interaction energies are computed with HF, second- and fourth-order Møller-Plesset perturbation theory (MP2, MP4) [63], and coupled-cluster with single and double excitations method (CCSD) [64,65].

To better understand charge transfer behavior, the equation-of-motion coupled-cluster method with single and double excitations for electron attachment (EOM-EA-CCSD) [66–68] is employed. EOM-EA-CCSD provides information on both ground- and excited-states PESs, allowing to relate charge transfer to the interaction of the

ground (GS) and excited states (ES) that have CT character. Chemically important regions of the excited-states PESs are computed on a tighter grid, such that the whole PES comprises 221 points computed with uneven displacements ranging from 0.005 Å to 0.1 Å.

The partial charge on the lithium atom is computed by means of Mulliken Population Analysis (MPA) [69], NBO theory [70], Chemical Electrostatic Potentials using a Grid (ChElPG) [71], as well as a simple estimate based on the dipole moment, μ :

$$Q_A^{\mu/z}(z) = \frac{\|\boldsymbol{\mu}\|}{z}, \quad (2.11)$$

where z is the separation between fragments and $\boldsymbol{\mu}$ is the dipole-moment vector defined as:

$$\boldsymbol{\mu} = \int d^3\mathbf{r} n(\mathbf{r}) z \hat{k}, \quad (2.12)$$

where $n(\mathbf{r})$ is the ground-state electron density and \hat{k} is the z -direction unitary vector.

Interaction energy curves are calculated as the difference between the total ground-state energy of the system, at each point, and the sum of the energies of the isolated fragments: the benzene molecule and the lithium atom,

$$E_{\text{int}}(z) = E_{\bigcirc\ldots\text{Li}}(z) - (E_{\bigcirc} + E_{\text{Li}}). \quad (2.13)$$

2.3 Results and Discussion

The discussion is divided into five parts. The first two parts analyze in detail atomic charges and molecular orbitals (MOs). The next two sections compare (single-state) DFT results with those of a multi-state approach. The final section discusses the description interaction energies.

2.3.1 Charge Distributions

The results of the charge-distribution analyses are summarized in Figure 2.4, where it can be verified that the calculated charge on the lithium atom depends strongly on both the nature of the approximate XC functional and the charge-distribution scheme employed. The discussion on the latter dependence comes first.

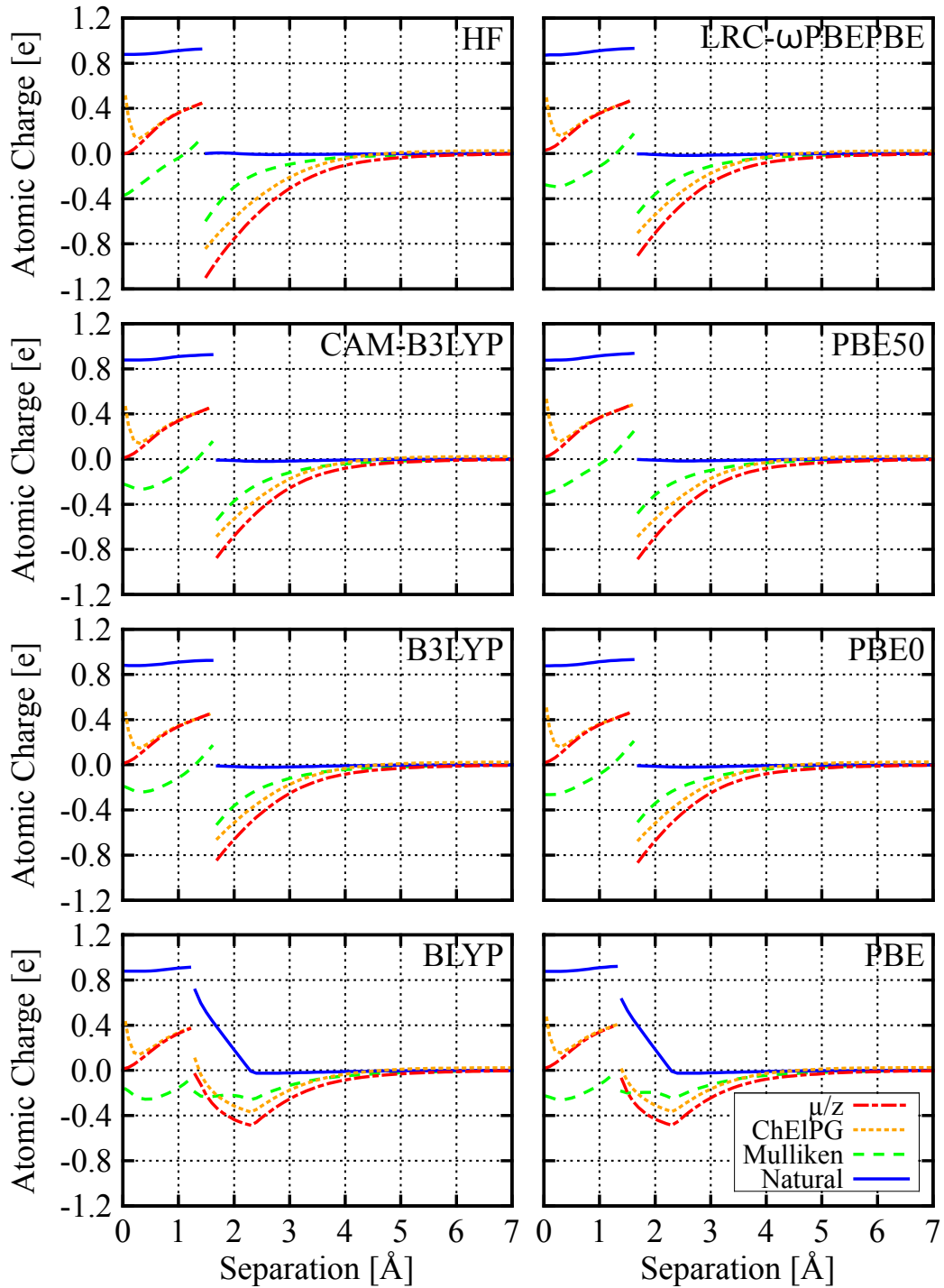


Figure 2.4. Charge accumulated over the lithium atom as a function of the separation between fragments in the lithium-benzene complex. Noteworthy, charge-distribution schemes produce diverse results. By admixing HF exchange, the description of the charge transfer changes.

Interestingly, in Figure 2.4, natural charges from NBO (blue, solid lines) and Mulliken charges (green, long-dashed lines) show opposite results. The Mulliken charge on lithium tends to be negative. This can be understood by examining the definition of the Mulliken charge for open-shell systems. The charge belonging to atom A , Q_A^{MPA} , is expressed by

$$Q_A^{\text{MPA}} = Z_A - \sum_{\nu \in A} \sum_{\mu} \sum_i \left(C_{\mu i}^{\alpha} C_{\nu i}^{\alpha*} + C_{\mu i}^{\beta} C_{\nu i}^{\beta*} \right) S_{\mu \nu}, \quad (2.14)$$

where Z_A is the atomic number of atom A , $C_{\mu i}^{\alpha}$ and $C_{\nu i}^{\alpha*}$ are the matrix elements representing the alpha coefficients of the basis functions μ and ν , respectively, in the i -th MO, and $S_{\mu \nu}$ is the matrix element representing the overlap-integral between basis functions μ and ν . The same notation applies for beta orbitals, substituting the α superscript by β . The second term on the right-hand side, often called gross atomic product, is computed by taking the sums of the product of the coefficients of two basis functions and their overlap. If several basis functions overlap on the lithium atom, which is the case at short distances, the corresponding gross atomic product increases, making the Mulliken charge more negative.

These effects had been previously observed, in general by Reed et al. [72] and Kim et al. [73], and in particular for the lithium-benzene complex by Vollmer et al. [35]. They pointed out that Mulliken populations and charges are highly susceptible to the basis set employed and become ambiguous when utilized with diffuse basis sets.

ChElPG is an alternative to explore atomic charges. It uses the electrostatic potential computed from the system's wave function on a grid, and then tries to match that potential by optimizing a set of trial point charges located at the nuclei. ChElPG curves (orange, short-discontinuous lines in Figure 2.4) are smooth at long and medium distances, in agreement with those of Mulliken. However, as the atom moves towards the cavity formed by the benzene ring, ChElPG shows a sheer behavior when the atom is too close to the ring's surface and the electrostatic potential is poorly described.

The dipole-based scheme of Equation (2.11) (red, dotted lines in Figure 2.4) agrees qualitatively with Mulliken and ChEIPG at medium and large distances, but the scheme clearly breaks down at short separations, where the classical expression for the dipole as generated by point charges is not adequate.

In contrast to other schemes, the variations of the natural charge on the lithium atom are solely due to changes in the occupation of bonding and non-bonding orbitals. In the NBO theory, orbitals are classified into three groups: non-bonding natural atomic orbitals, orbitals involved in bonding and anti-bonding, and Rydberg-type orbitals. Atomic and Rydberg orbitals are made of basis functions of single atoms, whereas bonding and anti-bonding orbitals are a combination of basis functions of two atoms. This resembles Lewis' idea of core, lone pair, and valence electrons. Thus, the NBO procedure treats the bonding and anti-bonding orbitals as linear combinations of two-atom basis functions, while Mulliken analysis treats all the orbitals as linear combinations of two-atom basis functions [17]. At the end, an orthonormal set of localized maximum-occupancy orbitals is produced. The leading N members of this set give a Lewis-like description of the total electron density.

Notably, the NBO scheme reveals extreme behaviors, showing either no charge accumulation on lithium at long separations, or a sudden change in the lithium charge at short separations. BLYP and PBE are the exceptions, showing an intermediate region in which there is an incremental accumulation of positive charge. In all cases, the lithium natural charges at short separations become positive and close to 1 e .

Different charge-distribution schemes thus provide qualitatively different results. Natural charges have the advantage of not being as susceptible to basis-set issues as Mulliken charges or to surface effects as ChEIPG charges [35]. As it will be shown in the next section, natural charges are in agreement with the analysis of the MOs for this system.

Figure 2.4 also provides a comparison between approximate XC functionals of similar complexity. At long distances, all DFT calculations and HF go to the correct separation limit with no partial charges on either fragment. At short separations,

all functionals and HF predict charge transfer from lithium to benzene. However, pure-DFT functionals, BLYP and PBE, show a different picture at intermediate separations. Namely, all charge schemes reveal a growth of fractional, positive charge on the lithium atom in the region between 2.3 Å and 1.3 Å for these two functionals. To understand this, valence MOs are analyzed next.

2.3.2 Frontier Molecular Orbitals

In Figure 2.5 the energies of relevant alpha MOs are plotted. A interdependence between the qualitative description of charge transfer described in the previous section, the energy difference between the highest occupied molecular orbital (HOMO) and the lowest unoccupied molecular orbital (LUMO), the character of the frontier MOs, and the contribution of E_X^{HF} becomes evident. For more clarity, the discussion of the the results of the functionals of the PBE family, shown on the right-hand side of Figure 2.5 comes first, and they are compared with HF (top left).

The HOMO-LUMO gap (also known as the approximated fundamental gap) width at *large* separation follows the trend:

$$\text{HF} > \text{LRC-}\omega\text{PBEPBE} > \text{PBE50} > \text{PBE0} > \text{PBE}.$$

Generally, the gap width decreases due to the stabilization of unoccupied orbitals (dotted lines) and destabilization of occupied orbitals (continuous line), following the same trend. Notably, for separations between 1.3 Å and 2.3 Å PBE and BLYP have no gap, promoting delocalization.

As shown in Figure 2.4, all charge distribution schemes except for NBO show some degree of charge transfer even at medium distances, reflecting HOMO delocalization between the lithium atom and the benzene ring. This is a manifestation of HOMO hybridization. When the character of the HOMO changes, it produces discontinuities in atomic-charge curves. PBE is the most interesting case, so it is discussed in detail using Figure 2.6, which compares HOMOs, at three characteristic separations, in HF (2.6(a), 2.6(d), 2.6(g)), PBE0 (2.6(b), 2.6(e), 2.6(h)), and PBE (2.6(c), 2.6(f), 2.6(i)). Figures 2.7 and 2.8 provide additional details supporting this discussion.

On the one hand, as shown in the top row of Figure 2.6, the contribution from benzene's π bonding orbital (or A_{2u})² to the long-range HF HOMO increases as the separation shortens, implying that the weight from benzene's basis functions is becoming predominant in the complex. As the atom approaches the ring, larger portions of lithium's p_z and benzene's p_z basis functions are incorporated into the HOMO, at the expense of a smaller share of lithium's s atomic orbitals (compare illustrations in Figures 2.6(d) with 2.6(g) and see Figures 2.7 and 2.8). Notwithstanding, there is no evidence of charge transfer in Figures 2.6(d) and 2.6(g) since the lithium atom always contributes to the HOMO.

On the other hand, inspection of the PBE HOMO at the bottom in Figure 2.6 suggests that at *large* separation it has a main contribution from lithium's s orbital and a minor contribution from benzene's A_{2u} orbital, similar to HF (compare Figures 2.6(g) and 2.6(i), and see Figures 2.7 and 2.8). Nonetheless, the contribution from p_z orbitals from both lithium and benzene is marginally greater in PBE, while the weight of lithium's s basis functions slightly decreases. This is reflected in a smoother and slightly more spread-out surface of the PBE HOMO over the benzene ring.

At *medium* separations, the character of the HOMO in PBE changes, in contrast with HF (compare Figures 2.6(d) and 2.6(f)). Instead of having an important contribution from benzene's π (A_{2u}), we see a predominant π^* (E_{2u}) anti-bonding character in PBE. In the same range of separations (1.3-2.3 Å), HOMO and LUMO energy curves in PBE become degenerate and experience a kink (see Figure 2.5). In this region, the frontier MOs consist of the E_{2u} orbital of benzene and a $s-p_z$ hybridized orbital on lithium (see Figure 2.6(f)). Also, natural charges suggest that this intermediate state involves a partial charge transfer between the lithium atom and benzene molecule (see Figure 2.4).

At *short* separations, PBE predicts complete electron transfer from lithium to benzene. The HOMO localizes over the benzene ring and misses any contribution from lithium's basis functions. Additionally, the character of the HOMO and LUMO

²Here and later benzene orbital symmetries are based on D_{6h} point group.

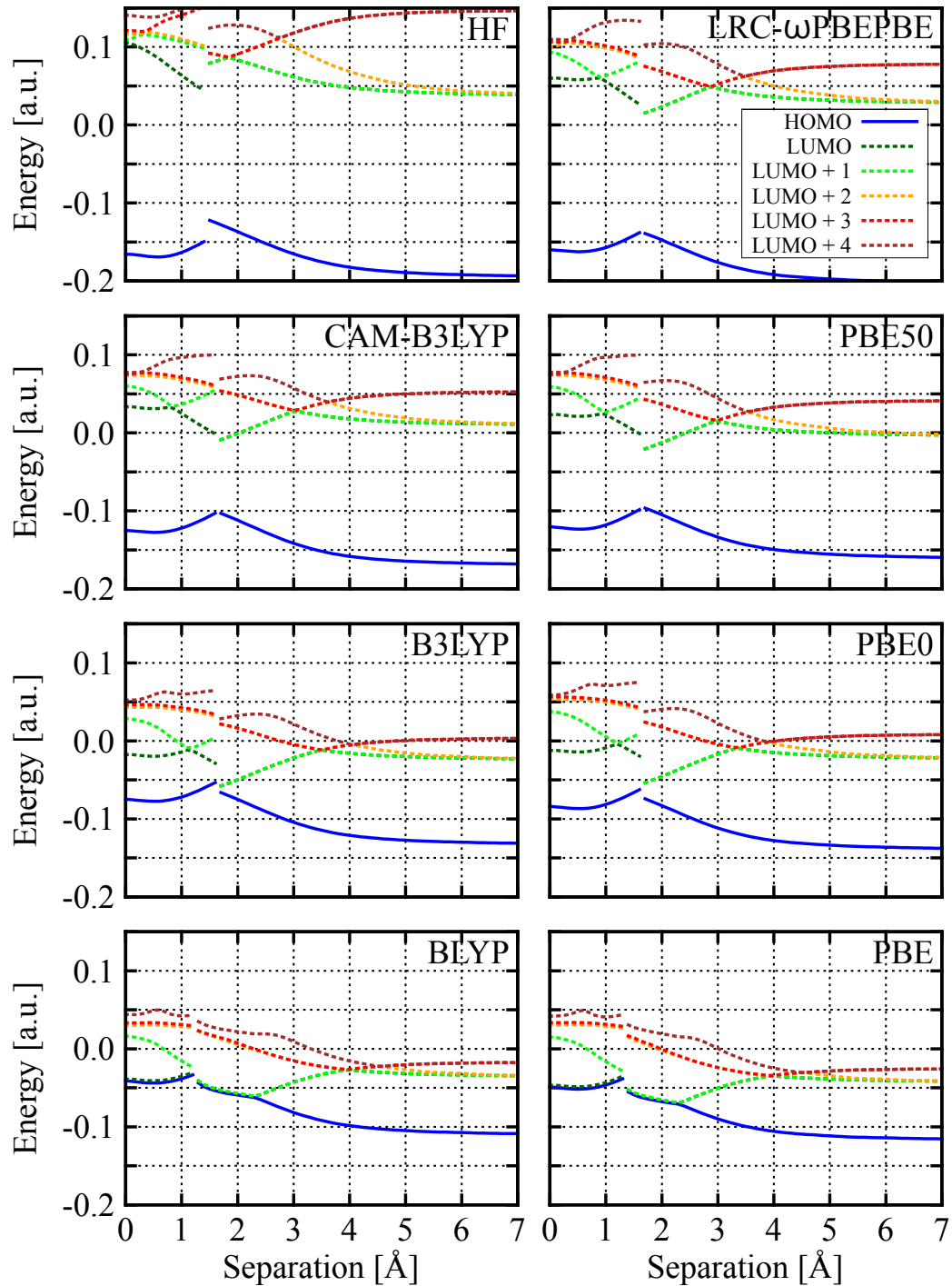


Figure 2.5. Frontier MO energies, as a function of the separation between fragments, for each density functional approximation applied to the lithium-benzene complex. When the HF character of the exchange functional increases, the occupied MOs are stabilized, while unoccupied MOs are destabilized.

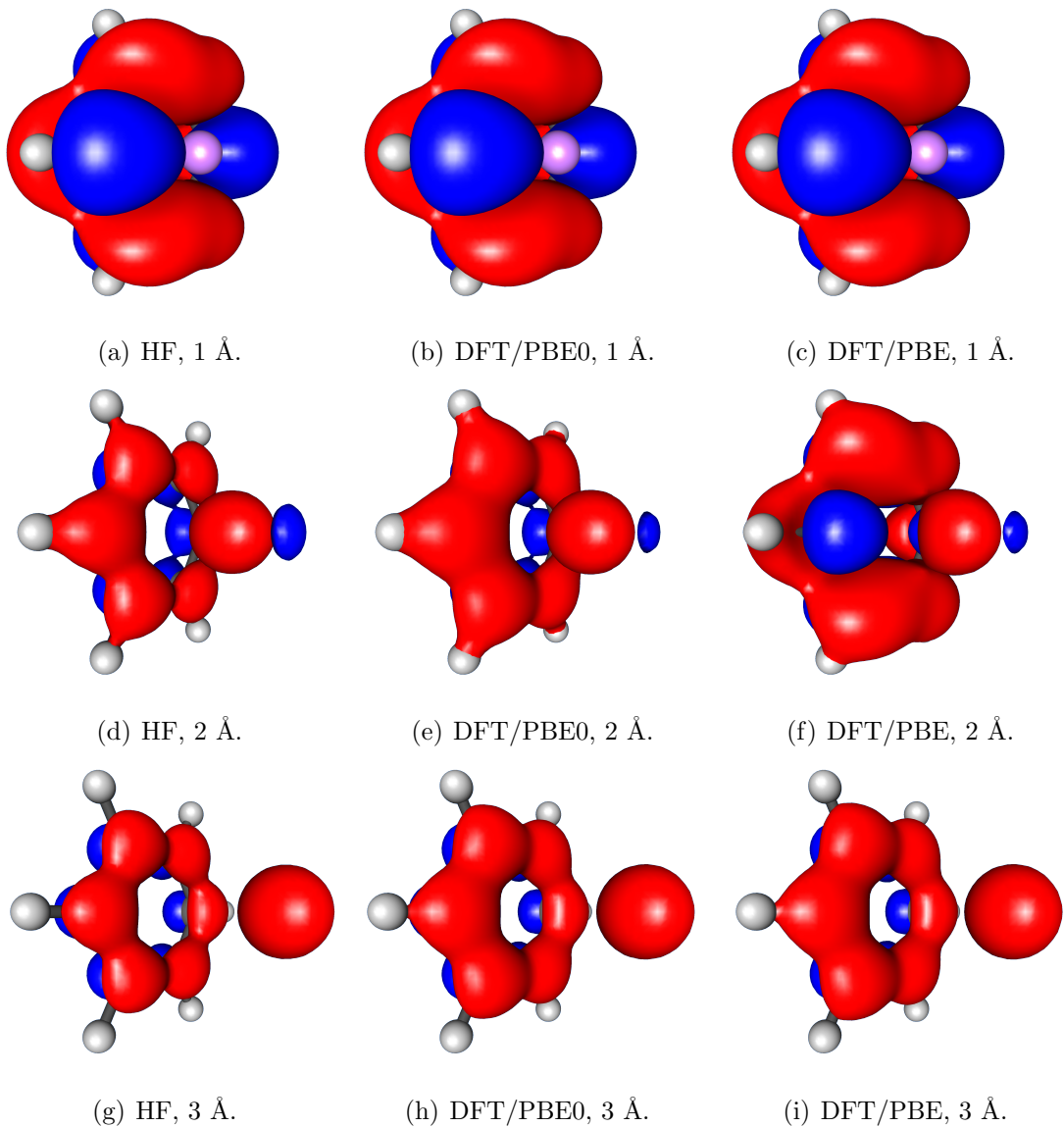


Figure 2.6. Evolution of the lithium-benzene HOMO as a function of the separation between fragments, for HF, PBE0, and PBE. The HOMO adopts one character a long separation and another one at short separation in HF and PBE0, whereas in PBE it exhibits three different characters. Interestingly, at separations shorter than 1.3 Å the HOMO is exclusively localized over the benzene molecule in all cases.

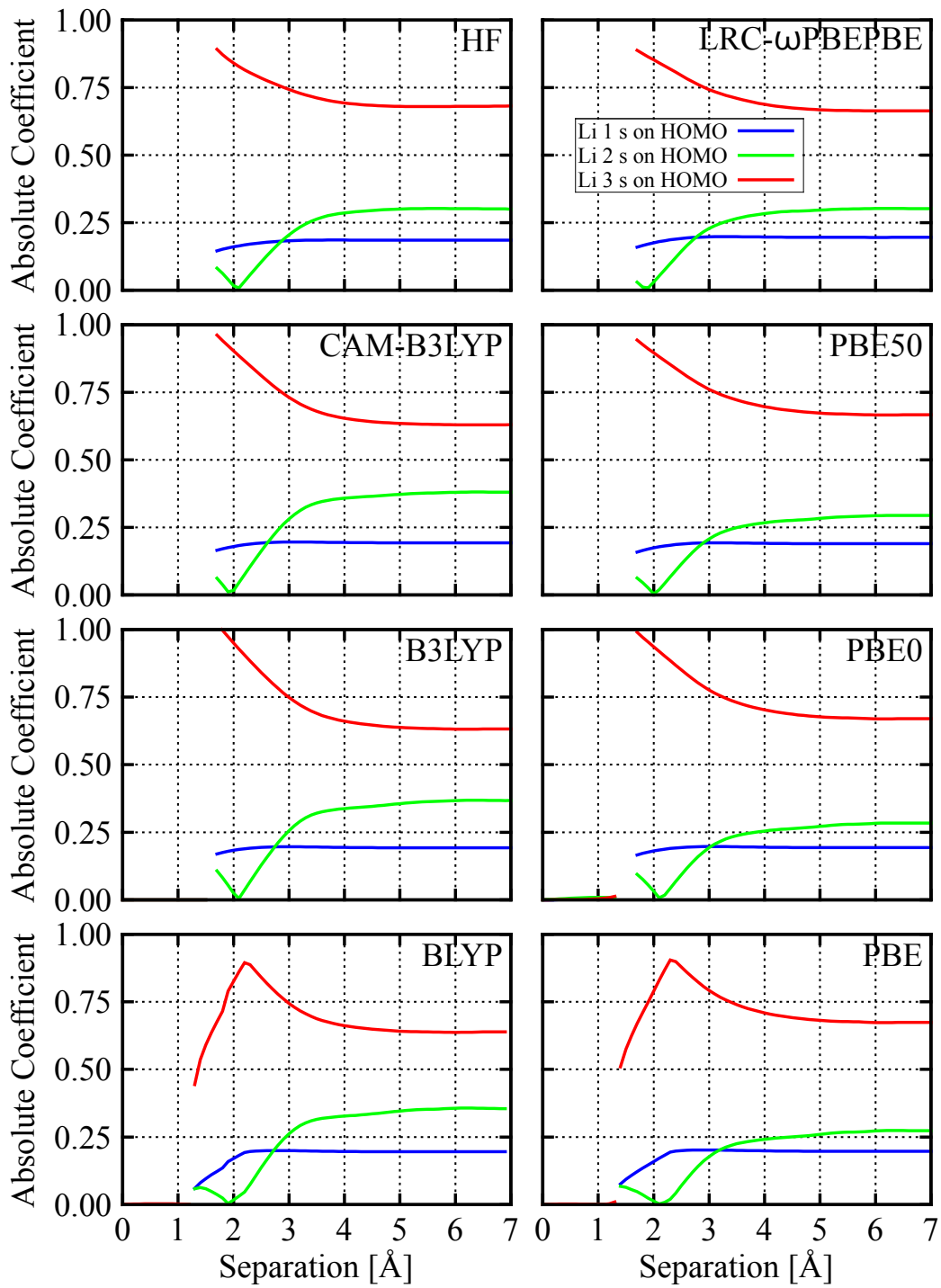


Figure 2.7. Contributions from s atomic orbitals on lithium to the HOMO of lithium-benzene as a function of the separation between fragments, for each functional applied to the complex.

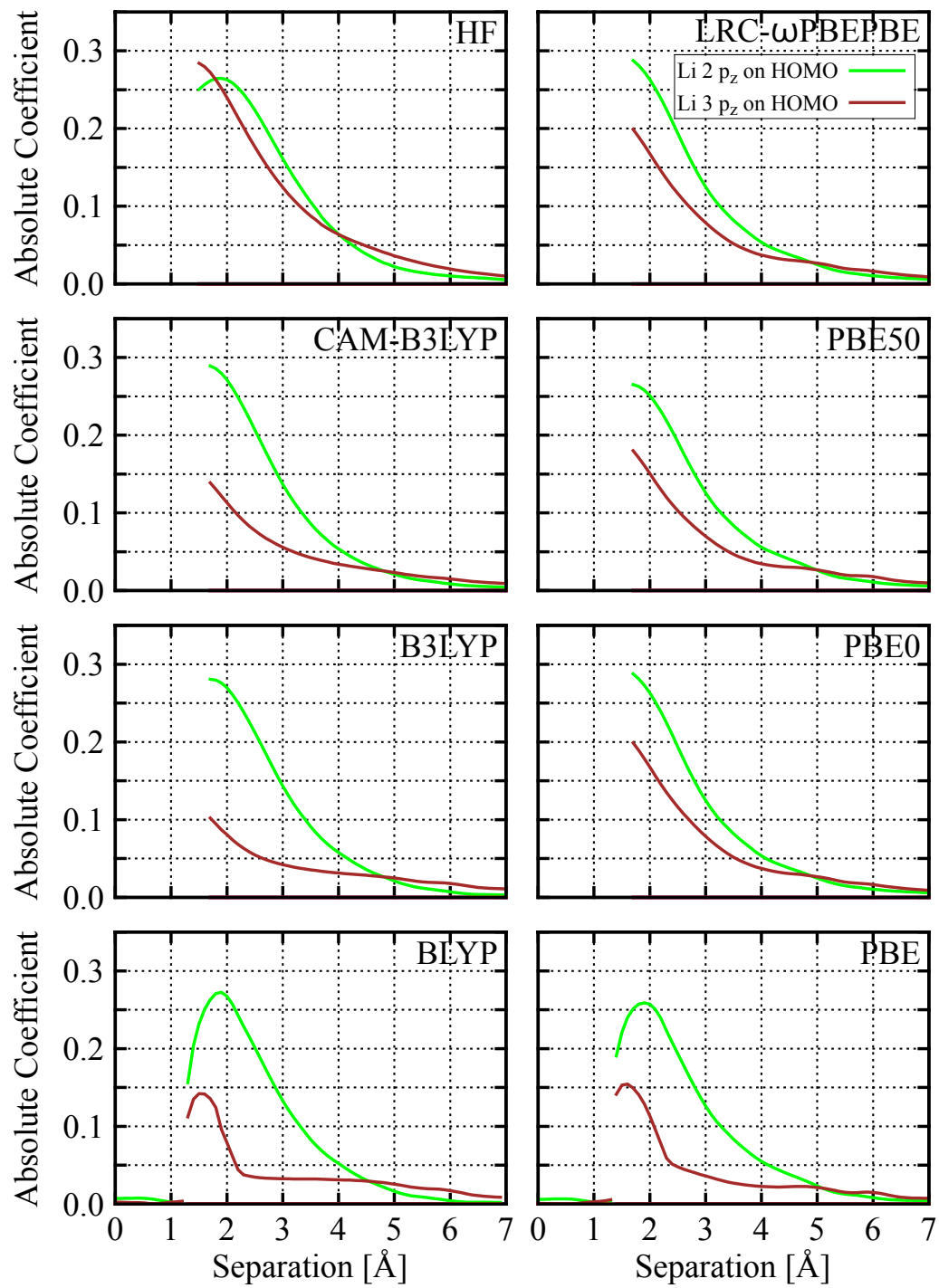


Figure 2.8. Contributions from p_z atomic orbitals on lithium to the HOMO of lithium-benzene as a function of the separation between fragments, for each functional applied to the complex.

changes again (compare Figures 2.6(c) and 2.6(f)), and the HOMO-LUMO degeneracy is broken (see Figure 2.5). Thus, at short separations, PBE and HF show the same CT state. (see Figures 2.4, 2.7, and 2.8).

The PBE0 HOMO, shown at the center in Figure 2.6, transforms as the HF HOMO. The main difference of PBE0 with respect to *pure* PBE is the absence of the intermediate-separation state (compare Figures 2.6(e) and 2.6(f)). In PBE0, the system abruptly switches from the long-range neutral state to the short-range CT state at $\sim 1.65 \text{ \AA}$ (see Figures 2.4 and 2.5). Likewise, the evolution of the HOMO in PBE50 and LRC- ω PBEPBE is analogous to that observed in HF.

The other set of functionals, including BLYP, B3LYP, and CAM-B3LYP, follows the previous description closely, as seen in Figures 2.4 and 2.5. As with PBE, an intermediate state is also observed with BLYP. In the BLYP-family functionals, the trend of the HOMO-LUMO gap is:

$$\text{HF} > \text{CAM-B3LYP} > \text{B3LYP} > \text{BLYP}.$$

Therefore, in both PBE and BLYP families of functionals, the character of the frontier MOs and their energies depend strongly upon the admixture of E_X^{HF} . The difference between the functionals in each set is the proportion of E_X^{HF} . Our calculations show that the HOMO-LUMO gap increases with the amount of E_X^{HF} and is the largest in HF. Additionally, functionals with a narrow HOMO-LUMO gap exhibit an intermediate partial-CT state. The charge transfer occurs at longer inter-monomer separation in functionals with no E_X^{HF} . Is the charge transfer between lithium and benzene a real phenomenon? Which functional and which partial-charge scheme provide the best description of the lithium-benzene complex? These questions are explored in detail in the next two sections of the paper.

2.3.3 State-crossing

In the first two sections of this discussion, the variation of charge accumulation on lithium was related to a change in character of the wave function along the lithium-benzene separation. The abrupt change in the wave-function character suggests the

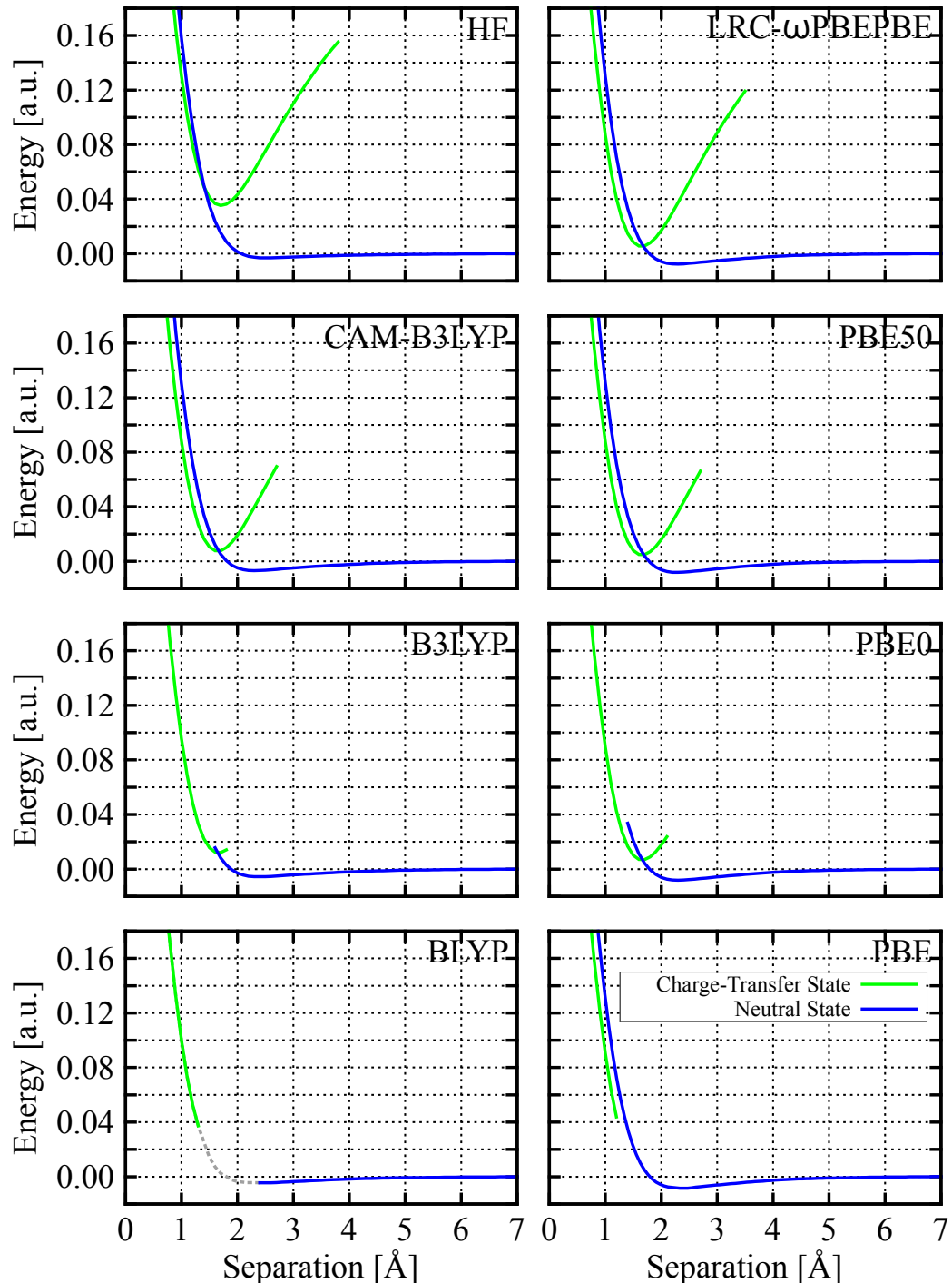


Figure 2.9. Energy of the electronic states as a function of the separation between the plane of benzene and the lithium atom, obtained by the maximum overlap method. The neutral state is plotted with a blue line. The CT state is depicted in green.

existence of a state crossing. While the description of a state crossing by single-reference methods is generally non-trivial, a few techniques are available, including wave-function stability analysis [74], symmetry-enforced self-consistent field convergence, constrained DFT methods [75, 76], etc. The MOM by Gilbert et al. [48] is employed, to find *the lowest energy solution* for each separation between lithium and benzene.

If the MOM is triggered on the first cycle of the self-consistent procedure, it holds the initial configuration by choosing occupancies that maximize the overlap of the new occupied orbitals with the set previously occupied. In this case, when the calculation of the PES starts from long separations, the MOM, accompanied by reading orbitals from a previous geometry, helps maintaining the neutral-state character [$\text{O}\cdots\text{Li}$]. On the other hand, starting from short separations, the CT state [O^-Li^+] can be enforced and kept.

Electronic energies of the neutral and CT states obtained with the MOM are presented in Figure 2.9. The curves are plotted using only those calculations in which the self-consistent field procedure converged under tight criteria. State crossings are clearly observed in all cases except BLYP and PBE, both of which become unstable in the region near the crossing. This instability is manifested by the presence of an intermediate state seen in Figure 2.5. Notably, the convergence of the higher-energy state is more stable when the proportion of E_X^{HF} is greater, such that the most stable MOM calculations are those of HF.

Comparison of HF and DFT state-crossing curves suggests that the CT state in HF is displaced to higher energies with respect to the neutral state, causing a shift of the crossing to shorter separations. Indeed, the crossing occurs at around 1.65 Å in all hybrid and LRC functionals, whereas in HF it is located at around 1.45 Å. A relative overstabilization of the CT state in functionals, with respect to HF, is consistent with narrower HOMO-LUMO gaps in functionals than in HF, as discussed in Section 2.3.2.

The separation at which the state crossing appears in B3LYP coincides with that at which HOMO and LUMO energies nearly collide in Figure 2.5. A similar situation is observed for PBE0, although the HOMO-LUMO gap is slightly wider. This suggests that one could correctly *estimate* the position of a state-crossing in PBE0 and B3LYP by monitoring the HOMO-LUMO gap. However, this is not true in general.

2.3.4 Excited-state Calculations

The calculations discussed hitherto are based on single-reference methods. To better understand the physics of charge transfer in our model system, the interaction of the ground and excited CT states is now calculated using a method that is capable of describing several electronic states on equal footing. For this purpose, it is possible to use a multi-reference method such as multi-configurational self-consistent field (MCSCF), multi-reference perturbation theory (CASPT2, MRPT, MCQDPT), or multi-reference configuration interaction (MRCI) [77]. In this case, an alternative method for describing electronic states in the lithium-benzene complex is used, namely EOM-EA-CCSD. This sophisticated treatment provides a robust description of radical systems, correctly capturing the multi-configurational nature of electronic states by using a single-reference formalism [68].

The closed-shell cation state $[\odot\cdots\text{Li}^+]$ is taken as a reference state in EOM-EA-CCSD, while electronic states of a neutral complex are obtained by creating an electron on any vacant orbital. These electronic configurations constitute single excitations. Additionally, electronic configurations in which the creation of an electron on a virtual orbital is accompanied by the excitation of another electron (double excitations) are also included in the subspace in which the Hamiltonian is diagonalized. Thus, in the EOM-EA-CCSD formalism both the ground and CT states of the lithium-benzene complex are obtained as single excitations from the cation reference-state and are expected to be described with similar quality. Therefore, EOM-EA-CCSD provides an accurate location of the state crossing, if there is one.

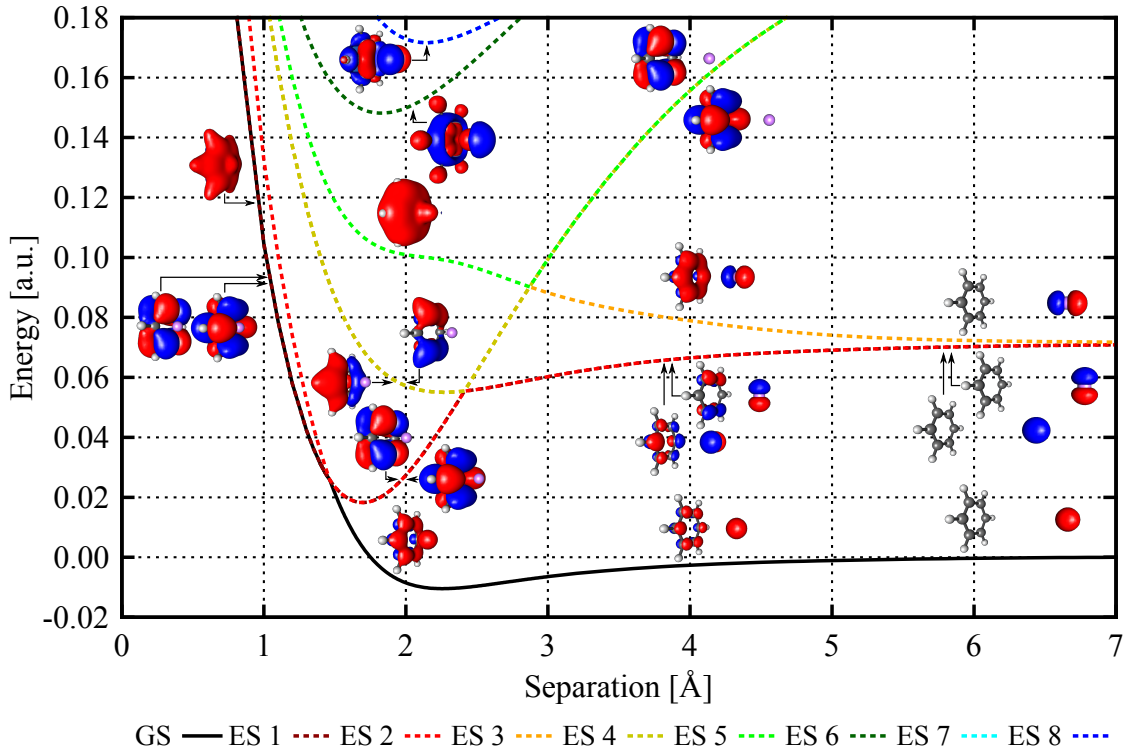


Figure 2.10. Energy of the electronic states as a function of the separation between the plane of benzene and the lithium atom, obtained by the EOM-EA-CCSD method. The ground state (GS) is plotted with a continuous black line. Dotted lines represent the first nine excited states (ES). SOMOs corresponding to the leading configuration of each state are shown at several separations. A crossing between the long-separation ground state, in which the SOMO is mainly localized over lithium, and a CT state, in which the SOMO localizes exclusively over the benzene molecule, occurs at 1.5 Å.

The results obtained with the EOM-EA-CCSD method are presented in Figure 2.10. The character of the electronic states might be derived from the shapes of the singly-occupied molecular orbitals (SOMO) of the leading configuration for each state. For example, in the large-separation limit, one can clearly see electronic states corresponding to excitations on lithium: the $1s^22s^1$ ground state (in black), the degenerate pair of $1s^22p_x^1$ and $1s^22p_y^1$ (in red), and the $1s^22p_z^1$ (in orange). A crossing of the ground and CT states is observed at 1.465 Å. At separations shorter than this,

the character of the ground state switches from a neutral state, with the SOMO represented mainly by the $2s$ orbital of the lithium atom; to a degenerate pair of the CT states, with the SOMO being one of the π^* orbitals of benzene. Note that the crossing of the ground and CT states is a real crossing, rather than an avoided crossing, because the states involved do not mix by symmetry. This is also true for other state crossings seen in Figure 2.10. The position of the state crossing between the ground and CT states predicted by EOM-EA-CCSD better agrees with HF than standard-hybrid or LRC functionals; and it disagrees with the description of pure functionals BLYP and PBE, which exhibit an unphysical intermediate state. In contrast to Mulliken and ChElPG, NBO charges respond consistently with the appearance of the crossing of the neutral and ionic state for each of the hybrid functionals and HF.

However, as it is obvious from Figure 2.10, the position of the state-crossing depends upon the shape and depth of the potential curves of both the ground and CT states. In particular, overstabilization of the ionic state results in an early charge transfer, as is observed in BLYP and PBE. These functionals produce an intermediate spurious state in which fractional atomic charges increase from 0 to almost 1 in the region between 1.3 \AA and 2.3 \AA , as seen in Figure 2.4. This raises a red flag when using standard DFT for modeling charge transfer in conjugated materials: The functional needs to be carefully selected to predict the charge transfer at the correct separation between moieties, or alternative computational schemes must be used. In the model system considered, B3LYP and PBE0 are close to the correct behavior.

2.3.5 Interaction Energy

The attention is now turned to the calculation of interaction energies from Equation (2.13). Figure 2.11 summarizes the results obtained via correlated wave-function methods and various density-functional approximations. As expected, the HF equilibrium distance, $\sim 2.5 \text{ \AA}$, is longer than the distance obtained with CCSD, $\sim 2.25 \text{ \AA}$, both in agreement with those reported by Baker and Head-Gordon [42]. An old experimental study by Manceron and Andrews [78] estimates a separation of ~ 1.8

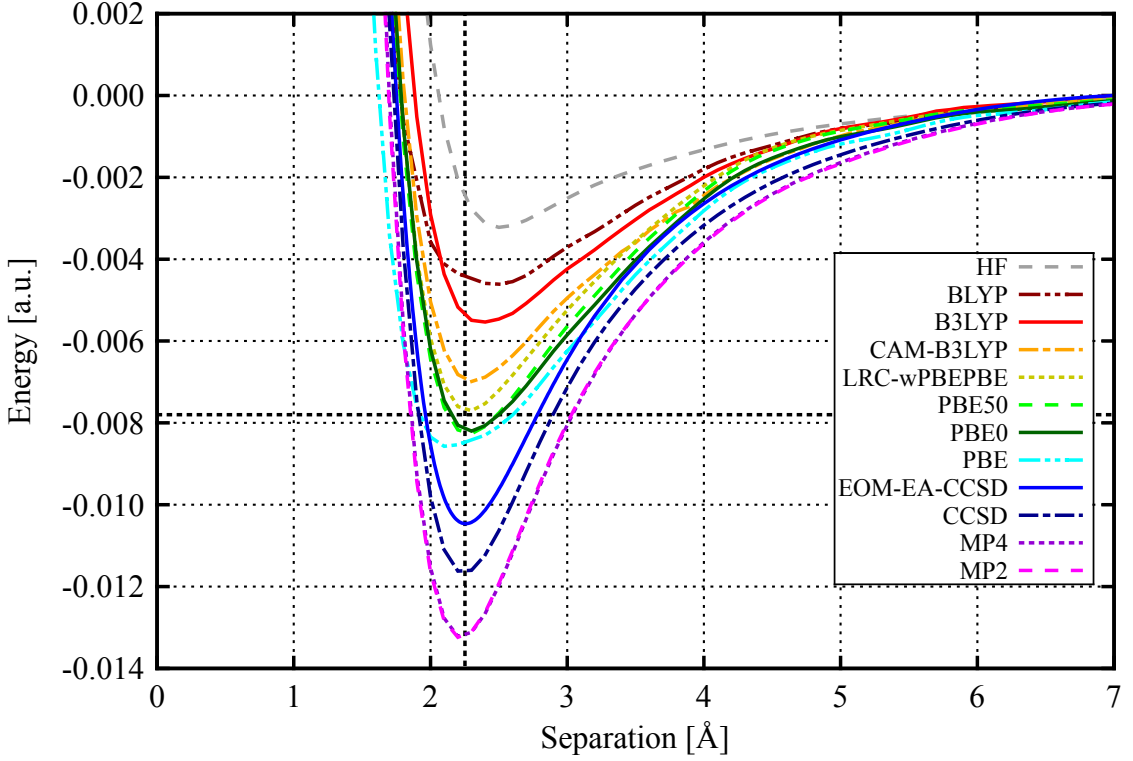


Figure 2.11. Interaction energy of the lithium-benzene complex computed by different methods. The black dotted horizontal line corresponds to the most accurate interaction energy in lithium-benzene found in the literature [43]. The black dotted vertical line indicates the most accurate equilibrium distance [42]. All results of the present work are obtained in 6-31G* basis.

Å based on gas-phase infrared spectra of lithium-benzene in argon, but it is unclear if this corresponds to the neutral or cationic species. A previous *in-silico* study by Vollmer et al. [35] on the neutral complex reports 2.252 Å (black, dashed, vertical line on Figure 2.11), calculated with MP2(FC)/6-31G(d). Zhengyu et al. [34] reported 2.600 Å with MP2/6-31G and 2.511 Å with HF/6-31G(d).

In agreement with the results by Vollmer et al., it is observed that HF underbinds the lithium-benzene complex, highlighting the importance of correlation effects. The HF interaction energy reported on Figure 2.11, -0.0031 a.u. , is close to the one they reported at the minimum: -0.0029 a.u. [35]. The most accurate interaction energy

in lithium-benzene is -0.0078 a.u. (black, dashed, horizontal line on Figure 2.11), reported by Denis and Iribarne [43], who calculated it at the CCSD(T)/CBS level, including corrections for core correlation and relativistic effects. Vollmer et al. [35] reported a value of -0.0092 a.u. using the G3(MP2) [79] method.

These results are now compared against the CCSD interaction curve on Figure 2.11 to meaningfully contrast the results from different methods without the influence of basis set and basis-set superposition errors. The minimum energy from the CCSD calculation is -0.0114 a.u. and the separation at that point is 2.2 \AA. MP2 and MP4 show very similar results and their curves overlap in Figure 2.11. Also, MP2 calculations agree with those of Vollmer et al. [35]. Nonetheless, it is known that the MP methods may overestimate the dispersion energy [14] and overbind the complex.

In general, approximate DFT calculations do better than HF, but they still underbind the complex when compared to CCSD. Even though GGAs and standard hybrids account for local and semi-local correlation, the long-range part of correlation is not properly described [17]. Functionals derived from PBE show similar interaction-energy curves, with a slight decrease in the binding energy when the amount of E_X^{HF} increases. That is, the binding energy follows the trend:

$$\text{HF} < \text{LRC-}\omega\text{PBE} < \text{PBE50} \approx \text{PBE0} < \text{PBE}.$$

The PBE binding energy shows an unphysical wide well near the equilibrium separation. This is because the character of the PBE ground state changes near the equilibrium distance (compare Figures 2.6(d) and 2.6(f)), such that the repulsive side of the well is determined by the intermediate state with partial-CT character. In other functionals of the PBE family and in HF, this intermediate state does not exist and the charge transfer occurs at a shorter-than-equilibrium distance, such that neither the interaction energy nor the equilibrium position are affected by the CT phenomenon.

A rather unexpected behavior is observed in BLYP-related functionals. The CAM-corrected functional describes the interaction energy better than either B3LYP or

BLYP. Thus, the trend is opposite to that of PBE-related functionals: the binding energy in the BLYP-derived functionals increases with the proportion of E_X^{HF} . It is hard to point out the exact origin of the difference, because neither E_X nor E_C are easily comparable between BLYP-related functionals (Table 2.1). Finally, similar to PBE, the BLYP binding curve exhibits a wider well due to a state crossing near the equilibrium separation.

2.4 Summary

An assessment of how several functionals model ground-state charge transfer and predict charge distributions in the lithium-benzene complex is presented. This model illustrates an all-too-common problem in computational chemistry: With results hinging on a delicate combination of methods, the interplay of approximate functionals and charge-distribution schemes can lead to drastically different qualitative pictures of ground-state charge transfer.

Functionals with an admixture of E_X^{HF} are useful in describing charge transfer in the lithium-benzene complex. The HOMO-LUMO gap is widened when the proportion of E_X^{HF} is increased, a consequence of the stabilization of the occupied MOs and the destabilization of the unoccupied MOs.

In spite of the existence of a state crossing that induces charge transfer, the crossing occurs in the repulsive region of the interaction curve, leaving the equilibrium region unaffected in hybrid functionals and HF. However, the equilibrium region is incorrectly described by pure functionals PBE and BLYP because of a crossing with an artificial state. Ground-state charge distributions display sharp features when state crossings occur, as is clear from Figures 2.4 and 2.9.

While modeling the state crossing is prone to errors when using single-reference methods, high computational cost might hinder the use of multi-reference or excited-state methods for larger systems relevant in materials science. In those situations, rigorous functionals capable of describing CT phenomena, or alternative computational schemes, are needed.

3. MODULAR IMPLEMENTATION OF TKATCHENKO-SCHEFFLER FUNCTIONAL MODEL FOR VAN DER WAALS INTERACTION

3.1 Introduction

In section 2.1, DFT was presented as the most widely used electronic structure method in science and engineering. Although DFT is in principle exact, modeling of interactions between electrons in practice requires approximations. These are formally included through the XC energy functional [26].

One of the reasons why DFT is so popular, is that often computationally inexpensive functionals yield accurate results, mostly thanks to the incorporation of local or semi-local electron correlation [80]. However, when aiming to describe van der Waals interactions accurately, most density functional approximations have serious limitations [81–85].

3.1.1 Motivation

van der Waals forces are essential to determine the structure and properties of biomolecules and materials. They play a fundamental role in fields as diverse as supramolecular chemistry, structural biology, polymer science, nano-technology, surface science, and condensed matter physic. They also provide explanations for chemical, physical, or biological phenomena such as how DNA bases stack, what gives structure to graphite, or why geckos stick to glass.

van der Waals interactions arise among all chemical groups and usually represent an important part of the total interaction energy in condensed matter, even though they are generally weaker than ionic and hydrogen bonds. They become stronger in elements with larger atomic radius, and they are usually stronger in larger molecules too. This is due to the increased polarizability of molecules with larger, more dis-

persed electron densities. Through this logic, van der Waals effects explain why fluorine and chlorine are gases at standard conditions, whereas bromine is a liquid, and iodine is a solid. They also become stronger with larger amounts of surface contact, giving clues to the answer of the questions formulated in the previous paragraph.

3.1.2 Background

The term van der Waals force is sometimes ambiguously used to refer to different types of intermolecular interactions. However, electron dispersion is usually the strongest attractive term for neutral, non-covalently-bonded molecules. Therefore the attractive interaction of van der Waals forces is known to chemists as dispersion [86].

Electron dispersion involves long-range and dynamic correlation. van der Waals interactions emerge as an electronic response to fluctuating polarization of the density. Thus, it is challenging to capture these phenomena with most functionals, which employ local or semi-local approximations and rule out instantaneous density variations.

It is known that the leading term of dispersion forces decays as $-1/r^6$, where r is the magnitude of the separation coordinate. Unfortunately, the asymptotic behavior of standard functionals depends on the overlap of the densities in the system, which decays exponentially along the separation coordinate.

The formulation of methods that are able to accurately capture van der Waals interactions is becoming an increasingly active field of density-functional development. It is recognized as one of the main challenges in the extension of the scope and quality of quantum chemical calculations [87]. Researchers in the field have taken different paths. Klimeš and Michaelides [80] proposed a Jacob's ladder to classify dispersion schemes in DFT.

In the ground level, Klimeš and Michaelides include those functionals that may be able to capture the binding accurately at separations around minima, but incorrectly describe asymptotic regions. Functionals as simple as the LDA, or as complex as the Minnesota set [88], are included in this group. In addition, there are functionals

designed to operate with pseudopotentials, instead of gaussian-based atomic orbitals. A pseudopotential is an attempt to replace the complicated effects of the motion of the core electrons of an atom and its nucleus with an effective potential. Schemes that add a specially constructed pseudopotential projector, such as dispersion corrected atom-centered potentials (DCACP) [89] or local atomic potentials (LAP) methods [90] also belong to this level.

Functionals that make use of simple $C^{(6)}$ corrections are classified within the first rung. In this case, the dispersive energy is described including a damping function that modulates the C_6/R^6 term, where $C^{(6)}$ is an empirical coefficient and R is the magnitude of the internuclear separation coordinate. Although highly popular, the main issue with these schemes is that a constant coefficient is assigned to an element regardless of its oxidation or hybridization state. The D and D2 corrections by Grimme's group [91, 92], or functionals with range-separated exchange and dispersion corrections, such as ω B97X-D by Head-Gordon's group [93], are examples of schemes classified in the first rung.

Environment-dependent $C^{(6)}$ corrections are considered as the second rung. In this approach the dispersive energy is described essentially with the same type of expression. However, variable $C^{(6)}$ coefficients are calculated using reference data, i.e. atomic polarizabilities. The D3 correction by Grimme's group [94], the approach of Tkatchenko and Scheffler (TS-vdW) [86], and the Becke-Johnson (BJ) or exchange-dipole model [95–98] are the most prominent examples of this rung. Given their simplicity, accuracy, and computational efficiency, these methods are becoming increasingly popular.

The models of third rung use no input parameters. Instead, the dispersion interaction is calculated directly from the density, which is in principle a more general strategy. In 2004, Dion et al. [99] proposed the most popular of these methods: a family of non-local correlation functionals, vdW-DF. They depend explicitly on the electronic coordinates, \mathbf{r} and \mathbf{r}' , to approximately account for van der Waals interactions as a part of the functional. However, it has been shown that the vdW-DF tends

to overestimate long range dispersion, thus several alternatives have been proposed too. For example, Van Voorhis' group has also developed several dispersion-corrected functionals [100], which in turn have been incorporated into other modern functionals such as ω B97X-V by Head-Gordon's group [101].

All the functionals that include effects beyond pairwise additivity, of which many popular versions exist, belong to the fourth rung. For example, the idea of using DFT in combination with the Symmetry-adapted Perturbation Theory (SAPT) to calculate dispersion energies was developed in 2001 [102–105]. Other common examples are the many-body dispersion (MBD), closely related to the TS-vdW, and schemes based on RPAs. Although accurate, these theories are far more complex and computationally expensive than the previously mentioned alternatives, thus limiting their range of applicability.

Among these methods, the TS-vdW scheme, in particular, is becoming popular. It has been implemented in Quantum Espresso and the Fritz Haber Institute *ab initio* molecular simulations (FHI-aims) package. In this chapter, the expressions for the force and the XC potential of the TS-vdW method are derived in detail. I present a portable code in *C*, developed in collaboration with Dr. Xavier Andrade and Dr. Alfredo A. Correa, that allows for modular implementation of the TS-vdW scheme. The code has the ability of being interfaced with computational chemistry packages that use various basis-set representations. This TS-vdW library uses the density and Hirshfeld partitioning as its unique input, and outputs the TS-vdW energy which can be added after the total energy is obtained, or applied as a self-consistent correction. The gradient of the van der Waals energy is also implemented, thus geometry optimizations and MD simulations can be performed. As an advantage, the scaling of DFT calculations is unaffected by the TS-vdW correction. A pilot implementation in the Octopus code is demonstrated, and its consistency validated against Quantum Espresso. Sample results include calculations of ground state and excited state properties in the benzene dimer and the hydrogen fluoride dimer, respectively.

3.2 The Model of Tkatchenko and Scheffler for van der Waals Interactions

One of the challenges in the implementation of the TS-vdW scheme is that, although the underlying idea is clearly explained, the mathematical details of the model are left out in Reference [86]. Therefore, in this section the implementation is explained in detail, and the expressions are derived step by step.

The following is a short summary of the conventions adopted in this chapter. Atomic units are used throughout; uppercase indices, such as A or B , are used to label atoms, while lowercase indices label orbitals. The \mathbf{r} symbol is used for electronic coordinates. To make mathematical expressions more compact and readable, dependence on \mathbf{r} is left implicit in functional notation. \mathbf{R}_A denotes the position of atom A , while \mathbf{R} is the set of positions of all atoms, and R_{AB} is the distance between atoms A and B . Superscripts enclosed by parenthesis are used to distinguish numeric labels from exponents. Units of magnitude in figures are enclosed in squared brackets.

3.2.1 van der Waals Energy

The TS-vdW scheme works by adding a term to the correlation functional. This term, $E_{\text{vdW}}[n](\mathbf{R})$, has the form of a standard pairwise van der Waals interaction between atoms, and depends on both the atomic positions and the electronic density:

$$E_{\text{vdW}}[n](\mathbf{R}) = \frac{1}{2} \sum_{\substack{AB \\ A \neq B}} \epsilon_{AB}[n](\mathbf{R}). \quad (3.1)$$

In this expression, the van der Waals energy is decomposed into pairwise energies, $\epsilon_{AB}[n](\mathbf{R})$, which are calculated as the product of a damping function and a typical dispersive energy expression,

$$\epsilon_{AB}[n](\mathbf{R}) = -f^{\text{damp}}(R_{AB}, R_{AB}^{(0)}[n]) \frac{C_{AB}^{(6)}[n]}{R_{AB}^6}. \quad (3.2)$$

As represented in Figure 3.1, the function f^{damp} gradually turns off the van der Waals interaction for closely-separated atoms,

$$f^{\text{damp}}(R_{AB}, R_{AB}^{(0)}[n]) = \frac{1}{1 + \exp \left[-d \left(\frac{R_{AB}}{s_R R_{AB}^{(0)}[n]} - 1 \right) \right]}, \quad (3.3)$$

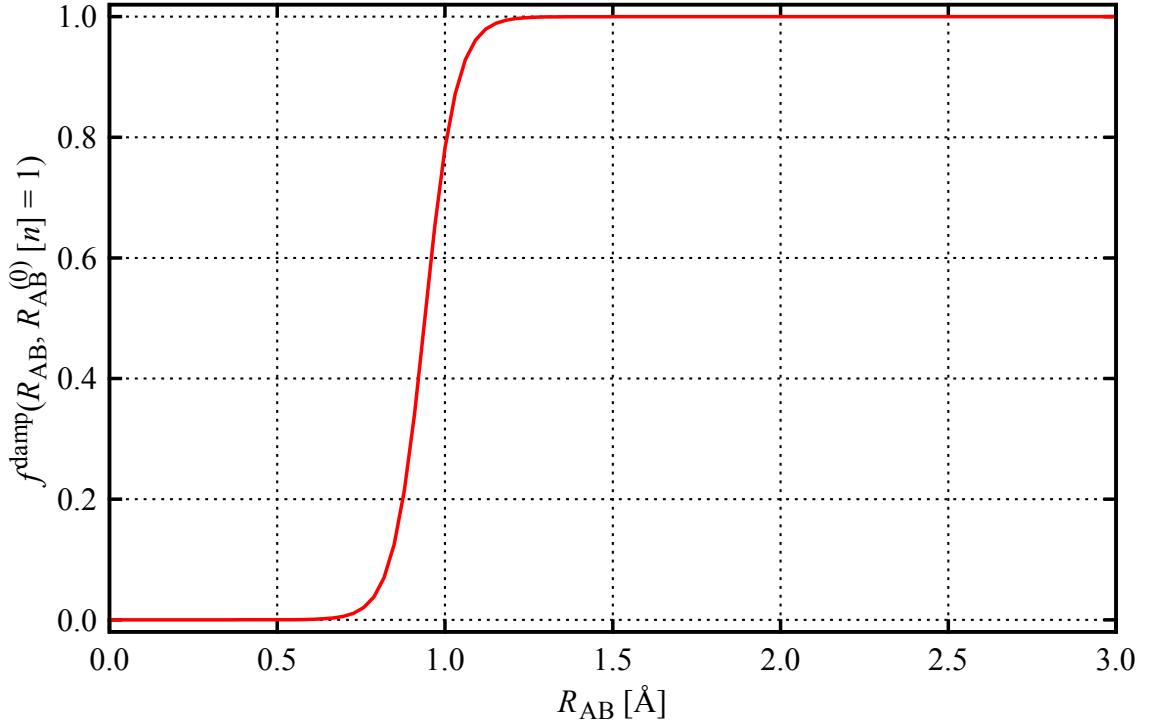


Figure 3.1. Damping function of Equation (3.3). Plotted using a fixed $R_{AB}^{(0)}[n] = 1$, $d = 20$, and $s_R = 0.96$.

where d and s_R are adjustable parameters that control the damping. The TS-vdW scheme sets $d = 20$ (it may take values between 12 and 45), while s_R depends on the functional used. For instance, the value is 0.96 for PBE and 0.94 for PBE0.

The strength of the van der Waals interaction is determined by $C_{AB}^{(6)}$ and $R_{AB}^{(0)}$. In the TS-vdW scheme, these parameters depend on the density through the fractional change in the atomic volume induced by the chemical environment, i.e. $\mathcal{V}_A[n]$ for an atom A .

On the one hand, using $\mathcal{V}_A[n]$ it is possible to relate the effective van der Waals coefficients, $C_{AB}^{(6)}[n]$, with respect to the corresponding quantities for the free atom:

$$C_{AB}^{(6)}[n] = \mathcal{V}_A[n]\mathcal{V}_B[n]C_{AB}^{(6),\text{free}} . \quad (3.4)$$

In turn, $C_{AB}^{(6),\text{free}}$ is determined using the static polarizabilities, $\alpha_A^{(0)}$ and $\alpha_B^{(0)}$, and the corresponding tabulated coefficients for the pure atomic species, $C_{AA}^{(6),\text{free}}$ and $C_{BB}^{(6),\text{free}}$,

$$C_{AB}^{(6),\text{free}} = \frac{2C_{AA}^{(6),\text{free}} C_{BB}^{(6),\text{free}}}{\frac{\alpha_B^{(0)}}{\alpha_A^{(0)}} C_{AA}^{(6),\text{free}} + \frac{\alpha_A^{(0)}}{\alpha_B^{(0)}} C_{BB}^{(6),\text{free}}}. \quad (3.5)$$

There is a special case where an atom is paired with another atom of the same species: A and B are of the same type, thus Equation (3.4) reduces to

$$C_{AA}^{(6)}[n] = (\mathcal{V}_A[n])^2 C_{AA}^{(6),\text{free}}. \quad (3.6)$$

On the other hand, $\mathcal{V}_A[n]$ and $R_A^{(0),\text{free}}$, the atomic radius of the free atomic species, determine

$$R_{AB}^{(0)}[n] = \sqrt[3]{\mathcal{V}_A[n]} R_A^{(0),\text{free}} + \sqrt[3]{\mathcal{V}_B[n]} R_B^{(0),\text{free}}, \quad (3.7)$$

which in the limiting case of a two-atom system, is a quantity corresponding to the radius of an atom A in a diatomic molecule with B .

In 2004, Chu and Dalgarno compiled the free volume coefficients for most atomic species. These data can be found in Reference [106], and for illustrative purposes is presented in Figure 3.2.

The fractional effective volume for atom A , $\mathcal{V}_A[n]$, in a chemical environment formed by atoms B , is expressed using the Hirshfeld partitioning approach [107]

$$\mathcal{V}_A[n] = \frac{1}{\mathcal{V}_A^{\text{free}}} \int d^3r \frac{n_A^{\text{free}}(\mathbf{R}_A - \mathbf{r})}{\sum_B n_B^{\text{free}}(\mathbf{R}_B - \mathbf{r})} (\mathbf{r} - \mathbf{R}_A)^3 n(\mathbf{r}). \quad (3.8)$$

The free atomic volume for atom A , $\mathcal{V}_A^{\text{free}}$, is derived directly from the electron density

$$\mathcal{V}_A^{\text{free}} = \int d^3r r^3 n_A^{\text{free}}(\mathbf{r}). \quad (3.9)$$

Therefore, to calculate the van der Waals energy for a given density, it is necessary to calculate the Hirshfeld volumes for all atoms first. These quantities are environment-dependent, and they resemble the response of the electron cloud of one atom to the presence of other chemical species nearby, as Figure 3.3 illustrates.

By design, the TS-vdW library relies on the calling code to calculate these effective volumes and pass them as arguments. The rationale behind this decision is that the

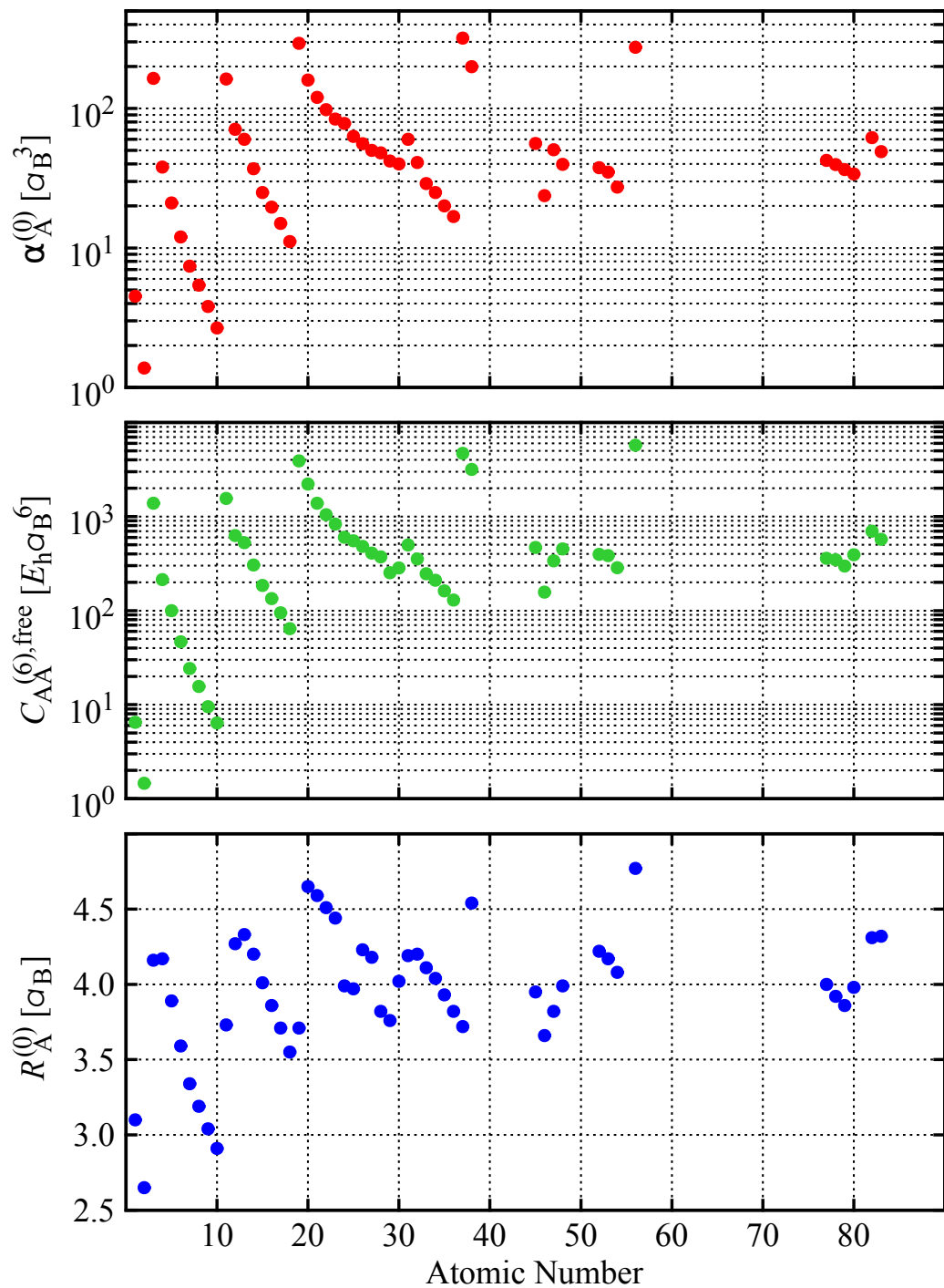


Figure 3.2. Parameters of the TS-vdW model as a function of atomic number. Values in atomic units are retrieved from Reference [106].

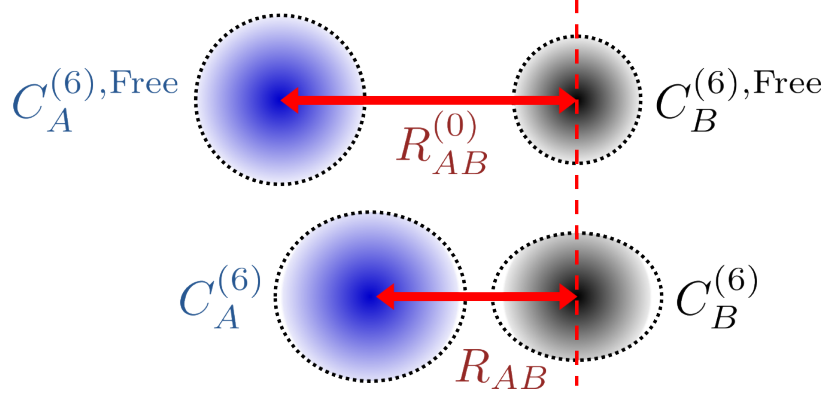


Figure 3.3. Visual representation of the change in effective volume of two non-interacting atoms (top) vs. two interacting atoms (bottom). This is the principle through which interactions are modeled in the TS-vdW scheme.

calculation of Hirshfeld volumes is highly dependent on how the density is represented, which can change considerably among electronic structure codes. The alternative would have been to force a simple representation, such as a uniform real-space grid, and force all codes to convert the total density and individual atomic densities to this representation. This is sometimes inefficient, and it still might involve a considerable amount of work.

3.2.2 Electronic Potential

To include the effect of the van der Waals interaction in the Kohn-Sham equations, Equation (2.1), it is necessary to calculate the van der Waals potential, $V_{\text{vdW}}[n](\mathbf{R})$, which is the functional derivative of the van der Waals energy with respect to the density. Since the density dependence enters the energy only through the effective volumes, this derivative can be split in two parts,

$$V_{\text{vdW}}[n](\mathbf{R}) = \frac{\delta E_{\text{vdW}}[n](\mathbf{R})}{\delta n(\mathbf{r})} = \sum_A \frac{\partial E_{\text{vdW}}[n](\mathbf{R})}{\partial \mathcal{V}_A[n]} \frac{\delta \mathcal{V}_A[n]}{\delta n(\mathbf{r})}. \quad (3.10)$$

The first part, $\partial E_{\text{vdW}}[n](\mathbf{R})/\partial \mathcal{V}_A$, does not depend on the representation, so it can be readily calculated and returned by the library. Effectively, Equation (3.10) works summing over all pairs of atoms:

$$\frac{\delta E_{\text{vdW}}[n](\mathbf{R})}{\delta n(\mathbf{r})} = \sum_{AB} \frac{\partial \epsilon_{AB}[n](\mathbf{R})}{\partial \mathcal{V}_A[n]} \frac{\delta \mathcal{V}_A[n]}{\delta n(\mathbf{r})} = \sum_A \frac{\delta \mathcal{V}_A[n]}{\delta n(\mathbf{r})} \sum_B \frac{\partial \epsilon_{AB}[n](\mathbf{R})}{\partial \mathcal{V}_A[n]}. \quad (3.11)$$

If the sum over derivatives of the pairwise energies with respect to the effective volumes is labeled K_A ,

$$K_A = \sum_B \frac{\partial \epsilon_{AB}[n](\mathbf{R})}{\partial \mathcal{V}_A[n]}, \quad (3.12)$$

Equation (3.11) is rewritten in the form that is implemented in the calling code:

$$\left(\frac{\delta E_{\text{vdW}}}{\delta n(\mathbf{r})} \right)_i = \sum_A K_A \left(\frac{\delta \mathcal{V}_A^{\text{Ratio}}}{\delta n(\mathbf{r})} \right)_i. \quad (3.13)$$

where the i subindex is used to label orbitals that belong to atom A .

The right-most factor in Equation (3.11) is a sum of the pairwise van der Waals energy derivatives with respect to effective atomic volumes. These quantities are computed by the library and then passed to the calling code. The calculation uses the expression:

$$\begin{aligned} \frac{\partial \epsilon_{AB}[n](\mathbf{R})}{\partial \mathcal{V}_A[n]} = & - \frac{\partial f^{\text{damp}}(R_{AB}, R_{AB}^{(0)}[n])}{\partial \mathcal{V}_A[n]} \frac{C_{AB}^{(6)}[n]}{R_{AB}^6} \\ & - f^{\text{damp}}(R_{AB}, R_{AB}^{(0)}[n]) \frac{\partial C_{AB}^{(6)}[n]}{\partial \mathcal{V}_A[n]} \frac{1}{R_{AB}^6}. \end{aligned} \quad (3.14)$$

The first term of the right-hand side of Equation (3.14) includes the partial derivative of the damping function with respect to the change in effective volume of species A . This derivative is calculated using the chain rule:

$$\frac{\partial f^{\text{damp}}(R_{AB}, R_{AB}^{(0)}[n])}{\partial \mathcal{V}_A[n]} = \frac{\partial f^{\text{damp}}(R_{AB}, R_{AB}^{(0)}[n])}{\partial R_{AB}^{(0)}[n]} \frac{\partial R_{AB}^{(0)}[n]}{\partial \mathcal{V}_A[n]}, \quad (3.15)$$

where the first factor of the right-hand side of Equation (3.15) is just

$$\frac{\partial f^{\text{Damp}}(R_{AB}, R_{AB}^{(0)}[n])}{\partial R_{AB}^{(0)}[n]} = - \frac{d \times R_{AB}}{s_R(R_{AB}^{(0)}[n])^2} \frac{\exp \left[-d \left(\frac{R_{AB}}{s_R R_{AB}^{(0)}[n]} - 1 \right) \right]}{\left\{ 1 + \exp \left[-d \left(\frac{R_{AB}}{s_R R_{AB}^{(0)}[n]} - 1 \right) \right] \right\}^2}; \quad (3.16)$$

and the second factor is straightforwardly derived using Equation (3.7),

$$\frac{\partial R_{AB}^{(0)}[n]}{\partial \mathcal{V}_A[n]} = \frac{R_A^{(0),\text{free}}}{3(\mathcal{V}_A[n])^{2/3}}. \quad (3.17)$$

Equation (3.17) completes the information required to solve Equation (3.15), which in turn provides what is necessary to solve the first term of the right-hand side of Equation (3.14).

Additionally, the second term of Equation (3.14) requires the partial derivative of the $C_{AB}^{(6)}[n]$ coefficient with respect to the change in effective volume of the species A :

$$\frac{\partial C_{AB}^{(6)}[n]}{\partial \mathcal{V}_A[n]} = \mathcal{V}_B[n] C_{AB}^{(6),\text{free}} = \frac{C_{AB}^{(6)}[n]}{\mathcal{V}_A[n]}. \quad (3.18)$$

Finally, the calling code is required to calculate the second part of Equation (3.10), which is given by:

$$\frac{\delta \mathcal{V}_A[n]}{\delta n(\mathbf{r})} = \frac{1}{\mathcal{V}_A^{\text{free}}} \frac{(\mathbf{r} - \mathbf{R}_A)^3 n_A^{\text{free}} (\mathbf{R}_A - \mathbf{r})}{\sum_B n_B^{\text{free}} (\mathbf{R}_B - \mathbf{r})}. \quad (3.19)$$

With the information provided by the library from Equation (3.14), the calling code can construct the potential. In this way, the calling code is made flexible to perform the sum in Equation (3.13) using the scheme that is more efficient for its own wavefunction representation. Otherwise, constructing and computing the potential in the module would have needed to pass a significant amount of information to the library, making it more complex, and requiring a significant amount of memory.

3.2.3 Atomic Forces

In order to calculate the forces, it is necessary to obtain the derivative of the energy, E , with respect to the atomic positions. Since the TS-vdW correction depends explicitly on the coordinates, additional terms appear with respect to standard DFT. For the self-consistent case:

$$\frac{dE}{d\mathbf{R}_A} = \sum_i \langle \varphi_i | \frac{\partial v_A}{\partial \mathbf{R}_A} | \varphi_i \rangle + \frac{\partial E_{\text{vdW}}[n](\mathbf{R})}{\partial \mathbf{R}_A}. \quad (3.20)$$

For a non-self-consistent calculation, an additional term appears:

$$\frac{dE}{d\mathbf{R}_A} = \sum_i \langle \varphi_i | \frac{\partial v_A}{\partial \mathbf{R}_A} | \varphi_i \rangle + \frac{\partial E_{\text{vdW}}[n](\mathbf{R})}{\partial \mathbf{R}_A} + \int d^3\mathbf{r} \frac{\delta E_{\text{vdW}}[n](\mathbf{R})}{\delta n(\mathbf{r})} \frac{\partial n(\mathbf{r})}{\partial \mathbf{R}_A}. \quad (3.21)$$

This additional term emerges since the orbitals are not stationary points of the energy functional. In other words, the density changes if the coordinates of the nuclei are modified. This term is quite involved to calculate as it requires a response calculation to obtain $\partial n(\mathbf{r})/\partial \mathbf{R}_A$ [108, 109]. Therefore, the implementation presented in this chapter is restricted to the first, self-consistent case.

The first term in Equation (3.20) corresponds to the usual forces in DFT. The second term represents the forces due to the van der Waals interaction,

$$\mathbf{F}_C^{\text{vdW}} = -\frac{\partial E_{\text{vdW}}[n](\mathbf{R})}{\partial \mathbf{R}_C}. \quad (3.22)$$

To calculate it, there are two different effects on the atomic displacements to be considered: the first is due to the direct dependency of the interaction energy on the distance between the atoms, the second comes from the change in the effective Hirshfeld volume of the atoms.

Taking this into consideration, the derivative of Equation (3.1) can be written as¹:

$$\frac{\partial E_{\text{vdW}}[n](\mathbf{R})}{\partial \mathbf{R}_C} = \sum_{AB} \frac{\partial E_{\text{vdW}}[n](\mathbf{R})}{\partial R_{AB}} \frac{\mathbf{R}_C - \mathbf{R}_A}{R_{AC}} + \sum_A \frac{\partial E_{\text{vdW}}[n](\mathbf{R})}{\partial \mathcal{V}_A[n]} \frac{\partial \mathcal{V}_A[n]}{\partial \mathbf{R}_C}. \quad (3.23)$$

This equation is implemented in the library using the pairwise potentials:

$$\frac{\partial E_{\text{vdW}}[n](\mathbf{R})}{\partial \mathbf{R}_C} = \sum_A \frac{\partial \epsilon_{AC}[n](\mathbf{R})}{\partial R_{AC}} \frac{\mathbf{R}_C - \mathbf{R}_A}{R_{AC}} + \sum_A \left(\sum_B \frac{\partial \epsilon_{AB}[n](\mathbf{R})}{\partial \mathcal{V}_A[n]} \right) \frac{\partial \mathcal{V}_A[n]}{\partial \mathbf{R}_C}. \quad (3.24)$$

The first term on the right-hand side of Equation (3.24) is straight-forward to calculate, and it consists of the pairwise energy derivatives with respect to the nuclear separation,

$$\frac{\partial \epsilon_{AB}[n](\mathbf{R})}{\partial R_{AB}} = -\frac{\partial f^{\text{damp}}(R_{AB}, R_{AB}^{(0)}[n])}{\partial R_{AB}} \frac{C_{AB}^{(6)}[n]}{R_{AB}^6} + 6f^{\text{damp}}(R_{AB}, R_{AB}^{(0)}[n]) \frac{C_{AB}^{(6)}[n]}{R_{AB}^7} \quad (3.25)$$

which, in addition, require:

$$\frac{\partial f^{\text{damp}}(R_{AB}, R_{AB}^{(0)}[n])}{\partial R_{AB}} = \frac{d}{s_R R_{AB}^{(0)}[n]} \frac{\exp \left[-d \left(\frac{R_{AB}}{s_R R_{AB}^{(0)}[n]} - 1 \right) \right]}{\left\{ 1 + \exp \left[-d \left(\frac{R_{AB}}{s_R R_{AB}^{(0)}[n]} - 1 \right) \right] \right\}^2}. \quad (3.26)$$

¹Note the use of an additional uppercase index, C , to denote a different species.

The second term on the right-hand side of Equation (3.24) includes two parts. The first part is, the sum of the derivatives of the van der Waals pairwise energies with respect to the effective volume. It is the same that appears in the calculation of the van der Waals potential, Equation (3.11), and it is returned by the library. The second part are the derivatives of the effective volume with respect to the atomic positions. Those are given by the following expression:

$$\begin{aligned} \frac{\partial \mathcal{V}_A[n]}{\partial \mathbf{R}_C} = & \int d^3\mathbf{r} \delta_{AC} \frac{n(\mathbf{r})}{\sum_B n_B^{\text{free}}(\mathbf{r} - \mathbf{R}_B)} (\mathbf{R}_A - \mathbf{r}) \\ & \times \left[3 |\mathbf{r} - \mathbf{R}_A| n_A^{\text{free}}(\mathbf{r} - \mathbf{R}_A) + (\mathbf{r} - \mathbf{R}_A)^2 n_A^{\text{free}'}(\mathbf{r} - \mathbf{R}_A) \right] \quad (3.27) \\ & - \frac{(\mathbf{r} - \mathbf{R}_A)^3 n_A^{\text{free}}(\mathbf{r} - \mathbf{R}_A) n(\mathbf{r})}{[\sum_B n_B^{\text{free}}(\mathbf{r} - \mathbf{R}_B)]^2} n_C^{\text{free}'}(\mathbf{r} - \mathbf{R}_C) \frac{\mathbf{R}_C - \mathbf{r}}{|\mathbf{r} - \mathbf{R}_C|}. \end{aligned}$$

This equation depends on the approach used to represent the density. Therefore, as in the case of the Hirshfeld volumes, it should be implemented in the code calling the library.

In principle, the values of these derivatives could be passed as an argument, as is done with the Hirshfeld volumes. This is not an optimal solution, as an array of size $3 \times N_{\text{Atoms}} \times N_{\text{Atoms}}$ would be required, which would be quite large for systems with hundreds or thousands of atoms. Moreover, the Kronecker delta, δ_{AC} , of Equation (3.27) cannot be applied when, due to the normalization condition, the displacement of one atom induces a change in the volume of a second atom. However, for this to happen, the two atoms must be close enough to interact. Otherwise, for atoms that are far-separated, a displacement of one atom has a negligible effect on the volume of the other. In the latter case, many of the values passed in the array would be null.

Instead an alternative approach is devised, requiring no derivatives to be stored and skipping the calculation of Equation (3.27) when the atoms are far away. First, a function g_A is defined as:

$$g_A = \sum_B \frac{\partial \epsilon_{AB}[n](\mathbf{R})}{\partial \mathcal{V}_A[n]}. \quad (3.28)$$

Then, using Equation (3.24), Equations (3.22) and (3.23) are rewritten as:

$$\mathbf{F}_C^{\text{vdW}} = \mathbf{f}_C - \sum_A g_A \frac{\partial \mathcal{V}_A[n]}{\partial \mathbf{R}_C}. \quad (3.29)$$

The approach is to return both the values of \mathbf{f}_C and g_A to the calling code, which then completes the calculation of the forces using Equations (3.27) and (3.29).

3.3 Implementation

In the previous section, an overview of the TS-vdW method with detailed information on how to calculate the van der Waals energy, potential, and atomic forces was presented. Now, the attention is turned to a demonstration of how the library works, with its implementation in the Octopus code [110].

3.3.1 Octopus

Octopus is a computational chemistry package designed to perform *ab initio* simulations on a wide variety of physicochemical systems. The package is released under the GNU Lesser General Public License (GPL), so anyone is free to download, use, and modify it. It is parallelized using MPI and OpenMP for optimal execution performance. It can scale to tens of thousands of processors. Execution on graphical processing units is also supported through OpenCL.

In Octopus, electronic interactions are treated at the quantum mechanics level, using DFT, and in its time-dependent form (TD-DFT) when doing simulations in time [111]. Nuclei are described classically as point particles. The interaction between electrons and nuclei is simplified with norm-conserving pseudopotential approximations. No basis sets are employed, instead the wave function is represented by real-space grid discretization.

The TS-vdW library implementation has been available in Octopus, as an experimental feature, since the release of the stable version 5.0, in October of 2015. A new keyword, `VDWcorrection`, was created in Octopus to call the library. As any experimental feature in Octopus, to run any calculation using the library, the input file also requires the `ExperimentalFeatures` keyword. Sample input files are pro-

vided in Appendices B and C. In addition, a sample of the output files is included in Appendix D.

3.3.2 Overview of the TS-vdW Library

The library consists of free-standing *C* functions. The code of the library, included in the Appendix A, starts with the copyright statements and the license information. The current version of the TS-vdW library is released under the GPL version 3 license.

The body of the library is composed of six functions. The last two are only used in test mode. One of them is a wrapper to enable a *Fortran 90* call to use the library. The other is the main test function, which allows for validation of numerical accuracy in different systems. The other four functions are explained in more detail in the forthcoming paragraphs.

The first of those functions is `get_vdw_params`. Provided with the atomic number of an element, `zatom`, it retrieves the parameters required by the TS-vdW model: `*alpha`, the atom's static polarizability; `*c6`, the $C^{(6)}$ coefficient of the free atom; and `*r0`, the free-atom van der Waals radius². In Section 3.2, these three variables correspond to $C_{AA}^{(6),\text{free}}$, $\alpha_A^{(0)}$, and $R_A^{(0),\text{free}}$, respectively. The values are coded within a `switch` statement, and they are taken from Reference [106].

The `fdamp` function, is the second. It is the implementation of the damping function of Equation (3.3). It takes two arguments: `rr`, the separation between two nuclei, and `r0ab`, the quantity $R_{AB}^{(0)}[n]$, as defined by Equation (3.7). The function outputs three values: `*ff`, the damping function value; `dffdrrab`, the value of the derivative of the damping function with respect to the separation between two atoms, $\partial f^{\text{damp}}(R_{AB}, R_{AB}^{(0)}[n])/\partial R_{AB}$ as defined by Equation (3.26); and `dffdrr0`, the value of the derivative of the damping function with respect to the separation between effective van der Waals radii, $\partial f^{\text{Damp}}(R_{AB}, R_{AB}^{(0)}[n])/ \partial R_{AB}^{(0)}[n]$ of Equation (3.16).

²The simplest way of defining consistent free-atom van der Waals radii is through the electron density for spherical free atoms. The density contour value corresponding to the van der Waals radius can be determined for the rare-gas atoms and then used to define the free radius for other elements in the same row of the periodic table. [86]

The third function is `distance`. It takes as input the indices of a pair of atoms in the system, `iatom` and `jatom`, and their positions, `coordinates[]`; and returns several powers of the separation between them, `*rr`, `*rr2`, `*rr6`, and `*rr7`.

The fourth, `vdw_calculate`, calculates the van der Waals energy and force based on the theory explained in Section 3.2. As input, it takes the total number of atoms in the system, `natoms`; their atomic numbers, `zatom[]`; their coordinates, `coordinates[]`; and their effective volumes, `volume_ratio[]`, as defined by Equation (3.8). It outputs the van der Waals energy, `*energy`; the van der Waals atomic forces, `force[]`; and the sum over derivatives of the pairwise energies with respect to the effective volumes, `derivative_coeff[]`, defined as K_A in Equation (3.12).

3.3.3 Features

One of the advantages of the TS-vdW library is that, in practice, it uses the density as its unique input. The density is an object that any package that performs DFT calculations must compute. The calling code also requires an implementation of the Hirshfeld partitioning, which is calculated using the density. Many quantum mechanics codes already have such routine. Therefore, interfacing the TS-vdW module with a calling code is simple.

In addition, by requiring only the density, the library can be connected to codes that use different wave-function representations, such as real-space grids, plane waves, or atomic orbitals. Removing the additional step of converting the density of the whole system and of the fragments, would involve an extra amount of work and sometimes make the executions slower, makes the library performance more efficient.

The inclusion of the functional derivative of the van der Waals energy with respect to the density means that the library can be used for ground-state and TD-DFT calculations. It also makes possible to add the TS-vdW energy self-consistently, or apply it as a correction after the self-consistent procedure has converged. It is up to the developer to decide how to implement it in the calling code. The developer could also implement it allowing the user to chose between both options. This flexibility

might be applied in ground-state calculations, but it is especially useful for excited-states procedures, because it can reduce the computational cost.

The gradient of the van der Waals energy is also implemented in the library, thus providing the atomic forces due to van der Waals effects. This means that the TS-vdW dispersion correction can be used during geometry optimizations and for *ab initio* MD. With this implementation it is now possible to simulate real-time electron dynamics with van der Waals interactions using real-space TD-DFT. So far, there are no reports of this type of application in the literature.

One of the reasons why the TS-vdW method is popular is its affordable computational cost: the standard scaling of DFT calculations is unaffected by the TS-vdW correction. The execution times of an Octopus calculation with and without the TS-vdW scheme are very similar. Depending on whether the correction is applied self-consistently or post self-consistently, there is a small increment of the prefactor, but in any case the scaling is unaffected.

3.4 Simple Tests

In this section, two simple tests are presented. The first test, validates the operation of TS-vdW library interfaced with Octopus against a previous implementation of the method in Quantum Espresso. The second test shows the potential of the library to be applied in previously unexplored problems in the field of electron dynamics.

3.4.1 Validation of the Implementation

The benzene dimer is used as a model system for validation of the van der Waals energy calculation using the library. Validation of the gradients was performed during coding, and an internal test function was left in the code for future checks.

A PES calculation is performed on the benzene dimer, in the sandwich conformation, along the coordinate of separation between the COM of each benzene molecule, perpendicular to the planes of both benzenes (see Figure 3.4).

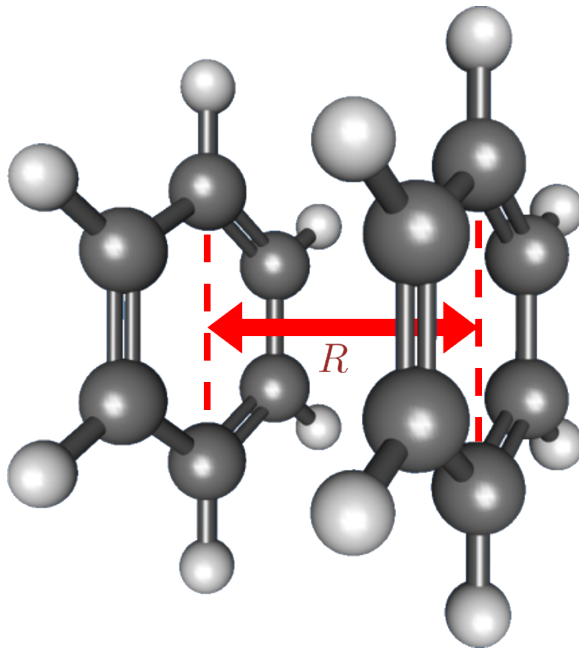


Figure 3.4. Benzene dimer in the sandwich conformation.

This is done in a series of single-point energy calculations, where both benzene molecules advance toward the origin along their main symmetry axis, oriented along the z -axis, while the geometry of the molecules is kept fixed. The initial separation of the dimer is set at 7.0 Å, guaranteeing minimal van der Waals interaction in the dimer. At each step, the molecules get closer at a rate of 0.2 Å per step. Chemically important regions of the curve are computed at uneven displacements ranging from 0.05 Å to 0.2 Å. The final separation of the dimer is 1.0 Å, to avoid superimposition of the atoms. The real-space grid settings were a spherical mesh radius of 5.0 Å and a grid spacing of 0.2 Å. The interaction and van der Waals energies are analyzed as a function of separation. For consistency, all calculations are carried out with the same pseudopotentials for hydrogen and carbon in both Octopus and Quantum Espresso. Appendices B and E contain a sample input for each program.

Figure 3.5 shows a comparison of the TS-vdW energy curve computed with each program. The TS-vdW energy includes the interaction and internal energies resulting from the TS-vdW correction. The curves fit well, with minor discrepancies probably

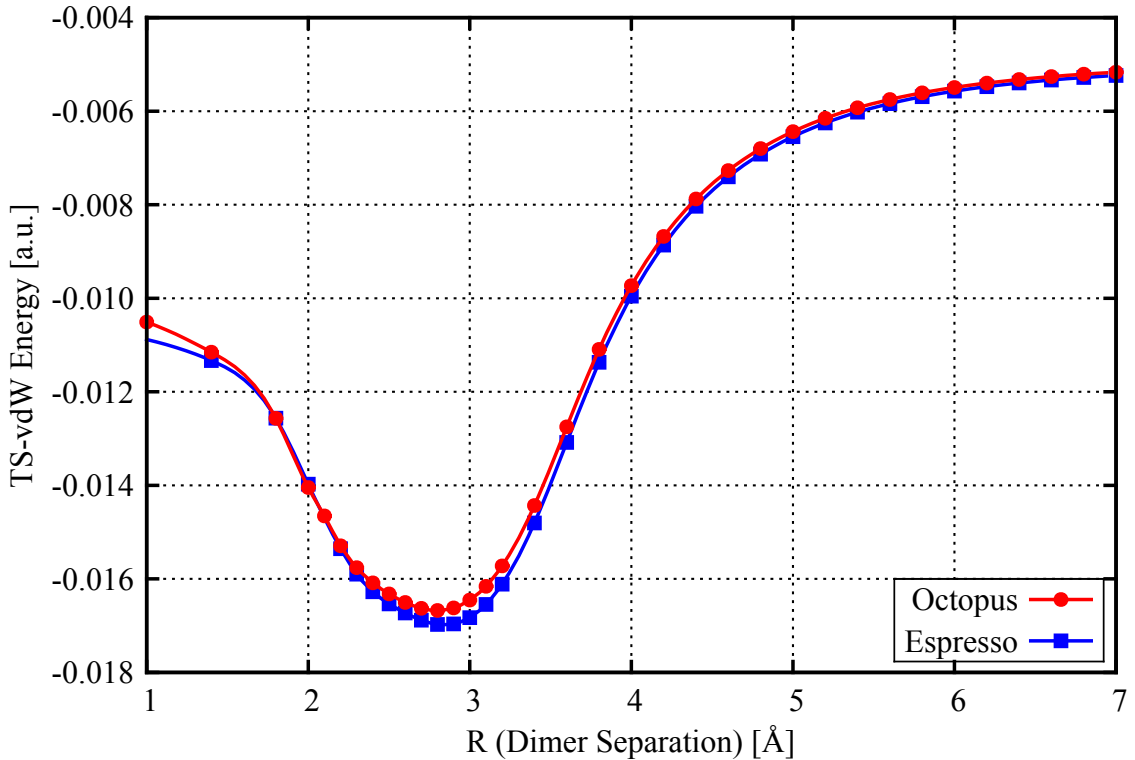


Figure 3.5. Comparison of the TS-vdW energy computed with two different implementations: Octopus and Quantum Espresso.

due to different representations of the wave function. Octopus uses a real-space grid, whereas Quantum Espresso works with plane waves.

Figure 3.6 shows a comparison of the interaction energy curve using the LDA and the TS-vdW-corrected LDA. Both curves are constructed with the data source as Figure 3.5, employing only the Octopus output. The results show a more negative interaction energy of the benzene dimer after the inclusion of the TS-vdW correction to LDA.

This test was designed to compare the output of two different implementations of TS-vdW method, not to assess the model itself. However, when comparing to highly accurate counterpoise-corrected CCSD(T)/aug-cc-pVQZ PES curves for the benzene dimer by Sinnokrot and Sherrill [112], the TS-vdW-corrected LDA interaction energy

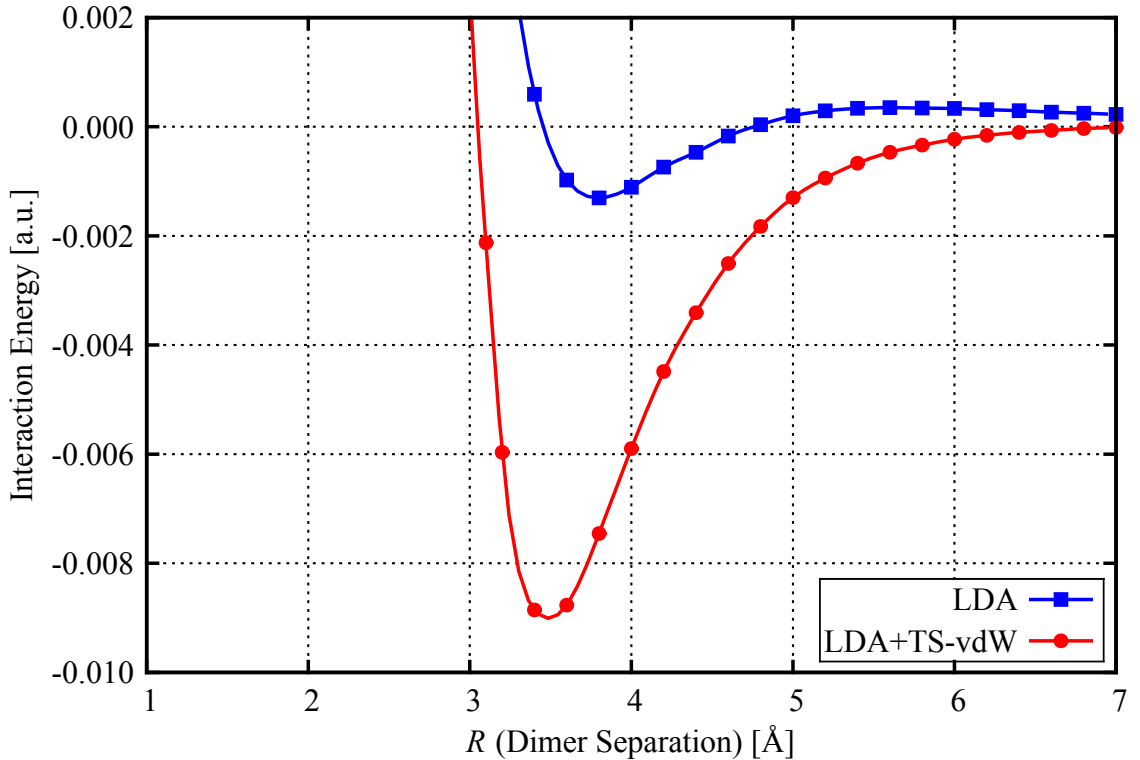


Figure 3.6. Comparison of the interaction energy computed with LDA vs. TS-vdW corrected LDA.

curve is clearly unphysical. Most probably, the obligated choice of pseudopotentials, which had to be compatible in both packages, along with the density and Hirshfeld effective volumes taken out of the LDA, were inappropriate for this case. Notwithstanding the poor chemical accuracy in this system, the values produced by both TS-vdW implementations resulted in agreement.

3.4.2 van der Waals-induced Shifts in Optical Spectra

The hydrogen fluoride dimer is used as a model system for an application of the TS-vdW functional correction to TD-DFT calculations. The hydrogen fluoride dimer is a conveniently small system on which tests with TD-DFT are computationally affordable.

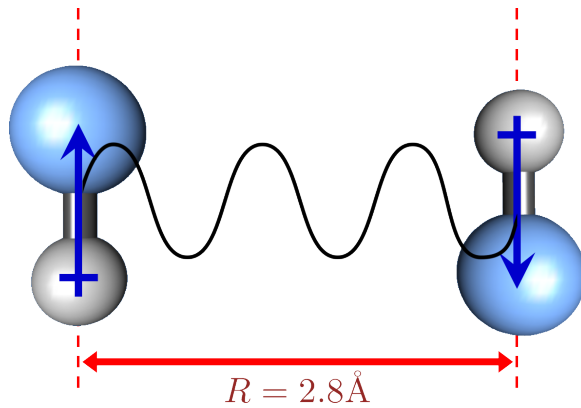


Figure 3.7. The hydrogen fluoride dimer in anti-parallel conformation.

First, the dimer geometry is setup as shown in Figure 3.7. The hydrogen fluoride molecules are placed in anti-parallel fashion, each one with its main symmetry axis oriented along the y -axis. The hydrogen fluoride bond in each monomer is 0.92 Å long, and the molecules are separated by 2.8 Å along the z -axis. At this distance, the van der Waals interaction between monomers is maximum.

To calculate absorption, the system is excited with an infinitesimal electric-field pulse, and then the TD Kohn-Sham equations are propagated for $30.38535 \hbar/eV$. The singlet dipole spectrum is evaluated from the TD dipole moment. The strength of the perturbation is set to 0.01 \AA^{-1} , and it is polarized in the z -axis. The time evolution is carried out using the Enforced Time-Reversal Symmetry (ETRS) propagator, with (default) time steps of $0.03352 \hbar/eV$.

The results on Figure 3.8 shows a small van der Waals-induced bathochromic-like (red) shift in the optical spectrum of the hydrogen fluoride dimer calculated with the LDA. This example opens the door for a new series of applications in supra-molecular chemistry, structural biology, polymer science, etc., that incorporate van der Waals effects on real-time electron dynamics.

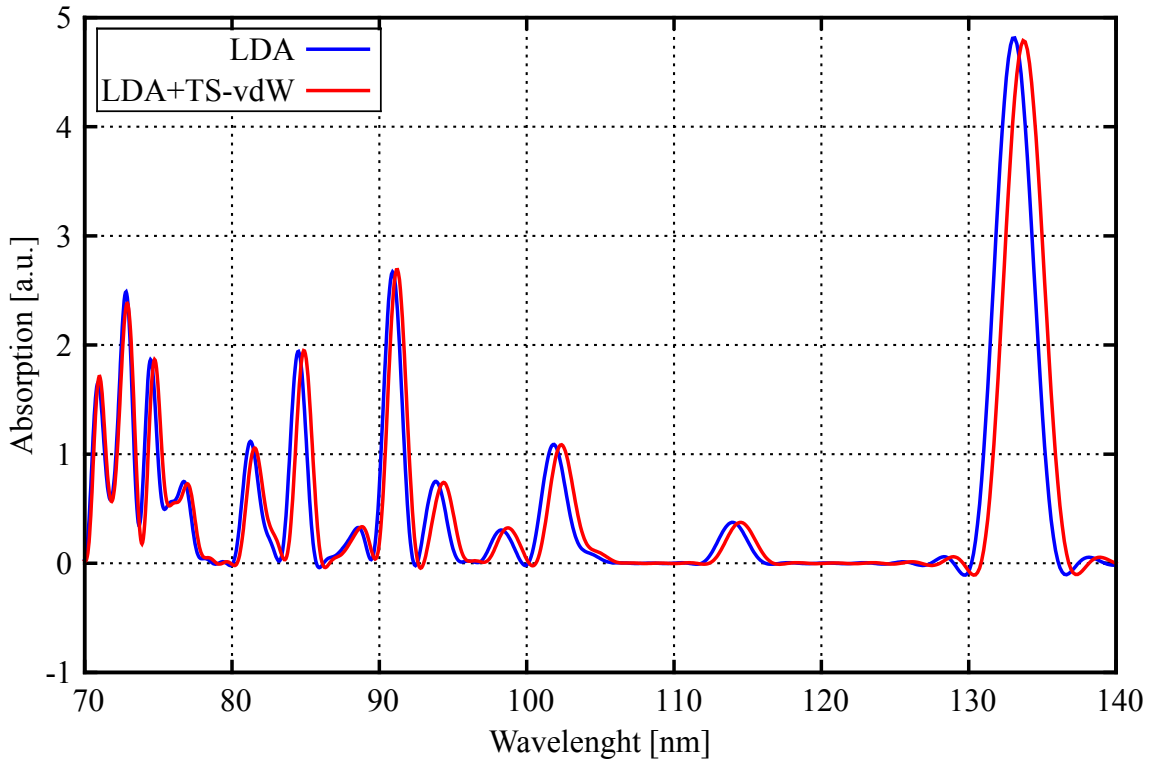


Figure 3.8. Absorption cross section spectrum of the hydrogen fluoride dimer with and without van der Waals effects.

3.5 Summary

van der Waals interactions are hard to capture in *ab initio* modeling, especially in DFT, since these originate from electron correlation. An overview of the current alternatives to include dispersion in standard functionals was presented. Among them, one of the most rigorous is the model by Tkatchenko and Scheffler.

A detailed description of the method, previously unavailable in the literature, was presented. The TS-vdW energy is a pair-wise term that depends on the chemical environment and polarizability of each atom. Environment dependence is derived from Hirshfeld partitioning of the electron density.

An implementation of the TS-vdW correction was introduced and explained. The library is a portable *C* code that can be connected to different materials-modeling

packages. The software has several advantages. The execution is independent from the basis functions. It uses the density as its unique input. It can be interfaced with different materials-modeling packages in a simple manner. The dispersion correction can be added after the total energy is obtained or applied self-consistently. The gradient of the van der Waals energy is also implemented, allowing for geometry optimization and MD simulations. The standard scaling of DFT calculations is unaffected by the TS-vdW correction.

Several aspects of this work could be further explored in future research. The dispersion energy, potential, and gradients were studied and implemented. However, the inclusion of the van der Waals Hessian is important for frequency calculations and thermochemistry. In addition, the implementation of the many-body dispersion model could prove useful. Another important step would be the efficient parallelization of the library. Finally, this modular implementation was meant to be interfaced with other computational chemistry packages. Good candidates are: NWChem, Psi4, Q-Chem, and GAMESS.

Inclusion of van der Waals interactions is especially important in describing aromatic, hydrocarbon, and halogen compounds, as well as molecular hydrogen phases, and water. It is now possible to simulate real-time electron dynamics with dispersion in all these systems using TD-DFT.

4. STANDARD AND LONG-RANGE-CORRECTED HYBRID FUNCTIONALS FOR EXCITATION ENERGIES

4.1 Introduction

The LDA was the first XC functional employed to study the electronic structure of molecules in Kohn-Sham DFT. Since then, the LDA has been a foundation for the development of functionals [113]. This chapter discusses the inclusion of HF-exchange, and its long-range-corrected form, on LDA-based functionals. It becomes apparent that these additions dominate over the generalized gradient corrections in the improvement of the quality of the fundamental gap and in the enhancement of excitation-energy estimations.

As an illustration of the wide range of possibilities created by this idea, the CAM-LDA0 functional is presented [2]: A three-parameter functional, with 1/4 global and 1/2 long-range HF interaction, respectively; a range separation factor of 1/3; and pure LDA exchange and correlation. CAM-LDA0 works for electronic excitations as well as the CAM-B3LYP functional, with the advantage of reduced computational cost due to the omission of the intricate generalized-gradient corrections.

4.1.1 Motivation

The LDA has been extensively used in solid-state physics and chemistry. One of its main applications is in the exploration of electronic and magnetic interactions in semiconductor materials. For example, until today, the LDA works well in predicting the Fermi level and band structure in doped semiconductor oxides. [114]

The LDA is based on this idea: for regions of a chemical system where the electron density is slowly varying, the XC energy, at each point, is approximately that of a locally-uniform electron gas of the same density. However, since its creation, Kohn

and Sham warned not to expect an accurate description of the chemical bond. [16] In ground-state calculations, covalent, metallic, and ionic bonds are usually well described with the LDA, although it has a slight tendency to overbind molecules [115]. The main shortcoming of the LDA is the description of hydrogen bonding and electron dispersion. As discussed throughout Chapter 3, dispersion interactions are hard to capture in DFT, not only with the LDA. This is because they involve long-range and dynamic electron-correlation effects. Moreover, the LDA is also subject to the self-interaction error, briefly discussed in Chapter 2.

In defiance of those limitations, the LDA has been key in functional development. More elaborate approximations to the XC energy, such as GGA or hybrid functionals, are designed to reproduce the exact results of the homogeneous electron gas for non-varying densities. Therefore, the LDA is often an explicit component of such functionals.

Even though accurate functionals for ground-states have been developed, creating suitable functionals for excited-states remains a challenge. One approach has been to use the ground-state functionals for calculation of excited states properties [116]. Although popular, this technique often yield results with limited accuracy.

A discussion motivating the inclusion of a portion of HF exchange into the XC functional of the LDA is presented in the forthcoming sections. It is shown that such addition refines the description of excited states properties, especially excitation energies. This scheme has the additional advantage of a higher computational efficiency when compared to GGA functionals.

4.1.2 Background

One of the main practical challenges in using DFT is that the universal functional for exchange and correlation is unknown, and exact models can be formulated only for the free electron gas. Nonetheless, various approximations have been designed to accurately calculate certain physical quantities quite accurately. The most common density functional approximations are described below.

4.1.2.1 Local Density Approximation

The oldest functional within Kohn-Sham DFT, the LDA, depends uniquely upon the value of the electron density at each point in space. It includes correlation, and is able to reproduce the ground-state features of the homogeneous electron gas: a system where electrons lie in a large periodic box, in such way that they are properly characterized by plane waves and a continuum energy spectrum. The LDA consists of kinetic, Hartree, exchange, and correlation contributions:¹

$$E^{\text{LDA}}[n] = T^{\text{TF}}[n] + E_{\text{H}}[n] + E_{\text{XC}}^{\text{LDA}}[n]. \quad (4.1)$$

The Hartree contribution was defined in Equation (2.7), and $T^{\text{TF}}[n]$ is the Thomas-Fermi kinetic-energy functional.

In the LDA, the XC contribution at each point is the energy of a locally-uniform electron gas of the same density,

$$E_{\text{XC}}^{\text{LDA}}[n] = \int d^3\mathbf{r} n(\mathbf{r}) \epsilon_{\text{XC}}^{\text{unif}}[n]. \quad (4.2)$$

It is common to split ϵ_{XC} into exchange and correlation potentials,

$$\epsilon_{\text{XC}}^{\text{unif}}[n] = \epsilon_{\text{X}}^{\text{unif}}[n] + \epsilon_{\text{C}}^{\text{unif}}[n]; \quad (4.3)$$

where the exchange potential is given by the Dirac functional, [117]

$$\epsilon_{\text{X}}^{\text{unif}}[n] = -\frac{3}{4} \sqrt[3]{\frac{3}{\pi}} n(\mathbf{r}). \quad (4.4)$$

Usually, the correlation potential, $\epsilon_{\text{C}}^{\text{unif}}[n]$, is parametrized with respect to a set of quantum Monte Carlo calculations for the uniform electron gas, performed by Ceperley and Alder [118]. Several approaches, using different analytic forms for the correlation potential, have generated several approximations for the correlation functional [22, 62, 119–121]. These approximations are functionals depending upon the Wigner-Seitz radius, r_s , and the relative spin-polarization, $\zeta(\mathbf{r})$.

¹Conventions adopted in this chapter: Atomic units are used throughout. The \mathbf{r} symbol is used for electronic coordinates. Dependence on \mathbf{r} is left implicit in functional notation. Units of magnitude in figures are enclosed in squared brackets.

The LDA is based on the assumption that the density is the same everywhere. Why does such a simple approximation work? The XC hole, $P_{\text{XC}}(\mathbf{r}, \mathbf{r}')$, is the probability of finding an electron at \mathbf{r}' given that there is an electron at \mathbf{r}' . It can be thought of as the hole the electron at \mathbf{r} creates for itself in the surrounding electron cloud. There are a number of properties which will be satisfied by the exact XC hole. One of them is that it should normalize to exactly one electron,

$$\int d^3\mathbf{r}' P_{\text{XC}}(\mathbf{r}, \mathbf{r}') = -1. \quad (4.5)$$

This is known as the sum rule, and the LDA satisfies that condition. Despite that the XC hole is poorly described by the LDA, the electron interaction depends mainly on the spherical average of the XC hole. The LDA works in part because it generates a reasonable estimate of that spherical average [122].

Additionally, when comparing the exchange and correlation energy densities of the LDA with the exact ones, especially in the bonding region, the exchange tends to be too negative, whereas the correlation tends to be more positive. Therefore, the errors in the exchange and correlation energy densities tend to cancel. [123].

4.1.2.2 Generalized Gradient Approximations

In molecular systems the density fluctuates and the LDA has a tendency to overestimate the XC energy. That induces typical errors in overestimated binding energies, underestimated lattice parameters, incorrect ordering of phase stability, and wrong energies in magnetic materials [124]. To correct for this tendency, it is common to include another functional dependence upon the gradient of the density to account for the non-homogeneity of actual electron densities,

$$E_{\text{XC}}^{\text{GGA}}[n] = \int d^3\mathbf{r} n(\mathbf{r}) \epsilon_{\text{XC}}[n, \nabla n]. \quad (4.6)$$

This allows for gradient corrections based on the changes in density away from point \mathbf{r} . These functionals are known as GGA. One of the most successful functionals of this type is the Perdew-Burke-Ernzerhof (PBE) [49]. Examining how the PBE functional works, serves as a GGA-model example.

On the one hand, the exchange energy is constructed using a contribution from the local spin-density approximation² multiplied by a function, $F_X(s)$, known as the enhancement factor,

$$E_X^{\text{GGA}} = \int d^3\mathbf{r} n(\mathbf{r}) \epsilon_X^{\text{unif}}(n) F_X(s). \quad (4.7)$$

The enhancement factor, in turn, depends upon s , a dimensionless density gradient. In other words, this GGA exchange functional is built multiplying the exchange of the uniform electron gas times an enhancement factor containing a generalized gradient correction. By construction, the enhancement factor is close to 1. Interestingly, to recover the correct homogeneous-electron-gas limit, the enhancement factor must be equal to 1 when the gradient is negligible, $F_X(0) = 1$. Although, not generally true, the generalized gradient contribution is, in practice, to multiply the local exchange by approximately 1.

On the other hand, the correlation energy incorporates an additional term, containing the generalized gradient correction, that is added to the contribution from the local spin-density approximation,

$$E_C^{\text{GGA}}[n_\uparrow, n_\downarrow] = \int d^3\mathbf{r} n(\mathbf{r}) [\epsilon_C^{\text{unif}}(r_s, \zeta) + H(r_s, \zeta, t)]. \quad (4.8)$$

The gradient contribution, $H(r_s, \zeta, t)$, depends partially on t , a dimensionless gradient [121]. In the slowly-varying limit, when the electron density is close to being uniform, $t \rightarrow 0$. The correlation energy resembles that of the homogeneous electron gas, and $H(r_s, \zeta, t)$ becomes a small number. In the rapidly-varying limit, when $t \rightarrow \infty$, the correlation has to vanish, therefore $H(r_s, \zeta, t) \rightarrow -\epsilon_C^{\text{unif}}$. In intermediate cases, the generalized gradient contribution, in practice, is to add a generally small quantity to local correlation.

The GGA retains correct features of LDA, and combines them with the most energetically important features of gradient-corrected non-locality. GGA functionals are typically better behaved than the LDA, with accuracy approaching that of correlated wave-function methods, such as MP2, and in some cases surpassing them [125].

²The local spin-density approximation (LSDA) is a generalization of the LDA to include electron spin.

Although this is not true in every case, GGA functionals reduce the bond dissociation energy error, and generally improve transition-state barriers with respect to the LDA.

4.1.2.3 Hybrid Approximations

GGA functionals are considered widely applicable because they usually provide reasonable results for most properties [126]. Yet, admixing a portion of HF exchange into the XC functional improves binding energies [127], bond lengths, vibration frequencies [54], lattice constants [128], fundamental gaps [129], and excitation energies [130].

The hybrid approach to constructing density functional approximations was introduced by Becke. On the adiabatic connection formula, he found the justification to admix non-local exchange to improve electronic structure calculations [54]. The reasoning is that including a portion of exact exchange with local density functionals enhances their accuracy by making the XC hole deeper and more localized around its electron [127].

Rather than utilizing the density, the exact-exchange energy functional is expressed in terms of the Kohn-Sham orbitals (the $1/|\mathbf{r} - \mathbf{r}'|$ operator sometimes is written as $1/r_{12}$),

$$E_X^{\text{HF}} = -\frac{1}{2} \sum_{i,j}^N \int d^3\mathbf{r} \int d^3\mathbf{r}' \phi_i^*(\mathbf{r}) \phi_j^*(\mathbf{r}) \frac{1}{|\mathbf{r} - \mathbf{r}'|} \phi_i(\mathbf{r}') \phi_j(\mathbf{r}'). \quad (4.9)$$

This is a type of implicit density functional, in which the dependence on the density goes through the Kohn-Sham orbitals.

In spite of the improvements, some authors in the field of density-functional development consider this alternative approach as a branch outside DFT. This is because, strictly speaking, the formulation of Kohn and Sham requires that all the orbitals, occupied and virtual, are subject to the same XC potential.

Seidl et al. introduced a system of interacting electrons, where the interaction is described by a simplified functional of the orbitals, which can depend on parameters [131]. This is known as the generalized Kohn-Sham method. Using density-functional

perturbation theory, Görling and Levy explained how to predict the optimum amount of exact exchange to be admixed with a functional [132, 133].

An application of this concept, is the famous recipe by Perdew et. al. to include 25% of HF exchange in the XC energy of a GGA [54]. If the GGA functional is the popular PBE [49], then one obtains the PBE0 hybrid [50, 51], a functional with only one parameter. In contrast, the most successful functionals are hybrids with more than three empirical parameters. The hybridization typically consists in combining different types of exchange and correlation functionals, leading to approximations such as the famous B3LYP [57].

4.1.2.4 Linear-response TD-DFT Properties

There is a close connection between the ground-state parametrized methods and their linear-response extensions. It is known that a purely local XC kernel³ in standard Kohn-Sham theory, like the adiabatic LDA, often produces an inaccurate optical gap, the energy threshold for photons to be absorbed. Almost all present applications of TD-DFT employ the adiabatic approximation for TD XC effects: in constructing the XC potential at time t , all functional dependence of the TD density prior to t is ignored. In both the ground-state and TD cases, the relaxation and compression of the orbital levels caused by the XC potential of the LDA is excessive with respect to pure HF calculations.

The addition of an appropriate fraction of orbital exchange reduces these effects by inducing orbital-specific screening. Nonetheless, the gradient-based corrections to the XC of the LDA, present in functionals like PBE, do not seem to produce a significant change on this widening of orbital levels, as reported in Section 4.4.

4.2 Theory

As discussed above, the GGA functionals were developed to improve energies with respect to those of the LDA. The purpose of the gradient corrections is mainly

³The XC kernel is defined as the functional derivative of the XC potential with respect to the electron density: $f_{xc} = \delta v_{xc} / \delta n(\mathbf{r})$.

to extend the LDA functional to the inhomogeneous electron gas case. Alternatively, hybrid approximations provide a better model of the XC hole, improving important chemical properties over GGA functionals. Still an important question arises from this discussion: is there any other way to retain the correct behavior of the LDA, and capture the energetically important features of inhomogeneous systems?

To investigate atoms and molecules, the gradient-corrected functionals give slightly more accurate ground-state properties than the LDA. For example, binding energies are improved because GGA functionals partially account for curvature variations in the density of the bonding regions during a dissociation. Granting all this, are the generalized-gradient corrections vital for the calculation of excited-states static properties such as the estimation of gaps and excitation energies? Or can they be calculated using hybrids of the LDA?

4.2.1 LDA-based, Hybrid Approximations

A family of LDA-based hybrid approximations [2] is introduced subsequently. $G_\lambda[n]$ is defined as an energy functional of a system of electrons, represented by a single Slater determinant, which interact through a partial Coulomb interaction:

$$G_\lambda[n] \equiv \min_{\Phi \rightarrow n} \langle \Phi | \hat{T} + \lambda \hat{W} | \Phi \rangle , \quad (4.10)$$

where \hat{T} and \hat{W} are the kinetic and repulsion energy operators⁴, respectively, and $\lambda > 0$ is a parameter modulating the Coulomb interaction.

The functional $G_\lambda[n]$ can be straight-forwardly expressed using the LDA as

$$G_\lambda[n] = T^{\text{TF}}[n] + \lambda E_{\text{HX}}^{\text{LDA}}[n] , \quad (4.11)$$

where $T^{\text{TF}}[n]$ is the Thomas-Fermi kinetic energy functional.

The partial LDA for the HXC energy is expressed as

$$E_{\text{HXC}}^{\text{LDA},\lambda}[n] = (1 - \lambda)(E_{\text{H}}[n] + E_{\text{X}}^{\text{LDA}}[n]) + E_{\text{C}}^{\text{LDA}}[n] , \quad (4.12)$$

⁴In second quantization, $\hat{W} = -\frac{1}{2} \iint d^3\mathbf{r} d^3\mathbf{r}' \hat{\psi}^\dagger(\mathbf{r}') \hat{\psi}^\dagger(\mathbf{r}) w(|\mathbf{r} - \mathbf{r}'|) \hat{\psi}(\mathbf{r}) \hat{\psi}(\mathbf{r}')$, and $w(|\mathbf{r} - \mathbf{r}'|)$ is the Coulomb repulsion potential.

where $E_H[n]$ is the Hartree repulsion energy functional, and λ behaves as a parameter that controls the contribution of the exact exchange energy functional.

By adding $G_\lambda[n]$ and $E_{\text{HXC}}^{\text{LDA},\lambda}[n]$ together, the LDA energy functional for the uniform-electron-gas limit is recovered with any value of λ [54]:

$$\begin{aligned} E^{\text{LDA}}[n] &= G_\lambda[n] + E_{\text{HXC}}^{\text{LDA},\lambda}[n] \\ &= T^{\text{TF}}[n] + \lambda E_{\text{HX}}^{\text{LDA}}[n] + (1 - \lambda) E_{\text{H}}[n] + (1 - \lambda) E_{\text{X}}^{\text{LDA}}[n] + E_{\text{C}}^{\text{LDA}}[n] \quad (4.13) \\ &= T^{\text{TF}}[n] + E_{\text{H}}[n] + E_{\text{XC}}^{\text{LDA}}[n]. \end{aligned}$$

Equations (4.11) and (4.12) define a family of LDA-based, one-parameter, hybrid approximations. Two functionals of that family are labeled. LDA0: with $\lambda = 1/4$, containing 25% of HF exchange,

$$E_{\text{HXC}}^{\text{LDA0}}[n] = E_{\text{H}}[n] + \frac{1}{4} E_{\text{X}}^{\text{HF}}[n] + \frac{3}{4} E_{\text{X}}^{\text{Slater}}[n] + E_{\text{C}}^{\text{VWN5}}[n]; \quad (4.14)$$

which is essentially PBE0 without the gradient contribution. And LDA1: with $\lambda = 3/10$, and 30% of HF exchange,

$$E_{\text{HXC}}^{\text{LDA1}}[n] = E_{\text{H}}[n] + \frac{3}{10} E_{\text{X}}^{\text{HF}}[n] + \frac{7}{10} E_{\text{X}}^{\text{Slater}}[n] + E_{\text{C}}^{\text{VWN5}}[n]; \quad (4.15)$$

resembling PBE0-1/3 [134] without the gradient contribution.

4.2.2 LDA-based, Range-separated-hybrid Approximations

Further parameterizations can be introduced for the auxiliary system of electrons. The Coulomb interaction between two electrons can be separated into a long- (lr) and a short-range (sr) contribution. If the Coulomb attenuated method (CAM) is used, such splitting requires additional parameters⁵ [58],

$$\frac{1}{|\mathbf{r} - \mathbf{r}'|} = \frac{1 - [\lambda + \zeta \operatorname{erf}(\mu |\mathbf{r} - \mathbf{r}'|)]}{|\mathbf{r} - \mathbf{r}'|} + \frac{[\lambda + \zeta \operatorname{erf}(\mu |\mathbf{r} - \mathbf{r}'|)]}{|\mathbf{r} - \mathbf{r}'|}. \quad (4.16)$$

The first term on the right-hand side controls the long-range contribution, while the second controls the short-range contribution.

⁵Some authors use α instead of λ , β instead of ζ , and ω instead of μ . The parameter ζ should not be confused with the relative spin polarization function $\zeta(\mathbf{r})$ introduced in Section 4.1.2.

Now a range-separated hybrid can be formulated,

$$G_{\lambda,\zeta}[n] \equiv \min_{\Phi \rightarrow n} \langle \Phi | \hat{T} + \lambda \hat{W} + \zeta \hat{W}_\mu^{\text{lr}} | \Phi \rangle , \quad (4.17)$$

which is similar to Equation (4.10), except for the inclusion of a third operator, \hat{W}_μ^{lr} , and the ζ parameter. The operator corresponds to the long-range repulsion. The partial HXC energy is:

$$E_{\text{HXC}}^{\lambda,\zeta}[n] = (1 - \lambda - \zeta) E_{\text{HX}}^{\lambda,\zeta}[n] + \zeta E_{\text{HX}}^{\text{sr},\lambda,\zeta}[n] + E_{\text{C}}^{\lambda,\zeta}[n]. \quad (4.18)$$

A new family of LDA-based, three-parameter, range-separated-hybrid approximations is defined with Equations (4.17) and (4.18). These functionals are exact for the homogeneous electron gas. The detailed derivation can be found in Reference [2]. In particular, a new functional, named CAM-LDA0, is defined with 1/4 global HF exchange (λ), 1/2 long-range HF exchange (ζ), and range separation factor (μ) of 1/3.

4.3 Computational Details

In order to study the performance of the LDA-based hybrid approximations, a subgroup of the benchmarking set previously reported by Peach et al. was used [130]. This subset maintains an even balance between the number of CT and local excitations. The excitation energies of the following molecules are analyzed (See Figure 4.1): dipeptide, β -dipeptide, hydrogen chloride (HCl), N-phenylpyrrole (PP), 4-(N,N-dimethylamino) benzonitrile (DMABN), carbon monoxide (CO), anthracene, and polyacetylene (PA) oligomers. A comparison of the accuracy of the adiabatic functionals PBE0 ($\lambda = 0.25$), LDA0 ($\lambda = 0.25$), LDA1 ($\lambda = 0.30$), and CAM-LDA0 is carried out. Additionally, data corresponding to B3LYP and CAM-B3LYP, calculated by Peach et al., is included.

All calculations were run using the NWChem 6.6 suite [135]. A sample input is included in Appendix F. First, all the molecular geometries were optimized employing the 6-31G* basis set for each functional: PBE0, LDA0, and LDA1. In most cases, the excitation-energy calculations with a certain adiabatic functional were performed at

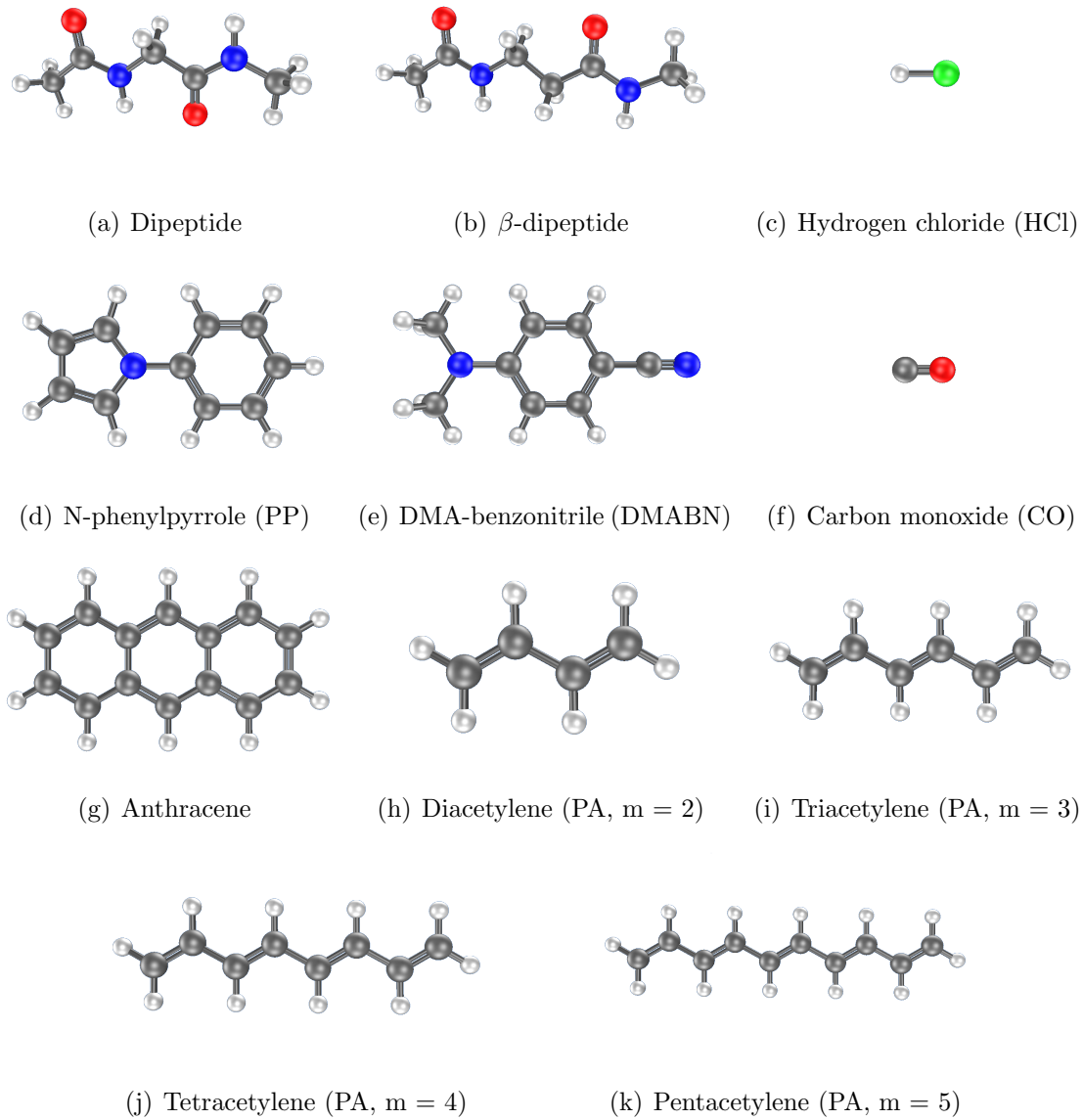


Figure 4.1. Testing set for excitation energies with the LDA-based hybrids.

the molecular geometry obtained with its ground-state equivalent functional. A few exceptions are noted: for the calculations with CAM-LDA0, the LDA0 geometry was used; and for the β -dipeptide molecule, the LDA0 optimal geometry was employed for all the excitation calculations. The linear response TD-DFT calculations were carried out with the correlation-consistent, polarized, triple zeta cc-pVTZ basis set,

except for CO, for which d-aug-cc-pVTZ was employed, as suggested by Peach et al. in Reference [130].

4.4 Results

The calculated excitation energies are presented in a table in Appendix G. Reference values are also included in the table. Most reference values are taken from gas-phase experiments, and a few are calculated either with complete active space with second-order perturbation theory (CASPT2) or second-order approximate coupled-cluster (CC2) methods. Figure 4.2 is plotted using the data contained in Appendix G. To compare between several popular hybrid functionals and the approximations formulated in Section 4.2, the mean absolute error (MAE)⁶ is the metric employed.

The excitation energies from LDA0 are around 0.1 eV less than those obtained using PBE0. Also, for this set of excitation energies, both PBE0 and LDA0 yield similar numbers as B3LYP. Further increments of the amount of HF exchange raises the excitation energies with respect to PBE0. Consider LDA1, with $\lambda = 0.3$, for example. Figure 4.2 shows that LDA1 is slightly more accurate than LDA0.

In addition, the convergence of the linear-response calculations with the adiabatic LDA0 functional is twice as fast as with PBE0; and both functionals display close mean absolute errors, as shown in Figure 4.2. The improved efficiency of LDA-based functionals is due to a faster convergence of the self-consistent procedure.

Figure 4.2 shows that local excitations are comparably described by all the tested functionals. It also appears that removing the gradient contributions improves the accuracy of Rydberg excitations. CT excitations are similar with all standard hybrids. But CAM functionals are significantly more accurate, with CAM-LDA0 working as well as CAM-B3LYP. Noteworthy, PBE0, LDA0, and LDA1 are unable to properly capture the CT excitation energies as the CAM functionals do. The improvement in the description of such processes lies in the addition of the long-range, HF exchange contribution.

⁶MAE is defined as $\frac{1}{n} \sum_{i=1}^n |f_i - y_i|$, where n is the number of measurements and f and y represent the experimental and true values, respectively.

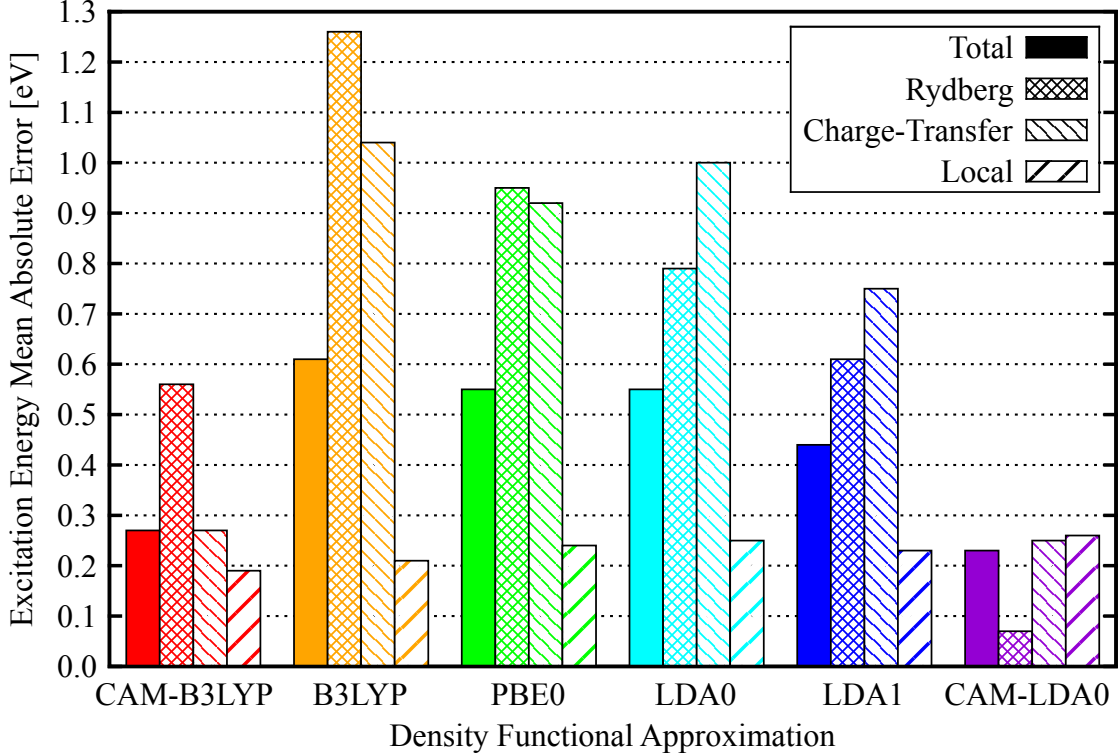


Figure 4.2. Comparison of the mean absolute error in eV of the excitation energies computed on the set shown in Figure 4.1.

Why does it work? The addition of non-local exchange increases the excitation energies, but does not raise the CT values high enough. A further increase of λ could be attempted, but this would induce errors in the non-CT excitations. Long-range, HF exchange effectively raises the energy of the long-range excitations, which are essentially of the CT type. For local excitations, the long-range, non-local exchange has little effect.

The CAM, is an extension of the work of Tsuneda et al. [136]. They showed that partitioning of the Coulombic interaction and use of HF exchange for the long-range interactions were of practical utility. These studies focus only on exchange interactions. The effect of non-local correlation is left unexplored.

The gradient corrections to the adiabatic LDA0 functional have little effect on the excitation energies. For example, compare CAM-B3LYP to CAM-LDA0. The latter

functional consists in setting $\lambda = 1/4$, $\zeta = 1/2$, and $\mu = 1/3$, while the residual parts of exchange and correlation are treated with LDA only. The factor $\mu = 1/3$ comes from the study of Tsuneda et al., and $\zeta = 1/2$ derives from the work of Yanai et al. As illustrated in Figure 4.2, the performance of CAM-LDA0 agrees with that of CAM-B3LYP.

Besides, CAM-LDA0 leads to computer times reduced by about 30% with respect to CAM-B3LYP. The cost cannot be reduced further due to the use of the error function. In situations where computational resources are limited, or need to be shared among many users, some increase in efficiency might be desired. Approximation and speed-up of exchange integrals is an ongoing field [137, 138]. If a boosting algorithm can be applied to a functional such as the adiabatic CAM-LDA0, then the time savings could be increased.

Furthermore, the robustness of the adiabatic LDA XC kernel has been pointed out by Baerends and collaborators [139, 140]. They noted cases where inclusion of asymptotic gradient corrections, such as in the van Leeuwen-Baerends functional [141], does not yield significant changes to excitation frequencies. Nonetheless, asymptotic corrections are crucial to correctly estimate sensitive properties such as multipole polarizabilities [142, 143].

Moreover, the tendency of gradient-dependent terms to produce small contributions to the excitation energies, for the standard theory with no parameters ($\lambda = 0$), can also be inferred from earlier studies. For instance, the data reported in References [144, 144, 145] suggest that for low-lying excitation energies the results change by a small amount when switching from the adiabatic PBE functional to the adiabatic LDA.

The purpose of the gradient corrections to the LDA XC energy is mainly to extend the LDA functional to the inhomogeneous electron gas case. To investigate atoms and molecules, the gradient-corrected functionals provide more accurate ground-state properties than the LDA. In a dissociation process, for example, the curvature of the density increases due to the reduction of the density in the bonding regions. Since

the GGA approximations partially account for this effect, the binding energies are improved. In contrast, the LDA0, or CAM-LDA0, is less suited for describing binding energies.

For large molecules, congruence between the approximations used is convenient for the excitation-energy estimations. For example, if a ground-state functional is employed, then its adiabatic equivalent should be considered for the Linear-Response TD-DFT calculations. There are indeed cases where an accurate description of the ground-state equilibrium geometry is required, and the XC ground-state functional and its adiabatic form need gradient corrections, or other type of improving terms.

The results in Figure 4.2 indicate that introduction of the parameters λ , ζ , and μ are useful to improve optical properties. Interestingly, the generalized Kohn-Sham method allows for inclusion of several types of auxiliary interactions between the auxiliary electrons to enhance the approximations in standard Kohn-Sham theory. It would be desirable to have a reference system where the value of the parameters λ , ζ , and μ could be estimated. There is a fundamental challenge in the search for approximations, though: the exact density functional is not an analytic function [146–148]. Assigning orbital dependent contributions to the auxiliary system of electrons introduces non-analyticities. However, the LDA and GGA functionals are analytic, which makes them essential in developing new approximations.

4.5 Summary

Two types of approximated functionals for excitation energies were introduced. One, a mostly unexplored class of LDA-based, one-parameter, standard-hybrid approximations; the other, a completely-new family, LDA-based, three-parameter, range-separated-hybrid approximations.

Initial examination of these adiabatic functionals showed promising results for linear-response properties. The LDA0 and LDA1 models proved that non-local exchange corrections to LDA can produce excitation energies comparable to functionals such as PBE0 or B3LYP. Excitation energies of the CAM-LDA0 functional are com-

parable to those of CAM-B3LYP, with the advantage of a reduced computational cost due to faster a convergence of the self-consistent field procedure. Although, an assessment of the description of geometries in the excited states with these functionals remains undone, the results gathered suggest that a portion of non-local exchange is a dominant factor for the enhancement of excitation energies over generalized gradient corrections.

It should be reminded that gradient corrections are important for binding energies, geometries, and vibrations. Also, different chemical systems, in principle, require different amounts of non-local HF exchange, which can motivate further work on transforming the parameters into purely *ab initio* quantities. Discretion and insight by the user are required to properly set up the correct amount of exchange, and related quantities. Such judgment can be enriched by knowledge deduced from reliable *ab initio* calculations and experimental measurements.

PART TWO

5. THE EFFECTIVE FRAGMENT POTENTIAL METHOD

5.1 Introduction

The EFP method is the main discussion topic on the subsequent four chapters of this thesis. Although the literature on this field is broad, dating back to the early 1980s, this is a complex topic to follow: different authors describe the method using diverse mathematical expressions, notations, and often times few details are provided.

Generally following the second section of the article by Ghosh et al. [149], this chapter introduces the method and provides basic information about its working mechanism. It also intends to be an accessible guide to EFP.

The chapter starts with a quick historical perspective. Subsequently, the most common derivations for each energy term are provided. Finally, it concludes with a short explanation of the basic steps required to run an EFP calculation.

5.2 Background

The EFP method is a computationally inexpensive way of modeling intermolecular interactions in non-covalently bound systems. Although in essence it is *ab initio*-based polarizable classical force field, the EFP approach can be viewed as a quantum-mechanics/molecular-mechanics (QM/MM) scheme with no empirical parameters.

The EFP method is designed to accurately describe intermolecular interactions and environmental effects. Therefore, compared to *ab initio* methods, it is a computationally inexpensive technique that can capture intermolecular interactions in large systems. It was originally formulated to simplify the treatment of complex chemical systems. However, it has undergone vast improvements since its origins.

5.2.1 The Origins

What is known today as the EFP method has evolved significantly since its creation. The original EFP method of Ohta et al. [150] is developed in 1983 to model the environment of a chemical system by means of a simplified effective potential. Their idea is to treat explicitly only those electrons directly involved in molecular interactions. Such approach resembles an extension of the atomic effective core potential approximation. The study by Ohta et al. presents an effective fragment (EF) of the ammonia molecule consisting of only the lone-pair electrons. However, their system containing the EFP of ammonia interacting with an all-electron ammonia or borazine provides promising results. This ancient version of a QM/MM scheme produces good-enough energy profiles to encourage a quick application of the EFP method to other molecules, including water [151].

A new potential energy expression more similar to the one known today, is introduced in 1987 by Honda and Kitaura [152]. They devise a different intermolecular potential with the idea of performing classical Monte Carlo and MD simulations of liquids, solutions, and other molecular assemblies. Their potential is expressed in terms of two main contributions: One depending on the intermolecular overlap integrals over localized molecular orbitals (LMO) of isolated molecules, and the other based on Coulomb potentials between fractional point charges placed on the nuclei. This potential function is easy to generate, and is applicable to a wide range of molecules.

5.2.2 The EFP1 Model

A series of auspicious breakthroughs, starting from 1994, mainly by Jensen and other collaborators of the Gordon group at Iowa State University [153, 154], advance the EFP method to a higher level of sophistication. Such advances make the method so popular that most of the literature attributes the origin of the EFP method to the Gordon group. Their approach, which has been extensively applied to model solvent effects, is known as EFP1.

Stone had shown that it is possible to relate the intermolecular interactions to the properties of the isolated molecules in a general way [155, 156]. As Jensen explains in his doctoral thesis [157], using perturbation theory, the interaction energy of the system is decomposed as an expansion of the perturbation energy, including short- and long-range terms. Then, the first order energy corresponds to the electrostatic interactions. The second order energy is comprised of polarization and dispersion¹ energies. They also rationalized that at shorter intermolecular distances the electron exchange becomes important. However, at that point they did not find an obvious way to relate the XR energy to the properties of the unperturbed molecules. Such contribution must be added to the total energy, therefore they introduce repulsive effective potentials, and employ the energy decomposition scheme by Morokuma and Kitaura [158] to formulate the reminder term.

The approach by Jensen et al. works under certain assumptions. The most important is that the internal geometry of the EF does not change, therefore its internal Hamiltonian and resulting energy is ignored. In other words, any energetic contribution from the internal structure of an EF is disregarded.

Although successful for water modeling [159–161], EFP1 still requires extensive parameterization for different molecules, mainly due to the parametrized form of the reminder term. Specifically, it requires the determination of dimer PES for each alternative molecule of interest, followed by a fitting procedure for the reminder term.

Further developments in the expression of the XR potential [162, 163], based on previous work by Murrell and collaborators [164, 165], produce a more general expression for intermolecular Pauli exclusion. In this approximation, the XR interaction between closed-shell fragments is estimated through the overlap of the isolated wave functions of the fragments.

¹It is important to note that the dispersion energy is not considered explicitly in the EFP1 model, although at its beginnings it was known that it could be derived from the second-order term.

5.2.3 The EFP2 Model

Based on those developments, in 2001, the method matures to what is known now as the EFP2 approach [166]: a general implementation replacing the fitted reminder term with a expression for exchange repulsion derived from first principles.

Then, the principle limitation of the new approach became the correlation contributions, most notably dispersion, which is not explicitly included yet. Such limitation was overcome with the implementation of a distributed dispersion by Adamovic and Gordon [167].

EFP2 is a significant improvement over its predecessor: The potential applications become broader than the original studies of aqueous solvent effects on biochemistry of peptides and enzymes for which EFP1 is initially developed. Since EFP2 incorporates most of the important physical interactions directly from quantum mechanics and requires no adjustable parameters, it is an appealing alternative to classical force fields in QM/MM simulations.

Continuous enhancements over the EFP2 method [168–170], as well as extensive tests [171, 172] and benchmarking studies [172–175] have transformed it into one of the most popular tools of *ab initio*-based classical modeling [176]. EFP2 has been successfully employed to study a variety of extended systems ranging from condensed phases and materials [177, 178] to proteins and macromolecules [179, 180].

5.3 The Effective Fragment Potential Method

The EFP method² is a systematic approach to describing intermolecular interactions. It can be thought of as a non-empirical polarizable force field that employs quantum mechanical-based potentials. It is efficient in the use of computational resources, yet at the same time is rigorous from the theoretical point of view. Moreover, the current implementation of the EFP method can be generally applied to a wide range of chemically relevant molecules.

²From now on EFP will generally refer to the EFP2 implementation.

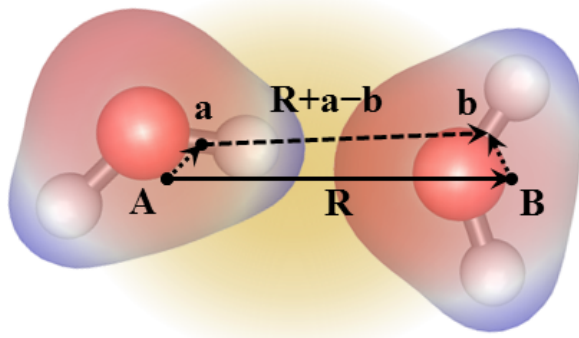


Figure 5.1. Schematic representation of fragments of water. **A** and **B** denote the positions of the COM of each fragment, the coordinates of **a** and **b** are points on fragments A and B, respectively; and $\mathbf{R} = \mathbf{B} - \mathbf{A}$ is the separation vector between the COM of the fragments.

Take the example of a small cluster of water, such as the one depicted in Figure 5.1. In the EFP approach each molecule could define a fragment. Assuming that the fragments have a fixed internal geometry and contribute no internal energy, the interaction energy between EFs in the EFP method is defined as

$$V^{\text{EFP}} = E_{\text{elec}} + E_{\text{pol}} + E_{\text{disp}} + E_{\text{xr}} + E_{\text{ct}}. \quad (5.1)$$

The EFP simulations throughout this thesis are carried out with the LibEFP library. The implementation of the EFP method in LibEFP uses an approximation in which the electrostatics term is parameterized on a smaller basis set to emulate a charge transfer via a stiffer potential. Labeling the electrostatics term of Equation (5.1) as “LBS”, and the approximated electrostatics term including implicit charge transfer as “SBS”:

$$E_{\text{elec}}^{\text{SBS}} \approx E_{\text{elec}}^{\text{LBS}} + E_{\text{ct}}. \quad (5.2)$$

Consequently, the total potential energy, as implemented in the LibEFP code, is effectively written as

$$V^{\text{EFP}} = E_{\text{elec}} + E_{\text{pol}} + E_{\text{disp}} + E_{\text{xr}}, \quad (5.3)$$

including explicit energy terms for: electrostatics, polarization, dispersion, and exchange repulsion. These terms are discussed in detail in the forthcoming sections.

5.3.1 Electrostatics

The electrostatics term, which captures Coulomb interactions between the fragments, is expressed using a set of classic point-multipoles. The distributed multipole moments are derived from the distributed multipole analysis (DMA) of Stone [155, 156]. In the EFP water model, for example, each water fragment has five points with distributed multipoles: two located at bond midpoints and one at each atom center.

The EFP electrostatic potential of a system with N fragments is expressed as

$$V_{\text{elec}} = \sum_k^K v_{\text{elec}}^{(k)}(\mathbf{x}), \quad (5.4)$$

where k is an index that counts multipole points; K is the total number of multipole points on the N fragments; and the contribution of a multipole-expansion point k , at \mathbf{k} , to the Coulomb potential at point \mathbf{x} , expanded up to octapoles, is written as

$$\begin{aligned} v_{\text{elec}}^{(k)}(\mathbf{x}) &= \hat{q}^{(k)} T(r_{\mathbf{kx}}) \\ &\quad - \sum_{\alpha}^{x,y,z} \hat{\mu}_{\alpha}^{(k)} T_{\alpha}(r_{\mathbf{kx}}) \\ &\quad + \frac{1}{3} \sum_{\alpha,\beta}^{x,y,z} \hat{\Theta}_{\alpha\beta}^{(k)} T_{\alpha\beta}(r_{\mathbf{kx}}) \\ &\quad - \frac{1}{15} \sum_{\alpha,\beta,\gamma}^{x,y,z} \hat{\Omega}_{\alpha\beta\gamma}^{(k)} T_{\alpha\beta\gamma}(r_{\mathbf{kx}}) \dots, \end{aligned} \quad (5.5)$$

where Greek letter subindices correspond to Cartesian-axis coordinates, x , y , and z ; $r_{\mathbf{kx}}$ is the distance between the coordinates \mathbf{x} and \mathbf{k} ; $q^{(k)}$, $\mu_{\alpha}^{(k)}$, $\Theta_{\alpha\beta}^{(k)}$, and $\Omega_{\alpha\beta\gamma}^{(k)}$, are the charge, dipole, quadrupole, and octapole moment operators at \mathbf{k} , respectively; and T , T_{α} , $T_{\alpha\beta}$, and $T_{\alpha\beta\gamma}$, are electrostatic tensors of zeroth-, first-, second-, and third-rank, respectively [177].

In general, the multipole moment operator of rank n takes the form [156]

$$\hat{\xi}_{\alpha\beta\dots\nu}^{(n)} = \frac{(-1)^n}{n!} \sum_a e^{(a)} a^{2n+1} \frac{\partial}{\partial a_\nu} \dots \frac{\partial}{\partial a_\beta} \frac{\partial}{\partial a_\alpha} \left(\frac{1}{a} \right). \quad (5.6)$$

where “a” denotes an index running over all charged particles on fragment A, $e^{(a)}$ denotes the charge of such particle, and a is the magnitude of its position vector.

Thus, Equation (5.6) gives the prescription to derive the charge moment operator,

$$\hat{q} = \sum_a e^{(a)}; \quad (5.7)$$

the dipole moment operator,

$$\hat{\mu}_\alpha = \sum_a e^{(a)} a_\alpha; \quad (5.8)$$

the quadrapole operator,

$$\hat{\Theta}_{\alpha\beta} = \sum_a e^{(a)} \left(\frac{3}{2} a_\alpha a_\beta - \frac{1}{2} a^2 \delta_{\alpha\beta} \right); \quad (5.9)$$

and the octapole operator,

$$\hat{\Omega}_{\alpha\beta\gamma} = \sum_a e^{(a)} \left[\frac{5}{2} a_\alpha a_\beta a_\gamma - \frac{1}{2} a^2 (a_\alpha \delta_{\beta\gamma} + a_\beta \delta_{\alpha\gamma} + a_\gamma \delta_{\alpha\beta}) \right]. \quad (5.10)$$

In general, the electrostatic tensor of order n is given by the expression [156]:

$$T_{\alpha\beta\dots\nu}^{(n)} = \frac{1}{4\pi\varepsilon_0 R} \nabla_\alpha \nabla_\beta \dots \nabla_\nu \frac{1}{R}, \quad (5.11)$$

where ε_0 is the vacuum permittivity constant and R is the magnitude of the separation vector between the fragments, as depicted in Figure 5.1.

Equation (5.11) gives the expression for the zeroth-order electrostatic tensor,

$$T = \frac{1}{4\pi\varepsilon_0} \frac{1}{R}; \quad (5.12)$$

the first-order electrostatic tensor,

$$T_\alpha = \frac{1}{4\pi\varepsilon_0 R} \nabla_\alpha \frac{1}{R} = -\frac{1}{4\pi\varepsilon_0} \frac{1}{R^3} R_\alpha; \quad (5.13)$$

the second-order electrostatic tensor,

$$T_{\alpha\beta} = \frac{1}{4\pi\varepsilon_0 R} \nabla_\alpha \nabla_\beta \frac{1}{R} = \frac{1}{4\pi\varepsilon_0} \frac{1}{R^5} (3R_\alpha R_\beta - R^2 \delta_{\alpha\beta}); \quad (5.14)$$

the third-order electrostatic tensor, omitting the explicit relation to the gradients,

$$T_{\alpha\beta\gamma} = -\frac{1}{4\pi\varepsilon_0}\frac{1}{R^7} [15R_\alpha R_\beta R_\gamma - 3R^2(R_\alpha\delta_{\beta\gamma} + R_\beta\delta_{\alpha\gamma} + R_\gamma\delta_{\alpha\beta})]; \quad (5.15)$$

and the fourth-order electrostatic tensor,

$$T_{\alpha\beta\gamma\delta} = \frac{1}{4\pi\varepsilon_0}\frac{1}{R^9} \begin{bmatrix} 105R_\alpha R_\beta R_\gamma R_\delta \\ -15R^2 \left(R_\alpha R_\beta \delta_{\gamma\delta} + R_\alpha R_\gamma \delta_{\beta\delta} + R_\alpha R_\delta \delta_{\beta\gamma} \right. \\ \left. + R_\beta R_\gamma \delta_{\alpha\delta} + R_\beta R_\delta \delta_{\alpha\gamma} + R_\gamma R_\delta \delta_{\alpha\beta} \right) \\ + 3R^4 (\delta_{\alpha\beta}\delta_{\gamma\delta} + \delta_{\alpha\gamma}\delta_{\beta\delta} + \delta_{\alpha\delta}\delta_{\beta\gamma}) \end{bmatrix}; \quad (5.16)$$

where R_α, \dots , and R_δ denote the magnitude of the components of the vector separation vector, and $\delta_{\alpha\beta}, \dots$, and $\delta_{\gamma\delta}$ are Kronecker delta functions³.

According to Stone [156], the electrostatic interaction of two multipole expansion points, at \mathbf{a} and \mathbf{b} , belonging to fragments A and B, respectively, as those illustrated in Figure 5.1, can be expressed in terms of the full electrostatic potential defined on Equation (5.5),

$$\epsilon_{\text{elec}}^{(ab)} = \sum_{n=0}^{\infty} \frac{1}{(2n-1)(2n-3)} \hat{\xi}_{\alpha\beta\dots\nu}^{(n),(b)} v_{\alpha\beta\dots\nu}^{(a)}. \quad (5.17)$$

If the multipole moments on \mathbf{b} , from the previous expression, are expanded and truncated at the level of octapoles, then the electrostatic energy of a pair of multipole expansion points a and b is

$$\epsilon_{\text{elec}}^{(ab)} = \hat{q}^{(b)} v^{(a)} + \hat{\mu}_\alpha^{(b)} v_\alpha^{(a)} + \frac{1}{3} \hat{\Theta}_{\alpha\beta}^{(b)} v_{\alpha\beta}^{(a)} + \frac{1}{15} \hat{\Omega}_{\alpha\beta\gamma}^{(b)} v_{\alpha\beta\gamma}^{(a)}, \quad (5.18)$$

where v_α , $v_{\alpha\beta}$, and $v_{\alpha\beta\gamma}$, are defined as $\partial v / \partial r_\alpha$, $\partial^2 v / \partial r_\alpha \partial r_\beta$, and $\partial^3 v / \partial r_\alpha \partial r_\beta \partial r_\gamma$, respectively.

³the Kronecker delta function is a function of two positive integers: $\delta_{ij} = \begin{cases} 0 & \text{if } i \neq j, \\ 1 & \text{if } i = j. \end{cases}$

Following Slipchenko and Gordon [169], if Equation (5.18) is truncated at the level of octapoles and negligible terms are omitted:

$$\begin{aligned}\epsilon_{\text{elec}}^{(ab)} = & \hat{q}^{(b)} \left[\hat{q}^{(a)} T(r_{ab}) - \hat{\mu}_{\alpha}^{(a)} T_{\alpha}(r_{ab}) + \frac{1}{3} \hat{\Theta}_{\alpha\beta}^{(a)} T_{\alpha\beta}(r_{ab}) - \frac{1}{15} \hat{\Omega}_{\alpha\beta\gamma}^{(a)} T_{\alpha\beta\gamma}(r_{ab}) \right] \\ & + \hat{\mu}_{\alpha}^{(b)} \left[\hat{q}^{(a)} T_{\alpha}(r_{ab}) - \hat{\mu}_{\beta}^{(a)} T_{\alpha\beta}(r_{ab}) + \frac{1}{3} \hat{\Theta}_{\beta\gamma}^{(a)} T_{\alpha\beta\gamma}(r_{ab}) \right] \\ & + \frac{1}{3} \hat{\Theta}_{\alpha\beta}^{(b)} \left[\hat{q}^{(a)} T_{\alpha\beta}(r_{ab}) - \hat{\mu}_{\gamma}^{(a)} T_{\alpha\beta\gamma}(r_{ab}) + \frac{1}{3} \hat{\Theta}_{\gamma\delta}^{(a)} T_{\alpha\beta\gamma\delta}(r_{ab}) \right] \\ & + \frac{1}{15} \hat{\Omega}_{\alpha\beta\gamma}^{(b)} \left[\hat{q}^{(a)} T_{\alpha\beta\gamma}(r_{ab}) \right].\end{aligned}\quad (5.19)$$

Equation (5.19) can be rearranged once more, and ordered in relation to the tensor rank:

$$\begin{aligned}\epsilon_{\text{elec}}^{(ab)} = & T(r_{ab}) \left[\hat{q}^{(b)} \hat{q}^{(a)} \right] \\ & + T_{\alpha}(r_{ab}) \left[\hat{q}^{(a)} \hat{\mu}_{\alpha}^{(b)} - \hat{q}^{(b)} \hat{\mu}_{\alpha}^{(a)} \right] \\ & + T_{\alpha\beta}(r_{ab}) \left[\frac{1}{3} \hat{q}^{(b)} \hat{\Theta}_{\alpha\beta}^{(a)} + \frac{1}{3} \hat{\Theta}_{\alpha\beta}^{(b)} \hat{q}^{(a)} - \hat{\mu}_{\alpha}^{(b)} \hat{\mu}_{\beta}^{(a)} \right] \\ & + T_{\alpha\beta\gamma}(r_{ab}) \left[\frac{1}{15} \hat{\Omega}_{\alpha\beta\gamma}^{(b)} \hat{q}^{(a)} - \frac{1}{15} \hat{q}^{(b)} \hat{\Omega}_{\alpha\beta\gamma}^{(a)} + \frac{1}{3} \hat{\mu}_{\alpha}^{(b)} \hat{\Theta}_{\beta\gamma}^{(a)} - \frac{1}{3} \hat{\Theta}_{\alpha\beta}^{(b)} \hat{\mu}_{\gamma}^{(a)} \right] \\ & + T_{\alpha\beta\gamma\delta}(r_{ab}) \left[\frac{1}{9} \hat{\Theta}_{\alpha\beta}^{(b)} \hat{\Theta}_{\gamma\delta}^{(a)} \right].\end{aligned}\quad (5.20)$$

This expression contains all the contributions to the electrostatic term of EFP:

$$E_{\text{elec}} = \frac{1}{2} \sum_a^K \sum_{b \neq a}^K \epsilon_{\text{elec}}^{(ab)}. \quad (5.21)$$

Those contributions related to higher-order tensors terms, namely octapole-dipole, octapole-quadrupole, octapole-octapole, etc., decay faster with respect to the intermolecular separation ($1/R^9$ or faster), effectively nullifying at intermediate separations. Notably, the quadrupole-quadrupole interaction is still relevant in many non-polar molecules, especially in certain cases involving high electron delocalization. Good examples are the acetylene dimers and trimers, or the benzene dimer [156, 168]. Therefore, as indicated in Equation (5.20) the quadrupole-quadrupole contribution is included in EFP.

Although distributed multipole expansions are effective in representing molecular electron densities and their potentials, the Coulomb point multipole model fails if the fragments become too close to each other. If two fragments are brought too close, their electron densities will overlap. Thus, the nuclei on one fragment will no longer be shielded by its own electron density, and will experience a greater attraction for the electron density associated with the other fragment. The energy difference resulting from the increased attraction is known as charge penetration. In those cases, the electron densities on the fragments cannot be correctly approximated by point multipoles: the electrostatic interactions become excessively repulsive, and must be modulated introducing a screening or damping function [168, 181].

There are several approaches to generating these damping functions. However, there are certain conditions that these functions must satisfy: go to the unity in the long-range regime and fall off toward zero as the intermolecular separation approaches zero; resemble the *ab initio* electrostatic potential of an isolated fragment properly in the region of its van der Waals radius; and give rise to tractable electrostatic integrals. Originally, simple exponential functions were used [166]. These functions enter as a multiplier regulating the magnitude of the multipole moment they act on. Later, *ab initio*-derived damping, based on the overlap of fragments, was designed as an additive energy term [169].

5.3.2 Polarization

The second term on the right-hand side of Equation (5.3) accounts for the polarization energy. When a molecule is placed in an electric field, its electron cloud responds by reshaping and reorienting. If the field is homogeneous and unidirectional, partial opposite charges separate along the direction of the field, as a way to minimize the total energy of the system.

In EFP, the polarization contribution is evaluated as an interaction of induced dipoles of each fragment with the static field due to the Coulomb multipoles and the induced field due to the induced dipoles of the other fragments. For example,

in a fragment of water, anisotropic, distributed-polarizability tensors are placed on the centroids of LMO, where the induced dipoles are to be modeled. Each water fragment has five distributed polarizability points: one at the oxygen, two on the center of each bond, and two at each of the centroids of the lone pairs on oxygen (not depicted) [177].

The contribution of a multipole-expansion point k , at \mathbf{k} , to the polarization potential at point \mathbf{x} , is expressed by Gordon et. al. [177] as:

$$v_{\text{pol}}^{(k)}(\mathbf{x}) = \frac{1}{2} \sum_{\alpha}^{x,y,z} \left(\hat{\mu}_{\alpha,\text{ind}}^{(k)} + \hat{\tilde{\mu}}_{\alpha,\text{ind}}^{(k)} \right) T_{\alpha}(r_{\mathbf{k}\mathbf{x}}), \quad (5.22)$$

with $r_{\mathbf{k}\mathbf{x}}$ being the distance between the coordinate \mathbf{x} and \mathbf{k} ; $\hat{\mu}_{\alpha,\text{ind}}^{(k)}$ and $\hat{\tilde{\mu}}_{\alpha,\text{ind}}^{(k)}$, the induced and conjugate induced dipoles at the polarization point k , respectively; and T_{α} , the first-rank electrostatic tensor.

The polarization energy between fragments is calculated self-consistently using an iterative procedure, therefore partially accounting for many-body effects that are important in aqueous and other polar systems. In an external field, a fragment A becomes polarized and develops induced dipoles located at polarizability points k . These induced dipoles are caused by the total field, comprised of a static external field and the field due to induced dipoles on the other fragments.

Thus, following the derivation by Jensen and Gordon [162], the total polarization energy of an EFP-only system is expressed as the sum of two contributions: the energy due to the interaction of the polarized fragment dipoles with the field, E_{int} ; and the energy required to induce the dipoles in the fragment, E_{sol} ,

$$E_{\text{pol}} = E_{\text{int}} + E_{\text{sol}}. \quad (5.23)$$

Assuming that the induced dipole is a linear function of the applied field,

$$\boldsymbol{\mu}^{(k)} = \tilde{\alpha}^{(k)} \boldsymbol{\mathcal{F}}^{(k)}, \quad (5.24)$$

is the induced dipole vector at polarizable point k , and $\mathcal{F}^{(k)}$ and $\tilde{\alpha}^{(k)}$ are the electric field vector⁴, at k , and the corresponding asymmetric anisotropic polarizability tensor⁵, respectively.

On the one hand, the energy due to the interaction of the dipoles in the polarized fragment with the field can be expressed as:

$$E_{\text{int}} = - \sum_k \boldsymbol{\mu}^{(k)} \cdot \left(\mathcal{F}_{\text{total}}^{(k)} - \frac{1}{2} \mathcal{F}_{\text{ind}}^{(k)} \right), \quad (5.25)$$

where $\mathcal{F}_{\text{total}}^{(k)}$ is the total electric field and $\mathcal{F}_{\text{ind}}^{(k)}$ is the field induced by dipoles on all other fragments, both acting on polarizable point k .

In a system with N fragments, the latter term is given by:

$$\mathcal{F}_{\text{ind}}^{(k)} = \sum_{B \neq A} \sum_{j \in B}^N \mathcal{F}_{j,B}^{(k)}, \quad (5.26)$$

where $\mathcal{F}_{j,B}^{(k)}$ is the field due to the induced dipole at point j , of fragment B , acting on polarizable point k , of fragment A .

The total electric field on an EFP-only system is given by:

$$\mathcal{F}_{\text{total}}^{(k)} = \mathcal{F}_{\text{static}}^{(k)} + \mathcal{F}_{\text{ind}}^{(k)}, \quad (5.27)$$

where $\mathcal{F}_{\text{static}}^{(k)}$ is the field at the polarizable point k due to the static multipoles in the other fragments, and $\mathcal{F}_{\text{ind}}^{(k)}$ is the field from the induced dipoles in the other fragments. Thus, replacing $\boldsymbol{\mu}^{(k)}$ according to Equation (5.24):

$$\begin{aligned} E_{\text{int}} &= - \sum_k \left(\tilde{\alpha}^{(k)} \mathcal{F}_{\text{total}}^{(k)} \right) \cdot \left(\mathcal{F}_{\text{total}}^{(k)} - \frac{1}{2} \mathcal{F}_{\text{ind}}^{(k)} \right) \\ &= - \sum_k \left[\left(\tilde{\alpha}^{(k)} \mathcal{F}_{\text{total}}^{(k)} \right) \cdot \mathcal{F}_{\text{total}}^{(k)} - \frac{1}{2} \left(\tilde{\alpha}^{\mathcal{T}(k)} \mathcal{F}_{\text{ind}}^{(k)} \right) \cdot \mathcal{F}_{\text{total}}^{(k)} \right] \\ &= - \sum_k \left[\boldsymbol{\mu}^{(k)} \cdot \mathcal{F}_{\text{total}}^{(k)} - \frac{1}{2} \boldsymbol{\mu}'^{(k)} \cdot \mathcal{F}_{\text{total}}^{(k)} \right] \\ &= - \sum_k \left(\boldsymbol{\mu}^{(k)} - \frac{1}{2} \boldsymbol{\mu}'^{(k)} \right) \cdot \mathcal{F}_{\text{total}}^{(k)}, \end{aligned} \quad (5.28)$$

⁴ \mathcal{F} will be employed throughout, although the most common notation for the electric field is \mathbf{E} . This label avoids confusion between energies and the electric field components, and also follows the notation in EFP literature.

⁵ $\tilde{\alpha}$ is not to be confused with the coordinate label α .

where the symbol, $\tilde{\alpha}^T$, represents the transposed⁶ polarizability tensor, and:

$$\boldsymbol{\mu}'^{(k)} = \tilde{\alpha}^{T(k)} \mathcal{F}_{\text{ind}}^{(k)}. \quad (5.29)$$

On the other hand, the energy required to induce the dipoles in the fragment has been shown to be [182]

$$E_{\text{sol}} = \frac{1}{2} \sum_k \boldsymbol{\mu}^{(k)} \cdot \mathcal{F}_{\text{total}}^{(k)}; \quad (5.30)$$

hence, the polarization energy is [162]:

$$\begin{aligned} E_{\text{pol}} &= - \sum_k \boldsymbol{\mu}^{(k)} \cdot \left(\mathcal{F}_{\text{total}}^{(k)} - \frac{1}{2} \mathcal{F}_{\text{ind}}^{(k)} \right) + \frac{1}{2} \sum_k \boldsymbol{\mu}^{(k)} \cdot \mathcal{F}_{\text{total}}^{(k)} \\ &= - \frac{1}{2} \sum_k \boldsymbol{\mu}^{(k)} \cdot \left(\mathcal{F}_{\text{total}}^{(k)} - \mathcal{F}_{\text{ind}}^{(k)} \right) \\ &= - \frac{1}{2} \sum_k \left(\tilde{\alpha}^{(k)} \mathcal{F}_{\text{total}}^{(k)} \right) \cdot \left(\mathcal{F}_{\text{total}}^{(k)} - \mathcal{F}_{\text{ind}}^{(k)} \right) \\ &= - \frac{1}{2} \sum_k \left(\boldsymbol{\mu}^{(k)} - \frac{1}{2} \boldsymbol{\mu}'^{(k)} \right) \cdot \mathcal{F}_{\text{total}}^{(k)}. \end{aligned} \quad (5.31)$$

In practice, a similar treatment as the one utilized for the electrostatic term can be applied to obtain its polarization analogue. As stated by Slipchenko and Gordon [169], the total field acting on fragment A is written as in Equation (5.27), summing over all polarizable points k belonging such fragment:

$$\mathcal{F}_{\text{total}}^A = \mathcal{F}_{\text{static}}^A + \mathcal{F}_{\text{ind}}^A. \quad (5.32)$$

The second term on the right-hand side of Equation (5.32), can be expressed in terms of the dipoles induced by the static external field, using tensor notation,

$$\mathcal{F}_{\alpha,\text{ind}}^A = \sum_{B \neq A}^{N-1} \sum_{\beta}^{x,y,z} T_{\alpha\beta}^{AB} \mu_{\beta,\text{ind}}^B, \quad (5.33)$$

where Greek letter subindices correspond to Cartesian-axis coordinates, x , y , and z .

In an external field, a fragment A becomes polarized and develops an induced dipole (in tensor notation),

$$\mu_{\beta,\text{ind}}^A = \tilde{\alpha}_{\alpha\beta}^A \mathcal{F}_{\alpha,\text{total}}^A. \quad (5.34)$$

⁶In the transposed tensor a given element α_{ij} becomes α_{ji} .

The sum on Equation (5.33) and the induced dipole, are then used to solve for the static field term in Equation (5.32), also in tensor notation:

$$\mathcal{F}_{\alpha,\text{static}}^A = (\tilde{\alpha}^{-1})_{\alpha\beta}^A \mu_{\beta,\text{ind}}^A - \sum_{B \neq A}^{N-1} \sum_{\beta}^{x,y,z} T_{\alpha\beta}^{AB} \mu_{\beta,\text{ind}}^B. \quad (5.35)$$

By introducing a new tensor,

$$D_{\alpha\beta}^{AB} = \begin{cases} (\tilde{\alpha}^{-1})_{\alpha\beta}^A & \text{if } A = B, \\ 0 & \text{if } A \neq B \text{ in the same fragment,} \\ -T_{\alpha\beta}^{AB} & \text{if } A \neq B \text{ in different fragments;} \end{cases} \quad (5.36)$$

Equation (5.35) is now simplified into⁷:

$$\mathcal{F}_{\alpha,\text{static}}^A = \sum_{B \neq A}^{N-1} \sum_{\beta}^{x,y,z} D_{\alpha\beta}^{AB} \mu_{\beta,\text{ind}}^B. \quad (5.37)$$

Next, the induced dipoles can be calculated rearranging Equation (5.37) and employing the inverse of $D_{\alpha\beta}^{AB}$,

$$\mu_{\alpha,\text{ind}}^A = \sum_{B \neq A}^{N-1} \sum_{\beta}^{x,y,z} (D^{-1})_{\alpha\beta}^{AB} \mathcal{F}_{\beta,\text{static}}^B. \quad (5.38)$$

Normally, by finding the inverse of $D_{\alpha\beta}^{AB}$, the induced dipoles are determined. This equation can also be solved iteratively, which can be computationally less expensive. However, direct diagonalization is more efficient and robust for small systems, and the code implementing the EFP method uses this technique. Once the induced dipoles are found, the polarization energy of the EFP system is calculated with:

$$E_{\text{pol}} = \frac{1}{2} \sum_A^N \sum_{\alpha}^{x,y,z} \mu_{\alpha,\text{ind}}^A \mathcal{F}_{\alpha,\text{static}}^A. \quad (5.39)$$

As with the electrostatic potential, polarization also requires damping at short distances. Besides the charge penetration error, there is an artifact known as the polarization catastrophe: during the iterative procedure, a fragment is over-polarized by the induction due to dipoles on the near fragments and, in turn, it over-polarizes

⁷The general form of the $D_{\alpha\beta}^{AB}$ tensor is discussed in further detail by Slipchenko and Gordon [169].

them, entering in a vicious cycle in which the polarization energy soon becomes infinite. That may happen due to breaking of the multipole approximation at short separations between the fragments.

5.3.3 Dispersion

In the EFP method, the dispersive energy is calculated as an inverse expansion of the fragment separation, R ,

$$E_{\text{disp}} = \sum C^{(n)} R^{-n}, \quad (5.40)$$

where the coefficients $C^{(n)}$ are derived from the imaginary frequency-dependent dynamic polarizabilities summed over the entire frequency range [167, 183].

Usually, the induced dipole-induced dipole interaction is the most relevant term. It decays as $1/R^6$, depends exclusively upon dipole polarizabilities, and is modulated by $C^{(6)}$. In the current implementation of the EFP method, an estimate of the $n = 8$ term is computed, in addition to the explicitly derived $n = 6$ term.

Customarily, the dispersive energy calculation is based on the interaction between molecular centers. Following the detailed derivation by Smith et. al. [175], the leading term of the expansion, in atomic units, is given by

$$\epsilon_{AB}^{(6)} = - \sum_{\alpha\beta\gamma\delta}^{x,y,z} T_{\alpha\beta}^{AB} T_{\gamma\delta}^{AB} \int_0^\infty d\omega \tilde{\alpha}_{\alpha\gamma}^A(i\omega) \tilde{\alpha}_{\beta\delta}^B(i\omega), \quad (5.41)$$

where A and B are fragments, $\tilde{\alpha}$ is the imaginary frequency-dependent dynamic polarizability tensor with an imaginary frequency denoted as $i\omega$, and Greek letter subindices correspond to Cartesian-axis coordinates, x , y , and z .

The atomic $C^{(6)}$ coefficients in Equation (5.41) are

$$C_{AB}^{(6)} = \int_0^\infty d\omega \tilde{\alpha}_{\alpha\gamma}^A(i\omega) \tilde{\alpha}_{\beta\delta}^B(i\omega), \quad (5.42)$$

and the $1/R^6$ dependence follows from a product of $T_{\alpha\beta}^{AB} T_{\gamma\delta}^{AB}$ tensors.

This strategy allows for an anisotropic dispersion energy expression, which is advantageous in most computational methods. However, there are known issues with

convergence when using the approach of Equation (5.41). Effectively, it requires higher terms in the multipolar expansion. The quadrupole polarizabilities, which are not included in the EFP method, are of particular importance in some cases [154]. Hence, the EFP dispersion energy is expressed in terms of LMO-LMO interactions, rather than atom-atom interactions. This is done by employing the distributed polarizability approximation,

$$\tilde{\alpha}_{\beta\delta}^B(i\omega) \approx \sum_{j \in B}^J \tilde{\alpha}_{\beta\delta}^{(j)}; \quad (5.43)$$

where the expansion points of fragment B are denoted as j . Introducing such approximation in Equation (5.41), the leading term of the dispersion energy becomes:

$$\epsilon_{AB}^{(6)} = - \sum_{k \in A}^K \sum_{j \in B}^J \sum_{\alpha\beta\gamma\delta}^{x,y,z} T_{\alpha\beta}^{(kj)} T_{\gamma\delta}^{(kj)} \int_0^\infty d\omega \tilde{\alpha}_{\alpha\gamma}^{(k)}(i\omega) \tilde{\alpha}_{\beta\delta}^{(j)}(i\omega). \quad (5.44)$$

The off-diagonal terms of the frequency-dependent polarizability tensor provide marginal contributions to the dispersion energy. This is because, in the case of the EFP method, the polarizability tensor is constructed using the principal orientation for a given molecule, thus maximizing the diagonal components [184]. By omitting the off-diagonal terms from the calculation, the total number of terms that must be calculated decreases significantly, without compromising accuracy,

$$\begin{aligned} \epsilon_{AB}^{(6)} &= - \sum_{k \in A}^K \sum_{j \in B}^J \sum_{\alpha\beta\gamma\delta}^{x,y,z} \delta_{\alpha\gamma} \delta_{\beta\delta} T_{\alpha\beta}^{(kj)} T_{\gamma\delta}^{(kj)} \int_0^\infty d\omega \tilde{\alpha}_{\alpha\gamma}^{(k)}(i\omega) \tilde{\alpha}_{\beta\delta}^{(j)}(i\omega) \\ &= - \sum_{k \in A}^K \sum_{j \in B}^J \sum_{\alpha\beta}^{x,y,z} T_{\alpha\beta}^{(kj)} T_{\alpha\beta}^{(kj)} \int_0^\infty d\omega \tilde{\alpha}_{\alpha\alpha}^{(k)}(i\omega) \tilde{\alpha}_{\beta\beta}^{(j)}(i\omega). \end{aligned} \quad (5.45)$$

Then, further simplifications can be achieved by introducing the isotropic dynamic polarizability for LMO j and frequency ω , $\bar{\alpha}^{(j)}(i\omega)$, as 1/3 of the trace of the polarizability tensor at a given imaginary frequency,

$$\bar{\alpha}^{(j)}(i\omega) \approx \frac{1}{3} \text{tr}(\tilde{\alpha}(i\omega)), \quad (5.46)$$

and employing the spherical atom approximation,

$$\tilde{\alpha}_{xx}^{(j)}(i\omega) \approx \tilde{\alpha}_{yy}^{(j)}(i\omega) \approx \tilde{\alpha}_{zz}^{(j)}(i\omega) = \bar{\alpha}^{(j)}(i\omega). \quad (5.47)$$

An advantage of using isotropic polarizabilities is that a vast amount $C^{(6)}$ values reported in the literature are isotropic [167], making the comparison with other methods adequate. When applied to Equation (5.45), these approximations yield:

$$\epsilon_{AB}^{(6)} = - \sum_{k \in A}^K \sum_{j \in B}^J \sum_{\alpha\beta}^{x,y,z} T_{\alpha\beta}^{(kj)} T_{\alpha\beta}^{(kj)} \int_0^\infty d\omega \bar{\alpha}^{(k)}(i\omega) \bar{\alpha}^{(j)}(i\omega). \quad (5.48)$$

The tensors sum on Equation (5.48) contains the dependence upon fragment-fragment separations,

$$\sum_{\alpha\beta}^{x,y,z} T_{\alpha\beta}^{(kj)} T_{\alpha\beta}^{(kj)} = \frac{6}{R_{kj}^6}; \quad (5.49)$$

and the integral corresponds to the $C^{(6)}$ coefficients,

$$C_{kj}^{(6)} = \int_0^\infty d\omega \bar{\alpha}^{(k)}(i\omega) \bar{\alpha}^{(j)}(i\omega). \quad (5.50)$$

In current implementations of the EFP method, the integration of Equation (5.50) is performed on-the-fly between all pairs of dispersion points of all fragments, using a 12-point Gauss-Legendre quadrature [185].

Finally, an empirical correction that accounts for the $n = 8$ term is added as approximately one-third of the $n = 6$ term,

$$\epsilon_{AB} = -\frac{4}{3} \sum_{k \in A}^K \sum_{j \in B}^J \frac{1}{R_{kj}^6} \int_0^\infty d\omega \bar{\alpha}^{(k)}(i\omega) \bar{\alpha}^{(j)}(i\omega), \quad (5.51)$$

which can be summarized as

$$\epsilon_{AB} = -\frac{4}{3} \sum_{k \in A}^K \sum_{j \in B}^J \frac{C_{kj}^{(6)}}{R_{kj}^6}; \quad (5.52)$$

therefore the dispersive energy of the EFP method is

$$E_{\text{disp}} = \frac{1}{2} \sum_{A \neq B} \sum_B \epsilon_{AB}. \quad (5.53)$$

Once more, the expression on Equation (5.52) needs to be corrected for short-range charge penetration effects. Otherwise, at the limit of $R \rightarrow 0$, the dispersive energy would become infinite. This can be remedied by introducing a damping function. Two popular forms of the damping function for dispersion are the method by Tang and Toennies [186] and the overlap approximation by Slipchenko and Gordon [169].

5.3.4 Exchange Repulsion

Exchange repulsion is an effect of the Pauli exclusion principle, thus it is purely quantum-mechanical. Its manifestations within the MO approximation are demonstrated by Jensen and Gordon [162], who considered two approaching one-electron systems, A and B, with the same spin.

According to the Pauli exclusion principle, the total wave function of the dimer system can be written in terms of the wave functions of the fragments. The total wave function must be antisymmetric if two electrons are swapped. Hence, such wave function is expressed as a Slater determinant

$$\Psi_{AB}(\mathbf{r}_1, \mathbf{r}_2) = \frac{1}{\sqrt{2 - 2\mathbf{S}^2}} [\chi_A(\mathbf{r}_1)\chi_B(\mathbf{r}_2) - \chi_A(\mathbf{r}_2)\chi_B(\mathbf{r}_1)] , \quad (5.54)$$

where the numeric subindices denote labels for electron coordinates, the uppercase straight letters are labels for fragments, and

$$\mathbf{S} = \langle \chi_A | \chi_B \rangle , \quad (5.55)$$

known as the overlap integral matrix, is an object that quantifies the superimposition of the wave functions.

The electron density of the dimer system is then described by

$$\begin{aligned} n_{AB}(\mathbf{r}_1) &= 2 \int d^3\mathbf{r}_1 d^3\mathbf{r}_2 |\Psi_{AB}(\mathbf{r}_1, \mathbf{r}_2)|^2 \\ &= \frac{1}{1 - \mathbf{S}^2} [| \chi_A(\mathbf{r}_1) |^2 - 2\mathbf{S}\chi_A(\mathbf{r}_1)\chi_B(\mathbf{r}_1) + | \chi_B(\mathbf{r}_1) |^2] . \end{aligned} \quad (5.56)$$

If the wave function of B is required to be orthogonal to the wave function of A,

$$\langle \chi_A | \chi'_B \rangle = 0 , \quad (5.57)$$

where χ'_B ,

$$\chi'_B = \frac{1}{\sqrt{1 - \mathbf{S}^2}} [\chi_B - \mathbf{S}\chi_A] ; \quad (5.58)$$

then, the total wave function can be simplified, and the electron density becomes:

$$n_{AB}(\mathbf{r}_1) = | \chi_A(\mathbf{r}_1) |^2 + | \chi'_B(\mathbf{r}_1) |^2 . \quad (5.59)$$

This approach connects the effect of the Pauli exclusion on the density to the orbitals. Murrell and collaborators [164,165] designed a method that incorporates Pauli repulsion into intermolecular interaction energies by enforcing orbital orthogonality. The exchange repulsion in the EFP method is based on their work.

The idea of Jensen and Gordon [162] is that the interaction energy between two molecules can be calculated building a total wave function from those of each isolated molecule, similar to the general procedure described above,

$$\Phi = \Psi_A \Psi_B . \quad (5.60)$$

Assuming that each isolated molecule can be correctly described within the framework of closed-shell theory, their corresponding wave functions may be expressed as single Slater determinants,

$$\Psi_A = |\chi_1 \dots \chi_i \dots \chi_{N_A}\rangle \quad \text{and} \quad \Psi_B = |\chi_{1+N_A} \dots \chi_{j+N_A} \dots \chi_{N_A+N_B}\rangle , \quad (5.61)$$

where

$$\chi = \alpha\psi , \quad (5.62)$$

are spin orbitals: the product of a spin function α or β and a spatial orbital ψ . The interaction energy of the dimer is then evaluated relative to the energies of the isolated molecules, E_A and E_B ,

$$\Delta E = \frac{\langle \Psi_A \Psi_B | \hat{\mathcal{A}} \hat{\mathcal{H}} | \Psi_A \Psi_B \rangle}{\langle \Psi_A \Psi_B | \hat{\mathcal{A}} \Psi_A \Psi_B \rangle} - E_A - E_B , \quad (5.63)$$

where the Δ emphasizes the energy change, $\hat{\mathcal{A}}$ is Dirac's antisymmetrizing operator⁸ and $\hat{\mathcal{H}}$ is the total Hamiltonian operator.

If the orbitals of molecules A and B are made orthonormal, the evaluation of Equation (5.63) is straight forward. Nevertheless, if ΔE is to be expressed in terms of the properties of molecules A and B, it is advantageous to preserve the original orbitals.

⁸ \mathcal{A} is a linear operator that makes a wave function of electrons antisymmetric under the exchange of the coordinates of any pair of electrons [187].

The total Hamiltonian operator, $\hat{\mathcal{H}}$, is a sum of the Hamiltonians for molecules A and B, plus the potential energy of interaction between A and B, denoted by \hat{V} :

$$\hat{\mathcal{H}} = \hat{\mathcal{H}}_A + \hat{\mathcal{H}}_B + \hat{V}. \quad (5.64)$$

Introducing this expression for $\hat{\mathcal{H}}$ in Equation (5.63) yields,

$$\Delta E = \frac{\left\langle \Psi_A \Psi_B \left| \hat{\mathcal{A}} \left(\hat{\mathcal{H}}_A + \hat{\mathcal{H}}_B \right) \right| \Psi_A \Psi_B \right\rangle}{\left\langle \Psi_A \Psi_B \left| \hat{\mathcal{A}} \Psi_A \Psi_B \right\rangle\right\rangle} - E_A - E_B + \frac{\left\langle \Psi_A \Psi_B \left| \hat{\mathcal{A}} \hat{V} \right| \Psi_A \Psi_B \right\rangle}{\left\langle \Psi_A \Psi_B \left| \hat{\mathcal{A}} \Psi_A \Psi_B \right\rangle\right\rangle}; \quad (5.65)$$

meaning that the change in total energy can be expressed in terms of the changes in the internal energies of the molecules, plus a term accounting for the energy due to the interaction:

$$\Delta E = \Delta E_A + \Delta E_B + E(V). \quad (5.66)$$

It is usually assumed that Ψ_A and Ψ_B are eigenfunctions of their respective Hamiltonians,

$$\hat{\mathcal{H}}_A \Psi_A = E_A \Psi_A; \quad (5.67)$$

in order to eliminate the first two terms in the previous equation,

$$\Delta E_A = \Delta E_B = 0. \quad (5.68)$$

The energy due to the interaction can be treated using density matrices and employing a similar approach to that of Jeziorski et al. [162, 188]:

$$E(V) = \int d^3 \mathbf{r}_1 \gamma_{\text{int}}^A (1|1) \hat{U}_B(\mathbf{r}_1) + \int d^3 \mathbf{r}_1 \gamma_{\text{int}}^B (1|1) \hat{U}_A(\mathbf{r}_1) + \int \int d^3 \mathbf{r}_1 d^3 \mathbf{r}_2 \left[\frac{\gamma_{\text{int}}^A (1|1) \gamma_{\text{int}}^B (2|2) - \gamma_{\text{int}}^A (1|2) \gamma_{\text{int}}^B (2|1)}{r_{12}} \right] + W_{AB}, \quad (5.69)$$

where W_{AB} is the intermolecular nuclear repulsion, and \hat{U}_A is the potential due to the nuclei in A. The density matrix of Ψ_A is written as

$$\gamma_{\text{int}}^A (1|2) = [\alpha(\mathbf{r}_1)\alpha(\mathbf{r}_2) + \beta(\mathbf{r}_1)\beta(\mathbf{r}_2)] \left[\sum_{i \in A} \sum_{m \in A, B} D_{mi} \psi_i^*(\mathbf{r}_1) \psi_m(\mathbf{r}_2) \right], \quad (5.70)$$

with D_{mi} being an element of the matrix

$$\mathbf{D} = (\mathbf{1} + \mathbf{S})^{-1}. \quad (5.71)$$

The \mathbf{S} matrix is composed of intermolecular overlap integrals between the orbitals of both molecules. The Pauli repulsion arises from terms in Equation (5.69) that contain elements of \mathbf{S} . Those elements are separated from the rest by rewriting the matrix \mathbf{D} as

$$\mathbf{D} = \mathbf{1} - \mathbf{S} (\mathbf{1} + \mathbf{S})^{-1} = \mathbf{1} + \mathbf{P}; \quad (5.72)$$

and the density matrix of Equation (5.70) as

$$\gamma_{\text{int}}^A (1|2) = \gamma_0^A (1|2) + \gamma_{\text{xr}}^A (1|2), \quad (5.73)$$

where the first term on the right-hand side is

$$\gamma_0^A (1|2) = [\alpha(\mathbf{r}_1)\alpha(\mathbf{r}_2) + \beta(\mathbf{r}_1)\beta(\mathbf{r}_2)] \left[\sum_{i \in A} \psi_i^*(\mathbf{r}_1) \psi_i(\mathbf{r}_2) \right]; \quad (5.74)$$

and the second is

$$\gamma_{\text{xr}}^A (1|2) = [\alpha(\mathbf{r}_1)\alpha(\mathbf{r}_2) + \beta(\mathbf{r}_1)\beta(\mathbf{r}_2)] \left[\sum_{i \in A} \sum_{m \in A, B} P_{mi} \psi_i^*(\mathbf{r}_1) \psi_m(\mathbf{r}_2) \right]. \quad (5.75)$$

The advantage of the procedure resulting in Equation (5.73) is that, by substituting $\gamma_{\text{int}}^A (1|2)$ into Equation (5.69), it allows for separation of the interaction energy into Coulomb and exchange terms:

$$E(V) = E_{\text{elec}}(V) + E_{\text{xr}}(V). \quad (5.76)$$

The Coulomb term is straight forward to evaluate as

$$E_{\text{elec}}(V) = \left\langle \Psi_A \Psi_A \left| \hat{V} \right| \Psi_B \Psi_B \right\rangle, \quad (5.77)$$

which depends exclusively upon $\gamma_0^A (1|1)$, $\gamma_0^B (2|2)$, and the intermolecular nuclear repulsion, W_{AB} .

The remaining terms are collected in $E_{\text{xr}}(V)$ and represent the Pauli repulsion energy:

$$\begin{aligned} E_{\text{xr}}(V) = & \int d^3\mathbf{r}_1 \gamma_{\text{xr}}^A(1|1) \left(\hat{U}_B(\mathbf{r}_1) + \int d^3\mathbf{r}_2 \frac{\gamma_0^B(1|1)}{r_{12}} \right) \\ & + \int d^3\mathbf{r}_1 \gamma_{\text{xr}}^B(1|1) \left(\hat{U}_A(\mathbf{r}_1) + \int d^3\mathbf{r}_2 \frac{\gamma_0^A(1|1)}{r_{12}} \right) \\ & + \int \int d^3\mathbf{r}_1 d^3\mathbf{r}_2 \left[\frac{\gamma_{\text{xr}}^A(1|1) \gamma_{\text{xr}}^B(2|2)}{r_{12}} \right] \\ & - \int \int d^3\mathbf{r}_1 d^3\mathbf{r}_2 \left[\frac{\gamma_{\text{int}}^A(1|2) \gamma_{\text{int}}^B(2|1)}{r_{12}} \right]. \end{aligned} \quad (5.78)$$

Further simplifications of Equation (5.78) can be achieved if \mathbf{P} is expanded as a series in \mathbf{S} ,

$$\mathbf{P} = -\mathbf{S} + \mathbf{S}^2 - \mathbf{S}^3 + \dots, \quad (5.79)$$

and truncated after the second term, yielding simplified exchange density matrices:

$$\gamma_{\text{xr}}^A(1|2) = - \begin{bmatrix} \alpha(\mathbf{r}_1)\alpha(\mathbf{r}_2) \\ +\beta(\mathbf{r}_1)\beta(\mathbf{r}_2) \end{bmatrix} \left[\sum_{i \in A} \sum_{j \in B} S_{ij} \begin{pmatrix} \psi_i^*(\mathbf{r}_1) \psi_j(\mathbf{r}_2) \\ - \sum_{k \in A} S_{kj} \psi_i^*(\mathbf{r}_1) \psi_k(\mathbf{r}_2) \end{pmatrix} \right]. \quad (5.80)$$

These density matrices are then plugged into Equation (5.78).

As pointed out by Williams et al. [165] the terms resulting from the interchange of a single pair of electrons between Ψ_A and Ψ_B are collected, by taking the product $\psi_i \psi_j$ to be of order S_{ij} and collecting all terms of order \mathbf{S}^2 . Hence, using standard integral notation, that is:

$$\langle i | \hat{K}_j | i \rangle = \langle ij | ij \rangle; \quad (5.81)$$

$$\langle i | \hat{J}_j | i \rangle = \langle ii | jj \rangle; \quad (5.82)$$

$$\langle ij | kl \rangle = \int \int d^3\mathbf{r}_1 d^3\mathbf{r}_2 \psi_i^*(\mathbf{r}_1) \psi_j(\mathbf{r}_1) \frac{1}{r_{12}} \psi_k^*(\mathbf{r}_2) \psi_l(\mathbf{r}_2); \quad (5.83)$$

$$V_{ij,A} = \int d^3\mathbf{r}_1 \psi_i^*(\mathbf{r}_1) \hat{U}_A(\mathbf{r}_1) \psi_j(\mathbf{r}_1); \quad (5.84)$$

the simplified expression for the exchange energy arising from the interaction becomes:

$$\begin{aligned}
E_{\text{xr}}(V) = & -2 \sum_{i \in A} \sum_{j \in B} \left\langle i \left| \hat{K}_j \right| i \right\rangle \\
& - 2 \sum_{i \in A} \sum_{j \in B} S_{ij} \begin{pmatrix} V_{ij,A} + V_{ij,B} \\ + \sum_{k \in A} \left\langle i \left| 2\hat{J}_k - \hat{K}_k \right| j \right\rangle \\ + \sum_{l \in B} \left\langle i \left| 2\hat{J}_l - \hat{K}_l \right| j \right\rangle \end{pmatrix} \\
& + 2 \sum_{i \in A} \sum_{j \in B} S_{ij} \begin{bmatrix} \sum_{k \in A} S_{kj} \left(V_{ik,B} + \sum_{l \in B} \left\langle i \left| 2\hat{J}_l \right| k \right\rangle \right) \\ + \sum_{l \in B} S_{il} \left(V_{jl,A} + \sum_{k \in A} \left\langle j \left| 2\hat{J}_k \right| l \right\rangle \right) \\ - \sum_{k \in A} \sum_{l \in B} S_{kl} \langle ik | lj \rangle \end{bmatrix}. \tag{5.85}
\end{aligned}$$

The density matrix formalism can also be used to treat the internal energy terms ΔE_A and ΔE_B . Take for example ΔE_A , the first term involving the internal Hamiltonian is calculated as

$$\begin{aligned}
\frac{\langle \Phi | \hat{\mathcal{A}} \hat{\mathcal{H}}_A | \Phi \rangle}{\langle \Phi | \hat{\mathcal{A}} \Phi \rangle} = & \int d^3 \mathbf{r}_1 \hat{h}_A(\mathbf{r}_{1'}) \gamma_{\text{int}}^A (1'|1) \Big|_{1' \rightarrow 1} \\
& + \frac{1}{2} \int \int d^3 \mathbf{r}_1 d^3 \mathbf{r}_2 \frac{\gamma_{\text{int}}^A (1|1) \gamma_{\text{int}}^A (2|2) - \gamma_0^A (1|2) \gamma_{\text{int}}^A (2|1)}{r_{12}}, \tag{5.86}
\end{aligned}$$

where, for shortness, $\Phi = \Psi_A \Psi_B$, as in Equation (5.60); and

$$\hat{h}_A = -\frac{1}{2} \nabla^2 + \hat{U}_A. \tag{5.87}$$

To subtract the second term, E_A , the result of Equation (5.73) is substituted into Equation (5.86). Then, the sum of those terms that depend uniquely upon γ_0^A equals E_A . The remaining terms correspond to the exchange energy contribution due to the internal energy of A. The result is

$$\begin{aligned}
\Delta E_A = & \int d^3 \mathbf{r}_1 \hat{h}_A(\mathbf{r}_{1'}) \gamma_{\text{xr}}^A (1'|1) \Big|_{1' \rightarrow 1} \\
& + \int \int d^3 \mathbf{r}_1 d^3 \mathbf{r}_2 \frac{\gamma_0^A (1|1) \gamma_{\text{xr}}^A (2|2) - \gamma_0^A (1|2) \gamma_{\text{xr}}^A (2|1)}{r_{12}} \\
& + \frac{1}{2} \int \int d^3 \mathbf{r}_1 d^3 \mathbf{r}_2 \frac{\gamma_{\text{xr}}^A (1|1) \gamma_{\text{xr}}^A (2|2) - \gamma_{\text{xr}}^A (1|2) \gamma_{\text{xr}}^A (2|1)}{r_{12}}. \tag{5.88}
\end{aligned}$$

An analogous expression can be derived for E_B , using this methodology.

The simplified exchange-density matrices defined by Equation (5.75) are then substituted into Equation (5.88), and into its analogous for E_B . As before, collecting all terms of order \mathbf{S}^2 yields:

$$\begin{aligned} \Delta E_A + \Delta E_B = & -2 \sum_{i \in A} \sum_{j \in B} S_{ij} \left(\begin{array}{l} 2T_{ij} + V_{ij,A} + V_{ij,B} \\ + \sum_{k \in A} \langle i | 2\hat{J}_k - \hat{K}_k | j \rangle \\ + \sum_{l \in B} \langle i | 2\hat{J}_l - \hat{K}_l | j \rangle \end{array} \right) \\ & + 2 \sum_{i \in A} \sum_{j \in B} S_{ij} \left[\begin{array}{l} \sum_{k \in A} S_{kj} \left(\begin{array}{l} T_{ik} + V_{ik,A} \\ + \sum_{k' \in A} \langle i | 2\hat{J}_{k'} - \hat{K}_{k'} | k \rangle \end{array} \right) \\ + \sum_{l \in B} S_{il} \left(\begin{array}{l} T_{jl} + V_{jl,B} \\ + \sum_{l' \in A} \langle j | 2\hat{J}_{l'} - \hat{K}_{l'} | l \rangle \end{array} \right) \end{array} \right], \end{aligned} \quad (5.89)$$

where T_{ij} is the electronic kinetic energy due to $\psi_i \psi_j$.

A great simplification of this equation is achieved by recognizing that all terms necessary to form Fock matrices corresponding to H_A and H_B are present [189]. Therefore,

$$\begin{aligned} \Delta E_A + \Delta E_B = & -2 \sum_{i \in A} \sum_{j \in B} S_{ij} (F_{ij}^A + F_{ij}^B) \\ & + 2 \sum_{i \in A} \sum_{j \in B} S_{ij} \left(\sum_{k \in A} S_{kj} F_{ik}^A + \sum_{l \in B} S_{il} F_{jl}^B \right). \end{aligned} \quad (5.90)$$

Fortunately, the implementation of this expression in a computational chemistry package is straightforward.

Now, knowing the exchange energy contribution due to the internal energy of the molecules, from Equation (5.90); and due to the interaction, from Equation (5.85),

$$E_{\text{xr}} = \Delta E_A + \Delta E_B + E_{\text{xr}}(V), \quad (5.91)$$

Equation (5.89) can be combined with Equation (5.85) to give the total exchange repulsion energy:

$$\begin{aligned}
E_{\text{xr}} = & -2 \sum_{i \in A} \sum_{j \in B} \left\langle i \left| \hat{K}_j \right| i \right\rangle \\
& + 2 \sum_{i \in A} \sum_{j \in B} 2S_{ij} F_{ij} \\
& + 2 \sum_{i \in A} \sum_{j \in B} S_{ij} \left[\begin{array}{l} \sum_{k \in A} S_{kj} \left(F_{ik}^A + V_{ik,B} + \sum_{l \in B} \langle i | 2J_l | k \rangle \right) \\ + \sum_{l \in B} \left(F_{jl}^B + V_{jl,A} + \sum_{k \in A} \langle j | 2J_k | l \rangle \right) \\ - \sum_{k \in A} \sum_{l \in B} S_{kl} \langle ik | jl \rangle \end{array} \right] . \tag{5.92}
\end{aligned}$$

However, in the EFP method, the LMO approximation is employed, requiring a series of adaptations over the previous expression.

First, if the basis set is large enough to approach the complete basis set limit, the MOs will approach the exact solution to

$$F^A \psi_i = \epsilon_i^A \psi_i , \tag{5.93}$$

where the Fock operator of fragment A provides the exact eigenvalues of the MOs on such fragment. This can significantly simplify the equations derived above since an off-diagonal element of the Fock matrix which connects ψ_i on A with ψ_j on B can be evaluated quite simply as

$$F_{ij}^A = \epsilon_i^A S_{ij} . \tag{5.94}$$

That means that ΔE_A and ΔE_B on Equation (5.89) vanish. Take the example of ΔE_A

$$\Delta E_A = -2 \sum_{i \in A} \sum_{j \in B} S_{ij} F_{ij}^A + 2 \sum_{i \in A} \sum_{j \in B} S_{ij} \sum_{k \in A} S_{kj} F_{ik}^A \approx 0 . \tag{5.95}$$

It has been shown that even for Gaussian double- ζ basis sets, such as 6-31+G(d,p), the error introduced by this approximation is approximately 4% with respect to the CBS extrapolation [163], and thus

$$E_{\text{xr}} \approx E_{\text{xr}}(V) . \tag{5.96}$$

Now, the interaction energy component $E_{\text{xr}}(V)$ can be divided into three terms based on their explicit \mathbf{S} dependence. The first term in the intermolecular exchange energy, depending on \mathbf{S}^0 , can be estimated using the spherical Gaussian overlap (SGO) approximation [190] in which,

$$\langle i \left| \hat{K}_j \right| i \rangle \approx 2 \sqrt{-\frac{2 \ln S_{ij}}{\pi}} \frac{S_{ij}^2}{R_{ij}}, \quad (5.97)$$

where R_{ij} is the distance between the two MO centroids. Hence,

$$E_{\text{xr}}(V; \mathbf{S}^0) \approx -2 \sum_{i \in A} \sum_{j \in B} 2 \sqrt{-\frac{2 \ln S_{ij}}{\pi}} \frac{S_{ij}^2}{R_{ij}}; \quad (5.98)$$

and again, such approximation has been shown to produce negligible errors in the total intermolecular exchange in the water dimer when LMOs are used.

The second term in the intermolecular exchange energy, depending on \mathbf{S}^1 , can be further simplified by rewriting the parenthesis on the second term of Equation (5.85) as

$$\begin{pmatrix} V_{ij,A} + V_{ij,B} \\ + \sum_{k \in A} \langle i \left| 2\hat{J}_k - \hat{K}_k \right| j \rangle \\ + \sum_{l \in B} \langle i \left| 2\hat{J}_l - \hat{K}_l \right| j \rangle \end{pmatrix} \approx (F_{ij}^A + F_{ij}^B - 2T_{ij}), \quad (5.99)$$

which in turn allows for reformulation of the \mathbf{S}^1 -dependent term as

$$E_{\text{xr}}(V; \mathbf{S}^1) \approx -2 \sum_{i \in A} \sum_{j \in B} S_{ij} (F_{ij}^A + F_{ij}^B - 2T_{ij}). \quad (5.100)$$

Substituting Equation (5.94) on the previous expression yields:

$$E_{\text{xr}}(V; \mathbf{S}^1) \approx -2 \sum_{i \in A} \sum_{j \in B} S_{ij} [S_{ij} (\epsilon_i^A + \epsilon_j^B) - 2T_{ij}], \quad (5.101)$$

and given that LMOs satisfy the more general self-consistent field equations

$$F\psi_i = \sum_k \lambda_{ik} \psi_k, \quad (5.102)$$

where

$$\lambda_{ik} = \begin{cases} \epsilon_i & \text{if } i = k, \\ F_{ik} & \text{if } i \neq k; \end{cases} \quad (5.103)$$

then, Equation (5.101) becomes:

$$E_{\text{xr}}(V; \mathbf{S}^1) \approx -2 \sum_{i \in A} \sum_{j \in B} S_{ij} \left(-2T_{ij} + \sum_{k \in A} F_{ik}^A S_{kj} + \sum_{l \in B} F_{jl}^B S_{il} \right). \quad (5.104)$$

Simplification of the third term in the intermolecular exchange energy, depending on \mathbf{S}^2 , requires an approximation to the exchange-density matrices of Equation (5.80):

$$\gamma_{\text{xr}}^A(1|2) \approx - \begin{bmatrix} \alpha(\mathbf{r}_1)\alpha(\mathbf{r}_2) \\ +\beta(\mathbf{r}_1)\beta(\mathbf{r}_2) \end{bmatrix} \left[\sum_{i \in A} \sum_{j \in B} S_{ij} \begin{pmatrix} \psi_i^*(\mathbf{r}_1) \psi_j(\mathbf{r}_2) \\ -S_{ij} \psi_i^*(\mathbf{r}_1) \psi_i(\mathbf{r}_2) \end{pmatrix} \right], \quad (5.105)$$

where all the off-diagonal terms $i \neq k$ have been neglected. Such assumption simplifies the second and (more importantly) the third terms of Equation (5.92) considerably:

$$\begin{aligned} E_{\text{xr}}(V) &\approx -2 \sum_{i \in A} \sum_{j \in B} \langle i | \hat{K}_j | i \rangle \\ &\quad - 2 \sum_{i \in A} \sum_{j \in B} S_{ij} \begin{pmatrix} V_{ij,A} + V_{ij,B} \\ + \langle i | \hat{K}_i | j \rangle + \sum_{k \in A} \langle i | 2\hat{J}_k | j \rangle \\ + \langle i | \hat{K}_j | j \rangle + \sum_{l \in B} \langle i | 2\hat{J}_l | j \rangle \end{pmatrix} \\ &\quad + 2 \sum_{i \in A} \sum_{j \in B} S_{ij}^2 \begin{pmatrix} V_{ii,B} + \sum_{l \in B} \langle i | 2\hat{J}_l | i \rangle \\ + V_{jj,A} + \sum_{k \in A} \langle j | 2\hat{J}_k | j \rangle \\ - \langle i | J_j | i \rangle \end{pmatrix}. \end{aligned} \quad (5.106)$$

Since the integrals on the third term of the previous expression are multiplied by the square of the MO overlap, a simple model of these integrals may be sufficient to represent Equation (5.106). Noting that all integrals in the previous expression can be modeled with classical electrostatics at long separations, the parenthesis on the third term can be approximated by

$$\begin{pmatrix} V_{ii,B} + \sum_{l \in B} \langle i | 2\hat{J}_l | i \rangle \\ + V_{jj,A} + \sum_{k \in A} \langle j | 2\hat{J}_k | j \rangle \\ - \langle i | J_j | i \rangle \end{pmatrix} \approx \begin{pmatrix} - \sum_{J \in B} \frac{Z_J}{R_{iJ}} + 2 \sum_{l \in B} \frac{1}{R_{il}} \\ - \sum_{I \in A} \frac{Z_I}{R_{Ij}} + 2 \sum_{k \in A} \frac{1}{R_{kj}} \\ - \frac{1}{R_{ij}} \end{pmatrix}, \quad (5.107)$$

yielding the expression for the \mathbf{S}^2 -dependent portion of the exchange energy (where Z denotes the atomic number, equivalent to the nuclear charge):

$$E_{\text{xr}}(V; \mathbf{S}^2) \approx 2 \sum_{i \in A} \sum_{j \in B} S_{ij}^2 \begin{pmatrix} -\sum_{J \in B} \frac{Z_J}{R_{iJ}} + 2 \sum_{l \in B} \frac{1}{R_{il}} \\ -\sum_{I \in A} \frac{Z_I}{R_{Ij}} + 2 \sum_{k \in A} \frac{1}{R_{kj}} \\ -\frac{1}{R_{ij}} \end{pmatrix}. \quad (5.108)$$

Finally, the three components are added up:

$$E_{\text{xr}} \approx E_{\text{xr}}(V; \mathbf{S}^0) + E_{\text{xr}}(V; \mathbf{S}^1) + E_{\text{xr}}(V; \mathbf{S}^2); \quad (5.109)$$

therefore, the EFP XR energy expression reads:

$$\begin{aligned} E_{\text{xr}} = & -2 \sum_{i \in A} \sum_{j \in B} 2 \sqrt{-\frac{2 \ln S_{ij}}{\pi}} \frac{S_{ij}^2}{R_{ij}} \\ & - 2 \sum_{i \in A} \sum_{j \in B} S_{ij} \left(+ \sum_{k \in A} F_{ik}^A S_{kj} + \sum_{l \in B} F_{jl}^B S_{il} - 2T_{ij} \right) \\ & + 2 \sum_{i \in A} \sum_{j \in B} S_{ij}^2 \begin{bmatrix} -\left(\sum_{J \in B} \frac{Z_J}{R_{iJ}}\right) + 2\left(\sum_{l \in B} \frac{1}{R_{il}}\right) \\ -\left(\sum_{I \in A} \frac{Z_I}{R_{Ij}}\right) + 2\left(\sum_{k \in A} \frac{1}{R_{kj}}\right) - \frac{1}{R_{ij}} \end{bmatrix}; \end{aligned} \quad (5.110)$$

where i , j , k , and l are LMOs; I and J are nuclei; S and T are the intermolecular-overlap and kinetic-energy integrals, respectively; and F is the intramolecular Fock matrix.

The previous expression can be rearranged to explicitly show the pairwise XR energy contribution of each pair of LMOs:

$$E_{\text{xr}} = \sum_{i \in A} \sum_{j \in B} \left\{ \begin{array}{l} -4 \sqrt{-\frac{2 \ln S_{ij}}{\pi}} \frac{S_{ij}^2}{R_{ij}} \\ -2S_{ij} \left(+ \sum_{k \in A} F_{ik}^A S_{kj} + \sum_{l \in B} F_{jl}^B S_{il} - 2T_{ij} \right) \\ + 2S_{ij}^2 \begin{bmatrix} -\left(\sum_{J \in B} \frac{Z_J}{R_{iJ}}\right) + 2\left(\sum_{l \in B} \frac{1}{R_{il}}\right) \\ -\left(\sum_{I \in A} \frac{Z_I}{R_{Ij}}\right) + 2\left(\sum_{k \in A} \frac{1}{R_{kj}}\right) - \frac{1}{R_{ij}} \end{bmatrix} \end{array} \right\}. \quad (5.111)$$

In practice, the overlap and kinetic-energy integrals are calculated on-the-fly between each pair of LMOs on different fragments A and B, and the intramolecular-Fock-matrix elements are precalculated during the parametrization process.

In summary, the XR energy in EFP is derived from the exact HF expression for the Pauli repulsion of two closed-shell molecules. Truncating the sequence at the quadratic term in the intermolecular overlap, and applying the infinite basis set and spherical Gaussian overlap approximations [190], leads to the expression for the XR energy of Equation (5.110) [162, 163].

5.4 Preparation of EFP Fragment Parameters

One of the most important advantages of the newest version of the EFP method is that fragment parameters can be generated for any type of molecule on which a HF calculation is attainable. Such parameterization process has been standardized for any general fragment in the GAMESS package [191] under the `RUNTYP` keyword: `MAKEFP`.

This procedure is required for each unique type of fragment present in a system. For instance, if a system contains only one type of fragment, the parameters from *ab initio* gas phase calculations need to be computed only once, and can be stored for future jobs that involve the same type of fragment.

5.4.1 Protocol of Parametrization Implemented in `MAKEFP`

Briefly, a `MAKEFP` run produces a set of parameters for a type of fragment. Electrostatics parameters contain data for a set of point multipoles obtained from an *ab initio* electronic density of the isolated fragment using the DMA of Stone. This is done expressing the molecular wave function, often computed with HF, in a Gaussian basis set. Then, spherical multipole expansions are calculated at the centers of the Gaussian basis function products. As explained in Section 5.3.1, these multipoles are translated to the EFP expansion points, atomic centers and bond midpoints, and truncated after the 4th term. The screening parameters for damping functions are

computed using a fitting procedure, once for every type of fragment. The procedure optimizes the screening parameters so that the sum of the differences between the *ab initio* Coulomb potential and the screened EFP electrostatics potential is minimized.

The polarization parameters involve the LMO centroids and polarizability tensors. The LMOs are obtained with the Boys localization procedure based on the *ab initio* electronic density. Polarizabilities are obtained from a coupled-HF calculation as the derivatives of the dipole moment with respect to electric field.

The dispersion parameters for a given fragment include the coordinates of the LMO centroids and, for each LMO, the sets of traces of the dynamic polarizability tensors obtained at 12 frequencies corresponding to the Gauss-Legendre quadrature intervals. Dynamic polarizabilities can be computed using TD-HF.

The XR parameters comprise the elements of the Fock matrix and the LMO orbital coefficients, LMO basis set, and the LMO centroids for each type of fragment. These parameters are extracted from a HF calculation followed by the orbital localization procedure, ordinarily performed with the Boys method.

5.4.2 MAKEFP Control Options

The **MAKEFP** keyword contains a series of options that control the generation of the EFP parameters from the wave function of a single monomer. A sample input of an **MAKEFP** run is provided in Appendix H. Generation of parameters can be achieved using restricted and restricted-open shell HF, although the latter lacks implementation of some options.

The parametrized potential of a fragment consists of: coordinates of atoms; coordinates of the multipolar expansion points, typically located on atoms and bond midpoints; distributed multipole moments, up to octopoles; electrostatic screening parameters; coordinates of LMO centroids; static and dynamic polarizability tensors at LMO centroids; the wave function and Fock matrix elements in the LMO basis; and the atomic labels of the species contained in the fragment.

According to GAMESS documentation, multipole moments for electrostatics are always generated, and by default all additional terms are generated too, unless the options NOPOL, NODISP, NOEXREP, or NOCHTR are turned on in the \$EFRAG input group, to ignore these terms.

A string of up to 8 letters identifies the fragment and is controlled by the option FRAG. For instance, WATER, BENZENE, or CH3OH are valid labels. By default unspecified labels are filled with the string FRAGNAME, which may be hand edited after the MAKEFP run.

The parameters employed by damping functions are controlled by the SCREEN options: a flag to generate screening information for the multipole electrostatics. If the parameterization is carried out with restricted HF, this option is set on by default. However, it has not been implemented for restricted-open shell HF parameterizations. In addition, there are three types of screening functions. SCREEN1 indicates the use of a Gaussian screening of the form A/e^{Br^2} for the distributed multipoles, which account for charge-charge penetration effects. SCREEN2 activates exponential screening of the form A/e^{Br} , which is the most common EFP-EFP screening. SCREEN3 signals the use of screening terms of the form A/e^{Br} for the distributed multipoles, which account for high-order penetration effects. In this case, higher terms include charge-charge, as for SCREEN1 or SCREEN2, but also charge-dipole, charge-quadrupole, and dipole-dipole and dipole-quadrupole terms.

The generation of dipole polarizabilities is managed by the POL option, which by default is set on. An alternative methodology that allows for faster generation of polarizabilities in large molecules can be utilized through the related option POLNUM belonging to the \$LOCAL group, which enforces numerical rather than analytical calculation of the polarizabilities.

The generation of dispersion, exchange repulsion, and charge transfer parameters are governed by the DISP, EXREP, and CHTR, respectively. These options are also set true by default. It should be noted, though, that the generation of dispersion parameters has not been implemented for restricted-open shell HF parameterizations.

As the implementation of EFP in GAMESS explicitly accounts for CT effects, there is another option `CTVVO` that manages what type of charge transfer data is generated. If set `.FALSE.` means all canonical virtual orbitals are used. If set `.TRUE.`, as by default, valence virtual orbitals (VVO) will be created, by forcing `VVOS` in `$SCF` group to be on. The VVOs are many fewer in number, so the charge transfer calculation is greatly accelerated.

5.4.3 Library of Precomputed Fragments

There are a few known tricks to improve the quality of the parameters derived from `MAKEFP` calculations. For example, better results are achieved employing geometries of small fragments optimized using MP2/cc-pVTZ. Also, EFP calculations run more efficiently when the explicit charge transfer term is omitted, and implicitly treated by parameterizing the electrostatics and screenings with a minimal basis set. Therefore, electrostatic multipoles and damping coefficients are usually obtained employing the HF/6-31+G(d), whereas all other parameters are computed with HF/6-311++G(3df,2p) when omitting the charge transfer term. Additionally, in QM/EFP calculations, polarization damping parameters can be controlled to improve stability with a minor impact in accuracy; and simplified water models, with a smaller number of multipole point, may be used for improved computational efficiency.

However, the common user is usually unaware of these details. Therefore, to simplify EFP calculations and make the method more accessible, a library of standard fragments with precomputed potentials has been developed. The idea is to avoid the need of performing `MAKEFP` calculations for simple fragments. This ever-growing library contains potentials for common solvents, ions, DNA bases, amino-acid residues, etc., and it is maintained at:

<https://github.com/ilyak/libefp/tree/master/fraglib/databases>

5.5 Range of Applicability of the EFP Method in Classical Simulations

Once the parameters for all types of fragments in a chemical system are made available, the next step is to perform the actual EFP run. There are several implementations of the method. The original implementation is contained in the GAMESS package. Since 2013, Kaliman and Slipchenko [192] have implemented the EFP method in a stand-alone parallelized library called LibEFP. This library comes together with a molecular simulation package called EFPMD, that is capable of performing dynamic simulations. Additionally, LibEFP offers the flexibility to be interfaced with most computational chemistry packages. Current versions of Q-Chem, Psi4, and NWChem contain the LibEFP library embedded.

LibEFP features single point energy and analytical gradient calculation; geometry optimizations with the Limited-memory Broyden-Fletcher-Goldfarb-Shanno (L-BFGS) optimizer; MD in the microcanonical (NVE), canonical (NVT), and isobaric-isothermal (NPT) ensembles; semi-numerical Hessian and normal mode analysis; and simulation of periodic systems, among other functionalities.

6. THE MELTING TEMPERATURE OF WATER WITH THE EFFECTIVE FRAGMENT POTENTIAL

6.1 Introduction

In this chapter, the thermodynamic equilibrium between water and ice is explored using MD with the EFP method (EFP-MD). Important characteristics of the EFP water model are discussed in connection with the time evolution of the energy and average properties, such as pair-correlation functions and densities. The melting point of the EFP ice is calculated analyzing the evolution of the total energy along simulations with constant temperature and pressure in the NPT ensemble at different temperatures.

6.1.1 Motivation

Molecular simulations based upon theoretical models are essential in explaining the properties of water with microscopic detail [193]. A great number of *in silico* studies simulate liquid water under standard ambient conditions, investigating the properties of both water as a homogeneous liquid and as a solvent [194]. Water is the molecule for which the greatest number of potential models have been proposed [195]. Yet capturing its complexity at the molecular scale is a challenge, a task that relies on both classical and quantum descriptions of intermolecular interactions.

In life and physical sciences, water plays a central role in the stabilization of biomolecules and acid-base chemical reactions [14]. In addition, insight on the basic mechanisms of ice formation are crucial in the understanding of environmental problems, as well as atmospheric phenomena [196]. Numerous relevant physicochemical experiments are carried out in water, at standard ambient conditions of temperature and pressure.

However, many classical water models are not adequate for the study of low-temperature systems because they overlook non-pairwise-additive effects; and quantum methods are limited to molecular systems of small dimensions. The correct description of the phase diagram of water is an important test for any model [197]. It is challenging, whether the method is based upon electronic structure or classical mechanics [3]. Even small errors in capturing the phase diagram of water with a particular model can result in an incorrect phase sampling when performing ambient temperature simulations [198]. Theoretical methods that can accurately account for the diverse types of intermolecular interactions existent in water are required.

6.1.2 Background

From the point of view of classical simulations, modeling the ice-liquid interface is particularly challenging [199]. This test gauges the quality of the force field. Ideally, water models must adequately capture the intermolecular interactions in all three relevant phases: ice, liquid, and vapor. For certain applications, it is essential to elucidate the phase behavior of water at tropospheric temperatures ranging from 188 K to 330 K [200]. If ions are present in the solvent, simulations become much more challenging, as in addition to the forces between water molecules they require a correct description of the water-solute interactions.

In the most frequently used models, water is represented as a rigid molecule with a fixed geometry, partial charges on the atoms (or additional sites), and a Lennard-Jones site on oxygen to treat the intermolecular van der Waals attraction and repulsion [201]. The most popular force fields of this kind are SPC [202], SPC/E [203], TIP3P, and TIP4P [204]. However, these simple models tend to be inaccurate in estimating the melting point of ice at standard pressure with temperatures of 190.5 K [205], 215 K [206], 146 K [205], and 230 K [206], respectively.

The above models often fail to reproduce important regions of the phase diagram. Consequently, large efforts have been devoted to the development of models capable of correctly describing the properties of water over a large range of phase variables.

Within the framework of the simple rigid point charge models, several new potentials, including TIP5P [207], TIP4P-Ew [208], TIP4P/2005 [209], TIP4P/Ice [210], and NvdE or NE6 [211], have recently been designed and tested over a broad range of temperatures, pressures, and phases. Being parametrized specifically to improve thermodynamical accuracy, these simple models can achieve melting points that are remarkably close to the experimental, 273.15 K [194]. In their respective order, their melting temperatures have been determined at: 272.5 K [212], 243.5 K , 250 K , 270 K [205], and 289 K [213]. Still, it is clear that there are limits to what can be achieved using rigid, non-polarizable models [194].

A prominent limitation of the models with constant point charges is the inability to redistribute the charge as a reaction to variations in local electrostatic fields [214]. A series of polarizable water models have emerged trying to correct this shortcoming. They mainly differ in the way the polarizability of a molecule is modeled, the number of sites, and other aspects (i.e. structural flexibility) [194]. The most recent and frequently used models are the fluctuating charge models such as TIP4P-FQ50 [215] or its TIP5P-based variants [216,217]; the charge-on-spring or Drude oscillator models [218,219]; the point dipole models, such as POL3 [220] and the Dang-Chang model [221]; and the mobile charge densities in harmonic oscillators (MCDHO) model [222]. However, as a trade off of the thermodynamical correctness gained by the inclusion of polarizability, usually these models tend to deviate in determining the melting point. For instance, the TIP4P-FQ50 water model melts at 303 K [223] and POL3 at 180 K [194].

With recent advances in force field method developments, now classical force fields can be parameterized with *ab initio* calculations as an alternative to fitting the parameters to empirical data [3]. Examples of popular force fields generated by fitting parameters to quantum mechanical calculations include iAMOEBA [224], TTM3-F [225], WHBB [226,227], and MB-Pol [228–230]. The iAMOEBA and TTM3-F potentials predicted melting temperatures of 261 K [224] and 248 K [194], respec-

tively, demonstrating that this type of approach offers an acceptable compromise between theoretical formality and practical accuracy.

In addition there are polarizable methods in which the parameters are derived directly from *ab initio* calculations, requiring no empirical fitting. The EFP method belongs to this category. It is special in the sense that it is a fully *ab initio*-derived polarizable force field by design [149].

While significant progress in DFT-based MD has been made in the recent years, the computationally affordable functionals, such as PBE and BLYP, yield a melting temperature that is excessively high, usually above 400 K [231,232]. Applying dispersion corrections significantly improve the description of intermolecular interactions, reducing the melting temperature to 350 K in the case of BLYP-D [233]. Although promising, this is still a computationally expensive approach with limited applicability. Thus, polarizable force fields currently represent an important tool with a large potential to improve the description and understanding of molecular systems.

6.2 Theory

The purpose of the study presented in this chapter is to explore the water-ice thermodynamic equilibrium using EFP-MD. In particular, it is aimed to determining the melting temperature of the EFP water model.

6.2.1 The Solid-liquid Equilibrium in Water

Above the melting point, a molecule in the liquid phase has a lower chemical potential than a molecule in the solid phase. When ice melts, water molecules convert from solid to liquid, where their chemical potential is lower, so ice shrinks. Below the melting point, molecules in the ice phase have a lower chemical potential, so ice grows. At the exact temperature of the melting point, the chemical potentials in water and ice are the same; therefore ice neither grows nor shrinks, and the system is in equilibrium.

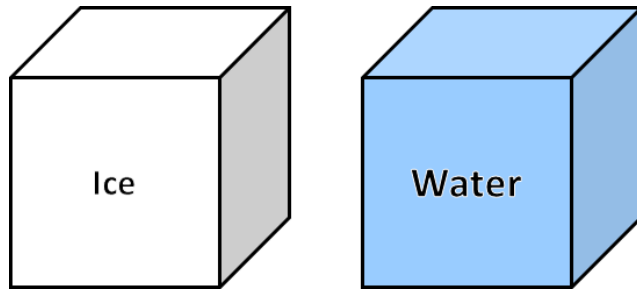
Studying such phenomena *in silico* is extremely challenging. Determining the chemical potential for a liquid is a straight forward task in simulations. However, one of the main difficulty lies in the determination of the chemical potential of the solid phase, which is extremely susceptible to the conformation the molecules adopt. Besides, due to the extremely complex many-body behavior of water and to the stochastic nature of crystal nucleation and growth, MD simulations of bulk water below the melting point generally produce super-cooled liquid, and not ice. To study the process of water freezing, or melting, alternative methodologies of simulation must be applied.

6.2.2 The Direct Coexistence Method

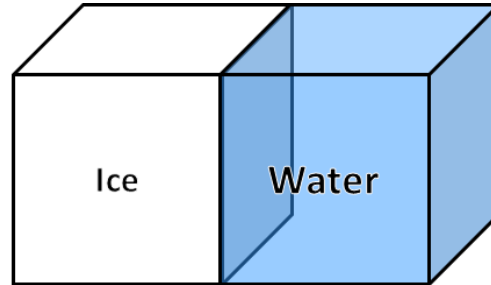
The direct coexistence method is one of the schemes to determine the melting point of a water model, and it was developed mainly from the work of Hoover and Ree [234]. In the direct coexistence approach, the simulation model is built putting solid and liquid in direct contact, with the intention of facilitating the phase-transition process. There are several variations of the method, but the one used in this particular study is illustrated in Figure 6.1.

It starts building a periodic-boundary box containing ice. The ice structure is aligned with the face corresponding to the secondary prismatic $1\bar{2}10$ plane of ice I_h pointing toward the $+z$ direction. The $1\bar{2}10$ plane of ice I_h is its fastest growing face. The box shape must have a vanishing total dipole moment, to avoid an antenna-like effect in which the system is polarized by construction.

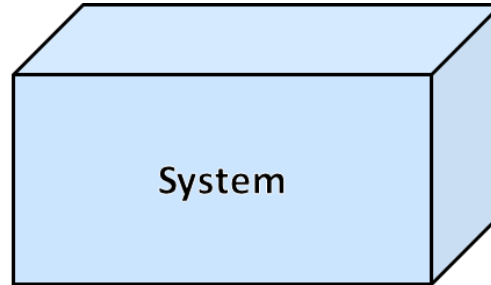
Once the ice box has been created, another box with the same dimensions is filled out with an equivalent amount of liquid water molecules. If the box is large enough, usually this is simply accomplished by generating a random initial conformation. In smaller boxes, the liquid must be firstly equilibrated in the microcanonical ensemble using short time steps, for a short time, and then re-equilibrated normally in the canonical ensemble at the desired simulation temperature. Periodic-boundary conditions (PBC) in every direction should be employed. In very small boxes, it might be



(a) Ice and liquid water PBC-boxes.



(b) Joined PBC-box with ice and liquid water.



(c) Equilibrated sample of water on a PBC-box.

Figure 6.1. Schematic representation of the direct coexistence method.

impossible to generate a box of liquid with the same exact dimensions of the ice box. In that case, the molecules must be accommodated by keeping the xy -face dimensions fixed and slightly varying the z -dimension of the box. Again, the total dipole moment of the system must be as close to null as possible. This procedure results in a sample of liquid water containing the same number of molecules as the ice box.

The next step is to join the boxes together by putting their xy faces in contact, as depicted in Figure 6.1(b). Joining the boxes implies that while the x - and y -

dimensions remain unmodified, the z -dimension of the joint box equals the sum of the z -dimension of the ice box plus the z -dimension of the water box. It also implies that the periodic boundaries are redefined in relation to the dimensions of the joint box. As some molecules of the liquid may be too close to the ice, the liquid must go through a three-step re-equilibration keeping the geometry of the ice fixed. The first two steps are equal to those described in the previous paragraph: an NVE equilibration to avoid system instabilities due to close contacts between molecules, especially between the ice block and the liquid molecules; and then a standard NVT equilibration under the desired temperature conditions. The third stage involves an NPT equilibration in which the pressure is set to standard conditions and the barostat is allowed to variate only the z -dimension of the joint box, while the x - and y -dimensions remain constant. Once this procedure is completed, the system is ready for the production run.

At this point, the ice molecules are set free to move and the system is allowed to evolve in time for a production run under the NPT ensemble with PBC. Once the production run is concluded, the total energy of the system is analyzed along the trajectory. Based on the behavior of the total energy, important information about the equilibrium can be extracted.

On the one hand, when performing MD simulations with the NPT ensemble at a sufficiently high temperature, if the total energy increases persistently with time, it implies that the thermostat is providing energy to the system. In other words, heat is being transferred from the universe to the system. Therefore, it can be assumed that the ice is melting. Usually, the last few layers of ice melt faster, and once the ice block is depleted, the system should reach an equilibrium again within a short lapse. After this moment, if the system is stable under the NPT ensemble, the total energy should reach a plateau, indicating that the ice block has completely melted, meaning that this simulation is performed above the melting point.

On the other hand, if the temperature is low enough, the total energy of an NPT system should generally decrease with time, implying that the thermostat is absorbing energy from the system. Thus, it can be assumed that the ice block is growing and

liquid water is freezing. Again, if all the liquid is frozen, a plateau would show up on a plot of total energy against time, indicating that the system has reached the equilibrium. In this case, this means that the simulation ran below the melting point of water.

In both cases, the rate at which the total energy changes along the trajectory is an indicative of how close the temperature of the simulation is to the melting point of the water model employed. If the energy increases or decreases rapidly during the initial part of the trajectory, the system is far from the melting point. If the energy changes are small enough to be masked by the thermal fluctuations of the system at equilibrium, the simulation temperature is closer to the melting point. This is because the difference between the theoretical melting point and the simulation temperature limits the heat exchange rate between the system and the thermostat. Therefore, the accuracy of the melting temperature of a water model determined through direct coexistence depends mainly on the length of the production run.

The advantage of the direct coexistence method is that it is straightforward to determine if the system is freezing or melting in short simulations. This is achieved simply by analyzing the average slope of a total NPT energy along the trajectory [234]. A rough estimate of the range of temperatures at which the melting point is located is easy to obtain. Considering that in MD simulations complete melting is easier to achieve than complete freezing, it is advisable to start the determination of the melting point with simulations at high temperature, reducing it until the point where the total energy starts decreasing in time [212].

6.3 Computational Details

With the intention of determining the melting point of the EFP water model under standard pressure conditions, MD simulations are performed. All the results presented in this chapter are gathered using the direct coexistence method. The procedure is carried out as described above with minor modifications, mostly due to

software and hardware limitations. Those differences are explained in detail in this section.

Executing MD simulations with polarizable force fields is computationally demanding [193]. The EFP method is no exception. Simulation times in top-benchmark machines for systems of hundreds of atoms can take tenths of thousands of times longer with respect to simple classical force fields. That is a limiting factor when choosing a methodology to determine the melting point of EFP water, even when using the direct coexistence method. Hence, when preparing the simulation, the first obvious consideration is the system size. Second, the length of the time steps and of the whole trajectory. Consequently, an alternative methodology, summarized in Figure 6.2, is designed and presented in the following paragraphs.

In the first step, a cuboid box containing 128 water molecules is prepared by orienting the structure of ice I_h with the $\bar{1}\bar{2}10$ face towards $+z$. This is done extracting a 128-molecule ice cube out of a 432-molecule crystal structure in Protein Data Bank (PDB) format. The dimensions of the resulting box are $14.760 \text{ \AA} \times 15.656 \text{ \AA} \times 18.072$

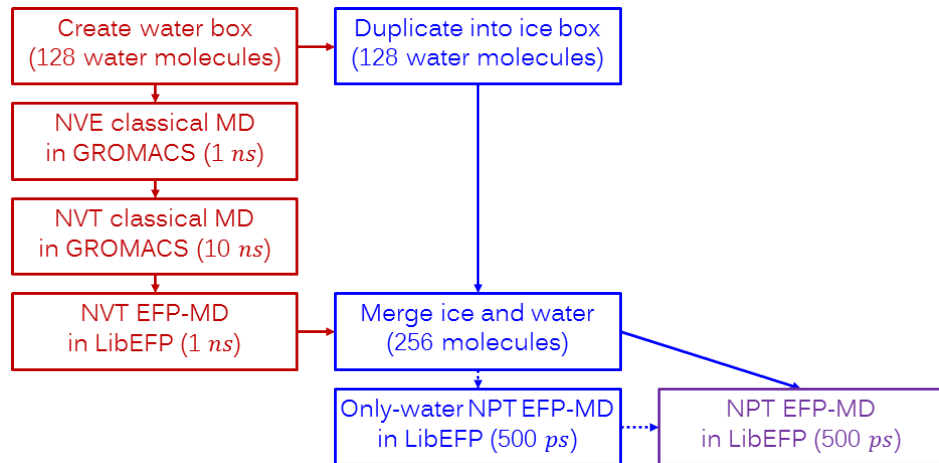


Figure 6.2. Schematic representation of the methodology of this study. Colors correspond to simulation steps involving the liquid (red), the ice (blue), and both (purple).

\AA , in x , y , and z , respectively. This box is then cloned into a separate PDB file to create the ice box, which is stored for the forthcoming stages of the process.

The process continues by converting the resulting box, extracted out of an ice structure, into a liquid sample. The general idea of this process is similar to the description provided in Section 6.2.2. Nevertheless, due to the cost of EFP-MD simulations, some adaptations are required to make this procedure more efficient.

Instead of using EFP, the more efficient TIP4P/Ice water model is used. Thus, the classical MD package GROMACS 5.0 [235] is employed to equilibrate the 128-water box in the NVE ensemble. In this preparatory run, periodic boundaries are enforced: Coulomb potentials are range-separated at 7.2 \AA , employing the Particle Mesh Ewald method [236] for the long-range regime; and van der Waals interactions are truncated at 7.2 \AA , with switching functions acting at 6.7 \AA . In addition, the average-kinetic-energy velocity-Verlet integrator [237] is set to operate at short steps of 0.1 ns , for a total time of 1 ns . Remaining options are set by default. The purpose of this equilibration stage is to randomize the orientation and position of the water molecules and, at the same time, produce a more stable conformation than the highly ordered I_h ice to proceed with the next steps. Once concluded, the resulting conformation is the starting point for several trajectories: The following steps must be repeated for each temperature of simulation.

The next step consist of a longer NVT equilibration stage, also run with the TIP4P/Ice water model in GROMACS 5.0. Again, periodic boundaries are employed with the same treatment for electrostatics and van der Waals interactions. This time, the integrator runs for 10 ns , at steps of 1 fs . In this case, the Berendsen thermostat [238] holds the reference temperature for the complete system, with a coupling constant of 0.1 ps . Initial velocities are read from the final frame of the previous NVE equilibration. Results at six different reference temperatures are presented in this chapter: 330 K , 360 K , 365 K , 375 K , 390 K , and 405 K . This step and the following are performed once at each temperature. The idea of this NVT run is to serve as an auxiliary equilibration to subsequent a NVT equilibration with the EFP

method: a well NVT-equilibrated system may help shorten the NVT equilibration with the EFP model [192], which is highly demanding.

The remaining stages of the process are carried out using the EFP method. The water fragment used in this chapter is retrieved from the EFP library of potentials. In particular, this water potential employs a geometry determined at the MP2/cc-pVTZ level of theory. The electrostatic parameters are derived with the 6-31+G* basis set, whereas the 6-311++G(3df,2p) basis set is employed for polarization, dispersion, and exchange repulsion. Charge transfer is not explicitly considered in this model, and its rather implicitly modeled with the minimal basis set-derived electrostatics parameters. DFT, with the PBE functional, is used in the parameterization of polarization; and as customarily, HF is employed for electrostatics, dispersion, and exchange repulsion parameters.

After reformatting the output of the last TIP4P/Ice run to the EFP model, the next step is to carry out a NVT equilibration with the EFP water model. The EF-PMD molecular simulation package is employed for all the subsequent simulations. EFPMD is provided with LibEFP [192], a stand-alone library with a full implementation of the EFP method. PBC with a box of equivalent dimensions to those of the previous step, are used in the simulations with EFPMD. Similarly, the cutoff distance for fragment-fragment interactions is set to 7.2 Å. The overlap scheme [169] is employed to damp electrostatics and dispersion interactions, whereas the Tang and Toennies approach [186] is used for polarization. In EFPMD, rigid body MD with the scheme by Dullweber et al. [239] is used to integrate the rotational motion of the fragments; while the velocity Verlet algorithm is employed to integrate translational motion of fragments. In this case, the integrator runs for 1 ns, at steps of 2 fs. The Nosé-Hoover thermostat [240] controls the temperature at the same reference value set since the previous step. Likewise, the temperature relaxation time parameter is set to 1 ps. Random initial velocities are assigned to fragments using a Gaussian distribution. Velocity magnitudes are chosen so that the initial temperature of the system is approximately equal to the target simulation temperature. This NVT equi-

libration intents to stabilize the system to run dynamics with the EFP method at the reference temperature.

Once the EFP-MD NVT equilibration is completed, the cloned ice box is retrieved and reformatted to the EFP model. Then, both boxes, the cloned ice box and the final configuration of the previous step, are joint together. The xy face of the water box is put in contact with the $\bar{1}\bar{2}10$ face of the ice box, as shown in Figure 6.3. The joint box contains 256 water molecules: 128 of ice I_h , and 128 of liquid equilibrated at the corresponding reference temperature. The new box dimensions are set to: $14.760 \text{ \AA} \times 15.656 \text{ \AA} \times 36.144 \text{ \AA}$, in x , y , and z , respectively. The system now resembles the state described by Figure 6.1(c).

Ideally, as indicated in the scheme of Figure 6.2, the following step would have been an NPT equilibration, under equivalent conditions to the production run, performed with the coordinates of the ice box frozen. This step would have improved the stability of the production run by allowing the liquid to relax and adapt to the presence of the ice box. However, due to the lack of a coordinate freezing functionality in EFPMD at the time the simulations were carried out, this is not done in this work.

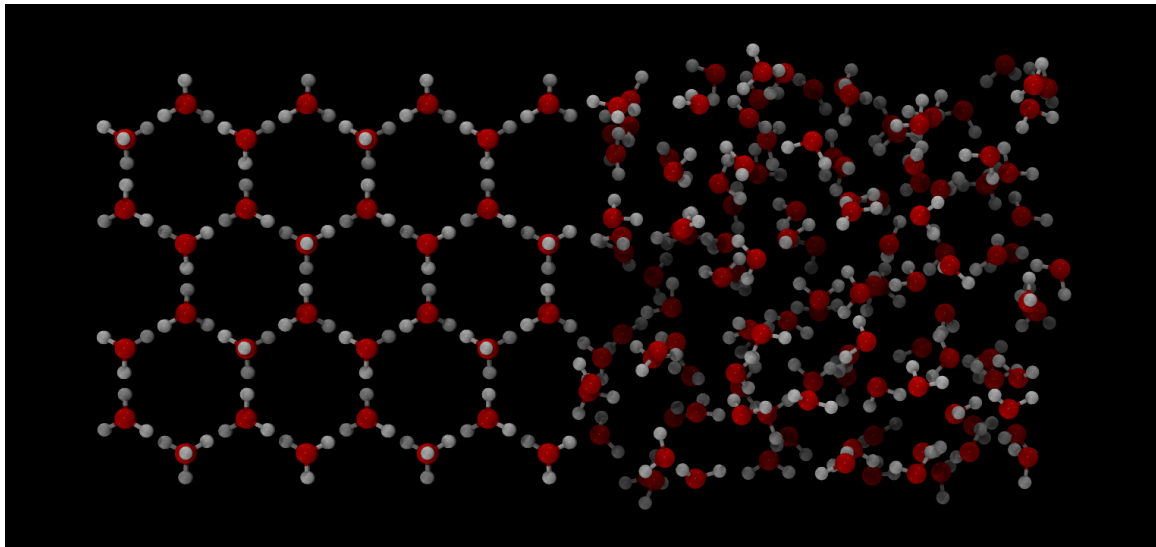


Figure 6.3. Unitary cell of the system after joining the ice and liquid water boxes.

Instead, an EFP-MD NPT production stage is performed. The settings chosen for this step are analogous to the previous. Periodic boundaries with the dimensions of the new joint-box are used with the same cutoff distance of 7.2 Å. Damping schemes are treated identically, and the integrator works with the same algorithms. The unmodified reference temperature is kept by the Nosé-Hoover thermostat, with a matching coupling constant. However, this time initial velocities are read from the last frame of the NVT equilibration trajectory. Additionally, as this is an NPT simulation, the Hoover barostat, as described by Melchionna et al. [241], is employed to hold the pressure at 1.0 *bar*, with a pressure relaxation time parameter of 10 *ps*. Adjustment of the volume of the box is allowed to variate only on the *z*-dimension. In this case, the integrator runs for 500 *ps*, at steps of 2 *fs*. Production output was written every 200 *fs*, providing the trajectories analyzed in the next section. A short sample input is provided in Appendix I.

6.4 Results

The thermodynamic equilibrium between liquid water and ice is probed looking at four aspects of the production trajectories. The time-evolution of the total energy, the conformation of the ice, the RDF, and density dependence on the temperature are analyzed in detail in this section.

6.4.1 Time-evolution of the Total Energy

The analysis starts by monitoring the total energy, that is the sum of the kinetic and potential energies. In this simulations, the potential energy includes electrostatics, polarization, dispersion, and exchange-repulsion terms. If the system is above the melting point the ice cube melts, whereas if the system is at a temperature below the melting point the liquid water freeze. As explained in Section 6.2.2, freezing produces a general decrease in the total energy, as opposed to melting which increases the total energy.

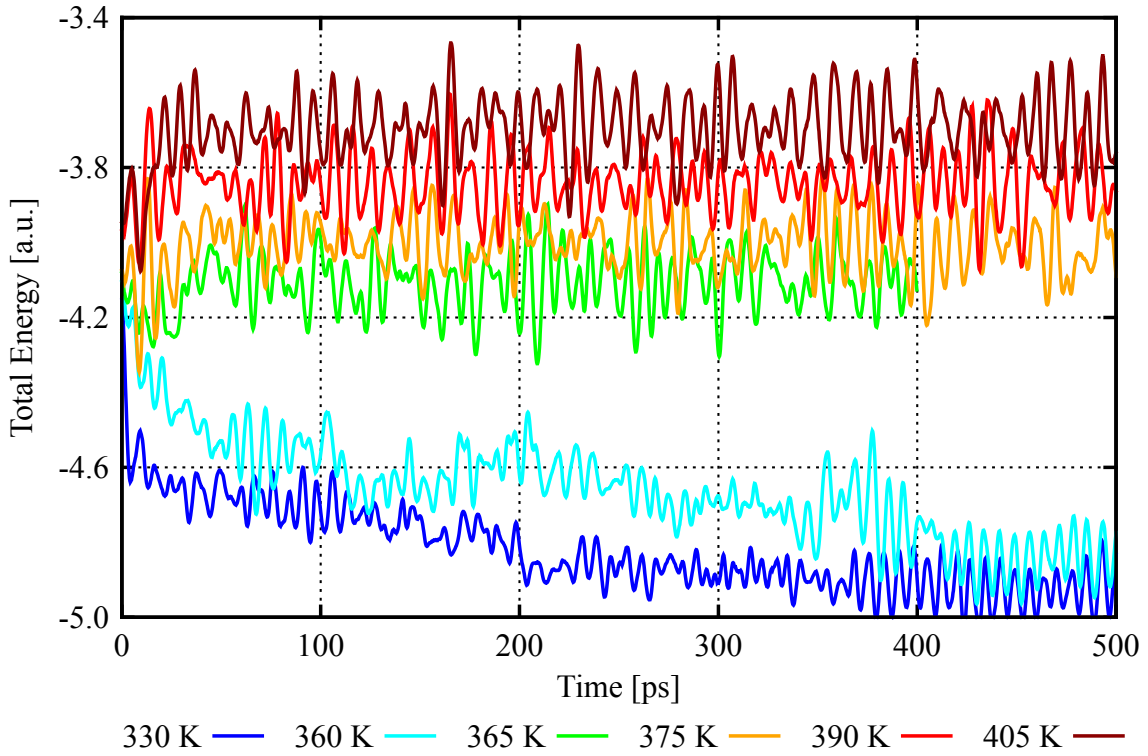


Figure 6.4. Time evolution of the total energy of the system along the trajectory.

Figure 6.4 shows the evolution of the total energy for six production runs at temperatures ranging from $330\text{ }K$ to $405\text{ }K$. Chronologically, higher temperature simulations at $405\text{ }K$, $390\text{ }K$, $375\text{ }K$ are run first. Knowing that the melting point of some water models is located above $400\text{ }K$ it is decided that the first simulations would start at $405\text{ }K$, reducing the temperature by $15\text{ }K$ for the next simulation, until the melting point is reached.

In the upper curves, with temperature ranging from $375\text{ }K$ up to $405\text{ }K$, the energy gradually increases as the time evolves, implying that the ice is melting. However, after the fourth simulation, at $360\text{ }K$, the energy clearly decreases along the trajectory. The next simulation at $330\text{ }K$, corroborates this behavior. Therefore, an additional trajectory is prepared and run at $365\text{ }K$.

The analysis of this last trajectory reveals ice melting. An additional trajectory is started at $363\text{ }K$. However the analysis of the initial 250 ps does not clearly

show if the energy is increasing or decreasing. This is because irregularities are more evident when close to the coexistence temperature. Hence, as it lacks relevancy, this trajectory is disregarded in this analysis. Inspection of the data compiled in Figure 6.4, clearly shows that the melting point of the EFP water model falls within the range of $360\text{ }K$ to $365\text{ }K$.

6.4.2 Visual Analysis

The analysis proceeds with an inspection of the trajectories, performed in VMD 1.9 [242], revealing a few interesting observations. The most relevant features are presented in the snapshots of Figure 6.5. The snapshots on the left column, correspond to the trajectory at $360\text{ }K$; those on the right, are extracted from the production run at $365\text{ }K$. The top row, shows the initial conformation, the middle row compares both systems at the 75 ps frame, and the bottom row exhibits the last frame of the trajectories.

First, looking at the bottom row, it is obvious that the last frame at $365\text{ }K$ shows a completely melted water sample, while the one at $360\text{ }K$ shows no clear indication of melting. It would be a leap to affirm that the system is freezing according to that last frame on Figure 6.5(e), albeit the ice block appears to be one layer larger. The result at $360\text{ }K$ is not ambiguous. It should be reminded that, in MD simulations, freezing is a much more complex phenomena to capture than melting. Then, it is plausible that the system is freezing, as the time evolution of the energy indicates, but the ice is growing a slow-enough rate that is difficult to perceive with such a short trajectory.

Second, the middle row displays a relatively early frame of both trajectories. While in the snapshot at $360\text{ }K$ there are no signs of melting, the system at $365\text{ }K$ reveals a highly disarranged structure that hardly resembles ice. This observation points out that, even at $365\text{ }K$, melting of the ice block occurs relatively fast. Visual inspection of the other trajectories above the melting point show complete melting by the 200

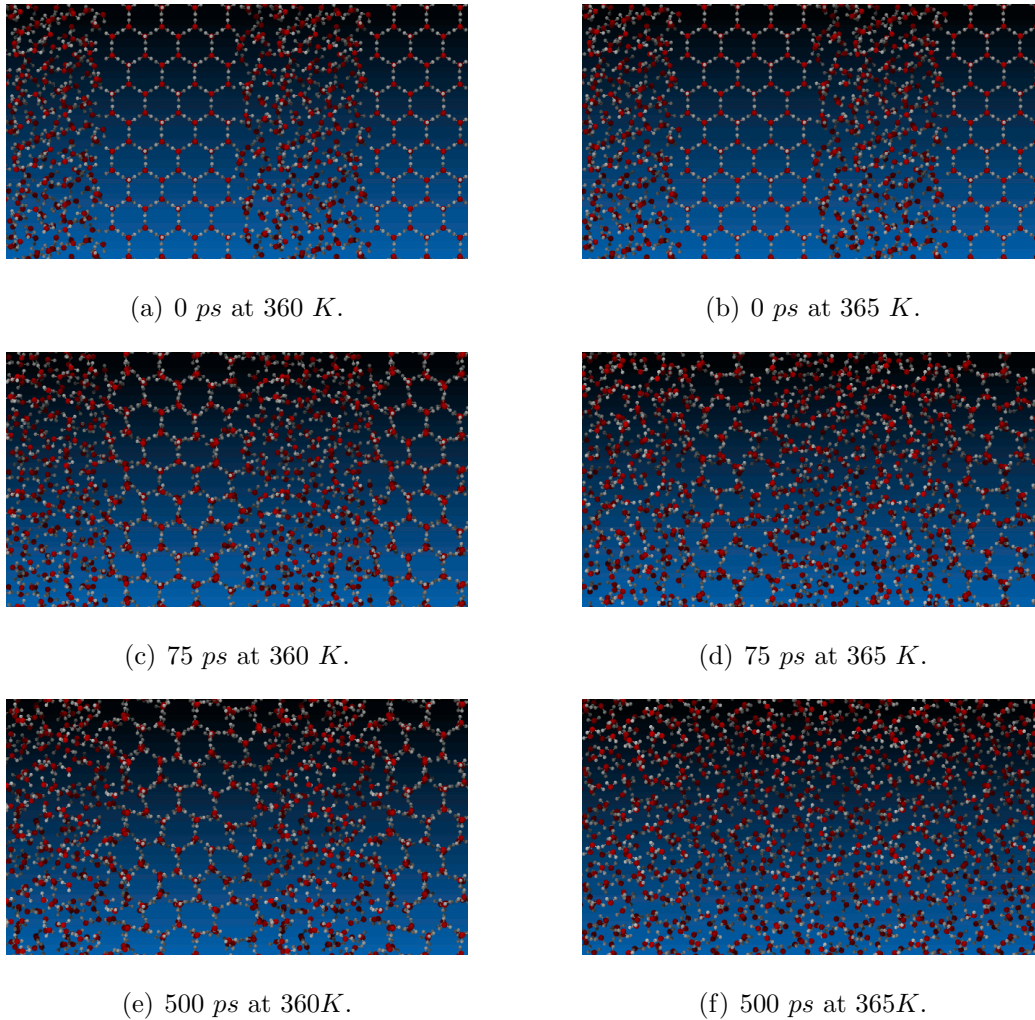


Figure 6.5. Representative snapshots sampling the time evolution of the configuration of the system along the trajectory.

ps frame, at latest. This is probably related to the size of the simulation box: the ice block contains only a few layers.

Third, in all cases, trajectories with a generally increasing total energy display complete melting, whereas in those where the energy decreases do not show signs of melting. In other words, Figures 6.4 and 6.5 show congruent results, validating the utility of the direct coexistence method for this particular water model.

6.4.3 Radial Distribution Functions

A structural analysis founded on the pair correlation function between oxygen atoms in the EFP water model is presented below. The RDF, $g_{\alpha\beta}(r)$, is a type of a pair correlation function that describes the orientation-normalized probability of finding a particle, of a given type, at a certain distance from a reference particle. For a system containing N_α particles of type α , and N_β particles of type β , the RDF is defined as

$$g_{\alpha\beta}(r) = \frac{1}{N_\alpha N_\beta} \sum_i^{N_\alpha} \sum_j^{N_\beta} \langle \delta(|\mathbf{r}_{ij}| - r) \rangle , \quad (6.1)$$

where the angled brackets signify a time average, δ denotes the Dirac delta function, $|\mathbf{r}_{ij}|$ is the magnitude of the separation vector between particles i and j , and r represents the average distance between particles in an ideal gas distribution.

The O-O RDF computed for trajectories at different reference temperatures are compiled in Figure 6.6. All oxygen atoms in the system are considered in these trajectories. In practice, it is difficult to determine which molecules belong to ice and to liquid, therefore analyzing RDF of each is extremely involved. The colors match those of Figure 6.4, and additionally, the experimental RDF of water at 273 K is shown in black [243].

Figure 6.6 supports the observations aforementioned in the previous sections. On the one hand, the RDF of simulations at temperatures higher than the melting point are less structured, noisier, with shallower valleys and lower peaks. These are manifestations of liquid behavior. On the other hand, the RDF at temperatures lower than the melting point are more structured, sharper, with deeper valleys and higher peaks; resembling a more ordered behavior, as expected due to the presence of the solid.

Furthermore, when comparing against the experimental RDF, the features of the EFP curves seem to be displaced to longer separations. If the first peak of the black curve is compared to that of all other curves, even in the case of the RDF containing

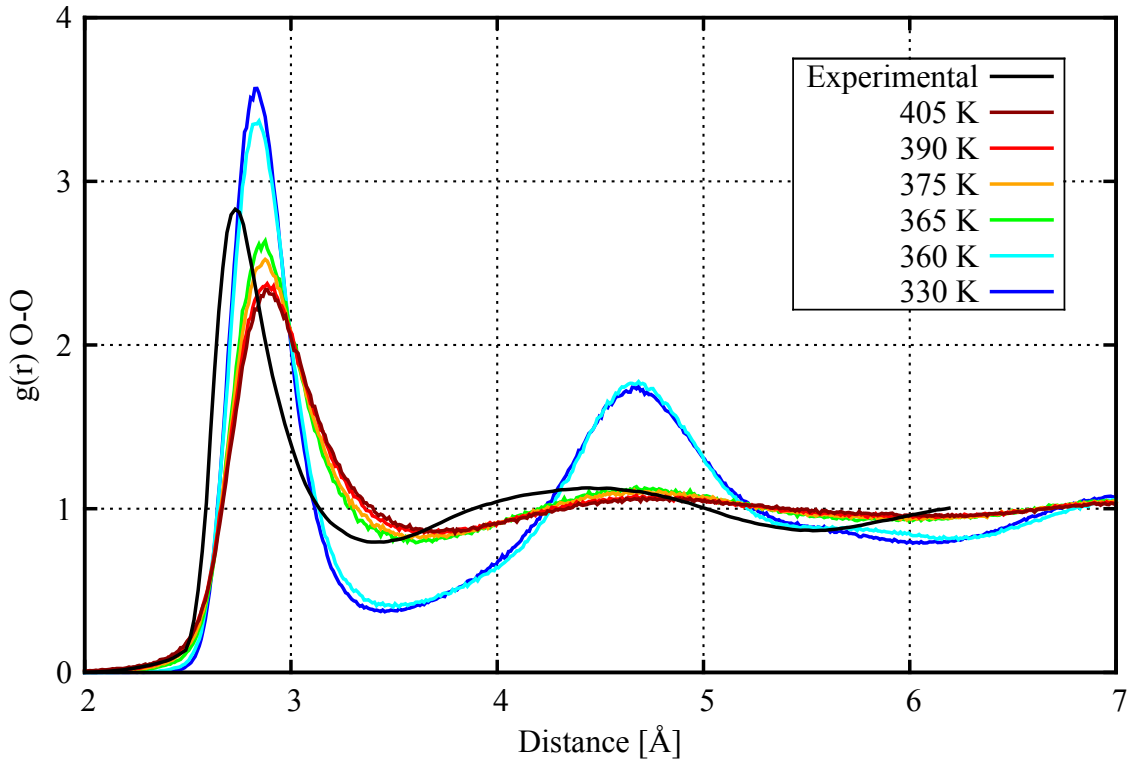


Figure 6.6. Oxygen-oxygen RDF of the EFP water model at the simulated temperature and comparison with the reference.

ice in the system, the EFP peaks are displaced by approximately 0.2 Å. This indicates that the potential is more repulsive than it should.

6.4.4 Density as a Function of Temperature

The information extracted from the statistical analysis of the density along the trajectory is presented here. A candlesticks plot with whisker bars was chosen to comprise the statistical information of all the trajectories in one plot. As this type of plot is atypical in the literature, a basic explanation is provided first.

As the schematic in Figure 6.7 shows, the shaded area is bound by the minimum and maximum values of the density along one trajectory. The arithmetic mean is marked by the black horizontal line, accompanied by candlesticks, centered on the median, representing the standard deviation. The whisker bars mark the lower and

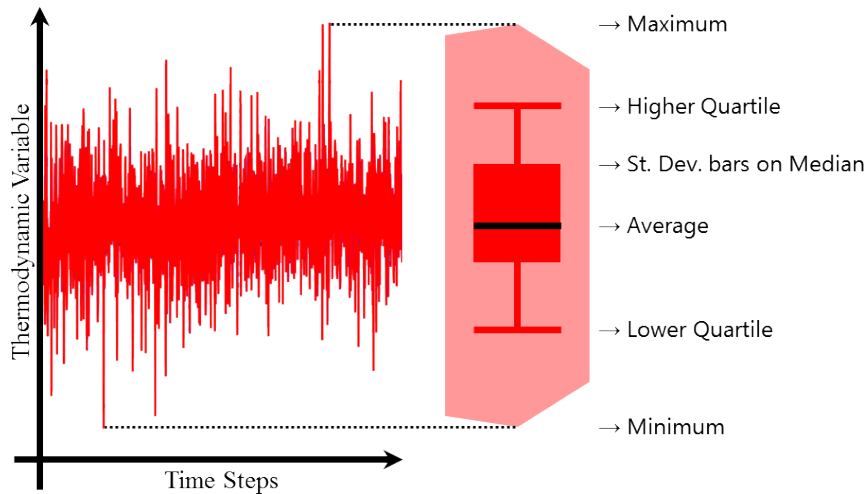


Figure 6.7. Schematic representation of the statistical analysis.

higher quartiles, meaning that 50% of all measurements are contained within these bars. The colors on each candlestick correspond to those of the previous figures, and the trajectory at each temperature is summarized in one candlestick.

Figure 6.8 comprises the statistical analysis of the density. Several observations are made. One, the density of the system is directly related to the volume of the periodic box at each step of the trajectory, therefore the total range of the density shows an ample variation.

However, the density of EFP water around the melting point is higher for the liquid than for the ice; two. This is in good agreement with the expectation of a decent water model, meaning that the EFP model correctly captures the differences in packaging of liquid water and ice.

Three, the density in the EFP water model around its melting point is lower than that of the experiments. In other words, the water fragments are more separated than they should be in the thermodynamical region close to the equilibrium. This supports previous indications that the EFP method produces potentials that are slightly too repulsive at close distances.

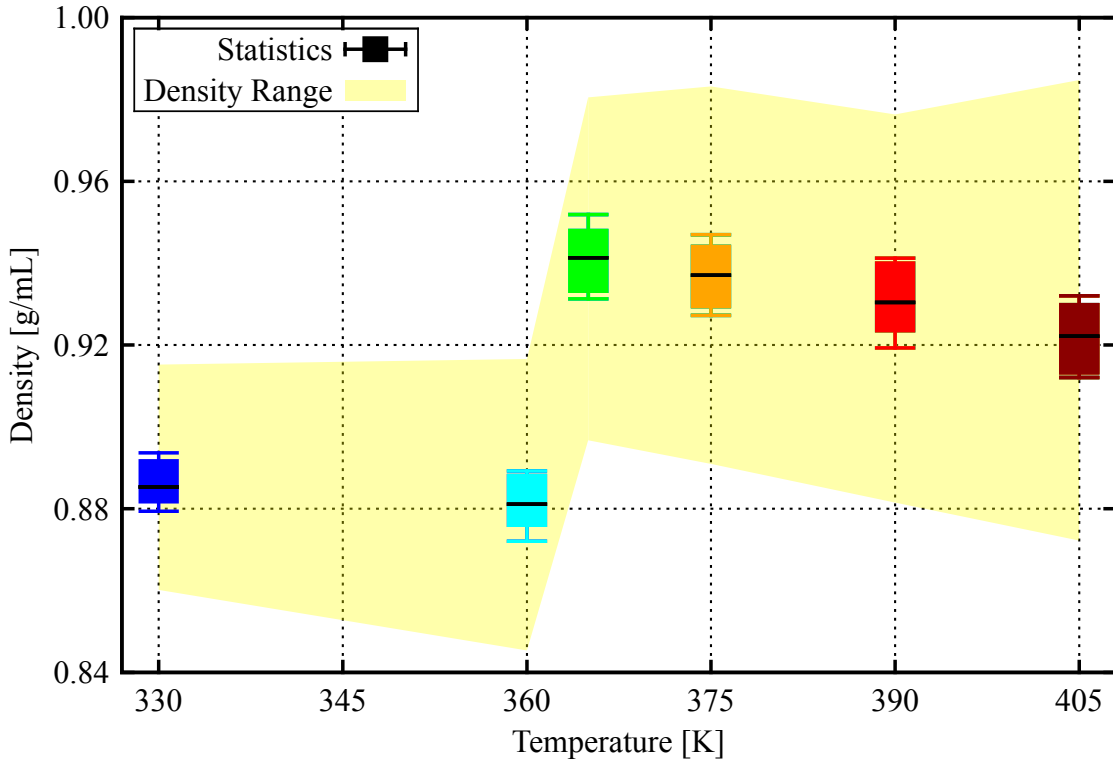


Figure 6.8. Statistical analysis of the density at different simulation temperatures.

6.5 Summary

Three important conclusions are derived from this work. The melting point of the EFP water model is located between 360 K and 365 K . The pair correlated functions between oxygens in the region close to the ice-liquid equilibrium show features displaced to longer separations in EFP model with respect to experimental measurements. And, the density of EFP water around the melting point is higher for water than for ice, as is expected. The following discussion provides a possible explanation.

Interaction energies between fragments are slightly overestimated with the EFP model. There is evidence of too strong hydrogen bonding in water. Flick et al. [244] demonstrated an overbinding of approximately 0.8 kcal/mol in the EFP water dimer, due to this effect. Stronger hydrogen bonds require additional energy to be broken, therefore pushing the melting temperature to values that are too high.

Interestingly, equilibrium distances in EFP water are also overestimated. Peaks in the RDF of EFP are displaced to longer distances, and densities are lower than the reference. It should be reminded that the computationally-expensive CT term is omitted in this water potential, and instead it is replaced with an electrostatics term with parameters derived with a smaller basis set. Stronger electrostatics usually overcomes well the lack of charge transfer. However, at short range the Pauli repulsion prevails, keeping the fragments apart from each other. At short separations, the fragment potential becomes too repulsive.

This study provides arguments to explore practical and efficient ways to include charge transfer in EFP-MD. It also opens the door to a wider exploration of the ice-liquid equilibrium. The inclusion of solutes, to investigate their effect on the melting point would be a good place to start. The simulations in this work are not aimed at understanding the effects of the size of the box. However, it would be an important check to perform. There is also the possibility to run longer trajectories to study the freezing process. An study of the impact of each EFP energy term on the melting temperature could also be of general interest.

7. COMPUTATIONAL EFFICIENCY OF MOLECULAR DYNAMICS WITH THE EFFECTIVE FRAGMENT POTENTIAL METHOD

7.1 Introduction

The EFP method is a systematic approach to describing intermolecular interactions in an efficient yet rigorous way [245]. EFP is a quantum mechanical based potential that can be thought of as a non-empirical polarizable force field [177]. Hence, the method is applicable in the field of MD simulations [246]. In this chapter, the computational cost of electrostatic, polarization, dispersion, and exchange-repulsion energies and analytic gradients of EFP is analyzed in small clusters of water, simulated under the microcanonical ensemble. Based on these results, it is concluded that the computational bottleneck of EFP-MD lays in the calculation of the XR energy.

7.1.1 Motivation

The EFP method was motivated by an investigation on how to simplify the description of environment effects in quantum mechanical calculations [162]. Therefore, it naturally emerged as a QM/MM methodology in which the classical region involves complex many-body effects [166].

When compared to semi-empirical and quantum mechanical methods, the EFP method provides an excellent description of the interaction energy [247]. The EFP method is capable of achieving high chemical accuracy and, at the same time, it is computationally more efficient than QM methods; thus it can be applied to a wider range of chemical systems [248]. And, even though its main focus was initially different, the EFP method also offers the possibility to be used as a classical potential to simulate molecules in motion [176].

The computational cost of a method is especially relevant for MD. To simulate the evolution of time, the integration of equations of motion is done iteratively in cycles that usually involve thousands or millions of repetitions. At every step, the execution time is determined by the computational efficiency of the computational method [199]. Therefore, more complex methods are limited in applicability.

In addition to the benefits mentioned previously, the EFP method has numerous advantages when employed as a force field in MD simulations. For instance, its parameters can be derived directly from *ab initio* calculations, making it systematically improvable and highly transferable [166]. It allows for explicit account of the most relevant short- and long-range intermolecular interactions [248]. And it describes polarization, including many-body effects [149].

However, by current standards, EFP-MD simulations are still considered computationally demanding. This is especially true when compared to MD simulations performed with classical force fields. Hence, the analysis of the computational efficiency of each of the energy components of the EFP method is of significant importance for molecular modeling.

7.1.2 Background

The MD trajectories calculated for determination of the melting point of the EFP water model, presented in Chapter 6, serve as an initial comparison of the computational demands of EFP-MD against a simpler model such as OPLS [249]. In that example, analogous calculations were performed with the TIP4P/Ice water model, in GROMACS, and with the EFP water model, in LibEFP/EFPMD.

The general specifications of those simulations are:

- 16 CPUs (2×8 -Core Intel Xeon-E5) + 32 GB of RAM
- 256 water molecules.
- Isothermal-Isobaric ensemble
- Periodic-boundaries box: $15 \text{ \AA} \times 15 \text{ \AA} \times 36 \text{ \AA}$

- Nosé-Hoover thermostat
- Parrinello-Rahman (GROMACS) vs. NPT Hoover barostat (EFPMD)
- Non-bonded interactions cutoff: 7.2 Å
- 500 *ps* at 2 *fs* per step, totaling 250,000 steps.

While GROMACS is capable of achieving about 1,000 *ns/day* under these conditions, LibEFP/EFPMD is able to complete only about 0.1 *ns/day*, in terms of simulated time per wall time. In other words, ruling out any comparison in regard to accuracy, an EFP-MD simulation is about four orders of magnitude more demanding than the simpler MD force field OPLS, in that particular system. Hence, the question is: where is the computational bottleneck in EFP-MD?

7.2 Theory

Standard classical force fields generally express the potential in terms of bonded and non-bonded interactions [199]. Usually, bonded interactions involving two, three, and four next-neighbor species are considered explicitly within the bonded potential, whereas all other interactions fall in the non-bonded potential. This non-bonded term is typically split in electrostatics and van der Waals interactions; and most traditional force fields usually stop at that level of detail [201].

As the bonded interactions have a clear cut-off reaching up to the fourth covalently-bonded neighbors, their computational complexity is low, with approximately linear scaling in terms of the number of atoms in the system [14]. The real cost of classical force fields arises from the non-bonded interactions, especially the electrostatics term [250]. Coulomb potentials decay with the inverse of the separation between species, and in some applications Coulomb interactions are still relevant at distances as long as 25 Å [251]. Thus, long-range interactions are often the bottleneck of classical MD simulations.

When the EFP method is employed as a force field, fragments are assumed to be internally rigid. Therefore, no bonded interactions are considered, and the internal

energy is neglected [153]. The non-bonded potential is thus effectively composed of the EFP energy terms. Long-range interactions are captured through explicit terms for electrostatics, polarization, and dispersion effects; whereas short-range forces are given by explicit modeling of exchange repulsion (and charge transfer).

Inspecting the theory behind each of the energy terms of the EFP method, as implemented in LibEFP, there are several clues that point to exchange repulsion, as the most intricate [149]. However, the computational cost of the EFP-MD energy contribution has not been formally addressed so far. Consequently, a methodology to explore the relative computational demands of each energy term of the EFP method is presented in the following section.

7.3 Computational Details

The objective is to analyze the computational cost of each EFP energy term independently to find where the computational bottleneck of EFP-MD simulations is. LibEFP features a functionality to choose which of the energy terms should be computed when performing an EFP calculation. There is a caveat: the polarization term depends on the electrostatic field due to static multipoles that is computed during the execution of the electrostatics term. Therefore if the polarization term is to be computed, the electrostatics term is also computed by default [192]. Otherwise, the electrostatics, dispersion, and exchange repulsion can be computed individually by switching off the calculation of all the other terms. Therefore, the main idea behind this methodology is that by timing the computation of short EFP-MD trajectories calculated using exclusively one energy term, it allows to compare its relative computational cost against that of the other terms.

A key element to this comparison is that the time required by the EFPMD code to setup each step of the calculation should be essentially independent from the computation of all energy terms. Several hardware considerations are made in that regard. To minimize the impact of computer architecture and parallel execution on timings, all calculations are executed on a single node, employing a single CPU, on

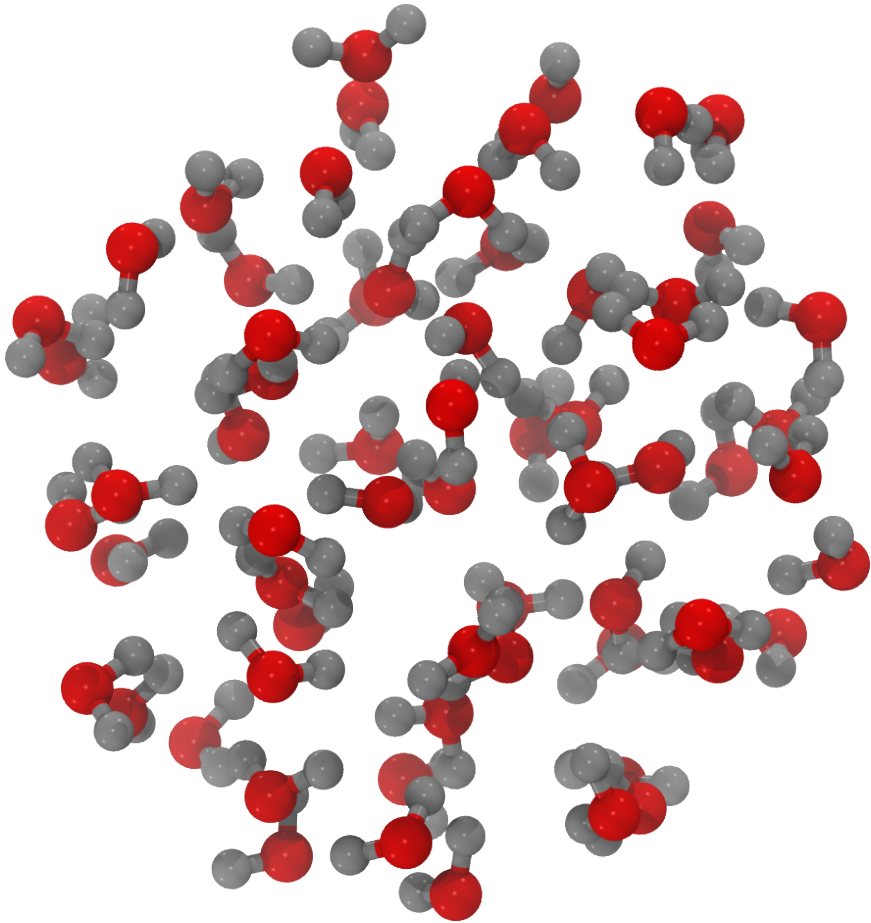


Figure 7.1. Spherical water cluster including 128 fragments.

the same machine, with equivalent amounts of memory, and writing to disk at each step.

In addition, software is also controlled carefully. For example, the calculation of damping functions is avoided. This is impractical in the case of the polarization term: as the polarization is calculated self-consistently, if no screening is applied, a polarization catastrophe occurs sooner or later [180]. Necessarily, the Gaussian-type screening approach is employed. Likewise, periodic boundaries are not utilized, because they imply the need to calculate cut-offs. Accordingly, the microcanonical ensemble is used, avoiding the use of temperature or pressure coupling techniques.

As in many cases EFP calculations include water fragments, small clusters of water are used as model system. These clusters, such as the one exhibited in Figure 7.1, comprise a minimum of 4 and up to 1,024 water fragments. The water potential employed in these simulations is equivalent to that used on Chapter 6.

For each system size, trajectories are computed switching one energy term on, exclusively. Three simulations are carried out for each energy term, starting from different random initial conformations; and 10 *ps* are simulated in 100,000 steps of 0.1 *fs* each. As these trajectories are run with only one of the terms switched on, and all other terms switched off, they are inherently unstable; particularly in the case of polarization and exchange repulsion. To remedy this situation, the time steps are made extremely short and the total lapse of execution is also short. Reference trajectories are computed with the full potential, under equivalent conditions. A total of 105 trajectories are computed and analyzed in this study.

7.4 Results

The computational demands of EFP-MD are analyzed and decomposed into each of its energy contributions, based upon trajectory timings. These timings are studied in detail in this section.

Total execution wall time, for each energy contribution and for the total potential, is plotted against the number of water fragments on Figure 7.2. The color code convention for this plot is: electrostatics timings are shown with orange squared data points, polarization in green circles, dispersion in blue triangles, exchange repulsion in red flipped triangles, and the full-EFP potential in black diamonds.

Fitting the timings of the total potential on Figure 7.2 to a parabolic curve results in a unitary squared correlation coefficient. This indicates that the computational scaling of these EFP-MD simulations is $\mathcal{O}(N^2)$, where N is the number of fragments in the system. The squared correlation coefficient of the parabolic fit for electrostatics and dispersion is also unitary, whereas the one for exchange repulsion and polariza-

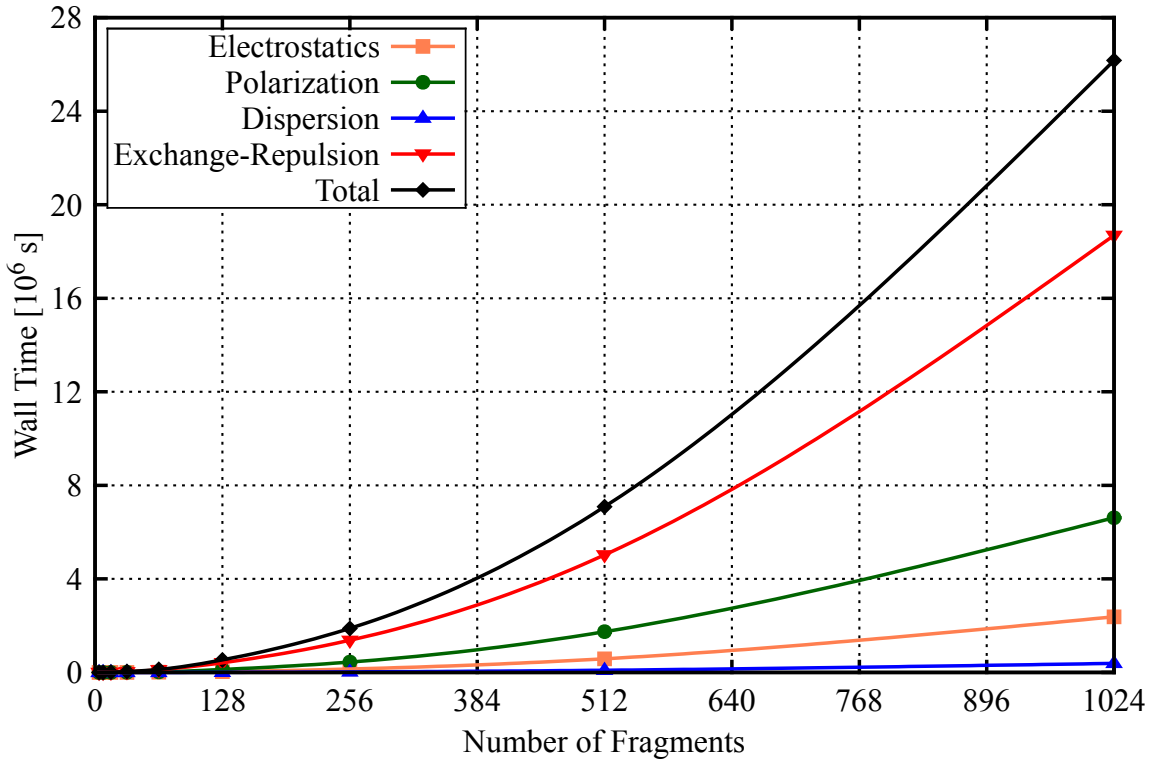


Figure 7.2. Execution times comparison for small water clusters of several sizes: all energy contributions scale with the square of the number of fragments.

tion is above 0.99. Therefore, under the conditions of these simulations, all energy contributions scale as $\mathcal{O}(N^2)$.

Figure 7.3 is produced rearranging the timings data, exploiting the squared dependence on the number of fragments, on a base-10 logarithmic y -axis and a base-2 logarithmic x -axis. The same color code of Figure 7.2 is utilized. None of the lines on Figure 7.3 ever cross, evincing that the relative computational cost of each term is similar at different system sizes. In all cases, the XR term is the most expensive, followed by the polarization, electrostatics, and dispersion terms, respectively.

In addition, the exchange repulsion (red) line is always close to the total potential (black) line. This implies that most of the computational cost of the full potential

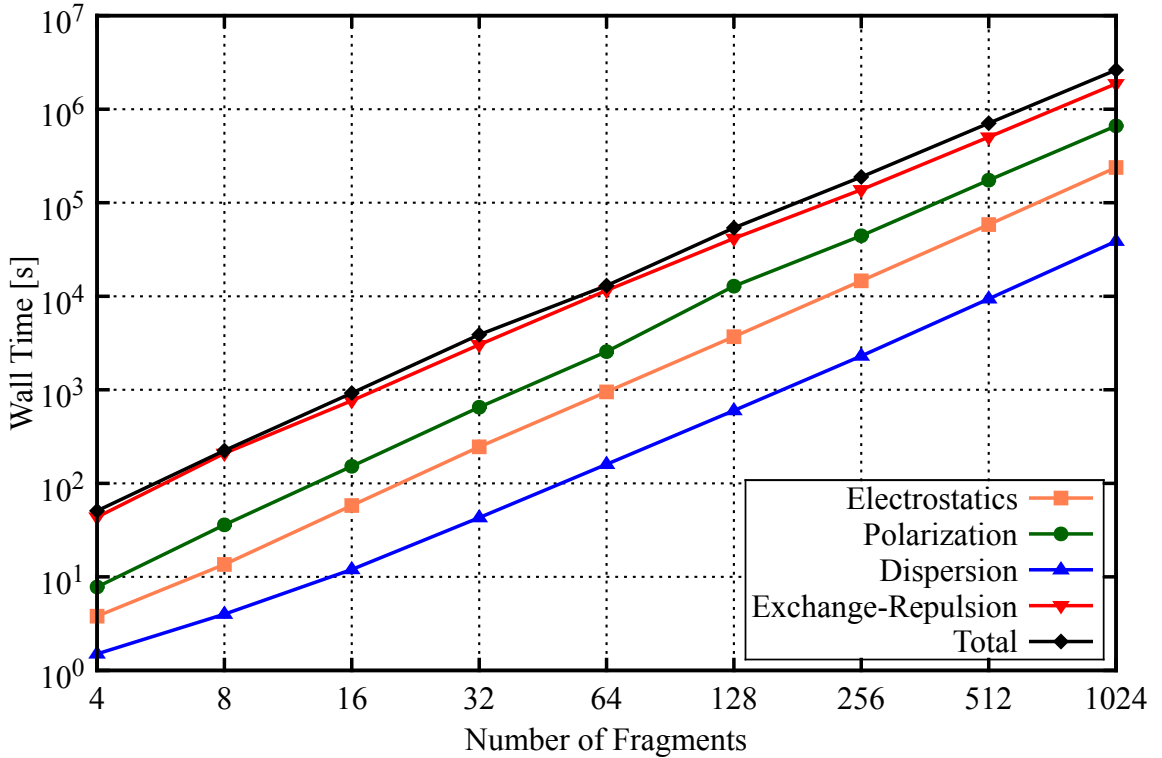


Figure 7.3. Execution times in logarithmic axes: exchange repulsion is the most computationally expensive component of EFP-MD, followed by polarization, electrostatics, and dispersion, respectively.

trajectories lies in the execution of the exchange repulsion routines. Namely, the computational bottleneck of EFP-MD is in the calculation of the XR energy.

Now, taking the timings of the full-EFP trajectories as a reference, the relative cost of each of the energy components is calculated proportionally, as a percentage. These results are displayed in Figure 7.4. Note that, as a consequence of uncontrollable factors such as the preparation time, or the time required to compute polarization screenings, which may have an impact on the timings, the sum of all proportions may not give exactly 100%. Still these proportions provide a good estimation of the relative cost of each term, and serve as a semi-quantitative metric for comparison.

Figure 7.4 shows that the exchange-repulsion computational cost is usually greater than 75%, while that of polarization, the second most expensive term, is often less

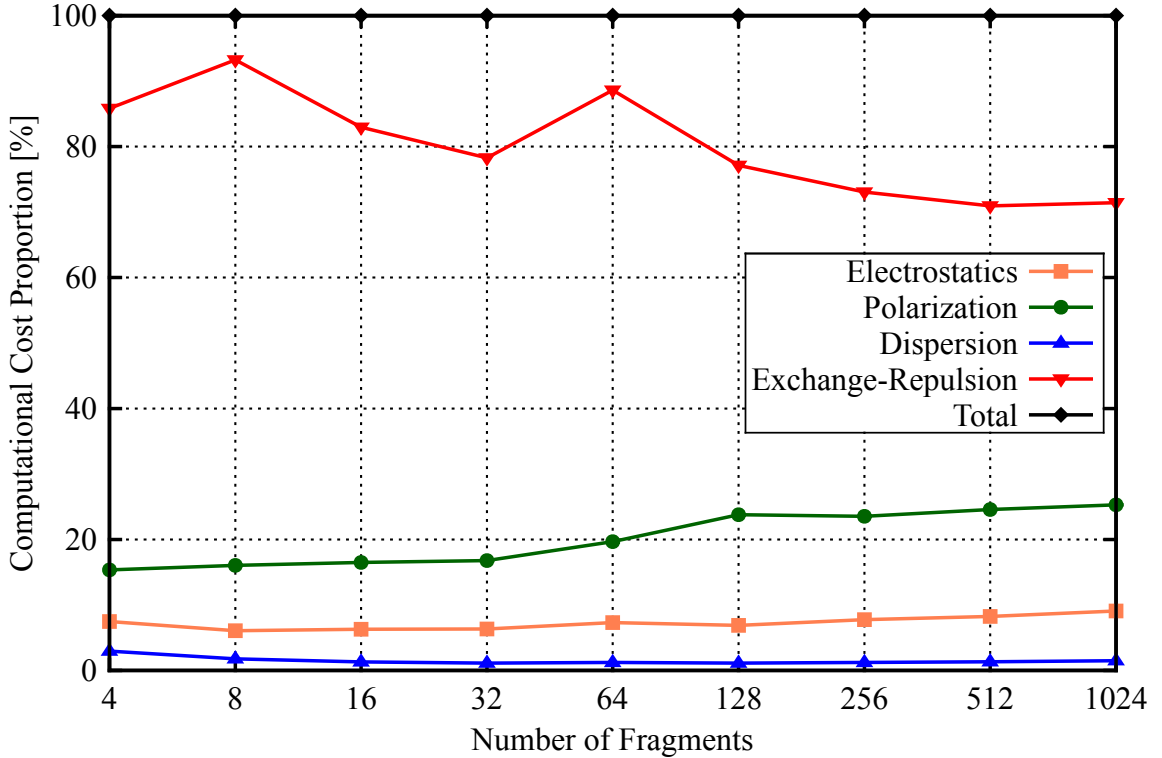


Figure 7.4. Relative cost of each energy component with respect to the full calculation. Exchange repulsion proportional cost decays with the size of the system, but it is always at least three times that of polarization.

than 25%. This is an indication that exchange repulsion is roughly three times more expensive than polarization, the second most demanding contribution.

As explained in Section 5.3, the calculation of the exchange-repulsion energy involves on-the-fly computation of the the overlap and kinetic-energy integrals between each pair of LMOs on all fragments. These integrals run over all space, and require the use of the spherical Gaussian overlap approximation [190]. Even though the wave function is precalculated during the parametrization process, this procedure is still quite convoluted, explaining why this term is so computationally expensive [149].

The polarization energy requires an iterative procedure to calculate the induced dipoles of each fragment. In this iterative procedure the induced dipole of each

fragment is adjusted self-consistently to account for the changes of the static and induced fields due to the other fragments [177]. Reaching self-consistency becomes more difficult as the size of the system increases, which is evident in Figure 7.4. Also, unless screenings are employed to modulate the polarization response, the iterative procedure is unstable and tends to produce a polarization catastrophe; adding more complexity to the calculation of the polarization energy. Moreover, the static field depends on the electrostatic potential, given by the multipole expansions employed in the calculation of the electrostatics energy term. Therefore, polarization cannot be untangled from the calculation of the electrostatic potential [192]. These three characteristics contribute to make polarization the second most expensive term to compute.

Oppositely, the dispersion energy term requires computation of the dispersion coefficients and fragment separations. Although the computational cost of measuring the separation between fragments can become more difficult in larger systems, it is often inexpensive. Besides, the dispersion coefficients are calculated on-the-fly between all pairs of dispersion points on all fragments, using a 12-point Gauss-Legendre quadrature [167]. The algorithms employed for such purpose usually run efficiently [149]. That explains how the dispersion energy is the least computationally demanding.

While the exchange repulsion decays exponentially with respect to fragment separation, polarization interactions decay as $1/R^3$. Consequently, the exchange repulsion vanishes at shorter separations than polarization. It is therefore possible to alleviate the relative cost of the exchange repulsion in large systems by implementing cut-offs and switching functions for the XR energy term.

7.5 Summary

Switching off all but one of the energy terms of the EFP force field, EFP-MD trajectories are performed and timed. Small clusters of water ranging from 4 to 1,024 fragments are employed as model systems. Timings for each energy contribution across all system sizes are analyzed concluding that the scaling of EFP-MD

calculations depends on the square of the number of fragments. The exchange-repulsion energy is the most computationally expensive of all, being at least three times more demanding than polarization, the second most convoluted contribution to compute. EFP-MD calculations could be made more efficient if the cost of the exchange-repulsion energy term would be reduced. Hence, this investigation motivates the search for alternative methodologies to compute the exchange repulsion energy more efficiently.

8. EXPLOITING THE TIMESCALE SEPARATION OF ENERGY CONTRIBUTIONS TO ACCELERATE MOLECULAR DYNAMICS IN THE EFFECTIVE FRAGMENT POTENTIAL METHOD

8.1 Introduction

This chapter presents a theory development that exploits the inherent timescale separation between energy contributions of the EFP method to accelerate MD simulations. It is verified that XR interactions are mildly dependent on molecular orientation, and evolve slowly with respect to the other types of interactions considered in the EFP method, as implemented in LibEFP/EFPMD. Therefore, a Taylor expansion, updated intermittently, can be used to estimate the XR force. These findings offer the possibility to improve the efficiency of EFP-MD simulations in small- and medium-sized systems.

8.1.1 Motivation

Chapter 7 concluded that the most demanding energy contribution in EFP-MD is the XR term. This is because the XR energy depends on the calculation of elements of the overlap integrals matrix, and these integrations are highly convoluted [149]. This makes the XR energy at least three times more expensive to compute than polarization, the next most intricate energy term.

However, if the relative cost of the exchange repulsion could be reduced, the execution of EFP-MD trajectories might be accelerated; making EFP-MD simulations more broadly applicable. Therefore, this study seeks an answer on how to make EFP-MD simulations more efficient.

8.1.2 Background

The EFP method, as implemented in LibEFP, is defined through the expression for the potential energy, which includes four explicit terms: electrostatics, polarization, dispersion, and exchange repulsion [192]. Thus, the total potential energy is written as:

$$V^{\text{EFP}} = E_{\text{elec}} + E_{\text{pol}} + E_{\text{disp}} + E_{\text{xr}}. \quad (8.1)$$

This expression is identical to that of Equation (5.3), and a detailed description of each term was provided in Section 5.3.

The EFPMD code calculates the gradient of the previous expression, which provides the force due to the potential,

$$\mathbf{F}^{\text{EFP}} = -\nabla V^{\text{EFP}}. \quad (8.2)$$

Likewise, the gradients of each contribution to the total potential energy provide the forces due to the corresponding type of interaction. Those forces are components that add up to the total force,

$$\mathbf{F}^{\text{EFP}} = \mathbf{F}_{\text{elec}} + \mathbf{F}_{\text{pol}} + \mathbf{F}_{\text{disp}} + \mathbf{F}_{\text{xr}}. \quad (8.3)$$

In the same way, the total force acting on a fragment i can also be decomposed into each type of interaction.

8.2 Theory Development

In 1978, Streett et al. [252] designed a multiple time-steps methodology which allows for extended times between updates of slower forces in a MD simulation. This methodology has progressed since and it was implemented for the Verlet algorithm in 1991 by Grübermuller et. al. [253]. Since then, it has been applied to numerous current dynamics methods [254, 255]. The idea is that by grouping fast- and slow-evolving forces acting on fragment i ,

$$\mathbf{F}_i = \mathbf{F}_{\text{fast},i} + \mathbf{F}_{\text{slow},i}, \quad (8.4)$$

two (or more) time steps, of different lapses, are used to integrate the equations of motion in systems governed by continuous potential functions. Applying this technique, computing speeds are increased by factors of three to eight over conventional MD integration methods in simulations of fluids, with only marginal increases in computer storage [252].

According to the observations made throughout Chapter 7, the most computationally demanding term is the XR energy. Assuming that the time-evolution of the XR force is much slower than that of any other terms,

$$\frac{d\mathbf{F}_{\text{elec}}}{dt}, \frac{d\mathbf{F}_{\text{pol}}}{dt}, \frac{d\mathbf{F}_{\text{disp}}}{dt} \gg \frac{d\mathbf{F}_{\text{xr}}}{dt}, \quad (8.5)$$

the EFP forces may be separated by grouping fast evolving forces,

$$\mathbf{F}_i^{\text{EFP}} = (\mathbf{F}_{\text{elec},i} + \mathbf{F}_{\text{pol},i} + \mathbf{F}_{\text{disp},i}) + \mathbf{F}_{\text{xr},i}, \quad (8.6)$$

and leaving the XR force aside as the slowest evolving force,

$$\mathbf{F}_i^{\text{EFP}} = \mathbf{F}_{\text{fast},i} + \mathbf{F}_{\text{xr},i}, \quad (8.7)$$

where

$$\mathbf{F}_{\text{fast},i} = \mathbf{F}_{\text{elec},i} + \mathbf{F}_{\text{pol},i} + \mathbf{F}_{\text{disp},i}. \quad (8.8)$$

Then, the time evolution of the fast-evolving forces can be calculated exactly at every sub-step, of length Δt , while the time evolution of the slow-evolving force, namely the exchange repulsion, can be estimated with a Taylor expansion using the information available at the initial step, t_0 ,

$$\mathbf{F}_{\text{slow},i}(t_0 + k\Delta t) = \mathbf{F}_{\text{slow},i}(t_0) + \mathbf{F}'_{\text{slow},i}(t_0) \frac{k\Delta t}{1!} + \dots + \mathbf{F}_{\text{slow},i}^{(m)}(t_0) \frac{(k\Delta t)^m}{m!}, \quad (8.9)$$

and explicitly recalculated every n -th step, with sub-steps $k = 1, 2, \dots, n - 1$; as illustrated in the scheme of Figure 8.1.

The theory of multiple time-steps has several advantages if applied to EFP-MD. First, it is in principle generalizable to any number of forces, because it only requires an adequate grouping of forces and careful selection of their time steps. In this case,

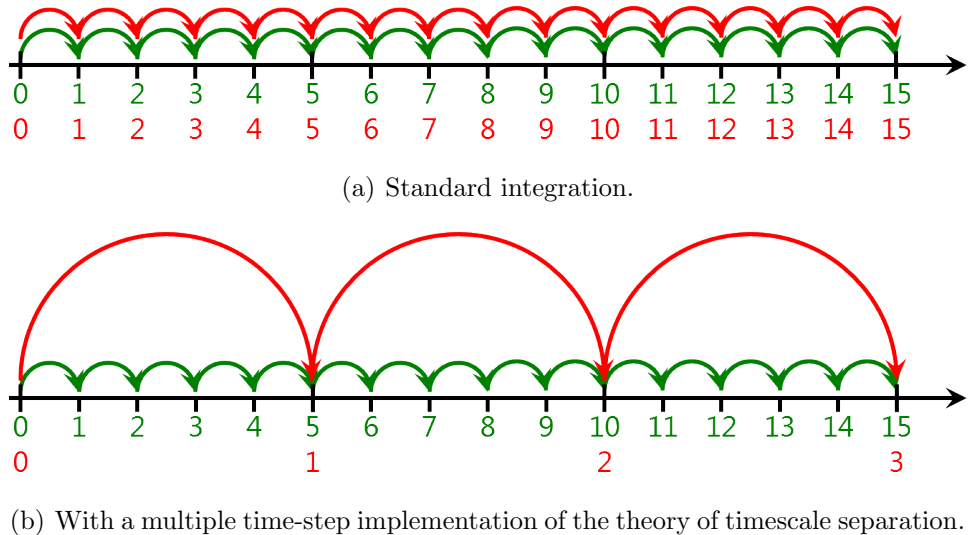


Figure 8.1. Illustration representing the idea of the multiple time-step theory of timescale separation. In the example of (b), by separating the time evolution in multiple time-steps polarization (green) is calculated at every step, whereas the exchange repulsion (red) is calculated every five steps and estimated in all other steps

it has been formulated to avoid recalculation of the XR energy. But it may be applied to the more intricate CT term, when implemented on LibEFP/EFPMD, or, if the system allows it, it might be used for the polarization term too.

Timescale separation methods have proven useful in reducing the computational cost of MD simulations by a factor of three to eight, in small or medium systems [252]. However, in large systems, it is probable that the implementation of cut-off distances for expensive interactions provides a better way to accelerate MD computations. Still, a one-third reduction in the computational cost of the exchange repulsion is just what is required to make it as efficient as polarization.

Besides, no additional hardware resources are required, except for a small increase in memory use, due to the storage of XR gradients required for the Taylor expansion [254]. Therefore, the computational requirements of a timescale-separated EFPMD simulation are similar to those of a standard run, extending the range of applicability of the EFP method in MD.

Finally, a basic implementation of the theory of timescale separation in EFPMD may be easily parallelized.

8.3 Computational Details

By exploiting the inherent timescale separation between each of the EFP energy contributions, EFP-MD simulations could be accelerated. However, that idea works under the assumption that the forces due to the exchange repulsion can be separated from the other components of the EFP force. Such separation of forces is applicable only if the time-evolution of the separated force shows slower fluctuations.

A methodology that can illustrate how the energy components of EFP-MD evolve in time must be formulated to test that idea. Consequently, EFP-MD simulations are performed in LibEFP/EFPMD employing the full potential energy. The model system is a small sphere-like water cluster containing 8 water fragments, as shown in Figure 8.2. The trajectories are computed in the microcanonical ensemble. No PBC are applied. The overlap scheme is used to compute damping functions for all

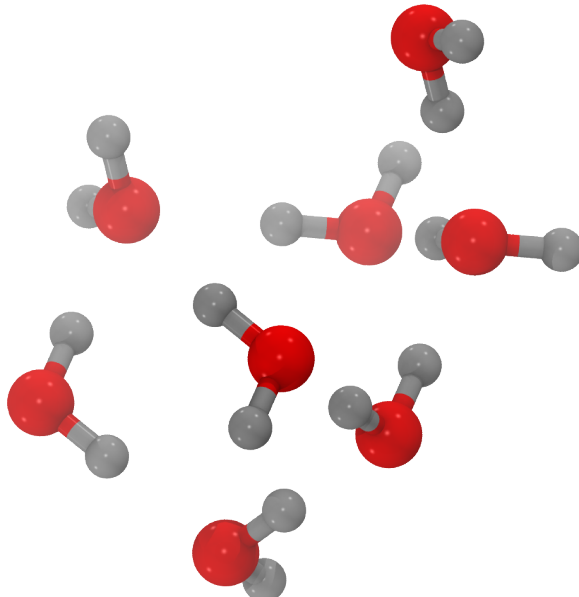


Figure 8.2. Small cluster of water including 8 fragments.

terms. 1 *ns* of simulation is carried out at steps of 2 *fs*. Analysis of the trajectory is performed only over the last *ps* of simulation.

8.4 Results

The total EFP energy during the final 1 *ps* of the trajectory described above is decomposed into each of its energy contributions. On the one hand, the time evolution of the electrostatics and polarization potentials are plotted superimposed on Figure 8.3. The *x*-axis in this plot shows the trajectory in time, on the bottom, and in steps, on the top. The left *y*-axis in orange gives the scale for the electrostatics energy, whereas the right *y*-axis in green shows the scale for the polarization energy.

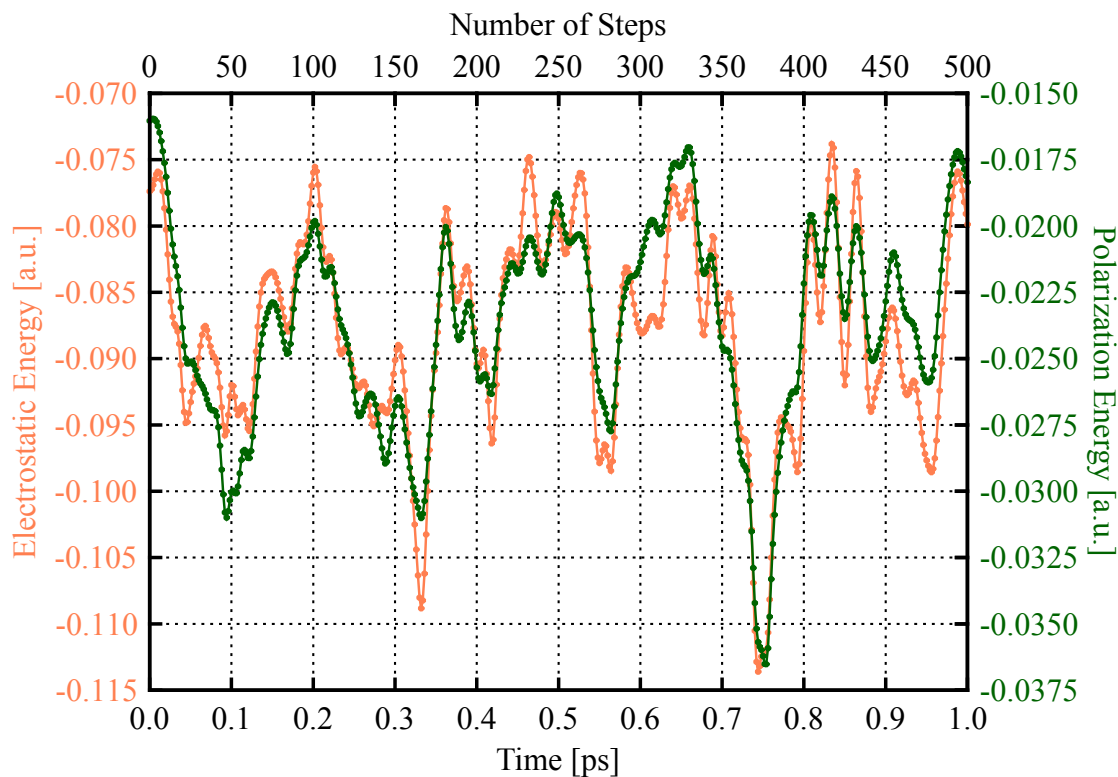


Figure 8.3. Comparison of the time-evolution of electrostatics (orange) and polarization (green). The fastest period elapses about 5 to 10 *fs*.

These scales have been chosen in a way that both curves maximally superimposed, to compare their characteristics.

Both curves on Figure 8.3 show very similar features. Oscillations in the electrostatics energy are a bit more sudden, while the evolution of the polarization energy looks slightly smoother. However, both curves seem to follow each other for the most part. This behavior points out that electrostatics and polarization evolve similarly in time.

As explained in Section 5.3, calculation of the polarization energy requires the multipole expansions computed with the electrostatics energy term. This is because the static field acting on a fragment depends on the electrostatic potential of all other fragments [162]. Therefore, the electrostatic and polarization potentials are intrinsically connected, explaining why the variations of both are related and share similar periods.

The fastest oscillations in electrostatics and polarization interactions elapse about 5 to 10 fs , and are visible in Figure 8.3 around 0.1 ps . This period is within the same order of magnitude of experimental measurements of typical vibrations of hydrogen bonds in liquid water. Visual analysis of the trajectory in VMD 1.9 reveals that one kind of molecular motion is mostly responsible for these fast oscillations. A hydrogen atom in the middle of two oxygens, bridged by a hydrogen bond, vibrates in and out of the vector connecting both oxygens, as depicted in Figure 8.4. This hydrogen-bond vibration-like mode is the fastest motion in the system, determining fluctuations in the electrostatics and polarization potentials.

Why do electrostatics and polarization energies evolve similarly? By construction, both types of potential are strongly dependent on the orientation of the interactions [149]. Both energy contributions can variate significantly when the interacting multipoles on different fragments rotate with respect to each other, especially when the geometry of the fragments is far from spherical. This hydrogen-bond motion reflects that characteristic: small variations on the orientation of water dimers produce

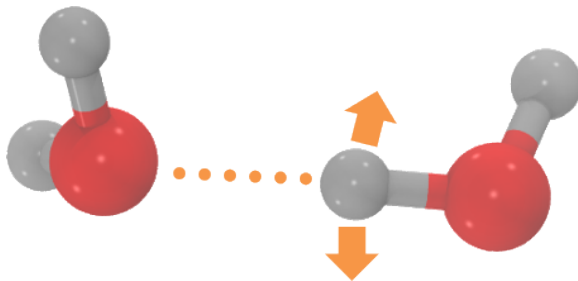


Figure 8.4. The hydrogen bond *vibration* is the fastest motion determining fluctuations in the electrostatics and polarization potentials.

the most important features in the time evolution of the electrostatics and polarization energies.

The time evolution of the dispersion and XR energies are plotted on Figure 8.5. The left *y*-axis in blue gives the scale for the dispersion energy, whereas the right *y*-axis in red shows the scale for the XR energy. Again, both curves on Figure 8.5 show a resembling behavior. In this case, the oscillations in the XR energy are sharper, while the dispersion energy looks much smoother. Similar to electrostatics and polarization, both curves on Figure 8.5 seem to follow each other. These observations indicate that dispersion and the exchange repulsion also evolve similarly in time.

Why do dispersion and the exchange repulsion evolve similarly? The dispersion coefficients are isotropic by construction, therefore diminishing the impact of molecular orientation on the dispersion energy [167]. Besides, the XR energy is calculated utilizing a representation of the wave function approximated with spherical Gaussian functions [162]. It appears that in the case of these water clusters, the XR energy is mildly dependent on orientation, too. Therefore, both energies depend more on translational, rather than rotational, degrees of freedom.

Now comparing Figures 8.3 and 8.5, dispersion and the exchange repulsion show longer periods of oscillation than electrostatics and polarization. It seems logical that the pair of energies with stronger dependences on orientation would evolve faster, considering that the fastest movement involves rotational oscillations of two water fragments. This observation is of significant importance, because it implies that the

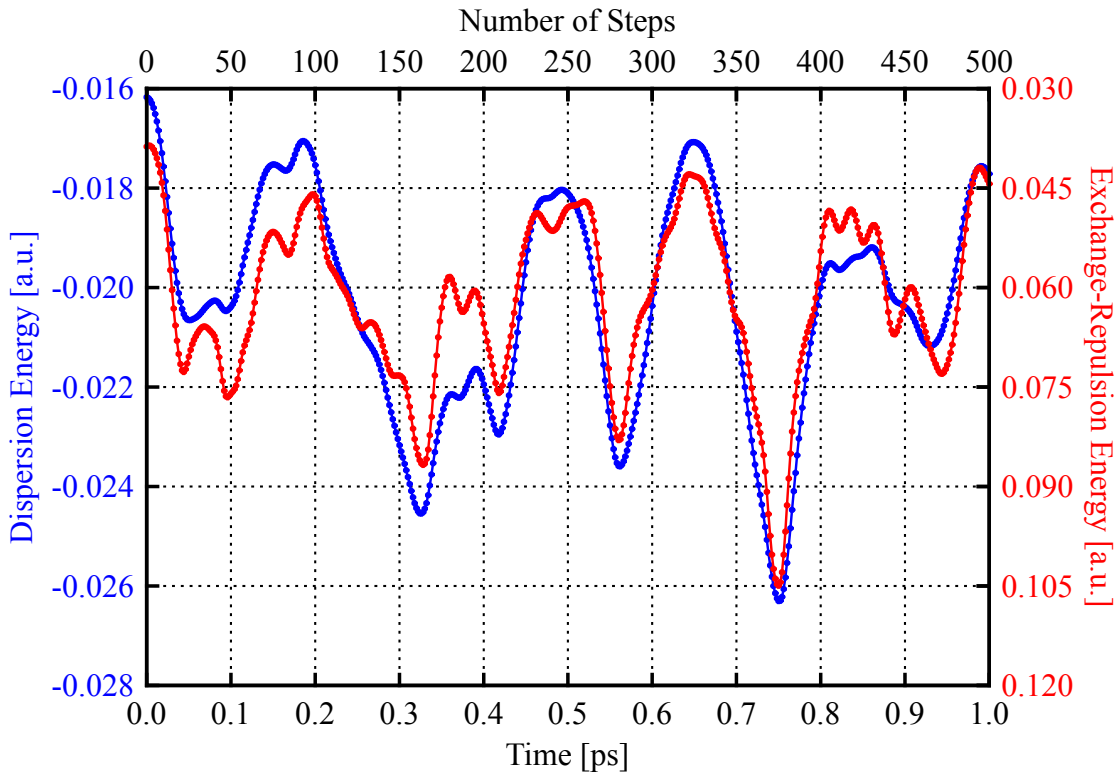


Figure 8.5. Comparison of the time-evolution of dispersion (blue) and the exchange repulsion (red). The fastest period elapses about 15 to 20 $f\text{s}$.

theory of timescale separations can be applied to reduce the computational cost of the exchange repulsion in water systems.

Finally, on Figure 8.6 each energy contribution is presented as a shaded area along the trajectory analyzed. First, it is obvious from this plot that electrostatics and the exchange repulsion have the largest absolute contributions to the EFP energy. In addition, electrostatics is negative, whereas the exchange repulsion is positive, meaning that the latter cancels out a significant portion of the former. Second, the fluctuations of the electrostatic energy are faster, and its absolute contribution is the most significant. Therefore it can be affirmed that the electrostatic forces are the main driver of the dynamics in EFP water. This affirmation is supported by observing

that the features of the black line on Figure 8.6, exhibiting the total potential energy of EFP, follow closely those of the orange curve, showing the electrostatics energy.

These effects are evident in small water clusters. However, different chemical systems may be driven by different types of intermolecular interactions. It is assumed that water is probably the most important model system, and thus no other systems are explored in this study. Nevertheless, internal consistency of the theory should be verified using other model systems, different than water. Good candidates for this tests are methane, benzene, and alcohol clusters; and their corresponding mixtures with water.

8.5 Implementation

An implementation of the multiple time-step theory of timescale separation would be based on Equation (8.9). If the code is written in the LibEFP library, it would require the creation of a keyword to enable the multiple time-step integration of the equations of motion for different energy terms. Instead of receiving a boolean values, such keyword, `enable_multi_time_steps [xr [pol [disp [elec]]]]`, could receive as arguments, the labels of the energy terms that would be computed with different time steps, i.e. `elec`, `pol`, `disp`, or `xr`.

Then, a keyword to specify the time step for each energy term would need to be created, for example: `time_step_xr <value>` or `time_step_pol <value>`. To simplify the following explanations, from now on the XR term will serve as the example of separated time step calculations. These time-step keywords would receive the length of their separated time steps as an argument: Δt on Equation (8.9), in femtoseconds. By default this value should be exactly the same as the one assigned as argument of the `time_step <value>` keyword. The separated time step must meet two conditions: it cannot be shorter than the fastest time step, and it must be a multiple of the fastest time step. If the forces of more than one EFP term are separated, then the slowest time step must be a multiple of the other separated time step. For instance, 1 *fs*, 2 *fs*, and 4 *fs*.

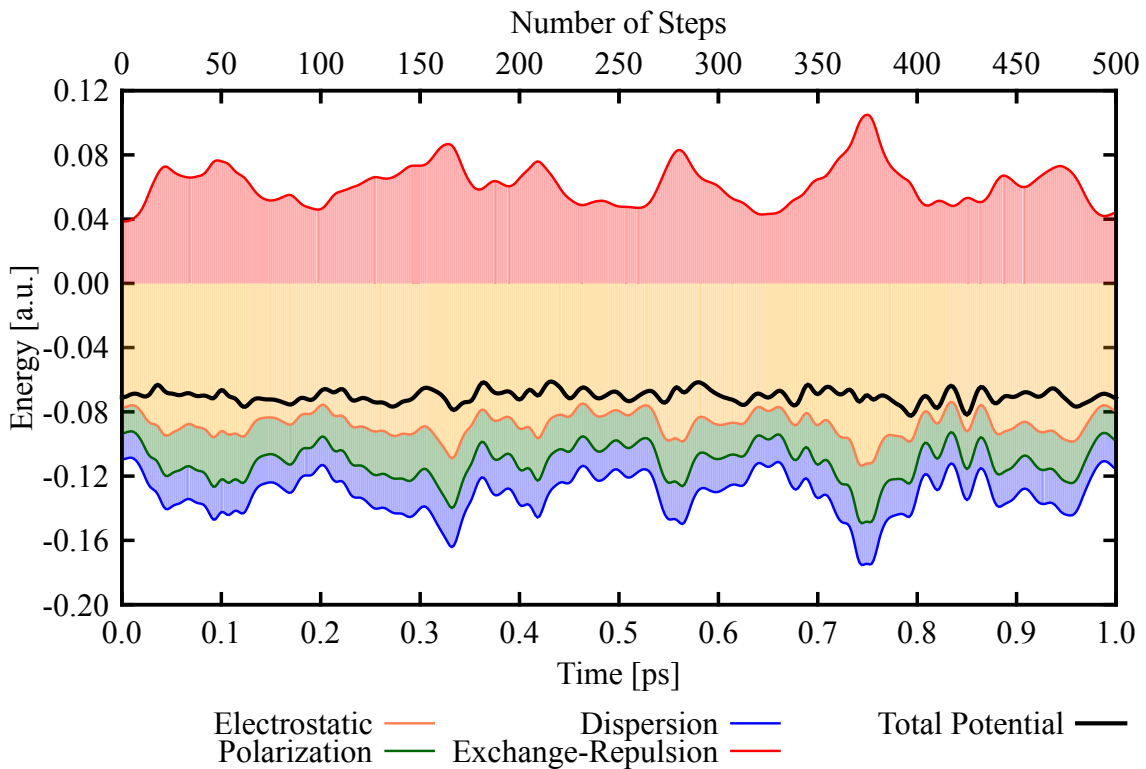


Figure 8.6. Comparison of the contributions of each energy term to the total energy. The shaded area represents each of the contributions to the total EFP potential energy. The black line shows the total energy along the trajectory. Features of the electrostatics energy are clearly visible in the total energy. Electrostatics is the main driver in EFP water dynamics.

There are two alternatives to the implementation of the `enable_multi_time_steps` [`xr [pol [disp [elec]]]`] keyword. The first one is to use it with a boolean argument, `enable_multi_time_steps [true|false]`. In this case, if set `true`, those energy terms with unspecified time steps should take by default the value given as argument of the `time_step <value>`, unless a different value is specified by the user through the `time_step_xr <value>` statement.

The second alternative is to use the `time_step_xr <value>` keyword only. This may be the most elegant option. In this case, the value of `time_step_xr` (and the

keywords corresponding to the other energy terms) is set by default to 0 or `false`, meaning that the exchange repulsion will be integrated using the fastest time step. Otherwise, if `time_step_xr <value>` is set to a value different than 0, then such value is the length of the separated time steps in femtoseconds.

Once a way of inputting the Δt , of Equation (8.9), is devised, the next stage involves the implementation of Equation (8.9). In principle, the Taylor expansion could be truncated at the first term, which means that the XR forces and torques are calculated at the first step and then left invariant for the length of the separated time step. Therefore, the storage of the forces and torques of the separated force, namely those of the exchange repulsion, would be required. Once stored they could be re-utilized at every fast step, until the end of the separated time step.

This implementation can be tested by comparing the analytic and numerical evolution of the separated energy and the total energy along a short trajectory. Such test could be carried out first on a helium dimer, where forces are more important than torques. A second test system would be the molecular hydrogen dimer, in which torques are already important. For more intensive tests, and for validation of the multiple time-step theory of timescale separation, water and methane clusters could be employed.

8.6 Summary

The discoveries gathered by this study prove that there is an inherent timescale separation between contributions to the EFP energy in water simulations. Evidently, dispersion and XR interactions have a longer periods of oscillation than electrostatics and polarization. The hydrogen-bond vibration is the fastest motion determining variations in the evolution of the electrostatics and polarization energies.

It is therefore implied that EFP-MD simulations can be accelerated by estimating the XR energy intermittently. The description of a possible implementation of the timescale separations theory for EFP-MD simulations in LibEFP/EFPMD is dis-

cussed. Once implemented, internal consistency of the theory should be verified using other model systems, different than water.

9. SUMMARY

This thesis addressed challenges in modern molecular modeling from two distinct theoretical perspectives: DFT and the EFP method. In the three chapters following the introduction, important problems in the field of DFT, such as the accurate description of charge transfer, dispersion, and excitation energies, were studied.

An assessment of how several functionals capture ground-state charge transfer and predict charge distributions in the lithium-benzene complex was presented in Chapter 2. This model system illustrated how the interplay of approximate functionals and charge-distribution schemes impacts the description of charge transfer resulting into drastically different qualitative interpretations depending on the combination of both.

Ground-state charge distributions display sharp features when state crossings occur. In spite of the existence of a state crossing that induces charge transfer in the model system, the crossing occurred in the repulsive region of the interaction curve, leaving the equilibrium region unaffected in hybrid functionals and HF. However, the equilibrium region was incorrectly described by pure functionals PBE and BLYP as a consequence of a crossing with an artificial state. Therefore, standard hybrid functionals were more useful in describing charge transfer in the lithium-benzene complex, because the gap is widened when the proportion of HF exchange is increased, eliminating the existence of the spurious state affecting pure functionals. Widening of the gap was a consequence of the stabilization of the occupied MOs and the destabilization of the virtual MOs.

While modeling state crossings is prone to errors when using single-reference methods, high computational cost might hinder the use of multi-reference or excited-state methods for larger systems relevant in materials science. This study motivated the

quest for more rigorous functionals capable of describing CT phenomena, or alternative computational schemes.

Chapter 3 treated the topic of dispersion in DFT. An overview of the current alternatives to include dispersion in standard functionals was presented. Among them, one of the most rigorous is the model by Tkatchenko and Scheffler: a pair-wise dispersion correction that depends on the chemical environment and polarizability of each atom. In the TS-vdW model the environment dependence is derived from Hirshfeld partitioning of the electron density. A detailed description of this method, previously unavailable in the literature, was presented.

An implementation of the TS-vdW correction was introduced and explained as well. The TS-vdW library is a portable *C* code that can be connected to different materials-modeling packages. The software has several advantages. The execution is independent from the basis functions. It uses the density as its unique input. It can be interfaced with different materials-modeling packages in a simple manner. The dispersion correction can be added after the total energy is obtained or applied self-consistently. The gradient of the van der Waals energy is also implemented, allowing for geometry optimization and MD simulations. The standard scaling of DFT calculations is unaffected by the TS-vdW correction.

Several aspects of this work could be further explored in future research. The dispersion energy, potential, and gradients were studied and implemented. However, the inclusion of the van der Waals Hessian is important for frequency calculations and thermochemistry. In addition, the implementation of the many-body dispersion model could prove useful. Another important step would be the efficient parallelization of the library. Finally, this modular implementation was meant to be interfaced with other computational chemistry packages. NWChem, Psi4, Q-Chem, and GAMESS were proposed as good candidates.

Two types of approximated functionals for excitation energies were introduced in Chapter 4. One, a mostly unexplored class of LDA-based, one-parameter, standard-

hybrid approximations; the other, a completely-new family of LDA-based, three-parameter, range-separated-hybrid approximations.

Initial examination of these adiabatic functionals showed promising results for linear-response properties. The LDA0 and LDA1 models proved that non-local exchange corrections to the LDA can produce excitation energies comparable to functionals such as PBE0 or B3LYP. Excitation energies of the CAM-LDA0 functional were comparable to those of CAM-B3LYP, with the advantage of a reduced computational cost due to faster a convergence of the self-consistent field procedure. Although, an assessment of the description of geometries in the excited states with these functionals remains undone, the results gathered suggest that a portion of non-local exchange is a dominant factor for the enhancement of excitation energies over generalized gradient corrections.

In principle, different chemical systems require different amounts of non-local HF exchange, which could motivate further work on transforming the parameters into purely *ab initio* quantities. It was suggested that discretion and insight by the user are required to properly set up the correct amount of exchange, and related quantities. Such judgment could be enriched by knowledge deduced from reliable *ab initio* calculations and experimental measurements.

Chapter 5 transitioned to the EFP method and provided an inclusive, fully-detailed, and up-to-date description of the method. The final three chapters above this summary engage important challenges in the vastly unexplored field of EFP-MD: the determination of the melting point of the EFP water model, analysis of the computational cost of MD simulations with the EFP method, and alternatives to achieve better efficiency when performing these simulations.

In Chapter 6 the melting point of the EFP water model was determined in the range between 360 *K* and 365 *K*, as a result of an exploration of the the thermodynamic equilibrium between liquid water and ice, performed with MD using the EFP method.

Interaction energies between fragments were found to be slightly overestimated in the EFP water model. Based on evidence of over-attractive hydrogen bonding in water, it was suggested that too-strong electrostatic interactions in the EFP water model require additional energy to be broken, therefore pushing the melting temperature to values that are too high.

It was also found that equilibrium distances in EFP water tend to be longer than they should. Peaks in the RDF of EFP water are displaced to longer distances, and densities are lower than in experiments. The computationally-expensive CT term is omitted in this water potential, and instead it is replaced with an electrostatics term with parameters derived with a small basis set. Stronger electrostatics usually overcomes well the lack of charge transfer. However, at short range the Pauli repulsion prevails, keeping fragments apart from each other. At short separations, the fragment potential becomes too repulsive.

This study motivated the investigation of more efficient ways to include charge transfer in EFP-MD. It also opens the door to a wider exploration of the ice-liquid equilibrium. The inclusion of solutes, to investigate their effect on the melting point would be a good place to start. There is also the possibility to run longer trajectories to study the freezing process. An analysis of the impact of each EFP energy term on the melting temperature could also be of general interest.

A computational efficiency study of EFP-MD was presented in Chapter 7, where small clusters of water ranging from 4 to 1,024 fragments were employed as model systems. Switching off all but one of the energy terms of the EFP force field at a time, EFP-MD trajectories were performed and timed for each EFP energy term. Timings for each contribution across all system sizes were analyzed concluding that the scaling of EFP-MD calculations depends on the square of the number of fragments.

The exchange repulsion term was found the most computationally expensive of all, being at least three times more demanding than polarization, the second most intricate contribution to compute. EFP-MD calculations could be made more efficient if the cost of the exchange repulsion energy term would be reduced. Hence,

this investigation motivated the search for alternative methodologies to compute the exchange-repulsion energy.

The information gathered in Chapter 8 proved that there is an inherent timescale separation between each contribution to the EFP interaction energy. Dispersion and exchange-repulsion interactions have a longer period than electrostatics and polarization. The hydrogen bond vibration-like mode was the fastest motion determining variations in the electrostatics and polarization energies of small clusters of water.

It was implied that EFP-MD simulations can be accelerated by estimating the exchange-repulsion energy intermittently. Therefore, a timescale separation of the exchange-repulsion term in EFP is formally derived. The description of a possible implementation of the timescale separations theory for EFP-MD simulations in LibEFP/EFPMD was discussed. Once implemented, internal consistency of the theory should be verified using other model systems, different than water.

Throughout the course of my doctorate, I also worked on several other studies which are not included in this thesis. Most of these other projects fall within the broad field of computational chemistry applications to pharmaceutical and atmospheric sciences. They were left out of this document because the main focus of my doctoral research was theoretical chemistry. Additionally, some of these projects were carried out in collaboration. However, they are still worth a brief mention in this closing chapter.

There were three studies related to applications on pharmaceutical sciences. The first of these was an analysis on the structural transformation due to water absorption in chitosan nano-hydrogels performed using all-atom classical MD [256]. Hydrogels are materials capable of absorbing water within networks of entangled hydrophilic polymers, and have been widely studied for their use in pharmaceutical products. However, the mechanistic details that explain water-absorbent features in hydrogels are not well understood. In this investigation, it was found that the swelling behavior of nano-scaled chitosan is pH-dependent, and that it is considerably more limited

than that of larger-scale hydrogels. Thus, this study suggests that properties of nano-hydrogels are significantly different from those of larger hydrogels.

The second project, carried out in collaboration, was an exploration on how chemically diverse substituents influence the effectiveness of novel cellulose polymers as crystallization inhibitors [257]. The bioavailability of a high percentage of new drug candidates is limited by their poor solubility. The use of the amorphous form of the drug is a good strategy to improve their solubility. However, the amorphous state is unstable, and the drug will crystallize over time, losing its solubility advantage. Polymers are used to stabilize amorphous formulations, and to maintain high supersaturations following dissolution of the formulation. While experimental studies with commercial polymers have shown differences in polymer effectiveness, the molecular mechanism of stabilization was still unclear, making the rational design of novel polymers challenging. Therefore, MD and quantum chemical calculations were used to inquire how chemical diversity modifies the polymer conformation and dynamics. These results helped to explain why two polymers with similar chemical groups may show opposite effectiveness due to strong intramolecular non-covalent interactions.

In another collaboration, MD simulations were used to assist the evaluation of the ability of several bile salts to maintain supersaturated aqueous solutions of three model drug compounds: celecoxib, nevirapine and fibanserin [258]. Bile salts are natural surfactants present in the human gastrointestinal tract. Therefore, it is essential to consider their effect on the dissolution and crystallization tendency of oral drug formulations. Although recently it has been shown that sodium taurocholate, a common bile salt, can delay nucleation of certain compounds, there is limited information about the crystallization inhibition properties of other bile salts. Experimentally, most bile salts included in this study delayed nucleation. However, their inhibitory effects varied depending on the structure and concentration of the bile salt and the drug. MD simulations indicated that van der Waals and hydrogen-bonding interactions occurred between the drug and bile salts, with variations in different systems.

These results are important to better understand the crystallization tendency of orally delivered poorly water-soluble compounds *in vivo*.

Transitioning into the applications to atmospheric chemistry, the photochemical degradation process of isoprene carbonyl nitrates was investigated to better understand their fate. Carbonyl nitrates are produced from NO₃-initiated isoprene oxidation, constituting a potentially important NO_X reservoir. In one collaborative project, the theoretical UV-absorption spectra of an isoprene carbonyl nitrate, methacrolein, and n-butyl nitrate in the gas phase were calculated and correlated, using TD-DFT [259]. In a second collaboration, the possible reaction paths of isobutyl nitrate in acidic water were explored using DFT [260].

REFERENCES

REFERENCES

- [1] Carlos H. Borca, Lyudmila V. Slipchenko, and Adam Wasserman. Ground-State Charge Transfer: Lithium–Benzene and the Role of Hartree–Fock Exchange. *J. Phys. Chem. A*, 120(41):8190–8198, 2016.
- [2] Martín A. Mosquera, Carlos H. Borca, Mark A. Ratner, and George C. Schatz. Connection between Hybrid Functionals and Importance of the Local Density Approximation. *J. Phys. Chem. A*, 120(9):1605–1612, 2016.
- [3] Kurt R. Brorsen, Soohaeng Yoo Willow, Sotiris S. Xantheas, and Mark S. Gordon. The Melting Temperature of Liquid Water with the Effective Fragment Potential. *J. Phys. Chem. Lett.*, 6(18):3555–3559, 2015.
- [4] John P. Perdew. Climbing the Ladder of Density Functional Approximations. *Mater. Res. Soc. Bull.*, 38(09):743–750, 2013.
- [5] Mildred S. Dresselhaus and Iran L. Thomas. Alternative Energy Technologies. *Nature*, 414(6861):332–337, 2001.
- [6] Ottmar Edenhofer, Ramón Pichs-Madruga, Youba Sokona, Kristin Seyboth, Patrick Matschoss, Susanne Kadner, Timm Zwickel, Patrick Eickemeier, Gerrit Hansen, Steffen Schlmer, and Christoph von Stechow. IPCC Special Report on Renewable Energy Sources and Climate Change Mitigation. Technical report, Intergovernmental Panel on Climate Change, Geneva (Switzerland). Working Group III, 2011.
- [7] John B. Goodenough, Héctor D. Abruña, and Michelle V. Buchanan. *Basic Research Needs for Electrical Energy Storage: Report of the Basic Energy Sciences Workshop for Electric Energy Storage*. US Department of Energy, Office of Basic Energy Science, 2007.
- [8] Kay Hyeok An, Won Seok Kim, Young Soo Park, J-M. Moon, Dong Jae Bae, Seong Chu Lim, Young Seak Lee, and Young Hee Lee. Electrochemical Properties of High-power Supercapacitors Using Single-walled Carbon Nanotube Electrodes. *Adv. Funct. Mater.*, 11(5):387–392, 2001.
- [9] Brian E. Conway. *Electrochemical Supercapacitors: Scientific Fundamentals and Technological Applications (POD)*. Kluwer Academic/Plenum: New York, 1999.
- [10] Oleg N. Kalugin, Vitaly V. Chaban, Valentin V. Loskutov, and Oleg V. Prezhdo. Uniform Diffusion of Acetonitrile Inside Carbon Nanotubes Favors Supercapacitor Performance. *Nano Lett.*, 8(8):2126–2130, 2008.

- [11] Youngseon Shim and Hyung J. Kim. Nanoporous Carbon Supercapacitors in an Ionic Liquid: A Computer Simulation Study. *ACS Nano*, 4(4):2345–2355, 2010.
- [12] Youngseon Shim, Youn Joon Jung, and Hyung J. Kim. Graphene-based Supercapacitors: A Computer Simulation Study. *J. Phys. Chem. C*, 115(47):23574–23583, 2011.
- [13] Guang Feng and Peter T. Cummings. Supercapacitor Capacitance Exhibits Oscillatory Behavior as a Function of Nanopore Size. *J. Phys. Chem. Lett.*, 2(22):2859–2864, 2011.
- [14] Errol Lewars. *Computational Chemistry*. Springer, 2010.
- [15] Pierre Hohenberg and Walter Kohn. Inhomogeneous Electron Gas. *Phys. Rev.*, 136(3B):B864, 1964.
- [16] Walter Kohn and Lu Jeu Sham. Self-consistent Equations Including Exchange and Correlation Effects. *Phys. Rev.*, 140(4A):A1133, 1965.
- [17] Frank Jensen. *Introduction to Computational Chemistry*. Wiley.com, 2007.
- [18] Michael M. Thackeray, Christopher Wolverton, and Eric D. Isaacs. Electrical Energy Storage for Transportation – Approaching the Limits of, and Going Beyond, Lithium-ion Batteries. *Energy Environ. Sci.*, 5(7):7854–7863, 2012.
- [19] Mel Levy. Electron Densities in Search of Hamiltonians. *Phys. Rev. A*, 26(3):1200, 1982.
- [20] Mel Levy and John P. Perdew. The Constrained Search Formulation of Density Functional Theory. In *Density Functional Methods in Physics*, pages 11–30. Springer, 1985.
- [21] Enrico Fermi and Edoardo Amaldi. Le Orbite Infinti s Degli Elementi. *Accad. Ital. Rome*, 6(119):17–149, 1934.
- [22] John P. Perdew and Alex Zunger. Self-interaction Correction to Density-functional Approximations for Many-electron Systems. *Phys. Rev. B*, 23(10):5048, 1981.
- [23] Yingkai Zhang and Weitao Yang. A Challenge for Density Functionals: Self-interaction Error Increases for Systems with a Noninteger Number of Electrons. *J. Chem. Phys.*, 109(7):2604–2608, 1998.
- [24] Paula Mori-Sánchez, Aron J. Cohen, and Weitao Yang. Many-electron Self-interaction Error in Approximate Density Functionals. *J. Chem. Phys.*, 125(20):201102, 2006.
- [25] Adrienn Ruzsinszky, John P. Perdew, Gábor I. Csonka, Oleg A. Vydrov, and Gustavo E. Scuseria. Spurious Fractional Charge on Dissociated Atoms: Pervasive and Resilient Self-interaction Error of Common Density Functionals. *J. Chem. Phys.*, 125(19):194112, 2006.
- [26] Kieron Burke. Perspective on Density Functional Theory. *J. Chem. Phys.*, 136(15):150901, 2012.

- [27] Aron J. Cohen, Paula Mori-Sánchez, and Weitao Yang. Insights into Current Limitations of Density Functional Theory. *Science*, 321(5890):792–794, 2008.
- [28] Lindsay E. Roy, Elena Jakubikova, M. Graham Guthrie, and Enrique R. Batista. Calculation of One-electron Redox Potentials Revisited. Is It Possible to Calculate Accurate Potentials with Density Functional Methods? *J. Phys. Chem. A*, 113(24):6745–6750, 2009.
- [29] Paula Mori-Sánchez, Aron J. Cohen, and Weitao Yang. Localization and Delocalization Errors in Density Functional Theory and Implications for Band-gap Prediction. *Phys. Rev. Lett.*, 100(14):146401, 2008.
- [30] Aron J. Cohen, Paula Mori-Sánchez, and Weitao Yang. Fractional Charge Perspective on the Band Gap in Density-functional Theory. *Phys. Rev. B*, 77(11):115123, 2008.
- [31] John P. Perdew, Robert G. Parr, Mel Levy, and Jose L. Balduz Jr. Density-functional Theory for Fractional Particle Number: Derivative Discontinuities of the Energy. *Phys. Rev. Lett.*, 49(23):1691, 1982.
- [32] Jonathan Nafziger and Adam Wasserman. Density-Based Partitioning Methods for Ground-State Molecular Calculations. *J. Phys. Chem. A*, 118(36):7623–7639, 2014.
- [33] John P. Perdew and Karla Schmidt. Jacob’s Ladder of Density Functional Approximations for the Exchange-correlation Energy. In Victor E. Van Doren, Christian Van Alsenoy, and Paul Geerlings, editors, *Density Functional Theory and Its Applications to Materials*, pages 1–20. American Institute of Physics, Melville, NY, 2001.
- [34] Zhou Zhengyu, Xu Jian, Zhang Chuansong, Zhou Xingming, Du Dongmei, and Zhang Kezhong. Theoretical Study of Inner-sphere Reorganization Energy of the Electron Transfer Reactions Between M-C₆H₆ and M⁺-C₆H₆ Complexes in the Gas Phase: An *Ab Initio* Computation. *J. Mol. Struct.: THEOCHEM*, 469(1):1–6, 1999.
- [35] James M. Vollmer, Anil K. Kandalam, and Larry A. Curtiss. Lithium-benzene Sandwich Compounds: A Quantum Chemical Study. *J. Phys. Chem. A*, 106(41):9533–9537, 2002.
- [36] Hong Seok Kang. Density Functional Study of Lithium-aromatic Sandwich Compounds and Their Crystals. *J. Phys. Chem. A*, 109(3):478–483, 2005.
- [37] Adolfo Ferre-Vilaplana. Storage of Hydrogen Adsorbed on Alkali Metal Doped Single-layer All-carbon Materials. *J. Phys. Chem. C*, 112(10):3998–4004, 2008.
- [38] Jose Ignacio Martinez, Iván Cabria, María J. López, and Julio A. Alonso. Adsorption of Lithium on Finite Graphitic Clusters. *J. Phys. Chem. C*, 113(3):939–941, 2008.
- [39] Michael S. Marshall, Ryan P. Steele, Kanchana S. Thanthiriwatte, and C. David Sherrill. Potential Energy Curves for Cation-π Interactions: Off-Axis Configurations Are Also Attractive. *J. Phys. Chem. A*, 113(48):13628–13632, 2009.

- [40] Roberto Olivares-Amaya, Michael Stopa, Xavier Andrade, Mark A. Watson, and Alán Aspuru-Guzik. Anion Stabilization in Electrostatic Environments. *J. Phys. Chem. Lett.*, 2(7):682–688, 2011.
- [41] Sergey A. Varganov, Pavel V. Avramov, and Sergey G. Ovchinnikov. *Ab Initio* Calculations of Endo-and Exohedral C₆₀ Fullerene Complexes with Li⁺ Ion and the Endohedral C₆₀ Fullerene Complex with Li₂ Dimer. *Phys. Solid State*, 42(2):388–392, 2000.
- [42] Thomas A. Baker and Martin Head-Gordon. Modeling the Charge Transfer Between Alkali Metals and Polycyclic Aromatic Hydrocarbons Using Electronic Structure Methods. *J. Phys. Chem. A*, 114(37):10326–10333, 2010.
- [43] Pablo A. Denis and Federico Iribarne. C_{2v} or C_{6v}: Which Is the Most Stable Structure of the Benzene-lithium Complex? *Chem. Phys. Lett.*, 573:15–18, 2013.
- [44] James B. Foresman and ÅEleen. Frisch. *Exploring Chemistry with Electronic Structure Methods*. Gaussian, Inc.: Pittsburgh, PA, 1996.
- [45] Yihan Shao, Laszlo Fusti Molnar, Yousung Jung, Jorg Kussmann, Christian Ochsenfeld, Shawn T. Brown, Andrew T.B. Gilbert, Lyudmila V. Slipchenko, Sergey V. Levchenko, Darragh P. O'Neill, and et al. Advances in Methods and Algorithms in a Modern Quantum Chemistry Program Package. *Phys. Chem. Chem. Phys.*, 8(27):3172–3191, 2006.
- [46] Yihan Shao, Zhengting Gan, Evgeny Epifanovsky, Andrew T.B. Gilbert, Michael Wormit, Joerg Kussmann, Adrian W. Lange, Andrew Behn, Jia Deng, Xintian Feng, and et al. Advances in Molecular Quantum Chemistry Contained in the Q-chem 4 Program Package. *Mol. Phys.*, 113(2):184–215, 2015.
- [47] Anna I. Krylov and Peter M. W. Gill. Q-Chem: An Engine for Innovation. *Wiley Interdiscip. Rev.: Comput. Mol. Sci.*, 3(3):317–326, 2013.
- [48] Andrew T. B. Gilbert, Nicholas A. Besley, and Peter M. W. Gill. Self-Consistent Field Calculations of Excited States Using the Maximum Overlap Method (MOM). *J. Phys. Chem. A*, 112(50):13164–13171, 2008.
- [49] John P. Perdew, Kieron Burke, and Matthias Ernzerhof. Generalized Gradient Approximation Made Simple. *Phys. Rev. Lett.*, 77(18):3865–3868, 1996.
- [50] Carlo Adamo, Gustavo E. Scuseria, and Vincenzo Barone. Accurate Excitation Energies from Time-dependent Density Functional Theory: Assessing the PBE0 Model. *J. Chem. Phys.*, 111(7):2889–2899, 1999.
- [51] Carlo Adamo and Vincenzo Barone. Inexpensive and Accurate Predictions of Optical Excitations in Transition-metal Complexes: the TDDFT/PBE0 route. *Theor. Chem. Acc.*, 105(2):169–172, 2000.
- [52] Yves A. Bernard, Yihan Shao, and Anna I. Krylov. General Formulation of Spin-flip Time-dependent Density Functional Theory Using Non-collinear Kernels: Theory, Implementation, and Benchmarks. *J. Chem. Phys.*, 136(20):204103, 2012.

- [53] Thomas M. Henderson, Benjamin G. Janesko, and Gustavo E. Scuseria. Generalized Gradient Approximation Model Exchange Holes for Range-separated Hybrids. *J. Chem. Phys.*, 128(19):194105, 2008.
- [54] John P. Perdew, Matthias Ernzerhof, and Kieron Burke. Rationale for Mixing Exact Exchange with Density Functional Approximations. *J. Chem. Phys.*, 105(22):9982–9985, 1996.
- [55] Fenglai Liu, Emil Proynov, Jian-Guo Yu, Thomas R. Furlani, and Jing Kong. Comparison of the Performance of Exact-exchange-based Density Functional Methods. *J. Chem. Phys.*, 137(11):114104, 2012.
- [56] Burkhard Miehlich, Andreas Savin, Hermann Stoll, and Heinzwerner Preuss. Results Obtained with the Correlation Energy Density Functionals of Becke and Lee, Yang and Parr. *Chem. Phys. Lett.*, 157(3):200–206, 1989.
- [57] Axel D. Becke. Density-functional Thermochemistry. III. The Role of Exact Exchange. *J. Chem. Phys.*, 98(7):5648–5652, 1993.
- [58] Takeshi Yanai, David P. Tew, and Nicholas C. Handy. A New Hybrid Exchange-correlation Functional Using the Coulomb-attenuating Method (CAM-B3LYP). *Chem. Phys. Lett.*, 393(1):51–57, 2004.
- [59] Axel D. Becke. Density-functional Exchange-energy Approximation with Correct Asymptotic Behavior. *Phys. Rev. A*, 38(6):3098, 1988.
- [60] Chengteh Lee, Weitao Yang, and Robert G. Parr. Development of the Colle-Salvetti Correlation-energy Formula into a Functional of the Electron Density. *Phys. Rev. B*, 37(2):785, 1988.
- [61] John Clarke Slater. *The Self-consistent Field for Molecules and Solids*, volume 4. McGraw-Hill New York, 1974.
- [62] Seymour H. Vosko, Leslie Wilk, and Marwan Nusair. Accurate Spin-dependent Electron Liquid Correlation Energies for Local Spin Density Calculations: A Critical Analysis. *Can. J. Phys.*, 58(8):1200–1211, 1980.
- [63] Christian Møller and Milton S. Plesset. Note on an Approximation Treatment for Many-electron Systems. *Phys. Rev.*, 46(7):618, 1934.
- [64] John A. Pople, Krishnan Raghavachari, H. Bernhard Schlegel, and J. Stephen Binkley. Electron Correlation Theories and Their Application to the Study of Simple Reaction Potential Surfaces. *Int. J. Quantum Chem.*, 14(5):545–560, 1978.
- [65] Rodney J. Bartlett and George D. Purvis. Many-body Perturbation Theory, Coupled-pair Many-electron Theory, and the Importance of Quadruple Excitations for the Correlation Problem. *Int. J. Quantum Chem.*, 14(5):561–581, 1978.
- [66] John F. Stanton and Rodney J. Bartlett. The Equation of Motion Coupled-cluster Method. A Systematic Biorthogonal Approach to Molecular Excitation Energies, Transition Probabilities, and Excited State Properties. *J. Chem. Phys.*, 98(9):7029–7039, 1993.

- [67] Marcel Nooijen and Rodney J. Bartlett. Equation of Motion Coupled Cluster Method for Electron Attachment. *J. Chem. Phys.*, 102(9):3629–3647, 1995.
- [68] Anna I. Krylov. Equation-of-motion Coupled-cluster Methods for Open-shell and Electronically Excited Species: The Hitchhiker’s Guide to Fock Space. *Annu. Rev. Phys. Chem.*, 59:433–462, 2008.
- [69] Robert S. Mulliken. Electronic Population Analysis on LCAO–MO Molecular Wave Functions. I. *J. Chem. Phys.*, 23:1833, 1955.
- [70] Alan E. Reed, Robert B. Weinstock, and Frank Weinhold. Natural Population Analysis. *J. Chem. Phys.*, 83:735, 1985.
- [71] Curt M. Breneman and Kenneth B. Wiberg. Determining Atom-centered Monopoles from Molecular Electrostatic Potentials. The Need for High Sampling Density in Formamide Conformational Analysis. *J. Comput. Chem.*, 11(3):361–373, 1990.
- [72] Alan E. Reed, Larry A. Curtiss, and Frank Weinhold. Intermolecular Interactions from a Natural Bond Orbital, Donor-acceptor Viewpoint. *Chem. Rev.*, 88(6):899–926, 1988.
- [73] Dongwook Kim, Shaowen Hu, P. Tarakeshwar, Kwang S. Kim, and James M. Lisy. Cation–Π Interactions: A Theoretical Investigation of the Interaction of Metallic and Organic Cations with Alkenes, Arenes, and Heteroarenes. *J. Phys. Chem. A*, 107(8):1228–1238, 2003.
- [74] Jiří Čížek and Josef Paldus. Stability Conditions for the Solutions of the Hartree-Fock Equations for Atomic and Molecular Systems. Application to the Pielectron Model of Cyclic Polyenes. *J. Chem. Phys.*, 47(10):3976–3985, 1967.
- [75] Qin Wu and Troy Van Voorhis. Constrained Density Functional Theory and Its Application in Long-range Electron Transfer. *J. Chem. Theory Comput.*, 2(3):765–774, 2006.
- [76] Troy Van Voorhis, Tim Kowalczyk, Benjamin Kaduk, Lee-Ping Wang, Chiao-Lun Cheng, and Qin Wu. The Diabatic Picture of Electron Transfer, Reaction Barriers, and Molecular Dynamics. *Annu. Rev. Phys. Chem.*, 61(1):149–170, 2010.
- [77] Kimihiko Hirao. *Recent Advances in Multireference Methods*, volume 4. World Scientific, 1999.
- [78] Laurent Manceron and Lester Andrews. Infrared Spectra and Structures of Lithium-benzene and Lithium-dibenzene Complexes in Solid Argon. *J. Am. Chem. Soc.*, 110(12):3840–3846, 1988.
- [79] Larry A. Curtiss, Paul C. Redfern, Krishnan Raghavachari, Vitaly Rassolov, and John A. Pople. Gaussian-3 Theory Using Reduced Møller-Plesset Order. *J. Chem. Phys.*, 110(10):4703–4709, 1999.
- [80] Jiří Klimeš and Angelos Michaelides. Perspective: Advances and Challenges in Treating van der Waals Dispersion Forces in Density Functional Theory. *J. Chem. Phys.*, 137(12):120901, 2012.

- [81] Sándor Kristyán and Péter Pulay. Can (Semi)Local Density Functional Theory Account for the London Dispersion Forces? *Chem. Phys. Lett.*, 229(3):175–180, 1994.
- [82] Pavel Hobza, Tomáš Reschel, et al. Density Functional Theory and Molecular Clusters. *J. Comput. Chem.*, 16(11):1315–1325, 1995.
- [83] José M. Pérez-Jordá and A. D. Becke. A Density-functional Study of van der Waals Forces: Rare Gas Diatomics. *Chem. Phys. Lett.*, 233(1–2):134–137, 1995.
- [84] José M. Pérez-Jordá, Emilio San-Fabián, and Angel J. Pérez-Jiménez. Density-functional Study of van der Waals Forces on Rare-gas Diatomics: Hartree–Fock Exchange. *J. Chem. Phys.*, 110(4):1916–1920, 1999.
- [85] Stefan Grimme. Density Functional Theory with London Dispersion Corrections. *Wiley Interdisciplinary Reviews: Computational Molecular Science*, 1(2):211–228, 2011.
- [86] Alexandre Tkatchenko, Lorenz Romaner, Oliver T. Hofmann, Egbert Zojer, Claudia Ambrosch-Draxl, and Matthias Scheffler. van der Waals Interactions between Organic Adsorbates and at Organic/Inorganic Interfaces. *MRS Bull.*, 35(06):435–442, 2010.
- [87] C. David Sherrill. Frontiers in Electronic Structure Theory. *J. Chem. Phys.*, 132(11):110902, 2010.
- [88] Yan Zhao, , and Donald G. Truhlar. Density Functionals for Noncovalent Interaction Energies of Biological Importance. *J. Chem. Theory Comput.*, 3(1):289–300, 2007.
- [89] O. Anatole von Lilienfeld, Ivano Tavernelli, Ursula Rothlisberger, and Daniel Sebastiani. Optimization of Effective Atom Centered Potentials for London Dispersion Forces in Density Functional Theory. *Phys. Rev. Lett.*, 93:153004, 2004.
- [90] Y. Y. Sun, Yong-Hyun Kim, Kyuho Lee, and S. B. Zhang. Accurate and Efficient Calculation of van der Waals Interactions within Density Functional Theory by Local Atomic Potential Approach. *J. Chem. Phys.*, 129(15):154102, 2008.
- [91] Stefan Grimme. Accurate Description of van der Waals Complexes by Density Functional Theory Including Empirical Corrections. *J. Comput. Chem.*, 25(12):1463–1473, 2004.
- [92] Stefan Grimme. Semiempirical GGA-type Density Functional Constructed with a Long-range Dispersion Correction. *J. Comput. Chem.*, 27(15):1787–1799, 2006.
- [93] Jeng-Da Chai and Martin Head-Gordon. Long-range Corrected Hybrid Density Functionals with Damped Atom–atom Dispersion Corrections. *Phys. Chem. Chem. Phys.*, 10(44):6615–6620, 2008.
- [94] Stefan Grimme, Jens Antony, Stephan Ehrlich, and Helge Krieg. A Consistent and Accurate ab initio Parametrization of Density Functional Dispersion Correction (DFT-D) for the 94 Elements H–Pu. *J. Chem. Phys.*, 132(15):154104, 2010.

- [95] Axel D. Becke. Real-space Post-Hartree–Fock Correlation Models. *J. Chem. Phys.*, 122(6):064101, 2005.
- [96] Erin R. Johnson and Axel D. Becke. A Post-Hartree–Fock Model of Intermolecular Interactions. *J. Chem. Phys.*, 123(2):024101, 2005.
- [97] Axel D. Becke and Erin R. Johnson. A Density-functional Model of the Dispersion Interaction. *J. Chem. Phys.*, 123(15):154101, 2005.
- [98] Axel D. Becke and Erin R. Johnson. Exchange-hole Dipole Moment and the Dispersion Interaction. *J. Chem. Phys.*, 122(15):154104, 2005.
- [99] Max Dion, Henrik Rydberg, Elsabeth Schröder, David C. Langreth, and Bengt I. Lundqvist. van der Waals Density Functional for General Geometries. *Phys. Rev. Lett.*, 92(24), 2004.
- [100] Oleg A. Vydrov and Troy Van Voorhis. Nonlocal van der Waals Density Functional Made Simple. *Phys. Rev. Lett.*, 103:063004, 2009.
- [101] Narbe Mardirossian and Martin Head-Gordon. ω B97X-V: A 10-parameter, Range-separated Hybrid, Generalized Gradient Approximation Density Functional with Nonlocal Correlation, Designed by a Survival-of-the-fittest Strategy. *Phys. Chem. Chem. Phys.*, 16:9904–9924, 2014.
- [102] Georg Jansen and Andreas Hesselmann. Comment on Using Kohn–Sham Orbitals in Symmetry-Adapted Perturbation Theory To Investigate Intermolecular Interactions. *J. Phys. Chem. A*, 105(49):11156–11157, 2001.
- [103] Andreas Heelmann and Georg Jansen. Intermolecular Dispersion Energies from Time-dependent Density Functional Theory. *Chem. Phys. Lett.*, 367(5–6):778–784, 2003.
- [104] Alston J. Misquitta, Bogumil Jeziorski, and Krzysztof Szalewicz. Dispersion Energy from Density-functional Theory Description of Monomers. *Phys. Rev. Lett.*, 91:033201, 2003.
- [105] Alston J. Misquitta, Rafa Podeszwa, Bogumi Jeziorski, and Krzysztof Szalewicz. Intermolecular Potentials Based on Symmetry-adapted Perturbation Theory with Dispersion Energies from Time-dependent Density-functional Calculations. *J. Chem. Phys.*, 123(21):214103, 2005.
- [106] Xi Chu and Alexander Dalgarno. Linear Response Time-dependent Density Functional Theory for van der Waals Coefficients. *J. Chem. Phys.*, 121(9):4083, 2004.
- [107] Fred L. Hirshfeld. Bonded-atom fragments for describing molecular charge densities. *Theoretica Chimica Acta*, 44(2):129–138, 1977.
- [108] Stefano Baroni, Stefano de Gironcoli, Andrea Dal Corso, and Paolo Giannozzi. Phonons and Related Crystal Properties from Density-functional Perturbation Theory. *Rev. Mod. Phys.*, 73(2):515–562, jul 2001.
- [109] Xavier Andrade, Silvana Botti, Miguel A. L. Marques, and Angel Rubio. Time-dependent Density Functional Theory Scheme for Efficient Calculations of Dynamic (Hyper)Polarizabilities. *J. Chem. Phys.*, 126(18):184106, 2007.

- [110] Xavier Andrade, David Strubbe, Umberto De Giovannini, Ask Hjorth Larsen, Micael JT Oliveira, Joseba Alberdi-Rodriguez, Alejandro Varas, Iris Theophilou, Nicole Helbig, Matthieu J Verstraete, et al. Real-space Grids and the Octopus Code as Tools for the Development of New Simulation Approaches for Electronic Systems. *Phys. Chem. Chem. Phys.*, 17(47):31371–31396, 2015.
- [111] Miguel A. L. Marques, Micael J. T. Oliveira, and Tobias Burnus. Libxc: A Library of Exchange and Correlation Functionals for Density Functional Theory. *Comp. Phys. Comm.*, 183(10):2272–2281, 2012.
- [112] Mutasem Omar Sinnokrot and C. David Sherrill. Highly Accurate Coupled Cluster Potential Energy Curves for the Benzene Dimer: Sandwich, T-shaped, and Parallel-displaced Configurations. *J. Phys. Chem. A*, 108(46):10200–10207, 2004.
- [113] Wolfram Koch and Max C. Holthausen. *A Chemist’s Guide to Density Functional Theory*. John Wiley & Sons, 2015.
- [114] M. Hussein. N. Assadi and Dorian A. H. Hanaor. Theoretical Study on Copper’s Energetics and Magnetism in TiO₂ Polymorphs. *J. Appl. Phys.*, 113(23):233913, 2013.
- [115] Axel D. Becke. Perspective: Fifty Years of Density-functional Theory in Chemical Physics. *J. Chem. Phys.*, 140(18):18A301, 2014.
- [116] Chiao-Lun Cheng, Qin Wu, and Troy Van Voorhis. Rydberg Energies Using Excited State Density Functional Theory. *J. Chem. Phys.*, 129(12):124112, 2008.
- [117] Paul A. M. Dirac. Note on Exchange Phenomena in the Thomas Atom. *Math. Proc. Cambridge Philos. Soc.*, 26(3):376–385, 1930.
- [118] David M. Ceperley and Bernard J. Alder. Ground State of the Electron Gas by a Stochastic Method. *Phys. Rev. Lett.*, 45(7):566, 1980.
- [119] Eugene Wigner. On the Interaction of Electrons in Metals. *Phys. Rev.*, 46(11):1002, 1934.
- [120] Lee A. Cole and John P. Perdew. Calculated Electron Affinities of the Elements. *Phys. Rev. A*, 25(3):1265, 1982.
- [121] John P. Perdew and Yue Wang. Accurate and Simple Analytic Representation of the Electron-gas Correlation Energy. *Phys. Rev. B*, 45(23):13244, 1992.
- [122] Robert O. Jones and Olle Gunnarsson. The Density Functional Formalism, its Applications and Prospects. *Rev. Mod. Phys.*, 61(3):689, 1989.
- [123] Randolph Q. Hood, M. Y. Chou, A. J. Williamson, G. Rajagopal, and R. J. Needs. Exchange and Correlation in Silicon. *Phys. Rev. B*, 57(15):8972, 1998.
- [124] Benny G. Johnson, Peter M. W. Gill, and John A. Pople. Preliminary Results on the Performance of a Family of Density Functional Methods. *J. Chem. Phys.*, 97(10):7846–7848, 1992.

- [125] Alain St-Amant, Wendy D. Cornell, Peter A. Kollman, and Thomas A Halgren. Calculation of Molecular Geometries, Relative Conformational Energies, Dipole Moments, and Molecular Electrostatic Potential Fitted Charges of Small Organic Molecules of Biochemical Interest by Density Functional Theory. *J. Comp. Chem.*, 16(12):1483–1506, 1995.
- [126] Philip J. Hasnip, Keith Refson, Matt I. J. Probert, Jonathan R. Yates, Stewart J. Clark, and Chris J. Pickard. Density Functional Theory in the Solid State. *Phil. Trans. R. Soc. A*, 372(2011):20130270, 2014.
- [127] Axel D. Becke. A New Mixing of Hartree–Fock and Local Densityfunctional Theories. *J. Chem. Phys.*, 98(2):1372–1377, 1993.
- [128] Jochen Heyd, Juan E. Peralta, Gustavo E. Scuseria, and Richard L. Martin. Energy Band Gaps and Lattice Parameters Evaluated with the Heyd-Scuseria-Ernzerhof Screened Hybrid Functional. *J. Chem. Phys.*, 123(17):174101, 2005.
- [129] Joseph Muscat, Adrian Wander, and Nicholas M. Harrison. On the Prediction of Band Gaps from Hybrid Functional Theory. *Chem. Phys. Lett.*, 342(3):397–401, 2001.
- [130] Michael J. G Peach, Peter Benfield, Trygve Helgaker, and David J. Tozer. Excitation Energies in Density Functional Theory: An Evaluation and a Diagnostic Test. *J. Chem. Phys.*, 128(4):044118, 2008.
- [131] Alexander Seidl, Andreas Görling, Peter Vogl, Jacek A. Majewski, and Mel Levy. Generalized Kohn-Sham Schemes and the Band-gap Problem. *Phys. Rev. B*, 53(7):3764, 1996.
- [132] Andreas Görling and Mel Levy. Exact Kohn-Sham Scheme Based on Perturbation Theory. *Phys. Rev. A*, 50(1):196, 1994.
- [133] Andreas Görling and Mel Levy. Hybrid Schemes Combining the Hartree–Fock Method and Density-functional Theory: Underlying Formalism and Properties of Correlation Functionals. *J. Chem. Phys.*, 106(7):2675–2680, 1997.
- [134] Ciro A. Guido, Eric Brémond, Carlo Adamo, and Pietro Cortona. Communication: One third: A New Recipe for the PBE0 Paradigm. *J. Chem. Phys.*, 138(2):021104, 2013.
- [135] Marat Valiev, Eric J. Bylaska, Niranjan Govind, Karol Kowalski, Tjerk P. Straatsma, Hubertus J. J. Van Dam, Dunyou Wang, Jarek Nieplocha, Edoardo Apra, Theresa L. Windus, et al. NWChem: A Comprehensive and Scalable Open-source Solution for Large Scale Molecular Simulations. *Comput. Phys. Commun.*, 181(9):1477–1489, 2010.
- [136] Takao Tsuneda, Jong-Won Song, Satoshi Suzuki, and Kimihiko Hirao. On Koopmans Theorem in Density Functional Theory. *J. Chem. Phys.*, 133(17):174101, 2010.
- [137] Frank Neese, Frank Wennmohs, Andreas Hansen, and Ute Becker. Efficient, Approximate and Parallel Hartree–Fock and Hybrid DFT Calculations. A Chain-of-spheres Algorithm for the Hartree–Fock Exchange. *Chem. Phys.*, 356(1):98–109, 2009.

- [138] Daniel Mejía-Rodríguez, Xiaomin Huang, Jorge M. del Campo, and Andreas M. Köster. Chapter Four-hybrid Functionals with Variationally Fitted Exact Exchange. *Adv. Quantum Chem.*, 71:41–67, 2015.
- [139] Stan J. A. Van Gisbergen, Jaap G. Snijders, and Evert Jan Baerends. Accurate Density Functional Calculations on Frequency-dependent Hyperpolarizabilities of Small Molecules. *J. Chem. Phys.*, 109(24):10657–10668, 1998.
- [140] Evert Jan Baerends, Giampaolo Ricciardi, Angela Rosa, and Stan J. A. Van Gisbergen. A DFT/TDDFT Interpretation of the Ground and Excited States of Porphyrin and Porphyrazine Complexes. *Coord. Chem. Rev.*, 230(1):5–27, 2002.
- [141] Robert Van Leeuwen and Evert Jan Baerends. Exchange-correlation Potential with Correct Asymptotic Behavior. *Physical Review A*, 49(4):2421, 1994.
- [142] Oleg V. Gritsenko, Pieter R.T. Schipper, and Evert Jan Baerends. Effect of Pauli Repulsion on the Molecular Exchange-correlation Kohn-Sham Potential: A Comparative Calculation of Ne_2 and N_2 . *Phys. Rev. A*, 57(5):3450, 1998.
- [143] Oleg V. Gritsenko, Pieter R.T. Schipper, and Evert Jan Baerends. Approximation of the Exchange-correlation Kohn-Sham Potential with a Statistical Average of Different Orbital Model Potentials. *Chem. Physics Lett.*, 302(3):199–207, 1999.
- [144] So Hirata and Martin Head-Gordon. Time-dependent Density Functional Theory within the Tamm–Dancoff Approximation. *Chem. Phys. Lett.*, 314(3):291–299, 1999.
- [145] Philipp Furche and Reinhart Ahlrichs. Adiabatic Time-dependent Density Functional Methods for Excited State Properties. *J. Chem. Phys.*, 117(16):7433–7447, 2002.
- [146] Paul W Ayers. Axiomatic Formulations of the Hohenberg-Kohn Functional. *Phys. Rev. A*, 73(1):012513, 2006.
- [147] Paul E. Lammert. Differentiability of Lieb Functional in Electronic Density Functional Theory. *Int. J. Quantum Chem.*, 107(10):1943–1953, 2007.
- [148] Simen Kvaal, Ulf Ekström, Andrew M. Teale, and Trygve Helgaker. Differentiable but Exact Formulation of Density-functional Theory. *J. Chem. Phys.*, 140(18):18A518, 2014.
- [149] Debashree Ghosh, Dmytro Kosenkov, Vitalii Vanovschi, Christopher F. Williams, John M. Herbert, Mark S. Gordon, Michael W. Schmidt, Lyudmila V. Slipchenko, and Anna I. Krylov. Noncovalent Interactions in Extended Systems Described by the Effective Fragment Potential Method: Theory and Application to Nucleobase Oligomers. *J. Phys. Chem. A*, 114(48):12739–12754, 2010.
- [150] Katsuhisa Ohta, Yasunori Yoshioka, Keiji Morokuma, and Kazuo Kitaura. The Effective Fragment Potential Method. An Approximate *Ab Initio* MO Method for Large Molecules. *Chem. Phys. Lett.*, 101(1):12–17, 1983.
- [151] Morris Krauss and Walter J. Stevens. Effective Potentials in Molecular Quantum Chemistry. *Annu. Rev. Phys. Chem.*, 35(1):357–385, 1984.

- [152] Kazuhiko Honda and Kazuo Kitaura. A New Form for Intermolecular Potential Energy Functions. *Chem. Phys. Lett.*, 140(1):53–56, 1987.
- [153] Jan H. Jensen, Paul N. Day, Mark S. Gordon, Harold Basch, Drora Cohen, David R. Garmer, Morris Kraus, and Walter J. Stevens. Effective Fragment Method for Modeling Intermolecular Hydrogen-bonding Effects on Quantum Mechanical Calculations. ACS Publications, 1994.
- [154] Paul N. Day, Jan H. Jensen, Mark S. Gordon, Simon P. Webb, Walter J. Stevens, Morris Krauss, David Garmer, Harold Basch, and Drora Cohen. An Effective Fragment Method for Modeling Solvent Effects in Quantum Mechanical Calculations. *J. Chem. Phys.*, 105(5):1968–1986, 1996.
- [155] Anthony J. Stone. Distributed Multipole Analysis, or How to Describe a Molecular Charge Distribution. *Chem. Phys. Lett.*, 83(2):233–239, 1981.
- [156] Anthony J. Stone. *The Theory of Intermolecular Forces*. OUP Oxford, 2013.
- [157] Jan H. Jensen. Glycine and the Hydrogen Bond: Toward a Model for Solvation. 1995.
- [158] Kazuo Kitaura and Keiji Morokuma. A New Energy Decomposition Scheme for Molecular Interactions within the Hartree–Fock Approximation. *Int. J. Quantum Chem.*, 10(2):325–340, 1976.
- [159] Grant N. Merrill and Mark S. Gordon. Study of Small Water Clusters Using the Effective Fragment Potential Model. *J. Phys. Chem. A*, 102(16):2650–2657, 1998.
- [160] Christian P. Petersen and Mark S. Gordon. Solvation of Sodium Chloride: An Effective Fragment Study of NaCl (H_2O)_n. *J. Phys. Chem. A*, 103(21):4162–4166, 1999.
- [161] Simon P. Webb and Mark S. Gordon. Solvation of the Menshutkin Reaction: A Rigorous Test of the Effective Fragment Method. *J. Phys. Chem. A*, 103(9):1265–1273, 1999.
- [162] Jan H. Jensen and Mark S. Gordon. An Approximate Formula for the Intermolecular Pauli Repulsion Between Closed Shell Molecules. *Mol. Phys.*, 89(5):1313–1325, 1996.
- [163] Jan H. Jensen and Mark S. Gordon. An Approximate Formula for the Intermolecular Pauli Repulsion Between Closed Shell Molecules. II. Application to the Effective Fragment Potential Method. *J. Chem. Phys.*, 108(12):4772–4782, 1998.
- [164] John N. Murrell, Milan Randic, and Denis R. Williams. The Theory of Intermolecular Forces in the Region of Small Orbital Overlap. In *Proc. R. Soc. London, Ser. A*, volume 284, pages 566–581. The Royal Society, 1965.
- [165] Denis R. Williams, Lawrence J. Schaad, and John N. Murrell. Deviations from Pairwise Additivity in Intermolecular Potentials. *J. Chem. Phys.*, 47(12):4916–4922, 1967.

- [166] Mark S. Gordon, Mark A. Freitag, Pradipta Bandyopadhyay, Jan H. Jensen, Visvaldas Kairys, and Walter J. Stevens. The Effective Fragment Potential Method: A QM-based MM Approach to Modeling Environmental Effects in Chemistry. *J. Phys. Chem. A*, 105(2):293–307, 2001.
- [167] Ivana Adamovic and Mark S. Gordon. Dynamic Polarizability, Dispersion Coefficient C₆ and Dispersion Energy in the Effective Fragment Potential Method. *Mol. Phys.*, 103(2-3):379–387, 2005.
- [168] Lyudmila V. Slipchenko and Mark S. Gordon. Electrostatic Energy in the Effective Fragment Potential Method: Theory and Application to Benzene Dimer. *J. Comp. Chem.*, 28(1):276–291, 2007.
- [169] Lyudmila V. Slipchenko and Mark S. Gordon. Damping Functions in the Effective Fragment Potential Method. *Mol. Phys.*, 107(8-12):999–1016, 2009.
- [170] Albert DeFusco, Noriyuki Minezawa, Lyudmila V. Slipchenko, Federico Zhariev, and Mark S. Gordon. Modeling Solvent Effects on Electronic Excited States. *J. Phys. Chem. Lett.*, 2(17):2184–2192, 2011.
- [171] Toni Smith, Lyudmila V. Slipchenko, and Mark S. Gordon. Modeling π–π Interactions with the Effective Fragment Potential Method: The Benzene Dimer and Substituents. *J. Phys. Chem. A*, 112(23):5286–5294, 2008.
- [172] Kamil P. Gierszal, Joel G. Davis, Michael D. Hands, David S. Wilcox, Lyudmila V. Slipchenko, and Dor Ben-Amotz. π-Hydrogen Bonding in Liquid Water. *J. Phys. Chem. Lett.*, 2(22):2930–2933, 2011.
- [173] Heather M. Netzloff and Mark S. Gordon. The Effective Fragment Potential: Small Clusters and Radial Distribution Functions. *J. Chem. Phys.*, 121(6):2711–2714, 2004.
- [174] Lyudmila V. Slipchenko and Mark S. Gordon. Water-benzene Interactions: An Effective Fragment Potential and Correlated Quantum Chemistry Study. *J. Phys. Chem. A*, 113(10):2092–2102, 2008.
- [175] Quentin A. Smith, Mark S. Gordon, and Lyudmila V. Slipchenko. Effective Fragment Potential Study of the Interaction of DNA Bases. *J. Phys. Chem. A*, 115(41):11269–11276, 2011.
- [176] Mark S. Gordon, Lyudmila V. Slipchenko, Hui Li, and Jan H. Jensen. The Effective Fragment Potential: A General Method for Predicting Intermolecular Interactions. *Annu. Rep. Comput. Chem.*, 3:177–193, 2007.
- [177] Mark S. Gordon, Dmitri G. Fedorov, Spencer R. Pruitt, and Lyudmila V. Slipchenko. Fragmentation Methods: A Route to Accurate Calculations on Large Systems. *Chem. Rev.*, 112(1):632–672, 2012.
- [178] Michael D. Hands and Lyudmila V. Slipchenko. Intermolecular Interactions in Complex Liquids: Effective Fragment Potential Investigation of Water–Tert-butanol Mixtures. *J. Phys. Chem. B*, 116(9):2775–2786, 2012.
- [179] Lyudmila V. Slipchenko. Effective Fragment Potential Method. In *Many-Body Effects and Electrostatics in Biomolecules*, pages 147–187. Pan Stanford, 2016.

- [180] Pradeep Kumar Gurunathan, Atanu Acharya, Debashree Ghosh, Dmytro Kosenkov, Ilya A. Kaliman, Yihan Shao, Anna I. Krylov, and Lyudmila V. Slipchenko. Extension of the Effective Fragment Potential Method to Macromolecules. *J. Phys. Chem. B*, 120(27):6562–6574, 2016.
- [181] Mark A. Freitag, Mark S. Gordon, Jan H. Jensen, and Walter J. Stevens. Evaluation of Charge Penetration Between Distributed Multipolar Expansions. *J. Chem. Phys.*, 112(17):7300–7306, 2000.
- [182] Peter Josef William Debye. *Polar Molecules*. Chemical Catalog Company, Incorporated, 1929.
- [183] Roger D. Amos, Nicholas C. Handy, Peter J. Knowles, Julia E. Rice, and Anthony J. Stone. AB-initio Prediction of Properties of Carbon Dioxide, Ammonia, and Carbon Dioxide···Ammonia. *J. Phys. Chem.*, 89(11):2186–2192, 1985.
- [184] Quentin A. Smith, Klaus Ruedenberg, Mark S. Gordon, and Lyudmila V. Slipchenko. The dispersion interaction between quantum mechanics and effective fragment potential molecules. *J. Chem. Phys.*, 136(24):244107, 2012.
- [185] William H. Press, Saul A. Teukolsky, William T. Vetterling, and Brian P. Flannery. *Numerical Recipes in C*, volume 2. Cambridge Univ Press, 1982.
- [186] Kwong-Tin Tang and J. Peter Toennies. An Improved Simple Model for the van der Waals Potential Based on Universal Damping Functions for the Dispersion Coefficients. *J. Chem. Phys.*, 80(8):3726–3741, 1984.
- [187] Paul Adrien Maurice Dirac. *The Principles of Quantum Mechanics*. Oxford: Clarendon Press, 1967.
- [188] Bogumił Jeziorski, Marek Bulski, and Lucjan Piela. First-Order perturbation treatment of the short-range repulsion in a system of many closed-shell atoms or molecules. *Int. J. Quantum Chem.*, 10(2):281–297, 1976.
- [189] John N. Murrell and António J. C. Varandas. Perturbation Calculations of Rare-gas Potentials Near the van der Waals Minimum. *Mol. Phys.*, 30(1):223–236, 1975.
- [190] Jan H. Jensen. Modeling Intermolecular Exchange Integrals Between Nonorthogonal Molecular Orbitals. *J. Chem. Phys.*, 104(19):7795–7796, 1996.
- [191] Mark S. Gordon and Michael W. Schmidt. Advances in Electronic Structure Theory: GAMESS a Decade Later. *Theory Appl. Comput. Chem.: First Forty Years*, pages 1167–1189, 2005.
- [192] Ilya A. Kaliman and Lyudmila V. Slipchenko. LIBEFP: A New Parallel Implementation of the Effective Fragment Potential Method as a Portable Software Library. *J. Comp. Chem.*, 34(26):2284–2292, 2013.
- [193] Bertrand Guillot. A Reappraisal of What We Have Learnt During Three Decades of Computer Simulations on Water. *J. Mol. Liq.*, 101(1-3):219–260, 2002.

- [194] Eva Muchova, Ivan Gladich, Sylvain Picaud, Paul N. M. Hoang, and Martina Roeselova. The Ice–Vapor Interface and the Melting Point of Ice I_h for the Polarizable POL3 Water Model. *J. Phys. Chem. A*, 115(23):5973–5982, 2011.
- [195] John L. Finney. Water? What’s So Special About It? *Philos. Trans. R. Soc., B*, 359(1448):1145–1165, 2004.
- [196] Marcelo A. Carignano, Paul B. Shepson, and Igal Szleifer. Molecular Dynamics Simulations of Ice Growth from Supercooled Water. *Mol. Phys.*, 103(21–23):2957–2967, 2005.
- [197] Eduardo Sanz, Carlos Vega, José L. F. Abascal, and Luís G. MacDowell. Phase Diagram of Water from Computer Simulation. *Phys. Rev. Lett.*, 92(25):255701, 2004.
- [198] Daan Frenkel and Berend Smit. *Understanding Molecular Simulation: From Algorithms to Applications*, volume 1. Academic press, 2001.
- [199] Andrew R. Leach. *Molecular Modelling: Principles and Applications*. Pearson Education, 2001.
- [200] Andrew J. Heymsfield and Robert M. Sabin. Cirrus Crystal Nucleation by Homogeneous Freezing of Solution Droplets. *J. Atmos. Sci.*, 46(14):2252–2264, 1989.
- [201] William L. Jorgensen and Julian Tirado-Rives. Potential Energy Functions for Atomic-level Simulations of Water and Organic and Biomolecular Systems. *Proc. Natl. Acad. Sci. U. S. A.*, 102(19):6665–6670, 2005.
- [202] Herman J. C. Berendsen, James P. M. Postma, Wilfred F. van Gunsteren, and Jan Hermans. Interaction Models for Water in Relation to Protein Hydration. In *Intermolecular forces*, pages 331–342. Springer, 1981.
- [203] Herman J. C. Berendsen, J. Raul Grigera, and Tjerk P. Straatsma. The Missing Term in Effective Pair Potentials. *J. Phys. Chem.*, 91(24):6269–6271, 1987.
- [204] William L. Jorgensen, Jayaraman Chandrasekhar, Jeffry D. Madura, Roger W. Impey, and Michael L. Klein. Comparison of Simple Potential Functions for Simulating Liquid Water. *J. Chem. Phys.*, 79(2):926–935, 1983.
- [205] Jose L. F. Abascal and Carlos Vega. The Melting Point of Hexagonal Ice (I_h) is Strongly Dependent on the Quadrupole of the Water Models. *Phys. Chem. Chem. Phys.*, 9(22):2775–2778, 2007.
- [206] Carlos Vega, Maria Martin-Conde, and Andrzej Patrykiejew. Absence of Superheating for Ice I_h with a Free Surface: A New Method of Determining the Melting Point of Different Water Models. *Mol. Phys.*, 104(22–24):3583–3592, 2006.
- [207] Michael W. Mahoney and William L. Jorgensen. A Five-site Model for Liquid Water and the Reproduction of the Density Anomaly by Rigid, Nonpolarizable Potential Functions. *J. Chem. Phys.*, 112(20):8910–8922, 2000.

- [208] Hans W. Horn, William C. Swope, Jed W. Pitera, Jeffry D. Madura, Thomas J. Dick, Greg L. Hura, and Teresa Head-Gordon. Development of an Improved Four-site Water Model for Biomolecular Simulations: TIP4P-Ew. *J. Chem. Phys.*, 120(20):9665–9678, 2004.
- [209] José L. F. Abascal and Carlos Vega. A General Purpose Model for the Condensed Phases of Water: TIP4P/2005. *J. Chem. Phys.*, 123(23):234505, 2005.
- [210] José L. F. Abascal, Eduardo Sanz, Ramón García Fernández, and Carlos Vega. A Potential Model for the Study of Ices and Amorphous Water: TIP4P/Ice. *J. Chem. Phys.*, 122(23):234511, 2005.
- [211] Nada, Hiroki and van der Eerden, Jan P. J. M. An Intermolecular Potential Model for the Simulation of Ice and Water Near the Melting Point: A Six-site Model of H₂O. *J. Chem. Phys.*, 118(16):7401–7413, 2003.
- [212] Ramón García Fernández, José L. F. Abascal, and Carlos Vega. The Melting Point of Ice I_h for Common Water Models Calculated from Direct Coexistence of the Solid-liquid Interface. *J. Chem. Phys.*, 124(14):144506, 2006.
- [213] José L. F. Abascal, Ramón García Fernández, Carlos Vega, and Marcelo A Carignano. The Melting Temperature of the Six-site Potential Model of Water. *J. Chem. Phys.*, 125(16):166101, 2006.
- [214] Guillaume Lamoureux and Benoit Roux. Modeling Induced Polarization with classical Drude Oscillators: Theory and Molecular Dynamics Simulation Algorithm. *J. Chem. Phys.*, 119(6):3025–3039, 2003.
- [215] Steven W. Rick, Steven J. Stuart, and Bruce J. Berne. Dynamical Fluctuating Charge Force Fields: Application to Liquid Water. *J. Chem. Phys.*, 101(7):6141–6156, 1994.
- [216] András Baranyai. A Polarizable, Four-point-charge Model of Water with Size Variation. *J. Mol. Liq.*, 148(2):88–93, 2009.
- [217] András Baranyai and Albert Bartók. Classical Interaction Model for the Water Molecule. *J. Chem. Phys.*, 126(18):184508, 2007.
- [218] Haibo Yu, Tomas Hansson, and Wilfred F. van Gunsteren. Development of a Simple, Self-consistent Polarizable Model for Liquid Water. *J. Chem. Phys.*, 118(1):221–234, 2003.
- [219] Guillaume Lamoureux, Alexander D. MacKerell Jr., and Benoit Roux. A Simple Polarizable Model of Water Based on Classical Drude Oscillators. *J. Chem. Phys.*, 119(10):5185–5197, 2003.
- [220] James W. Caldwell and Peter A. Kollman. Structure and Properties of Neat Liquids Using Nonadditive Molecular Dynamics: Water, Methanol, and N-methylacetamide. *J. Phys. Chem.*, 99(16):6208–6219, 1995.
- [221] Liem X. Dang and Tsun-Mei Chang. Molecular Dynamics Study of Water Clusters, Liquid, and Liquid-vapor Interface of Water with Many-body Potentials. *J. Chem. Phys.*, 106(19):8149–8159, 1997.

- [222] Humberto Saint-Martin, Jorge Hernández-Cobos, Margarita I. Bernal-Uruchurtu, Iván Ortega-Blake, and Herman J. C. Berendsen. A Mobile Charge Densities in Harmonic Oscillators (MCDHO) Molecular Model for Numerical Simulations: The Water–water Interaction. *J. Chem. Phys.*, 113(24):10899–10912, 2000.
- [223] Benjamin F. Nicholson, Paulette Clancy, and Steven W. Rick. The Interface Response Function and Melting Point of the Prism Interface of Ice I_h Using a Fluctuating Charge Model (TIP4P-FQ). *J. Cryst. Growth*, 293(1):78–85, 2006.
- [224] Lee-Ping Wang, Teresa Head-Gordon, Jay W. Ponder, Pengyu Ren, John D. Chodera, Peter K. Eastman, Todd J. Martinez, and Vijay S. Pande. Systematic Improvement of a Classical Molecular Model of Water. *J. Phys. Chem. B*, 117(34):9956–9972, 2013.
- [225] George S. Fanourgakis and Sotiris S. Xantheas. Development of Transferable Interaction Potentials for Water. V. Extension of the Flexible, Polarizable, Thole-type Model Potential (TTM3-F, v. 3.0) to Describe the Vibrational Spectra of Water Clusters and Liquid Water. *J. Chem. Phys.*, 128(7):074506, 2008.
- [226] Alex Shank, Yimin Wang, Alexey Kaledin, Bastiaan J. Braams, and Joel M. Bowman. Accurate *Ab Initio* and Hybrid Potential Energy Surfaces, Intramolecular Vibrational Energies, and Classical IR Spectrum of the Water Dimer. *J. Chem. Phys.*, 130(14):144314, 2009.
- [227] Yimin Wang and Joel M Bowman. *Ab Initio* Potential and Dipole Moment Surfaces for Water. II. Local-monomer Calculations of the Infrared Spectra of Water Clusters. *J. Chem. Phys.*, 134(15):154510, 2011.
- [228] Volodymyr Babin, Claude Leforestier, and Francesco Paesani. Development of a First Principles Water Potential with Flexible Monomers: Dimer Potential Energy Surface, VRT Spectrum, and Second Virial Coefficient. *J. Chem. Theory Comput.*, 9(12):5395–5403, 2013.
- [229] Volodymyr Babin, Gregory R Medders, and Francesco Paesani. Development of a First Principles Water Potential with Flexible Monomers. II: Trimer Potential Energy Surface, Third Virial Coefficient, and small Clusters. *J. Chem. Theory Comput.*, 10(4):1599–1607, 2014.
- [230] Gregory R Medders, Volodymyr Babin, and Francesco Paesani. Development of a First-Principles Water Potential with Flexible Monomers. III. Liquid Phase Properties. *J. Chem. Theory Comput.*, 10(8):2906–2910, 2014.
- [231] Patrick H.-L. Sit and Nicola Marzari. Static and Dynamical Properties of Heavy Water at Ambient Conditions from First-principles Molecular Dynamics. *J. Chem. Phys.*, 122(20):204510, 2005.
- [232] Soohaeng Yoo, Xiao Cheng Zeng, and Sotiris S. Xantheas. On the Phase Diagram of Water with Density Functional Theory Potentials: The Melting Temperature of Ice I_h with the Perdew-Burke-Ernzerhof and Becke-Lee-Yang-Parr Functionals. *J. Chem. Phys.*, 130(22):221102, 2009.
- [233] Valéry Weber and Dilip Asthagiri. Communication: Thermodynamics of Water Modeled Using *Ab Initio* Simulations. *J. Chem. Phys.*, 133(14):1101, 2010.

- [234] William G. Hoover and Francis H. Ree. Use of Computer Experiments to Locate the Melting Transition and Calculate the Entropy in the Solid Phase. *J. Chem. Phys.*, 47(12):4873–4878, 1967.
- [235] Mark James Abraham, Teemu Murtola, Roland Schulz, Szilárd Pál, Jeremy C. Smith, Berk Hess, and Erik Lindahl. GROMACS: High Performance Molecular Simulations Through Multi-level Parallelism from Laptops to Supercomputers. *SoftwareX*, 1:19–25, 2015.
- [236] Tom Darden, Darrin York, and Lee Pedersen. Particle Mesh Ewald: An $N \cdot \log(N)$ Method for Ewald Sums in Large Systems. *J. Chem. Phys.*, 98(12):10089–10092, 1993.
- [237] Loup Verlet. Computer "Experiments" on Classical Fluids. I. Thermodynamical Properties of Lennard-Jones Molecules. *Phys. Rev.*, 159(1):98, 1967.
- [238] Herman J. C. Berendsen, James P. M. Postma, Wilfred F. van Gunsteren, Alfredo R. H. J. DiNola, and Jeffrey R. Haack. Molecular Dynamics with Coupling to an External Bath. *J. Chem. Phys.*, 81(8):3684–3690, 1984.
- [239] Andreas Dullweber, Benedict Leimkuhler, and Robert McLachlan. Symplectic Splitting Methods for Rigid Body Molecular Dynamics. *J. Chem. Phys.*, 107(15):5840–5851, 1997.
- [240] William G. Hoover. Canonical Dynamics: Equilibrium Phase-space Distributions. *Phys. Rev. A*, 31(3):1695, 1985.
- [241] Simone Melchionna, Giovanni Ciccotti, and Brad Lee Holian. Hoover NPT Dynamics for Systems Varying in Shape and Size. *Mol. Phys.*, 78(3):533–544, 1993.
- [242] William Humphrey, Andrew Dalke, and Klaus Schulten. VMD: Visual Molecular Dynamics. *J. Mol. Graphics*, 14(1):33–38, 1996.
- [243] Alan K. Soper. The Radial Distribution Functions of Water and Ice from 220 to 673 K and at Pressures up to 400 MPa. *Chem. Phys.*, 258(2):121–137, 2000.
- [244] Joanna C. Flick, Dmytro Kosenkov, Edward G. Hohenstein, C. David Sherrill, and Lyudmila V. Slipchenko. Accurate Prediction of Noncovalent Interaction Energies with the Effective Fragment Potential Method: Comparison of Energy Components to Symmetry-adapted Perturbation Theory for the S22 Test Set. *J. Chem. Theory Comput.*, 8(8):2835–2843, 2012.
- [245] Mark S. Gordon, Quentin A. Smith, Peng Xu, and Lyudmila V. Slipchenko. Accurate First Principles Model Potentials for Intermolecular Interactions. *Annu. Rev. Phys. Chem.*, 64:553–578, 2013.
- [246] Cheol Ho Choi, Suyong Re, Michael Feig, and Yuji Sugita. Quantum Mechanical/Effective Fragment Potential Molecular Dynamics (QM/EFP-MD) Study on Intra-molecular Proton Transfer of Glycine in Water. *Chem. Phys. Lett.*, 539:218–221, 2012.
- [247] Jan Rezáč, Kevin E. Riley, and Pavel Hobza. S66: A Well-balanced Database of Benchmark Interaction Energies Relevant to Biomolecular Structures. *J. Chem. Theory Comp.*, 7(8):2427–2438, 2011.

- [248] Mark S. Gordon, Jonathan M. Mullin, Spencer R. Pruitt, Luke B. Roskop, Lyudmila V. Slipchenko, and Jerry A. Boatz. Accurate Methods for Large Molecular Systems. *J. Phys. Chem. B*, 113(29):9646–9663, 2009.
- [249] William L. Jorgensen, David S. Maxwell, and Julian Tirado-Rives. Development and Testing of the OPLS All-atom Force Field on Conformational Energetics and Properties of Organic Liquids. *J. Am. Chem. Soc.*, 118(45):11225–11236, 1996.
- [250] Berk Hess, Carsten Kutzner, David Van Der Spoel, and Erik Lindahl. GROMACS 4: Algorithms for Highly Efficient, Load-balanced, and Scalable Molecular Simulation. *J. Chem. Theory Comp.*, 4(3):435–447, 2008.
- [251] Jan Norberg and Lennart Nilsson. On the Truncation of Long-range Electrostatic Interactions in DNA. *Biophys. J.*, 79(3):1537–1553, 2000.
- [252] William B. Streett, Dominic J. Tildesley, and Graham Saville. Multiple Time-step Methods in Molecular Dynamics. *Mol. Phys.*, 35(3):639–648, 1978.
- [253] Helmut Grubmüller, Helmut Heller, Andreas Windemuth, and Klaus Schulten. Generalized Verlet Algorithm for Efficient Molecular Dynamics Simulations with Long-range Interactions. *Mol. Simul.*, 6(1-3):121–142, 1991.
- [254] Mark E. Tuckerman, Bruce J. Berne, and Glenn J. Martyna. Molecular Dynamics Algorithm for Multiple Time Scales: Systems with Long Range Forces. *J. Chem. Phys.*, 94(10):6811–6815, 1991.
- [255] Ryan P. Steele. Multiple-timestep Ab Initio Molecular Dynamics Using an Atomic Basis Set Partitioning. *J. Phys. Chem. A*, 119(50):12119–12130, 2015.
- [256] Carlos H. Borca and Carlos A. Arango. Molecular Dynamics of a Water-Absorbent Nanoscale Material Based on Chitosan. *J. Phys. Chem. B*, 120(15):3754–3764, 2016.
- [257] Laura I. Mosquera-Giraldo, Carlos H. Borca, Xiangtao Meng, Kevin J. Edgar, Lyudmila V. Slipchenko, and Lynne S. Taylor. Mechanistic Design of Chemically Diverse Polymers with Applications in Oral Drug Delivery. *Biomacromolecules*, 17(11):3659–3671, 2016.
- [258] Na Li, Laura I. Mosquera-Giraldo, Carlos H. Borca, James D. Ormes, Michael Lowinger, John D. Higgins, Lyudmila V. Slipchenko, and Lynne S. Taylor. A Comparison of the Crystallization Inhibition Properties of Bile Salts. *Cryst. Growth Des.*, 16:7286–7300, 2016.
- [259] Fulizi Xiong, Carlos H. Borca, Lyudmila V. Slipchenko, and Paul B. Shepson. Photochemical Degradation of Isoprene-derived 4,1-Nitrooxy Enal. *Atmos. Chem. Phys.*, 16(9):5595–5610, 2016.
- [260] Joel D. Rindelaub, Carlos H. Borca, Matthew A. Hostettler, Jonathan H. Slade, Mark A. Lipton, Lyudmila V. Slipchenko, and Paul B. Shepson. The Acid-catalyzed Hydrolysis of an α -pinene-derived Organic Nitrate: Kinetics, Products, Reaction mechanisms, and Atmospheric Impact. *Atmos. Chem. Phys.*, 16(23):15425–15432, 2016.

APPENDICES

A. PORTABLE C LIBRARY OF THE TKATCHENKO-SCHEFFLER VAN DER WAALS MODEL

```

/*
** Copyright (C) 2015 Xavier Andrade, Carlos Borca, Alfredo Correa
**
** This library is free software: you can redistribute it and/or modify
** it under the terms of the GNU Lesser General Public License as published by
** the Free Software Foundation, either version 3 of the License, or
** (at your option) any later version.
**
** This library is distributed in the hope that it will be useful,
** but WITHOUT ANY WARRANTY; without even the implied warranty of
** MERCHANTABILITY or FITNESS FOR A PARTICULAR PURPOSE. See the
** GNU Lesser General Public License for more details.
**
** You should have received a copy of the GNU Lesser General Public License
** along with this program. If not, see <http://www.gnu.org/licenses/>.
*/
#include <stdio.h>
#include <math.h>

#ifndef _TEST
#include "config.h"
#endif

/* Function to retrieve Van der Waals parameters of the free atoms. */
void get_vdw_params (const int zatom, double * c6, double * alpha, double * r0)
{

    switch(zatom)
    {

        // Hydrogen (H)
        case 1:
            *alpha = 4.500000;
            *c6 = 6.500000;
}

```

```

*r0 = 3.100000;
break;

.

.

.

// Bismuth (Bi)
case 83:
    *alpha = 49.02;
    *c6 = 571.0;
    *r0 = 4.32;

// Elements from 84 - Polonium (Po) to 118 - Ununoctium (Uuo) are not included.

}

}

/* Damping function. */
void fdamp (const double rr, const double r0ab, double * ff, double * dffdrab, double
* dffdr0)
{
    const double dd = 20.0;
    const double sr = 0.94; // Value for PBE. Should be 0.96 for PBE0.

    // Calculate the damping coefficient.
    double ee = exp(-dd*((rr/(sr*r0ab)) - 1.0));
    *ff = 1.0/(1.0 + ee);
    double dee = ee*(*ff)*(*ff);

    // Calculate the derivative of the damping function with respect to the distance
    // between atoms A and B.
    *dffdrab = (dd/(sr*r0ab))*dee;

    // Calculate the derivative of the damping function with respect to the distance
    // between effective van der Waals radii.
    *dffdr0 = -dd*rr/(sr*r0ab*r0ab)*dee;

}

/* Calculation of the square of separations. */

```

```

void distance (const int iatom, const int jatom, const double coordinates[], double *
               rr, double * rr2, double * rr6, double *rr7)
{
    double x_ij = coordinates[3*iatom + 0] - coordinates[3*jatom + 0];
    double y_ij = coordinates[3*iatom + 1] - coordinates[3*jatom + 1];
    double z_ij = coordinates[3*iatom + 2] - coordinates[3*jatom + 2];

    *rr2 = x_ij*x_ij + y_ij*y_ij + z_ij*z_ij;
    *rr6 = rr2[0]*rr2[0]*rr2[0]; // This is the same as: *rr6 = (*rr2)*(*rr2)*(*rr2)
    *rr = sqrt(rr2[0]); // This is the same as: *rr = sqrt(*rr2)
    *rr7 = rr6[0]*rr[0]; // This is the same as: *rr6 = (*rr6)*(*rr)

    // Print information controls.
    //printf("R_(%i-%i) = %f\n", iatom+1, jatom+1, *rr);
    //printf("R_(%i-%i)^2 = %f\n", iatom+1, jatom+1, *rr2);
    //printf("R_(%i-%i)^6 = %f\n", iatom+1, jatom+1, *rr6);

}

/* Function to calculate the Van der Waals energy... and forces */
void vdw_calculate (const int natoms, const int zatom[], const double coordinates[],
                     const double volume_ratio[], double * energy, double force[], double
                     derivative_coeff[])
{
    int ia;

    *energy = 0.0;

    // Loop to calculate the pair-wise Van der Waals energy correction.
    for (ia = 0; ia < natoms; ia++)
    {
        double c6_a, alpha_a, r0_a;
        int ib;

        force[3*ia + 0] = 0.0;
        force[3*ia + 1] = 0.0;
        force[3*ia + 2] = 0.0;

        derivative_coeff[ia] = 0.0;

        get_vdw_params(zatom[ia], &c6_a, &alpha_a, &r0_a);
    }
}

```

```

for (ib = 0; ib < natoms; ib++)
{
    double c6_b, alpha_b, r0_b;

    if (ia == ib) continue;

    // Pair-wise calculation of separations.
    double rr, rr2, rr6, rr7;
    distance(ia, ib, coordinates, &rr, &rr2, &rr6, &rr7);

    get_vdw_params(zatom[ib], &c6_b, &alpha_b, &r0_b);

    // Determination of c6abfree, for isolated atoms a and b.
    double num = 2.0*c6_a*c6_b;
    double den = (alpha_b/alpha_a)*c6_a + (alpha_a/alpha_b)*c6_b;

    double c6abfree = num/den;

    // Determination of c6ab, for bonded atoms a and b.
    double c6ab = volume_ratio[ia]*volume_ratio[ib]*c6abfree;

    // Determination of the effective radius of atom a.
    double r0ab = cbrt(volume_ratio[ia])*r0_a + cbrt(volume_ratio[ib])*r0_b;

    // Pair-wise calculation of the damping coefficient
    double ff;
    double dffdrab;
    double dffdr0;
    fdamp(rr, r0ab, &ff, &dffdrab, &dffdr0);

    // Pair-wise correction to energy.
    *energy += -0.5*ff*c6ab/rr6;

    // Calculation of the pair-wise partial energy derivative with respect to the
    // distance between atoms A and B.
    double deabdrab = -dffdrab*c6ab/rr6 + 6.0*ff*c6ab/rr7;

    // Derivative of the AB van der Waals separation with respect to the volume
    // ratio of atom A.
    double dr0dvra = r0_a/(3.0*pow(volume_ratio[ia], 2.0/3.0));

    // Derivative of the damping function with respect to the volume ratio of atom
    // A.
    double dffdvra = dffdr0*dr0dvra;
}

```

```

// Calculation of the pair-wise partial energy derivative with respect to the
// volume ratio of atom A.
double deabdvra = -dffdvra*c6ab/rr6 - ff*volume_ratio[ib]*c6abfree/rr6;

force[3*ia + 0] += -deabdrab*(coordinates[3*ia + 0] - coordinates[3*ib + 0])/rr;
force[3*ia + 1] += -deabdrab*(coordinates[3*ia + 1] - coordinates[3*ib + 1])/rr;
force[3*ia + 2] += -deabdrab*(coordinates[3*ia + 2] - coordinates[3*ib + 2])/rr;

derivative_coeff[ia] += deabdvra;

// Print information controls.
//printf("Distance between atoms %i and %i = %f. \n", ia+1, ib+1, rr);
//printf("Atom %i, c6= %f, alpha= %f, r0= %f. \n", ia+1, c6_a, alpha_a, r0_a);
//printf("Atom %i, c6= %f, alpha= %f, r0= %f. \n", ib+1, c6_b, alpha_b, r0_b);
//printf("For atoms %i and %i, c6ab= %f. \n", ia+1, ib+1, c6abfree);

}

}

//printf("The final van der Waals energy correction is = %f. \n", *energy);
//printf("The final van der Waals force correction is = %f. \n", *force);

}

#endif _TEST
/* This is a wrapper to be called from Fortran. */
void FC_FUNC_(f90_vdw_calculate, F90_VDW_CALCULATE) (const int * natoms, const int
zatom[], const double coordinates[], const double volume_ratio[], double * energy,
double force[], double derivative_coeff[])
{
    vdw_calculate(*natoms, zatom, coordinates, volume_ratio, energy, force,
derivative_coeff);

}
#endif

/* Main test function. */
#ifndef _TEST
int main ()
{
    const int natoms = 3;
    const int zatom[] = {23, 29, 31};
    const double volume_ratio[] = {1.0, 1.0, 1.0};
}

```

```
double energy;
double force[natoms*3];
double derivative_coeff[natoms];

double x;
for(x = 0.1; x < 10; x += 0.1)
{

    double coordinates[] = {0.2, -0.3, 0.5, -0.7, 1.1, -1.3, x, 0.0, 0.0};

    vdw_calculate(natoms, zatom, coordinates, volume_ratio, &energy, force,
                  derivative_coeff);

    coordinates[5] += 0.001;
    double energy_2;

    vdw_calculate(natoms, zatom, coordinates, volume_ratio, &energy_2, force,
                  derivative_coeff);
    printf("%f %f %f\n", x, energy, force[5], -(energy_2-energy)/0.001);

}

#endif
```

B. OCTOPUS SAMPLE INPUT: TS-VDW GROUND-STATE CALCULATION

CalculationMode = gs
 UnitsInput = eV_Angstrom

Radius = 5
 Spacing = 0.23

VDWcorrection = yes
 ExperimentalFeatures = yes

d = 2.800000

%Coordinates

'C' | 0.000 | 1.396 | d/2
 'C' | 1.209 | 0.698 | d/2
 'C' | 1.209 |-0.698 | d/2
 'C' | 0.000 |-1.396 | d/2
 'C' |-1.209 |-0.698 | d/2
 'C' |-1.209 | 0.698 | d/2
 'H' | 0.000 | 2.479 | d/2
 'H' | 2.147 | 1.240 | d/2
 'H' | 2.147 |-1.240 | d/2
 'H' | 0.000 |-2.479 | d/2
 'H' |-2.147 |-1.240 | d/2
 'H' |-2.147 | 1.240 | d/2
 'C' | 0.000 | 1.396 |-d/2
 'C' | 1.209 | 0.698 |-d/2
 'C' | 1.209 |-0.698 |-d/2
 'C' | 0.000 |-1.396 |-d/2
 'C' |-1.209 |-0.698 |-d/2
 'C' |-1.209 | 0.698 |-d/2
 'H' | 0.000 | 2.479 |-d/2
 'H' | 2.147 | 1.240 |-d/2
 'H' | 2.147 |-1.240 |-d/2
 'H' | 0.000 |-2.479 |-d/2
 'H' |-2.147 |-1.240 |-d/2
 'H' |-2.147 | 1.240 |-d/2

```
%  
  
#Output = wfs+density+potential+elf  
#OutputHow = cube  
ExtraStates = 4  
ConvRelDens = 1e-7
```

C. OCTOPUS SAMPLE INPUT: TS-VDW EXCITED-STATES CALCULATION

```
CalculationMode = td
UnitsInput = eV_Angstrom

fromScratch = yes

Radius = 5
Spacing = 0.20

VDWcorrection = yes
ExperimentalFeatures = yes

d = 2.800000

%Species
'H' | species_pseudo | file | 'H.pbe-vbc.UPF'
'F' | species_pseudo | file | 'F.pbe-hgh.UPF'
%

%Coordinates
'H' | 0.000 | 0.460 | d/2
'F' | 0.000 |-0.460 | d/2
'H' | 0.000 |-0.460 |-d/2
'F' | 0.000 | 0.460 |-d/2
%

#Output = wfs+density+potential+elf
#OutputHow = cube

TDDeltaStrength = 0.01
TDPolarizationDirection = 3
TDPropagationTime = 30.38535
```

D. OCTOPUS SAMPLE OUTPUT: TS-VDW GROUND-STATE CALCULATION

Screen output on execution of the sample input file of Appendix B:

This program is free software; you can redistribute it and/or modify it under the terms of the GNU General Public License as published by the Free Software Foundation; either version 2, or (at your option) any later version.

This program is distributed in the hope that it will be useful, but WITHOUT ANY WARRANTY; without even the implied warranty of MERCHANTABILITY or FITNESS FOR A PARTICULAR PURPOSE. See the GNU General Public License for more details.

You should have received a copy of the GNU General Public License along with this program; if not, write to the Free Software Foundation, Inc., 51 Franklin Street, Fifth Floor, Boston, MA

Running octopus

```

Version          : tetricus
Revision        : 14565
Build time      : Mon Sep 14 17:49:16 EDT 2015
Configuration options : max-dim=3 sse2
Optional libraries   : newuo
Architecture       : x86_64
C compiler         : gcc
C compiler flags    : -I/usr/include -g -O2
Fortran compiler     : gfortran (GCC version 4.8.4)
Fortran compiler flags : -pipe -O3 -funroll-loops -ffast-math -ffree-line-length-none

```

The octopus is swimming in Lawrencium (Linux)

Calculation started on 2017/02/13 at 17:25:11

```
***** Calculation Mode *****
Input: [CalculationMode = gs]
*****
```

Reading Coordinates from Coordinates block
 Input: [PseudopotentialSet = standard]

```
***** Species *****
Reading pseudopotential from file:
  '/home/carlosborca/octopus/share/octopus/pseudopotentials/PSF/C.psf'
  Calculating atomic pseudo-eigenfunctions for species C ....
Info: l = 0 component used as local potential.
Info: l = 1 is maximum angular momentum considered.
Number of orbitals: total = 16, bound = 4
Reading pseudopotential from file:
  '/home/carlosborca/octopus/share/octopus/pseudopotentials/PSF/H.psf'
  Calculating atomic pseudo-eigenfunctions for species H ....
Info: l = 0 component used as local potential.
Info: l = 0 is maximum angular momentum considered.
Number of orbitals: total = 16, bound = 1
*****
```

```
***** Symmetries *****
Symmetry elements : (i) 3*(C2) 3*(sigma)
Symmetry group    : D2h
```

```
*****
```

Input: [SpinComponents = unpolarized]
 Input: [SmearingFunction = semiconducting]
 Input: [SymmetrizeDensity = no]

```
***** States *****
```

Total electronic charge = 60.000
 Number of states = 30
 States block-size = 4

```
*****
```

Input: [CurvMethod = curv_uniform]
 Input: [DerivativesStencil = stencil_star]

```
***** Parallelization *****
```

Info: Octopus will run in *serial*

```
*****
```

Info: Generating weights for finite-difference discretization of x-gradient
 Info: Generating weights for finite-difference discretization of y-gradient
 Info: Generating weights for finite-difference discretization of z-gradient
 Info: Generating weights for finite-difference discretization of Laplacian

```
***** Grid *****
```

Simulation Box:

Type = minimum
 Radius [b] = 9.449
 Octopus will run in 3 dimension(s).
 Octopus will treat the system as periodic in 0 dimension(s).

Main mesh:

Spacing [b] = (0.378, 0.378, 0.378) volume/point [b^3] = 0.05399
 # inner mesh = 216737
 # total mesh = 285121
 Grid Cutoff [H] = 34.547134 Grid Cutoff [Ry] = 69.094267

```
*****
```

Info: states-block size = 8.7 MiB
 Input: [StatesOrthogonalization = gram_schmidt]

```
***** Hartree *****
```

The chosen Poisson solver is 'interpolating scaling functions'

```
*****
```

```
***** Theory Level *****
```

Input: [TheoryLevel = dft]

Exchange-correlation:

Exchange

Slater exchange (LDA)

[1] PAM Dirac, Proceedings of the Cambridge Philosophical Society 26, 376 (1930)

[2] F Bloch, Zeitschrift fuer Physik 57, 545 (1929)

Correlation

Perdew & Zunger (Modified) (LDA)

[1] Perdew and Zunger, Phys. Rev. B 23, 5048 (1981)

[2] Modified to improve the matching between the low- and high-rs parts

Input: [SICCorrection = sic_none]

Input: [FilterPotentials = filter_TS]

Info: Pseudopotential for C

Radii for localized parts:

local part = 2.6 b

non-local part = 1.9 b

orbitals = 9.0 b

Info: Pseudopotential for H

Radii for localized parts:

local part = 2.1 b

non-local part = 0.0 b

orbitals = 8.8 b

Input: [RelativisticCorrection = non_relativistic]

Input: [AbsorbingBoundaries = not_absorbing]

***** Approximate memory requirements *****

Mesh

global : 5.1 MiB

local : 6.5 MiB

total : 11.6 MiB

States

real : 65.3 MiB (par_kpoints + par_states + par_domains)

complex : 130.5 MiB (par_kpoints + par_states + par_domains)

Info: Generating external potential

done.

Info: Octopus initialization completed.

Info: Starting calculation mode.
 Info: Allocating ground state wave-functions
 Info: Blocks of states

Block	1 contains	4 states:	1 -	4
Block	2 contains	4 states:	5 -	8
Block	3 contains	4 states:	9 -	12
Block	4 contains	4 states:	13 -	16
Block	5 contains	4 states:	17 -	20
Block	6 contains	4 states:	21 -	24
Block	7 contains	4 states:	25 -	28
Block	8 contains	2 states:	29 -	30

 Info: Ground-state allocation done.
 Input: [MixField = density] (what to mix during SCF cycles)
 Input: [TypeOfMixing = broyden]

**** Eigensolver ****

 Input: [Eigensolver = cg]
 Input: [Preconditioner = pre_filter]
 Input: [SubspaceDiagonalization = standard]

 Input: [LCAOStart = lcao_full]
 Input: [LCAOScaleFactor = 1.000]
 Input: [LCAOMaximumOrbitalRadius = 20.00 b]
 Info: Single-precision storage for 30 extra orbitals will be allocated.
 Info: Unnormalized total charge = 59.999872
 Info: Renormalized total charge = 60.000000
 Info: Setting up Hamiltonian.
 Info: Performing initial LCAO calculation with 60 orbitals.
 Info: Getting Hamiltonian matrix elements.
 ETA:1.....2.....3.....4.....5.....6.....7.....8.....9.....0

Eigenvalues [H]

#st	Spin	Eigenvalue	Occupation
1	--	-0.966903	2.000000
2	--	-0.963962	2.000000
3	--	-0.866420	2.000000
4	--	-0.866399	2.000000
5	--	-0.860990	2.000000
6	--	-0.860965	2.000000
7	--	-0.719428	2.000000
8	--	-0.719414	2.000000
9	--	-0.718021	2.000000
10	--	-0.718007	2.000000
11	--	-0.624059	2.000000
12	--	-0.622229	2.000000

13	--	-0.612828	2.000000
14	--	-0.611358	2.000000
15	--	-0.565646	2.000000
16	--	-0.560824	2.000000
17	--	-0.547016	2.000000
18	--	-0.547012	2.000000
19	--	-0.546518	2.000000
20	--	-0.546509	2.000000
21	--	-0.516699	2.000000
22	--	-0.492427	2.000000
23	--	-0.492236	2.000000
24	--	-0.489621	2.000000
25	--	-0.489423	2.000000
26	--	-0.468404	2.000000
27	--	-0.435489	2.000000
28	--	-0.435483	2.000000
29	--	-0.387285	2.000000
30	--	-0.387282	2.000000

Info: Ground-state restart information will be written to 'restart/gs'.

Info: SCF using real wavefunctions.

Info: Starting SCF iteration.

ETA:1.....2.....3.....4.....5.....6.....7.....8.....9.....0

***** SCF CYCLE ITER # 1 *****

etot = -7.59030455E+01 abs_ev = 4.89E+00 rel_ev = 1.51E-01
abs_dens = 1.12E+01 rel_dens = 1.86E-01

Matrix vector products: 810

Converged eigenvectors: 0

#	State	Eigenvalue [H]	Occupation	Error
1		-0.867988	2.000000	(1.1E-04)
2		-0.855002	2.000000	(1.9E-04)
3		-0.771223	2.000000	(2.3E-04)
4		-0.771153	2.000000	(2.3E-04)
5		-0.758989	2.000000	(2.0E-04)
6		-0.758917	2.000000	(2.0E-04)
7		-0.648223	2.000000	(4.3E-04)
8		-0.648159	2.000000	(4.1E-04)

[output of 13 eigenvalues skipped: maximum error = 2.2E-03]

22		-0.419322	2.000000	(3.0E-04)
23		-0.418604	2.000000	(2.5E-04)
24		-0.413505	2.000000	(2.2E-04)
25		-0.412776	2.000000	(2.2E-04)

26	-0.368565	2.000000	(2.6E-04)
27	-0.332246	2.000000	(2.1E-04)
28	-0.332202	2.000000	(2.1E-04)
29	-0.275144	2.000000	(2.4E-04)
30	-0.275096	2.000000	(2.4E-04)

Density of states:

```
=====
=====
=====
=====
=====
=====
=====
=====
=====
=====
=====
=====
=====
=====
=====
=====
=====
=====
=====
=====
=====
=====
=====
=====
=====
=====
=====
=====
=====
=====
=====
=====
=====
=====
=====
=====
=====
=====
=====
=====
=====
=====
=====
=====
=====
=====
=====
=====
=====
=====
=====
=====
=====
=====
=====
=====
=====
=====
=====
=====
=====
=====
=====
=====
=====
=====
=====
=====
=====
=====
=====
=====
=====
=====
=====
=====
=====
=====
=====
=====
=====
=====
=====
=====
=====
=====
=====
=====
=====
=====
=====
=====
=====
=====
=====
=====
=====
=====
=====
=====
=====
=====
=====
=====
=====
=====
=====
=====
=====
=====
=====
=====
=====
=====
=====
=====
=====
=====
=====
=====
=====
=====
=====
=====
=====
=====
=====
=====
=====
=====
=====
=====
=====
=====
=====
=====
=====
=====
=====
=====
=====
=====
=====
=====
=====
=====
=====
=====
=====
 
%-%-----%-%-----%-%-----%-%-----%-%-----%
~
```

Elapsed time for SCF step 1: 45.07

ETA:1.....2.....3.....4.....5.....6.....7.....8.....9.....0

***** SCF CYCLE ITER # 2 *****

etot = -7.57295644E+01 abs_ev = 2.90E+00 rel_ev = 9.83E-02

abs_dens = 6.65E+00 rel_dens = 1.11E-01

Matrix vector products: 810

Converged eigenvectors: 0

#	State	Eigenvalue [H]	Occupation	Error
1		-0.819613	2.000000	(9.0E-06)
2		-0.805560	2.000000	(7.7E-06)
3		-0.721753	2.000000	(9.9E-06)
4		-0.721676	2.000000	(1.1E-05)
5		-0.708496	2.000000	(8.5E-06)
6		-0.708418	2.000000	(8.5E-06)
7		-0.597912	2.000000	(4.4E-05)
8		-0.597852	2.000000	(2.1E-05)

[output of 13 eigenvalues skipped: maximum error = 3.9E-05]

22 -0.366532 2.000000 (9.7E-05)

23	-0.365865	2.000000	(3.4E-05)
24	-0.360084	2.000000	(3.6E-05)
25	-0.359404	2.000000	(3.2E-05)
26	-0.330421	2.000000	(5.2E-05)
27	-0.295954	2.000000	(2.6E-05)
28	-0.295896	2.000000	(2.4E-05)
29	-0.235627	2.000000	(1.2E-04)
30	-0.235563	2.000000	(1.1E-04)

Density of states:

```
-----
-----
-----
-----
-----
-----%
-----%
-----%
-----%
-----%
-----%
-----%
-----%
-----%
-----%
```

Elapsed time for SCF step 2: 80.36

ETA:1.....2.....3.....4.....5.....6.....7.....8.....9.....0

***** SCF CYCLE ITER # 3 *****

etot = -7.56423407E+01 abs_ev = 3.07E+00 rel_ev = 1.16E-01
abs_dens = 1.03E+00 rel_dens = 1.72E-02

Matrix vector products: 810

Converged eigenvectors: 0

#	State	Eigenvalue [H]	Occupation	Error
1		-0.774754	2.000000	(7.8E-06)
2		-0.759087	2.000000	(4.5E-06)
3		-0.671603	2.000000	(1.7E-05)
4		-0.671560	2.000000	(1.7E-05)
5		-0.656802	2.000000	(1.4E-05)
6		-0.656758	2.000000	(1.3E-05)
7		-0.542909	2.000000	(4.1E-05)
8		-0.542850	2.000000	(3.4E-05)

[output of 13 eigenvalues skipped: maximum error = 5.9E-05]

22	-0.306244	2.000000	(7.8E-05)
23	-0.305652	2.000000	(6.0E-05)
24	-0.298760	2.000000	(5.9E-05)
25	-0.298154	2.000000	(6.2E-05)
26	-0.297781	2.000000	(6.2E-05)
27	-0.264485	2.000000	(5.8E-05)
28	-0.264443	2.000000	(5.3E-05)
29	-0.200360	2.000000	(1.6E-04)
30	-0.200311	2.000000	(1.3E-04)

Density of states:

```
-----
-----
```

%

-----%-----%%-----%%-%%-----%%-----%-----%

-----%-----%%-----%%-----%%-----%%-----%-----%

^

Elapsed time for SCF step 3: 79.39

```
*****
```

ETA:1.....2.....3.....4.....5.....6.....7.....8.....9.....0

```
***** SCF CYCLE ITER # 4 *****
```

etot = -7.56405183E+01 abs_ev = 3.08E-01 rel_ev = 1.15E-02
 abs_dens = 2.96E-01 rel_dens = 4.93E-03

Matrix vector products: 810

Converged eigenvectors: 0

#	State	Eigenvalue [H]	Occupation	Error
1		-0.781423	2.000000	(2.3E-06)
2		-0.765753	2.000000	(1.4E-06)
3		-0.677743	2.000000	(2.3E-06)
4		-0.677702	2.000000	(2.1E-06)
5		-0.662955	2.000000	(2.1E-06)
6		-0.662913	2.000000	(2.0E-06)

7	-0.548213	2.000000	(1.8E-05)
8	-0.548158	2.000000	(5.1E-06)

[output of 13 eigenvalues skipped: maximum error = 1.3E-05]

22	-0.310188	2.000000	(3.5E-05)
23	-0.309601	2.000000	(1.7E-05)
24	-0.304359	2.000000	(8.5E-06)
25	-0.302710	2.000000	(7.7E-06)
26	-0.302110	2.000000	(8.0E-06)
27	-0.270800	2.000000	(5.8E-06)
28	-0.270759	2.000000	(6.0E-06)
29	-0.206931	2.000000	(2.7E-05)
30	-0.206886	2.000000	(2.5E-05)

Density of states:

```
-----
-----
```

%

% %

% % % %

% % % % % %

~

Elapsed time for SCF step 4: 79.81

ETA:1.....2.....3.....4.....5.....6.....7.....8.....9.....0

***** SCF CYCLE ITER # 5 *****

etot = -7.56405372E+01 abs_ev = 1.25E-01 rel_ev = 4.70E-03
abs_dens = 9.32E-02 rel_dens = 1.55E-03

Matrix vector products: 766

Converged eigenvectors: 0

#	State	Eigenvalue [H]	Occupation	Error
1		-0.778219	2.000000	(1.1E-06)
2		-0.762574	2.000000	(6.6E-07)
3		-0.675436	2.000000	(7.8E-07)

4	-0.675393	2.000000	(9.5E-07)
5	-0.660675	2.000000	(6.9E-07)
6	-0.660630	2.000000	(8.5E-07)
7	-0.546553	2.000000	(1.1E-05)
8	-0.546503	2.000000	(7.8E-07)

[output of 13 eigenvalues skipped: maximum error = 8.8E-06]

22	-0.308308	2.000000	(1.9E-05)
23	-0.307724	2.000000	(5.3E-06)
24	-0.301976	2.000000	(3.3E-06)
25	-0.300837	2.000000	(3.3E-06)
26	-0.300239	2.000000	(3.3E-06)
27	-0.268665	2.000000	(2.9E-06)
28	-0.268624	2.000000	(2.9E-06)
29	-0.204824	2.000000	(8.4E-06)
30	-0.204778	2.000000	(8.3E-06)

Density of states:

```
-----
-----
```

%

%

%

%

~

Elapsed time for SCF step 5: 78.73

ETA:1.....2.....3.....4.....5.....6.....7.....8.....9.....0

***** SCF CYCLE ITER # 6 *****

etot = -7.56404768E+01 abs_ev = 2.28E-02 rel_ev = 8.58E-04
abs_dens = 4.78E-02 rel_dens = 7.97E-04

Matrix vector products: 661

Converged eigenvectors: 6

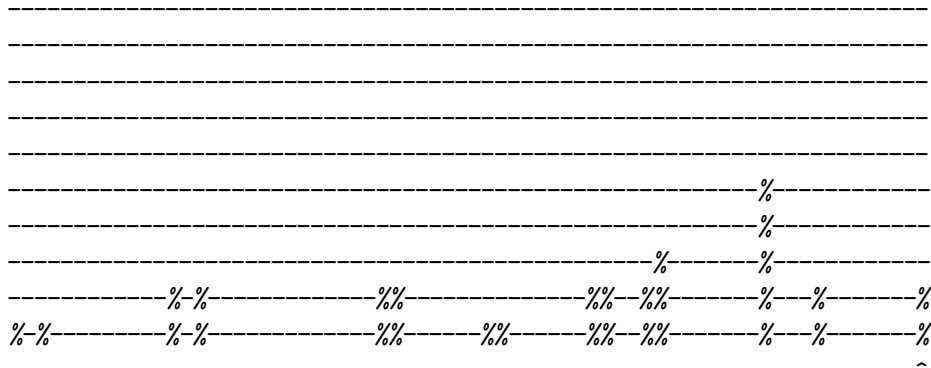
State Eigenvalue [H] Occupation Error

1	-0.778565	2.000000	(9.7E-07)
2	-0.762928	2.000000	(9.1E-07)
3	-0.675806	2.000000	(8.2E-07)
4	-0.675763	2.000000	(8.5E-07)
5	-0.661052	2.000000	(8.1E-07)
6	-0.661008	2.000000	(7.5E-07)
7	-0.546958	2.000000	(6.8E-06)
8	-0.546908	2.000000	(7.2E-07)

[output of 13 eigenvalues skipped: maximum error = 5.5E-06]

22	-0.308779	2.000000	(1.1E-05)
23	-0.308196	2.000000	(9.0E-07)
24	-0.302162	2.000000	(8.1E-07)
25	-0.301317	2.000000	(1.0E-06)
26	-0.300719	2.000000	(8.9E-07)
27	-0.268847	2.000000	(9.8E-07)
28	-0.268806	2.000000	(7.6E-07)
29	-0.205034	2.000000	(1.5E-06)
30	-0.204989	2.000000	(1.4E-06)

Density of states:



Elapsed time for SCF step 6: 74.22

ETA:1.....2.....3.....4.....5.....6.....7.....8.....9.....0

***** SCF CYCLE ITER # 7 *****

etot = -7.56404730E+01 abs_ev = 1.50E-03 rel_ev = 5.65E-05
abs_dens = 2.32E-02 rel_dens = 3.87E-04

Matrix vector products: 572

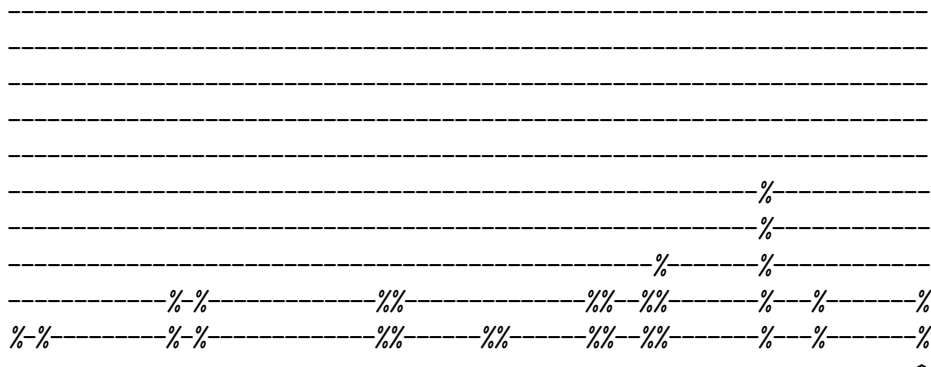
Converged eigenvectors: 6

#	State	Eigenvalue [H]	Occupation	Error
1		-0.778526	2.000000	(8.7E-07)
2		-0.762893	2.000000	(7.2E-07)
3		-0.675766	2.000000	(9.4E-07)
4		-0.675723	2.000000	(7.6E-07)
5		-0.661014	2.000000	(8.3E-07)
6		-0.660969	2.000000	(7.9E-07)
7		-0.546931	2.000000	(4.3E-06)
8		-0.546882	2.000000	(6.8E-07)

[output of 13 eigenvalues skipped: maximum error = 3.3E-06]

22	-0.308792	2.000000	(6.1E-06)
23	-0.308209	2.000000	(8.8E-07)
24	-0.302056	2.000000	(8.3E-07)
25	-0.301331	2.000000	(9.3E-07)
26	-0.300734	2.000000	(9.5E-07)
27	-0.268744	2.000000	(8.1E-07)
28	-0.268704	2.000000	(8.1E-07)
29	-0.204937	2.000000	(9.8E-07)
30	-0.204892	2.000000	(9.7E-07)

Density of states:



Elapsed time for SCF step 7: 68.71

ETA:1.....2.....3.....4.....5.....6.....7.....8.....9.....0

***** SCF CYCLE ITER # 8 *****

etot = -7.56404884E+01 abs_ev = 8.29E-03 rel_ev = 3.11E-04
abs_dens = 2.53E-03 rel_dens = 4.22E-05

Matrix vector products: 572

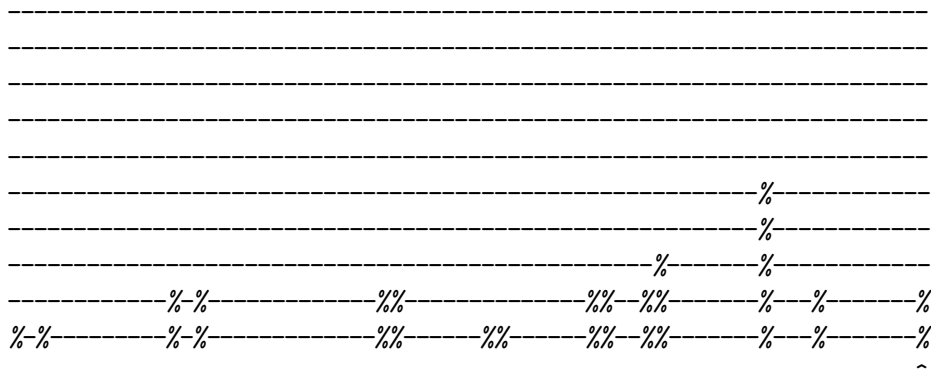
Converged eigenvectors: 6

#	State	Eigenvalue [H]	Occupation	Error
1		-0.778433	2.000000	(9.4E-07)
2		-0.762798	2.000000	(8.9E-07)
3		-0.675625	2.000000	(8.0E-07)
4		-0.675582	2.000000	(7.0E-07)
5		-0.660869	2.000000	(6.9E-07)
6		-0.660825	2.000000	(9.8E-07)
7		-0.546763	2.000000	(2.6E-06)
8		-0.546715	2.000000	(9.7E-07)

[output of 13 eigenvalues skipped: maximum error = 1.6E-06]

22	-0.308648	2.000000	(3.7E-06)
23	-0.308066	2.000000	(9.6E-07)
24	-0.301925	2.000000	(7.8E-07)
25	-0.301184	2.000000	(8.2E-07)
26	-0.300589	2.000000	(8.5E-07)
27	-0.268608	2.000000	(8.0E-07)
28	-0.268568	2.000000	(7.7E-07)
29	-0.204794	2.000000	(9.5E-07)
30	-0.204749	2.000000	(9.4E-07)

Density of states:



Elapsed time for SCF step 8: 68.82

ETA:1.....2.....3.....4.....5.....6.....7.....8.....9.....0

***** SCF CYCLE ITER # 9 *****
 etot = -7.56404884E+01 abs_ev = 4.58E-04 rel_ev = 1.72E-05
 abs_dens = 1.54E-03 rel_dens = 2.57E-05

Matrix vector products: 355

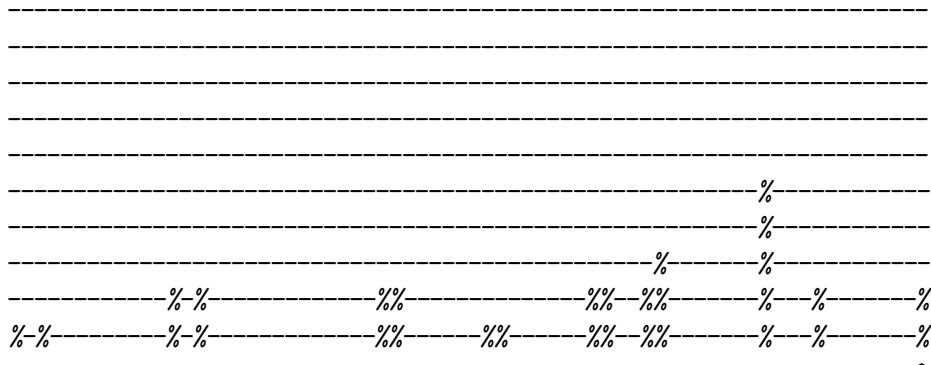
Converged eigenvectors: 6

#	State	Eigenvalue [H]	Occupation	Error
1		-0.778445	2.000000	(9.8E-07)
2		-0.762810	2.000000	(9.3E-07)
3		-0.675634	2.000000	(9.3E-07)
4		-0.675591	2.000000	(8.8E-07)
5		-0.660879	2.000000	(6.6E-07)
6		-0.660835	2.000000	(7.1E-07)
7		-0.546769	2.000000	(2.1E-06)
8		-0.546720	2.000000	(8.1E-07)

[output of 13 eigenvalues skipped: maximum error = 9.9E-07]

22	-0.308653	2.000000	(1.3E-06)
23	-0.308071	2.000000	(9.0E-07)
24	-0.301938	2.000000	(9.7E-07)
25	-0.301189	2.000000	(7.9E-07)
26	-0.300594	2.000000	(8.0E-07)
27	-0.268619	2.000000	(7.6E-07)
28	-0.268579	2.000000	(7.9E-07)
29	-0.204805	2.000000	(9.3E-07)
30	-0.204760	2.000000	(9.6E-07)

Density of states:



Elapsed time for SCF step 9: 56.57

ETA:1.....2.....3.....4.....5.....6.....7.....8.....9.....0

***** SCF CYCLE ITER # 10 *****

etot = -7.56404882E+01 abs_ev = 3.74E-04 rel_ev = 1.40E-05
 abs_dens = 4.88E-04 rel_dens = 8.13E-06

Matrix vector products: 297

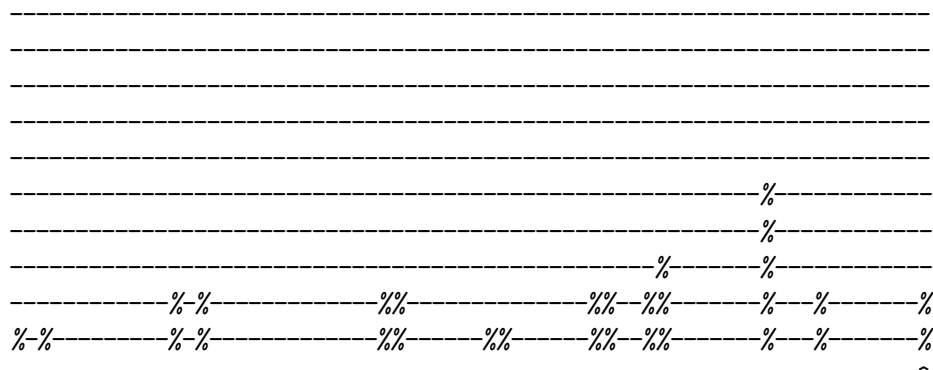
Converged eigenvectors: 6

#	State	Eigenvalue [H]	Occupation	Error
1		-0.778453	2.000000	(9.1E-07)
2		-0.762818	2.000000	(9.4E-07)
3		-0.675640	2.000000	(7.2E-07)
4		-0.675598	2.000000	(9.9E-07)
5		-0.660886	2.000000	(8.7E-07)
6		-0.660842	2.000000	(9.0E-07)
7		-0.546775	2.000000	(1.5E-06)
8		-0.546726	2.000000	(9.0E-07)

[output of 13 eigenvalues skipped: maximum error = 9.3E-07]

22	-0.308658	2.000000	(9.9E-07)
23	-0.308076	2.000000	(8.3E-07)
24	-0.301946	2.000000	(9.6E-07)
25	-0.301194	2.000000	(9.6E-07)
26	-0.300599	2.000000	(9.7E-07)
27	-0.268628	2.000000	(7.4E-07)
28	-0.268587	2.000000	(7.7E-07)
29	-0.204814	2.000000	(8.1E-07)
30	-0.204769	2.000000	(8.1E-07)

Density of states:



```
Elapsed time for SCF step    10:      53.58
*****
```

Info: Writing states. 2017/02/13 at 17:38:36

Info: Finished writing states. 2017/02/13 at 17:38:36

Info: SCF converged in 10 iterations

Info: Finished writing information to 'restart/gs'.

Calculation ended on 2017/02/13 at 17:38:37

Walltime: 13m 26.282s

Octopus emitted 3 warnings.

Octopus used 1 experimental feature:

Since you used one or more experimental features, results are likely wrong and should not be considered as valid scientific data. Check

http://www.tddft.org/programs/octopus/experimental_features

or contact the octopus developers for details.

Static information output file produced after the execution of the sample input file of Appendix B, file located at the execution directory, in static/info:

```
***** Grid *****

```

Simulation Box:

Type = minimum

Radius [b] = 9.449

Octopus will run in 3 dimension(s).

Octopus will treat the system as periodic in 0 dimension(s).

Main mesh:

Spacing [b] = (0.378, 0.378, 0.378) volume/point [b^3] = 0.05399

inner mesh = 216737

total mesh = 285121

Grid Cutoff [H] = 34.547134 Grid Cutoff [Ry] = 69.094267

```
*****
```

```
***** Theory Level *****
Input: [TheoryLevel = dft]

Exchange-correlation:
  Exchange
    Slater exchange (LDA)
    [1] PAM Dirac, Proceedings of the Cambridge Philosophical Society 26, 376 (1930)
    [2] F Bloch, Zeitschrift fuer Physik 57, 545 (1929)
  Correlation
    Perdew & Zunger (Modified) (LDA)
    [1] Perdew and Zunger, Phys. Rev. B 23, 5048 (1981)
    [2] Modified to improve the matching between the low- and high-rs parts

Input: [SICCorrection = sic_none]
*****
```

SCF converged in 10 iterations

Some of the states are not fully converged!

Eigenvalues [H]

#st	Spin	Eigenvalue	Occupation
1	--	-0.778453	2.000000
2	--	-0.762818	2.000000
3	--	-0.675640	2.000000
4	--	-0.675598	2.000000
5	--	-0.660886	2.000000
6	--	-0.660842	2.000000
7	--	-0.546775	2.000000
8	--	-0.546726	2.000000
9	--	-0.534756	2.000000
10	--	-0.534702	2.000000
11	--	-0.482849	2.000000
12	--	-0.471651	2.000000
13	--	-0.412841	2.000000
14	--	-0.410092	2.000000
15	--	-0.404155	2.000000
16	--	-0.400829	2.000000
17	--	-0.382412	2.000000
18	--	-0.382268	2.000000
19	--	-0.373296	2.000000
20	--	-0.373149	2.000000
21	--	-0.370697	2.000000
22	--	-0.308658	2.000000
23	--	-0.308076	2.000000
24	--	-0.301946	2.000000

25	--	-0.301194	2.000000
26	--	-0.300599	2.000000
27	--	-0.268628	2.000000
28	--	-0.268587	2.000000
29	--	-0.204814	2.000000
30	--	-0.204769	2.000000

Energy [H] :

Total	=	-75.64054979
Free	=	-75.64054979

Ion-ion	=	338.25899740
Eigenvalues	=	-26.61740922
Hartree	=	394.93708687
Int[n*v_xc]	=	-32.45161684
Exchange	=	-21.58017611
Correlation	=	-3.19991780
vanderWaals	=	-0.01657402
Delta XC	=	0.00000000
Entropy	=	0.00000000
-TS	=	-0.00000000
Kinetic	=	56.67577259
External	=	-840.71583199
Non-local	=	-22.79318626

Dipole: [b] [Debye]

<x>	=	-1.44403E-13	-3.67035E-13
<y>	=	-2.28201E-14	-5.80028E-14
<z>	=	5.28862E-13	1.34423E-12

Convergence:

abs_dens	=	4.87789436E-04	(0.0000000E+00)
rel_dens	=	8.12982393E-06	(1.0000000E-05)
abs_ev	=	3.73783986E-04	(0.0000000E+00) [H]
rel_ev	=	1.40428388E-05	(0.0000000E+00)

Forces on the ions [H/b]

Ion		x	y	z
1	C	-0.000000	-0.019538	0.009550
2	C	-0.017220	-0.010639	0.009872
3	C	-0.017220	0.010639	0.009872
4	C	0.000000	0.019538	0.009550
5	C	0.017220	0.010639	0.009872
6	C	0.017220	-0.010639	0.009872
7	H	0.000000	0.006036	-0.000638
8	H	0.004896	0.002826	-0.000657

9	H	0.004896	-0.002826	-0.000657
10	H	0.000000	-0.006036	-0.000638
11	H	-0.004896	-0.002826	-0.000657
12	H	-0.004896	0.002826	-0.000657
13	C	-0.000000	-0.019538	-0.009550
14	C	-0.017220	-0.010639	-0.009872
15	C	-0.017220	0.010639	-0.009872
16	C	0.000000	0.019538	-0.009550
17	C	0.017220	0.010639	-0.009872
18	C	0.017220	-0.010639	-0.009872
19	H	0.000000	0.006036	0.000638
20	H	0.004896	0.002826	0.000657
21	H	0.004896	-0.002826	0.000657
22	H	0.000000	-0.006036	0.000638
23	H	-0.004896	-0.002826	0.000657
24	H	-0.004896	0.002826	0.000657
<hr/>				
Max abs force		0.017220	0.019538	0.009872
Total force		0.000000	0.000000	0.000000
Total torque		-0.000000	-0.000000	0.000000

E. QUANTUM ESPRESSO SAMPLE INPUT: TS-VDW LIBRARY VALIDATION

```

&control
  calculation = 'scf',
  prefix = 'BZ_Dimer',
  pseudo_dir='./'
/
&system
  ibrav = 0,
  nat = 24,
  ntyp = 2,
  ecutwfc = 60,
  vdw_corr = 'ts'
/
&electrons
  mixing_beta = 0.7
  conv_thr=1.d-8
/
&ions
/
ATOMIC_SPECIES
H 1.000 H.pbe-vbc.UPF
C 12.000 C.pbe-hgh.UPF
ATOMIC_POSITIONS (angstrom)
C 0.000 1.396 2.800/2
C 1.209 0.698 2.800/2
C 1.209 -0.698 2.800/2
C 0.000 -1.396 2.800/2
C -1.209 -0.698 2.800/2
C -1.209 0.698 2.800/2
H 0.000 2.479 2.800/2
H 2.147 1.240 2.800/2
H 2.147 -1.240 2.800/2
H 0.000 -2.479 2.800/2
H -2.147 -1.240 2.800/2
H -2.147 1.240 2.800/2
C 0.000 1.396 -2.800/2
C 1.209 0.698 -2.800/2

```

C 1.209 -0.698 -2.800/2
C 0.000 -1.396 -2.800/2
C -1.209 -0.698 -2.800/2
C -1.209 0.698 -2.800/2
H 0.000 2.479 -2.800/2
H 2.147 1.240 -2.800/2
H 2.147 -1.240 -2.800/2
H 0.000 -2.479 -2.800/2
H -2.147 -1.240 -2.800/2
H -2.147 1.240 -2.800/2
CELL_PARAMETERS (angstrom)
20 0 0
0 20 0
0 0 40
K_POINTS (gamma)

F. NWChem SAMPLE INPUT: CAM-LDA0 TD-DFT CALCUALTION

```
start mol
title "CAM-LDA0 TD-DFT Calcualtion"

charge 0

memory 1000 mb
scratch_dir /home/user/scratch
permanent_dir /home/user/permanent

geometry units angstroms print xyz
  load mol.xyz
  symmetry C1
end

basis
* library cc-pVDZ
end

dft
grid fine
xc xcamlsd 1.0 hfexch 1.0 vwn_5 1.0
cam 0.3333 cam_alpha 0.25 cam_beta 0.50
mult 1
iterations 400
direct
end

tddft
rpa
notriplet
nroots 10
algorithm 1
end

task tddft energy
```

G. CALCULATED EXCITATION ENERGIES FOR SEVERAL HYBRID FUNCTIONALS

Table G.1.

Calculated excitation energies in *eV* by using several adiabatic functionals. Additional reference values included. Excitation types, CT: Charge transfer, L: Local, R: Rydberg. MAE: mean absolute error. For the dipeptide molecules the subindex 1 and 2 refer to the first and second carbonyl groups, respectively. The variable *m* is the number of units in the oligomer.

System	Transition	Type	CAM-B3LYP	B3LYP	PBE0	LDA0	LDA1	CAM-LDA0	Ref.
HCl	II	CT	7.79	7.65	7.84	7.70	7.90	7.83	8.23
CO	Σ^+	R	11.79	10.97	11.23	11.40	11.60	12.37	12.40
	Π	R	10.90	10.19	10.53	10.69	10.87	11.45	11.53
	Σ^+	R	10.80	10.13	10.46	10.62	10.80	11.34	11.40
	Σ^+	R	10.37	9.80	10.10	10.26	10.42	10.87	10.78
	Δ	L	10.08	10.03	10.05	10.00	10.23	9.98	10.23
	Σ^-	L	9.71	9.72	9.65	9.52	9.74	9.47	9.88
	Π	L	8.47	8.39	8.36	8.26	8.41	8.35	8.51
PA <i>m</i> = 2	B_u	L	6.04	5.88	5.89	5.83	5.97	5.99	5.92
PA <i>m</i> = 3	B_u	L	5.03	4.81	4.80	4.74	4.88	4.97	4.95
PA <i>m</i> = 4	B_u	L	4.39	4.13	4.67	4.63	4.19	4.63	4.41
PA <i>m</i> = 5	B_u	L	3.94	3.66	3.62	3.56	3.70	3.86	4.27
DMABN	B_2	L	4.72	4.44	4.43	4.35	4.52	4.70	4.25
	A_2	CT	4.91	4.64	4.74	4.67	4.83	4.96	4.56
PP	B_2	L	5.06	4.76	4.79	4.72	4.95	5.12	4.85
	A_1	L	5.12	4.96	4.86	4.79	5.00	5.19	5.13
	B_2	CT	5.27	4.58	4.91	4.83	5.04	5.46	5.47
	A_1	CT	5.92	4.64	5.15	5.08	5.34	6.28	5.94
Anthracene	B_{2u}	L	4.67	4.38	4.46	4.40	4.56	4.71	4.88
	B_{3u}	L	4.62	4.47	4.55	4.48	4.64	4.63	4.46
β -dipeptide	$n_1 \rightarrow \pi_2^*$	CT	8.38	7.26	6.96	6.92	7.33	9.05	9.13
	$\pi_1 \rightarrow \pi_2^{**}$	CT	8.01	7.20	6.73	6.66	6.92	8.37	7.99
	$n_1 \rightarrow \pi_1^*$	L	5.67	5.66	5.61	5.59	5.65	5.72	5.40
	$n_2 \rightarrow \pi_2^*$	L	5.76	5.56	5.69	5.67	5.73	5.79	5.10
Dipeptide	$n_1 \rightarrow \pi_2^*$	CT	7.84	6.31	6.74	6.64	7.12	8.41	8.07
	$\pi_1 \rightarrow \pi_2^*$	CT	7.00	6.15	6.50	6.32	6.72	7.23	7.18
	$n_1 \rightarrow \pi_1^*$	L	5.69	5.55	5.76	5.64	5.88	5.78	5.63
	$n_2 \rightarrow \pi_2^*$	L	5.92	5.77	6.03	5.94	6.16	6.10	5.79
MAE			0.27	0.61	0.55	0.55	0.44	0.23	

H. GAMESS SAMPLE INPUT: BASIC MAKEFP RUN

```
!
! Sample GAMESS input for EFP generation
!
$contrl units=angs local=boys runtyp=makefp
  mult=1 icharg=0 coord=cart icut=11 $end
$system timlim=99999 mwords=200 $end
$scf dirscf=.t. soscf=.f. diis=.t. conv=1.0d-06 $end
$basis gbasis=n311 ngauss=6 npfunc=2 ndfunc=3 nffunc=1
  diffsp=.t. $end
$makefp pol=.t. disp=.t. exrep=.t. chtr=.f. $end
$stone bigexp=0.0 $end
$data
  h2o
c1
  O1      8.0   0.0000000000   0.0000000000   0.0978796835
  H2      1.0   -0.4928822363  -0.5688163788  -0.4653163417
  H3      1.0    0.4928822363   0.5688163788  -0.4653163417
$end
```

I. EFPMD SAMPLE INPUT: BASIC EFP-MD RUN

```
run_type md
ensemble npt
time_step 2
print_step 100
velocitize false
pressure 1.0
coord points
terms elec pol disp xr
elec_damp overlap
disp_damp overlap
pol_damp tt
enable_pbc true
periodic_box 14.760 15.656 36.144
enable_cutoff true
swf_cutoff 7.2
max_steps 250000
userlib_path .
temperature 360

fragment water
    1.577      1.227      14.758
    1.857      1.687      15.558
    0.617      1.247      14.798

fragment water
    2.497      2.537      17.018
    2.217      2.077      17.818
    3.447      2.517      17.058

.
.
.

fragment water
    0.477      -3.913     -8.672
    0.287      -3.283     -7.972
    0.987      -3.413     -9.312
```

VITA

VITA

Carlos H. Borca was born in Cali, Colombia in 1986. He was the only child of Stella Paredes Rodríguez, a Colombian architect, and Néstor Pedro Borca, an Argentinian veterinarian.

From a young age, he attended La Pájara Pinta pre-kindergarten. Then, he coursing his primary and secondary education at Colegio Berchmans, where due to the excellent quality of his science teachers, and continuous feedback from his father, he became naturally curious about topics in chemistry and physics. Seeking answers for unholly questions in these fields, he chose to major in Chemistry. Left with no other practical option at the time, he started attending Universidad del Valle, in 2004.

As a freshman, sitting on a Physical Chemistry seminar, Carlos heard about something the speaker dubbed *The Holy Trinity of Chemistry*. It was an idea of how experimentalists, theoreticians, and computational chemists should work together in solving problems that would be best engaged in collaboration. It became clear how combining the power of theory and computation was essential to the advance of chemistry. The seed of curiosity, that was planted on him that day, would later grow as the inspiration to study theoretical and computational chemistry. The speaker, Prof. Julio C. Arce, would later become his undergraduate research mentor, advising him until graduation with honors for a meritorious thesis in 2009.

Immediately after his graduation, Carlos started working as a Physical Chemistry Laboratory Lecturer at Universidad Icesi, where he discovered that sharing knowledge was genuinely rewarding. He soon became a Young Scientist and Innovator Scholar with funding from the Administrative Department of Science, Technology and Innovation of the Colombian Government (Colciencias), and began working as

a researcher in theoretical and computational chemistry advised by Prof. Carlos A. Arango.

Prof. Arango strongly encouraged Carlos to continue with his graduate studies. Therefore, in 2009, he moved out of his hometown, for the first time, and traveled to the United States to attend Purdue University in West Lafayette, Indiana. He initially worked with Prof. Adam Wasserman, and then transitioned to join Prof. Lyudmila V. Slipchenko's research group. He also worked with Dr. Xavier Andrade and Dr. Alfredo A. Correa, for a brief period of time, as a research intern at the Lawrence Livermore National Laboratory, in California, during the Computational Chemistry and Materials Science Institute of 2015.

His doctoral research was mainly focused on Polarizable Molecular Dynamics and Density Functional Approximations to approach intermolecular interactions. After graduation, Carlos hopes to continue his path in academia with a postdoctoral research appointment in the group of Prof. C. David Sherrill at the Georgia Institute of Technology. His final goal is to become a research professor in theoretical and computational chemistry.

PUBLICATIONS

Ground-State Charge Transfer: Lithium–Benzene and the Role of Hartree–Fock Exchange

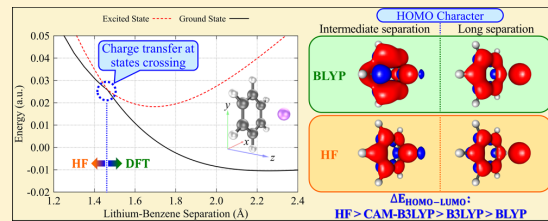
Carlos H. Borca,[†] Lyudmila V. Slipchenko,^{*,†} and Adam Wasserman^{*,†,‡}

[†]Department of Chemistry, Purdue University, 560 Oval Drive, West Lafayette, Indiana 47907, United States

[‡]Department of Physics and Astronomy, Purdue University, 525 Northwestern Avenue, West Lafayette, Indiana 47907, United States

Supporting Information

ABSTRACT: Most approximations to the exchange-correlation functional of Kohn–Sham density functional theory lead to delocalization errors that undermine the description of charge-transfer phenomena. We explore how various approximate functionals and charge-distribution schemes describe ground-state atomic-charge distributions in the lithium–benzene complex, a model system of relevance to carbon-based supercapacitors. To understand the trends, we compare Hartree–Fock (HF) and correlated post-HF calculations, confirming that the HOMO–LUMO gap is narrower in semilocal functionals but widened by hybrid functionals with large fractions of HF exchange. For semilocal functionals, natural bond orbital (NBO) and Mulliken schemes yield opposite pictures of how charge transfer occurs. In PBE, for example, when lithium and benzene are <1.5 Å apart, NBO yields a positive charge on the lithium atom, but the Mulliken scheme yields a negative charge. Furthermore, the partial charges in conjugated materials depend on the interplay between the charge-distribution scheme employed and the underlying exchange-correlation functional, being critically sensitive to the admixture of HF exchange. We analyze and explain why this happens, discuss implications, and conclude that hybrid functionals with an admixture of about one-fourth of HF exchange are particularly useful in describing charge transfer in the lithium–benzene model.



1. INTRODUCTION

Porous carbon materials have great potential for the construction of novel electric energy storage (EES) devices such as supercapacitors.^{1–3} Because of experimental limitations, high costs of nanotechnology research, and importance of quantum effects, computational-aided fabrication of carbon materials for supercapacitors is promising.^{4–7} Often, classical force fields provide useful data for calculations of chemical stability, adsorption and desorption dynamics, and other properties of these materials.⁸ Yet the exploration of quantum phenomena such as charge transfer, which is at the heart of the working mechanism of supercapacitors, requires ab initio treatment. The goal of this study is to investigate whether standard approximations in Kohn–Sham density functional theory (KS-DFT),^{9,10} when used in combination with popular charge-distribution schemes,¹¹ provide an adequate description of the ground-state charge transfer that occurs in a very simple model system: the lithium–benzene complex. Some of the key features observed in this system are due to the interaction between a lithium atom that can be easily ionized and a benzene ring whose valence electrons are delocalized due to aromaticity, so our observations are relevant to the much more complex simulations of carbon nanoporous electrodes in supercapacitors,¹² where such interactions are ubiquitous. More generally, we want to determine how different charge-distribution schemes perform for various families of approx-

imate exchange-correlation (XC) functionals and understand the trends.

KS-DFT is an extraordinarily popular electronic structure method applied throughout science and engineering.¹³ As is well known, however, approximate KS-DFT calculations suffer from problems that need to be addressed.¹⁴ For instance, most standard approximations to the XC functional underestimate charge-transfer excitation energies and overestimate binding energies of charge-transfer complexes.^{15,16} Mori-Sánchez et al.¹⁷ and Cohen et al.¹⁸ demonstrated that this problem can be traced back to the delocalization error of approximate functionals: their tendency to minimize the energy by unrealistically spreading-out the electronic density, especially at large separations between the fragments involved in the charge transfer. As discussed by Cohen et al.,¹⁵ this inaccuracy is closely related to the self-interaction error, and it is caused by the unphysical convex behavior of the energy as a function of fractional charge.

Properties of alkali-conjugated complexes have been explored in several computational studies.^{19–25} For instance, studying the conformation of complexes of lithium and C₆₀ fullerenes, Varganov et al. found a strong ionic interaction between the atom and the fullerene.²⁶ The structures and dissociation

Received: September 6, 2016

Revised: September 22, 2016

Published: September 23, 2016

energies of lithium and benzene sandwich complexes were researched by Vollmer et al. using several quantum-mechanical methods.²⁰ Kang studied the formation of neutral lithium–aromatic complexes and found that it originates in the charge transfer from the lithium atom to the aromatic rings.²¹ An emerging discussion about the existence of charge transfer between lithium and aromatic carbon compounds motivated Ferre-Vilaplana²² and Martinez et al.²³ to look into the lithium–benzene complex. Marshall et al. explored cation–π interactions, modeling the approach of alkali cations to a benzene ring from different angles and inclinations, pointing out that nonperpendicular interactions in cation–benzene complexes are attractive.²⁴

In response to the controversy about charge transfer, Baker and Head-Gordon²⁷ studied a set of polycyclic aromatic carbon systems with lithium, which included the lithium–benzene complex, and suggested that some density-functional approximations may produce artificial charge transfer due to the self-interaction error, whereas Hartree–Fock (HF) underestimates the amount of charge transfer as a result of overlocalization. Inspired by that work, Denis and Iribarne²⁸ used the lithium–benzene complex as a prototype system to understand the interaction in lithium-doped carbon compounds, focusing on the relationship between its symmetry and stability. Employing highly sophisticated techniques, they concluded that charge transfer does indeed occur.

We ask two questions that are relevant in this context: (1) What do popular charge-distribution schemes such as NBO, MPA, and ChEIPG tell us about ground-state charge transfer in the lithium–benzene complex? (2) How does the answer to question (1) depend on the approximation employed for the XC functional? As will be made clear, the admixture of HF exchange in the functional plays a critical role. Resorting to HF and post-HF multistate calculations, we explain why. First, we summarize in the next section the computational methods employed.

2. COMPUTATIONAL METHODS

Ground-state electron transfer is studied as a function of the separation between a lithium atom and the center of a benzene ring. A potential energy rigid scan (PES) is performed along the coordinate of separation between the center of mass (COM) of the benzene molecule and the lithium atom, perpendicular to the plane of benzene (see Figure 1). This is done in a series of unrestricted single-point calculations,²⁹ where the lithium atom advances toward the benzene molecule along the main symmetry axis, while the geometry of the benzene molecule, optimized with B3LYP/6-31G*, is kept fixed. The atom starts its path toward the ring at 7.0 Å, moving at 0.1 Å steps, and totaling 71 points. Initial separation of 7.0 Å guarantees minimal interaction between the two fragments. The electronic structure and the atomic charge on lithium are analyzed as a function of separation. For consistency, all calculations are carried out with the same basis set, 6-31G*, in the computational chemistry package Q-Chem 4.3.^{30–32} The self-consistent field convergence criteria are chosen such that the Direct Inversion in the Iterative Subspace error is below 1.0×10^{-9} . For each geometry, the lowest energy solution was found by employing the maximum overlap method (MOM)³³ when necessary.

Two sets of approximate functionals are employed. Each set has functionals from different rungs in Perdew's Jacob's ladder of approximations¹³ or levels of sophistication. On the one

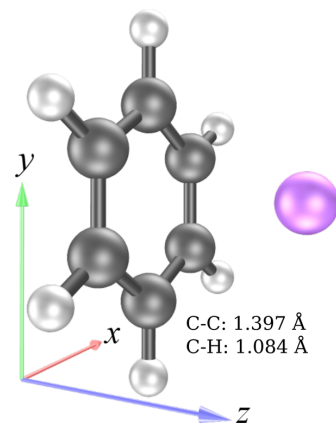


Figure 1. Lithium–benzene complex. The lithium atom is displaced along the *z* axis toward the center of the benzene ring.

hand, PES calculations are performed with PBE,³⁴ PBE0,³⁵ PBE50,³⁶ and LRC- ω PBEPBE³⁷ functionals. PBE is a non-empirical generalized gradient approximation (GGA) with exchange and correlation expressions derived from physical constraints. The hybrids PBE0 and PBE50 are prepared by admixing 25 and 50% of E_x^{HF} , respectively, as this inclusion is believed to improve atomization energies, energy barriers, and energy gaps in materials without impacting computational performance.^{38,39} A different way of including a fraction of E_x^{HF} in hybrids is through the long-range correction (LRC), as in LRC- ω PBEPBE. In LRC functionals, the $1/r_{12}$ dependence of the exchange potential is decomposed into an error function of ωr_{12} , which accounts for the amount of E_x^{HF} and governs the long-range behavior, and its complementary, which corresponds to pure-DFT-exchange, E_x^{DFT} , and rules short-range interactions. ω is a range-separation parameter that adjusts the distance at which the E_x^{DFT} vanishes.

On the other hand, BLYP,⁴⁰ B3LYP,⁴¹ and CAM-B3LYP⁴² were used. BLYP is a simple GGA constructed by putting together the pure-DFT Becke88-exchange⁴³ and the Lee–Yang–Parr correlation⁴⁴ functionals. Replacing the exchange with a mixture of Slater-,^{9,10,45} Becke88-, and HF-exchange and combining VWNS-⁴⁶ and LYP-correlation produces the highly popular B3LYP hybrid. CAM-B3LYP is another LRC hybrid prepared by using the Coulomb Attenuated Method (CAM) for long-range exchange correction. The decomposition of $1/r_{12}$ in the calculation of E_x is done by including two parameters. The second parameter avoids vanishing of E_x^{HF} at short distances and of E_x^{DFT} at long distances. Notably, CAM-B3LYP does not include Slater-exchange, as opposed to B3LYP.

In addition to the KS-DFT calculations, lithium–benzene interaction energies are computed with HF, second- and fourth-order Moller–Plesset perturbation theory (MP2, MP4),⁴⁷ and coupled-cluster with single and double excitations method (CCSD).^{48,49}

To better understand charge-transfer behavior, we employ the equation-of-motion coupled-cluster method with single and double excitations for electron attachment (EOM-EA-CCSD).^{50–52} EOM-EA-CCSD provides information on both ground- and excited-state PESs, allowing us to relate charge-transfer to the interaction of the ground state and the excited states that have charge-transfer character. Chemically important

regions of the excited-state PESs are computed on a tighter grid, such that the whole PES comprises 221 points computed with uneven displacements ranging from 0.005 to 0.1 Å.

The partial charge on the lithium atom is computed by means of Mulliken Population Analysis (MPA),⁵³ natural bonding orbital theory (NBO),⁵⁴ Chemical Electrostatic Potentials using a Grid (ChEIPG),⁵⁵ as well as a simple estimate based on the magnitude of the dipole moment, μ

$$Q_A^{\mu/z}(z) = \frac{\mu}{z} \quad (1)$$

where z is the separation between fragments and $\vec{\mu}$ is the dipole-moment vector defined as

$$\vec{\mu} = \int d\vec{r} n(\vec{r}) z \hat{k} \quad (2)$$

where $n(\vec{r})$ is the ground-state electron density and \hat{k} is the z -direction unitary vector.

Interaction energy curves are calculated as the difference between the total ground-state energy of the system, at each point, and the sum of the energies of the isolated fragments: the benzene molecule and the lithium atom

$$E_{\text{int}}(z) = E_{\text{C}_6\text{H}_6\text{Li}}(z) - (E_{\text{C}_6\text{H}_6} + E_{\text{Li}}) \quad (3)$$

3. RESULTS AND DISCUSSION

We divide the discussion into five parts. The first two parts analyze in detail atomic charges and molecular orbitals (MOs). The next two sections compare (single-state) KS-DFT results with those of a multistate approach. The final section discusses the description interaction energies.

3.1. Charge Distributions. We summarize our results of the charge-distribution analyses in Figure 2, where the reader can verify that the calculated charge on the lithium atom strongly depends on both the nature of the approximate XC functional and the charge-distribution scheme employed. We discuss the latter dependence first.

Interestingly, in Figure 2, natural charges from NBO (blue solid lines) and Mulliken charges (green long-dashed lines) show opposite results. The Mulliken charge on lithium tends to be negative. This can be understood by examining the definition of the Mulliken charge for open-shell systems. The charge belonging to atom A , Q_A^{MPA} , is expressed by

$$Q_A^{\text{MPA}} = Z_A - \sum_{\nu \in A} \sum_{\mu} \sum_i (C_{\mu i}^{\alpha} C_{\nu i}^{\alpha*} + C_{\mu i}^{\beta} C_{\nu i}^{\beta*}) S_{\mu \nu} \quad (4)$$

where Z_A is the atomic number of atom A , $C_{\mu i}^{\alpha}$ and $C_{\nu i}^{\alpha*}$ are the matrix elements representing the alpha coefficients of the basis functions μ and ν , respectively, in the i th MO, and $S_{\mu \nu}$ is the matrix element representing the overlap-integral between basis functions μ and ν . The same notation applies for beta orbitals, substituting the α superscript by β . The second term on the right-hand side, often called the gross atomic product, is computed by taking the sums of the product of the coefficients of two basis functions and their overlap. If several basis functions overlap on the lithium atom, which is the case at short distances, the corresponding gross atomic product increases, making the Mulliken charge more negative.

These effects had been previously observed, in general, by Reed et al.⁵⁶ and Kim et al.,⁵⁷ and, in particular, for the lithium–benzene complex by Vollmer et al.²⁰ They pointed out that Mulliken populations and charges are highly susceptible to

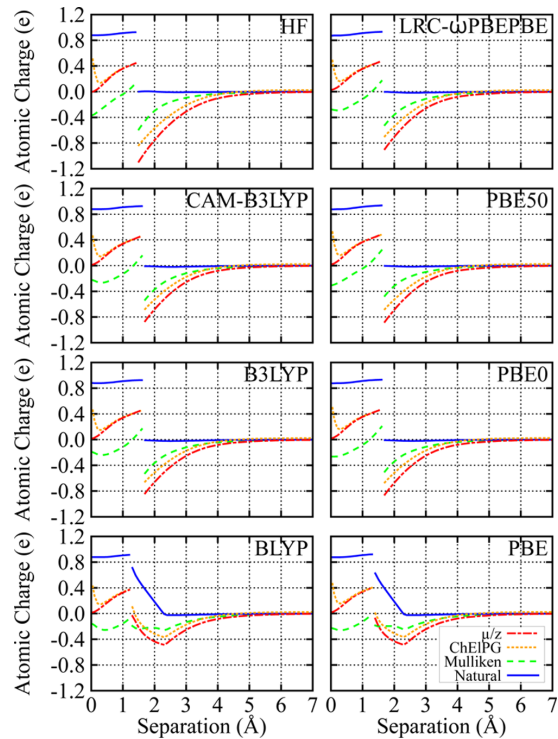


Figure 2. Charge accumulated over the lithium atom as a function of the separation between fragments in the lithium–benzene complex. Noteworthy, charge-distribution schemes produce diverse results. By admixing HF exchange, the description of the charge transfer changes.

the basis set employed and become ambiguous when utilized with diffuse basis sets.

ChEIPG is an alternative to explore atomic charges. It uses the electrostatic potential (ESP) computed from the system's wave function on a grid and then tries to match that ESP by optimizing a set of trial point charges located at the nuclei. ChEIPG curves (orange short-discontinuous lines in Figure 2) are smooth at long and medium distances, in agreement with those of Mulliken. However, as the atom moves toward the cavity formed by the benzene ring, ChEIPG shows a sheer behavior when the atom is too close to the ring's surface and the ESP is poorly described.

The dipole-based scheme of eq 1 (red dotted line in Figure 2) agrees qualitatively with Mulliken and ChEIPG at medium and large distances, but the scheme clearly breaks down at short separations, where the classical expression for the dipole as generated by point charges is not adequate.

In contrast with other schemes, the variations of the natural charge on the lithium atom are solely due to changes in the occupation of bonding and nonbonding orbitals. In the NBO theory, orbitals are classified into three groups: nonbonding natural atomic orbitals, orbitals involved in bonding and antibonding, and Rydberg-type orbitals. Atomic and Rydberg orbitals are made of basis functions of single atoms, whereas bonding and antibonding orbitals are a combination of basis functions of two atoms. This resembles Lewis' idea of core, lone pair, and valence electrons. Thus, the NBO procedure treats the bonding and antibonding orbitals as linear combinations of

two-atom basis functions, while Mulliken analysis treats all of the orbitals as linear combinations of two-atom basis functions.¹¹ At the end, an orthonormal set of localized maximum-occupancy orbitals is produced. The leading N members of this set give a Lewis-like description of the total electron density.

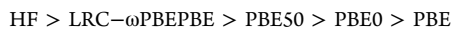
Notably, the NBO scheme reveals extreme behaviors, showing either no charge accumulation on lithium at long separations or a sudden change in the lithium charge at short separations. BLYP and PBE are the exceptions, showing an intermediate region in which there is an incremental accumulation of positive charge. In all cases, the lithium natural charges at short separations become positive and close to 1 e .

Different charge-distribution schemes thus provide qualitatively different results. Natural charges have the advantage of not being as susceptible to basis-set issues as Mulliken charges or to surface effects as ChElPG charges.²⁰ As it will be shown in the next section, natural charges are in agreement with the analysis of the MOs for this system.

Figure 2 also provides a comparison between approximate XC functionals of similar complexity. At long distances, all KS-DFT calculations and HF go to the correct separation limit with no partial charges on either fragment. At short separations, all functionals and HF predict charge transfer from lithium to benzene. However, pure-DFT functionals, BLYP and PBE, show a different picture at intermediate separations. Namely, all charge schemes reveal a growth of fractional, positive charge on the lithium atom in the region between 2.3 and 1.3 Å for these two functionals. To understand this, we analyze valence MOs next.

3.2. Frontier Molecular Orbitals. We plot in **Figure 3** the energies of relevant alpha MOs. A correlation between the qualitative description of charge transfer described in the previous section, the energy difference between the highest occupied molecular orbital (HOMO) and the lowest unoccupied molecular orbital (LUMO), the character of the frontier MOs, and the contribution of E_x^{HF} becomes evident. For more clarity, we discuss first the results of the functionals of the PBE family, shown on the right-hand side of **Figure 3**, and compare them with HF (top left).

The HOMO–LUMO gap width at large separation follows the trend



In general, the gap width decreases due to the stabilization of unoccupied orbitals (dotted lines) and destabilization of occupied orbitals (continuous line) following the same trend. Notably, for separations between 1.3 and 2.3 Å, PBE and BLYP have no gap, promoting delocalization.

As shown in **Figure 2**, all charge distribution schemes except for NBO show some degree of charge transfer even at medium distances, reflecting HOMO delocalization between the lithium atom and the benzene ring. This is a manifestation of HOMO hybridization. When the character of the HOMO changes, it produces discontinuities in atomic-charge curves. PBE is the most interesting case, so we discuss it in detail using **Figure 4**, which compares HOMOs, at three characteristic separations, in HF (**Figure 4a–c**), PBE0 (**Figure 4d–f**), and PBE (**Figure 4g–i**). The reader may also refer to the Supporting Information for additional details supporting this discussion.

On the one hand, as shown in the top row of **Figure 4**, the contribution from benzene's π bonding orbital (or A_{2u}) (here and later benzene orbital symmetries are based on D_{6h} point

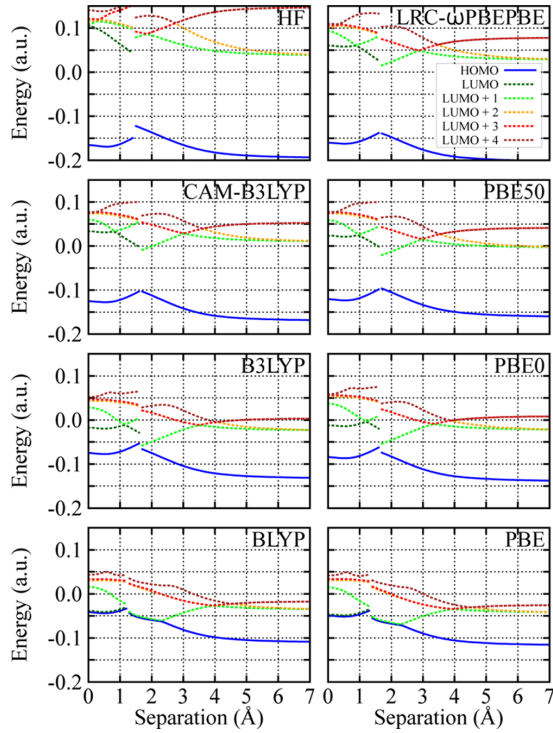


Figure 3. Frontier molecular orbital energies, as a function of the separation between fragments, for each density functional approximation applied to the lithium–benzene complex. When the HF character of the exchange functional increases, the occupied molecular orbitals are stabilized, while the unoccupied orbitals are destabilized.

group) to the long-range HF HOMO increases as the separation shortens, implying that the weight from benzene's basis functions is becoming predominant in the complex. As the atom approaches the ring, larger portions of lithium's p_z and benzene's p_z basis functions are incorporated into the HOMO, at the expense of a smaller share of lithium's s atomic orbitals (compare **Figure 4b** and c and see Supporting Information). Notwithstanding, we find no evidence of charge transfer in **Figure 4b** and c because the lithium atom always contributes to the HOMO.

On the other hand, inspection of the PBE HOMO at the bottom in **Figure 4** suggests that at large separation it has a main contribution from lithium's s orbital and a minor contribution from benzene's A_{2u} orbital, similar to HF (compare **Figure 4c** and i and see Supporting Information). Nonetheless, the contribution from p_z orbitals from both lithium and benzene is marginally greater in PBE, while the weight of lithium's s basis functions slightly decreases. This is reflected in a smoother and slightly more spread-out surface of the PBE HOMO over the benzene ring.

At medium separations, the character of the HOMO in PBE changes, in contrast with HF (compare **Figure 4b** and h). Instead of having an important contribution from benzene's π (A_{2u}), we see a predominant π^* (E_{2u}) antibonding character in PBE. In the same range of separations (1.3 to 2.3 Å), HOMO and LUMO energy curves in PBE become degenerate and experience a kink (see **Figure 3**). In this region, the frontier

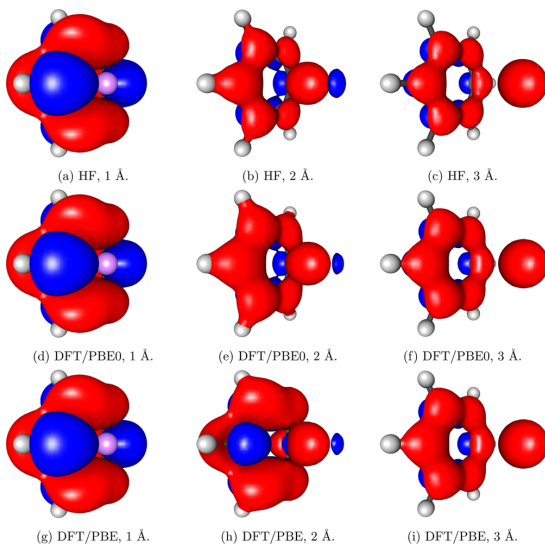


Figure 4. Evolution of the lithium–benzene highest occupied molecular orbital (HOMO) as a function of the separation between fragments, for HF, PBE0, and PBE. The HOMO adopts one character at long separation and another one at short separation in HF and PBE0, whereas in PBE it exhibits three different characters. Interestingly, at separations shorter than 1.3 Å, the HOMO is exclusively localized over the benzene molecule in all cases.

MOs consist of the E_{2u} orbital of benzene and an s-p_z hybridized orbital on lithium (see Figure 4g). Also, natural charges suggest that this intermediate state involves a partial charge transfer between the lithium atom and benzene molecule (see Figure 2).

At short separations, PBE predicts complete electron transfer from lithium to benzene. The HOMO localizes over the benzene ring and misses any contribution from lithium's basis functions. Additionally, the character of the HOMO and LUMO changes again (compare Figure 4g and h), and the HOMO–LUMO degeneracy is broken (see Figure 3). Thus, at short separations, PBE and HF show the same charge-transfer state (see Figure 2 and Supporting Information).

The PBE0 HOMO, shown at the center in Figure 4, transforms as the HF HOMO. The main difference of PBE0 with respect to pure PBE is the absence of the intermediate-separation state (compare Figure 4e and h). In PBE0, the system abruptly switches from the long-range neutral state to the short-range charge-transfer state at ~1.65 Å (see Figures 2 and 3). Likewise, the evolution of the HOMO in PBE0 and LRC- ω PBEPBE is analogous to that observed in HF.

The other set of functionals, including BLYP, B3LYP, and CAM-B3LYP, follows the previous description closely, as seen in Figures 2 and 3. As with PBE, an intermediate state is also observed with BLYP. In the BLYP-family functionals, the trend of the HOMO–LUMO gap is



Therefore, in both PBE and BLYP families of functionals, the character of the frontier MOs and their energies depend strongly upon the admixture of E_x^{HF} . The difference between the functionals in each set is the proportion of E_x^{HF} . Our calculations show that the HOMO–LUMO gap increases

with the amount of E_x^{HF} and is the largest in HF. Additionally, functionals with a narrow HOMO–LUMO gap exhibit an intermediate partial-charge-transfer state. The charge transfer occurs at longer intermonomer separation in functionals with no E_x^{HF} . Is the charge transfer between lithium and benzene a real phenomenon? Which functional and which partial-charge scheme provide the best description of the lithium–benzene complex? We explore these questions in detail in the next two sections of the paper.

3.3. State-Crossing. In the first two sections of this discussion, the variation of charge accumulation on lithium was related to a change in character of the wave function along the lithium–benzene separation. The abrupt change in the wave function character suggests the existence of a state crossing. While the description of a state crossing by single-reference methods is generally nontrivial, a few techniques are available, including wave function stability analysis,⁵⁸ symmetry-enforced self-consistent field convergence, constrained DFT methods,^{59,60} and so on. To find the lowest energy solution for each separation between lithium and benzene, we employed the MOM by Gilbert et al.³³

If the MOM is triggered on the first cycle of the self-consistent procedure, it holds the initial configuration by choosing occupancies that maximize the overlap of the new occupied orbitals with the set previously occupied. In our case, when the calculation of the PES starts from long separations, the MOM, accompanied by reading orbitals from a previous geometry, helps maintaining the neutral-state character [$\square\cdots\text{Li}^-$]. On the contrary, starting from short separations, the charge-transfer state [$\square\text{Li}^+$] can be enforced and kept.

Electronic energies of the neutral and charge-transfer states obtained with the MOM are presented in Figure 5. The curves are plotted using only those calculations in which the self-consistent field procedure converged under tight criteria. State crossings are clearly observed in all cases except BLYP and PBE, both of which become unstable in the region near the crossing. This instability is manifested by the presence of an intermediate state seen in Figure 3. We note that the convergence of the higher energy state is more stable when the proportion of E_x^{HF} is greater, such that the most stable MOM calculations are those of HF.

Comparison of HF and DFT state-crossing curves suggests that the charge-transfer state in HF is displaced to higher energies with respect to the neutral state, causing a shift of the crossing to shorter separations. Indeed, the crossing occurs at ~1.65 Å in all hybrid and LRC functionals, whereas in HF it is located at ~1.45 Å. A relative overstabilization of the charge-transfer state in functionals, with respect to HF, is consistent with narrower HOMO–LUMO gaps in functionals than in HF, as discussed in Section 3.2.

The separation at which the state crossing appears in B3LYP coincides with that at which HOMO and LUMO energies nearly collide in Figure 3. A similar situation is observed for PBE0, although the HOMO–LUMO gap is slightly wider. This suggests that one could correctly estimate the position of a state-crossing in PBE0 and B3LYP by monitoring the HOMO–LUMO gap. However, this is not true in general.

3.4. Excited-State Calculations. The calculations discussed hitherto are based on single-referenced methods. To better understand the physics of charge transfer in our model system, we now calculate the interaction of the ground and excited charge-transfer states using a method that is capable of describing several electronic states on equal footing. For this

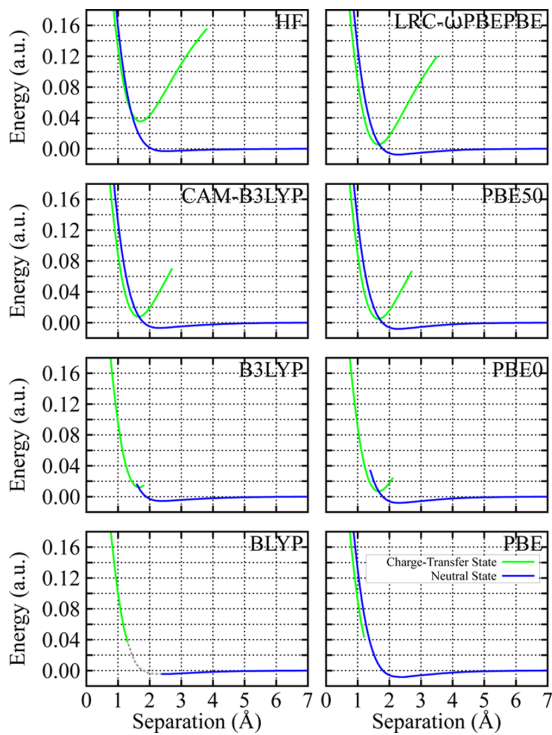


Figure 5. Energy of the electronic states as a function of the separation between the plane of benzene and the lithium atom, obtained by the maximum overlap method. The neutral state is plotted with a blue line. The charge-transfer state is depicted in green.

purpose, it is possible to use a multireference method such as multiconfigurational self-consistent field (MCSCF), multireference perturbation theory (CASPT2, MRPT, MCQDPT), or multireference configuration interaction (MRCI).⁶¹ We use an alternative method for describing electronic states in the lithium–benzene complex, namely, EOM-EA-CCSD. This sophisticated treatment provides a robust description of radical systems, correctly capturing the multiconfigurational nature of electronic states by using a single-reference formalism.⁵²

The closed-shell cation state $[\square \cdots \text{Li}^+]$ is taken as a reference state in EOM-EA-CCSD, while electronic states of a neutral complex are obtained by creating an electron on any vacant orbital. These electronic configurations constitute single excitations. Additionally, electronic configurations in which the creation of an electron on a virtual orbital is accompanied by the excitation of another electron (double excitations) are also included in the subspace in which the Hamiltonian is diagonalized. Thus, in the EOM-EA-CCSD formalism both the ground and charge-transfer states of the lithium–benzene complex are obtained as single excitations from the cation reference state and are expected to be described with similar quality. Therefore, EOM-EA-CCSD provides an accurate location of the state crossing if there is one.

The results obtained with the EOM-EA-CCSD method are presented in Figure 6. The character of the electronic states might be derived from the shapes of the singly occupied molecular orbitals (SOMOs) of the leading configuration for each state. For example, in the large-separation limit, one can

clearly see electronic states corresponding to excitations on lithium: the $1s^22s^1$ ground state (in black), the degenerate pair of $1s^22p_x^1$ and $1s^22p_y^1$ (in red), and the $1s^22p_z^1$ (in orange). A crossing of the ground and charge-transfer states is observed at 1.465 Å. At separations shorter than this, the character of the ground state switches from a neutral state, with the SOMO represented mainly by the 2s orbital of the lithium atom, to a degenerate pair of the charge-transfer states, with the SOMO being one of the π^* orbitals of benzene. Note that the crossing of the ground and charge-transfer states is a real crossing, rather than an avoided crossing because the states involved do not mix by symmetry. This is also true for other state crossings seen in Figure 6. The position of the state crossing between the ground and charge-transfer states predicted by EOM-EA-CCSD better agrees with HF than standard-hybrid or LRC functionals, and it disagrees with the description of pure functionals BLYP and PBE, which exhibit an unphysical intermediate state. In contrast with Mulliken and ChelpG, NBO charges respond consistently with the appearance of the crossing of the neutral and ionic states for each of the hybrid functionals and HF.

However, as it is obvious from Figure 6, the position of the state crossing depends upon the shape and depth of the potential curves of both the ground and charge-transfer states. In particular, overestabilization of the ionic state results in an early charge transfer, as is observed in BLYP and PBE. These functionals produce an intermediate spurious state in which fractional atomic charges increase from 0 to almost 1 in the region between 1.3 and 2.3 Å, as seen in Figure 2. This raises a red flag when using standard KS-DFT for modeling charge transfer in conjugated materials: The functional needs to be carefully selected to predict the charge transfer at the correct separation between moieties, or alternative computational schemes must be used. In the model system considered, B3LYP and PBE0 are close to the correct behavior.

3.5. Interaction Energy. We now turn our attention to the calculation of interaction energies from Equation 3. Figure 7 summarizes our results obtained via correlated wave function methods and various density-functional approximations. As expected, the HF equilibrium distance, ~2.5 Å, is longer than the distance obtained with CCSD, ~2.25 Å, both in agreement with those reported by Baker and Head-Gordon.²⁷ An old experimental study by Manceron and Andrews⁶² estimates a separation of ~1.8 Å based on gas-phase infrared spectra of lithium–benzene in argon, but it is unclear if this corresponds to the neutral or cationic species. A previous *in silico* study by Vollmer et al.²⁰ on the neutral complex reports 2.252 Å (black, dashed, vertical line on Figure 7), calculated with MP2(FC)/6-31G(d). Zhengyu et al.¹⁹ reported 2.600 Å with MP2/6-31G and 2.511 Å with HF/6-31G(d).

In agreement with the results by Vollmer et al., we observe that HF underbinds the lithium–benzene complex, highlighting the importance of correlation effects. Our HF interaction energy, −0.0031 a.u., is close to the one they reported at the minimum: −0.0029 a.u.²⁰ To our knowledge, the most accurate interaction energy in lithium–benzene is −0.0078 a.u. (black, dashed, horizontal line on Figure 7), reported by Denis and Iribarne,²⁸ who calculated it at the CCSD(T)/CBS level, including corrections for core correlation and relativistic effects. Vollmer et al.²⁰ reported a value of −0.0092 a.u. using the G3(MP2)⁶³ method.

We now compare against our CCSD interaction curve to meaningfully contrast the results from different methods without the influence of basis set and basis-set superposition

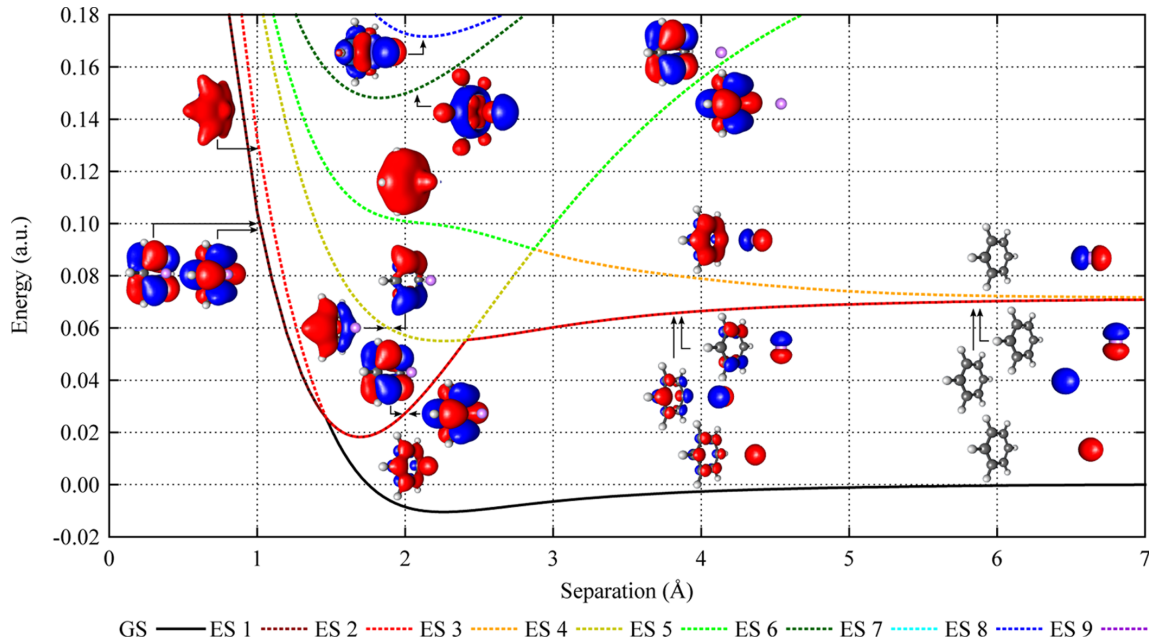


Figure 6. Energy of the electronic states as a function of the separation between the plane of benzene and the lithium atom, obtained by the EOM-EA-CCSD method. The ground-state (GS) is plotted with a continuous black line. Dotted lines represent the first nine excited states (ESs). Singly occupied molecular orbitals (SOMOs) corresponding to the leading configuration of each state are shown at several separations. A crossing between the long-separation ground state, in which the SOMO is mainly localized over lithium, and a charge-transfer state, in which the SOMO localizes exclusively over the benzene molecule, occurs at about 1.5 Å.

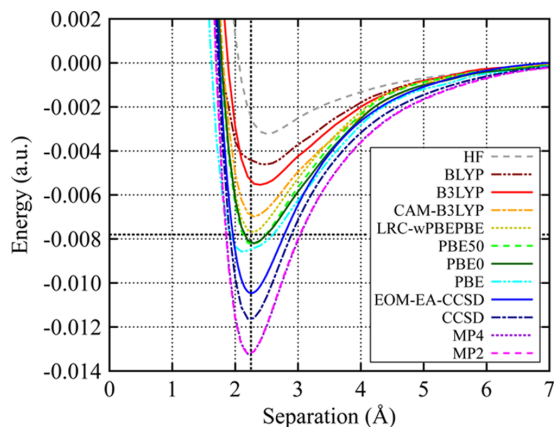


Figure 7. Interaction energy of the lithium–benzene complex computed by different methods. The black dotted horizontal line corresponds to the most accurate interaction energy in lithium–benzene found in the literature.²⁸ The black dotted vertical line indicates the most accurate equilibrium distance.²⁷ All results of the present work are obtained in 6-31G* basis.

errors. The minimum energy from our CCSD calculation is -0.0114 a.u. and the separation at that point is 2.2 Å. MP2 and MP4 show very similar results and their curves overlap in Figure 7. Also, MP2 calculations agree with those of Vollmer et al.²⁰ Nonetheless, it is known that the MP methods may overestimate the dispersion energy⁸ and overbind the complex.

In general, approximate DFT calculations do better than HF, but they still underbind the complex when compared to CCSD. Even though GGAs and standard hybrids account for local and semilocal correlation, the long-range part of correlation is not properly described.¹¹ Functionals derived from PBE show similar interaction-energy curves, with a slight decrease in the binding energy when the amount of E_x^{HF} increases. That is, the binding energy follows the trend

$$\text{HF} < \text{LRC}-\omega\text{PBE/PBEPBE} < \text{PBE50} \approx \text{PBE0} < \text{PBE}$$

The PBE binding energy shows an unphysical wide well near the equilibrium separation. This is because the character of the PBE ground state changes near the equilibrium distance (compare Figure 4b and h), such that the repulsive side of the well is determined by the intermediate state with partial charge-transfer character. In other functionals of the PBE family and in HF, this intermediate state does not exist and the charge transfer occurs at a shorter-than-equilibrium distance, such that neither the interaction energy nor the equilibrium position is affected by the charge-transfer phenomenon.

A rather unexpected behavior is observed in BLYP-related functionals. The CAM-corrected functional describes the interaction energy better than either B3LYP or BLYP. Thus the trend is opposite to that of PBE-related functionals: The binding energy in the BLYP-derived functionals increases with the proportion of E_x^{HF} . It is hard to point out the exact origin of the difference because neither E_x nor E_c is easily comparable between BLYP-related functionals. Finally, similar to PBE, the BLYP binding curve exhibits a wider well due to a state crossing near the equilibrium separation.

4. CONCLUSIONS

We assessed how several functionals model ground-state charge transfer and predict charge distributions in the lithium–benzene complex. This model illustrates an all-too-common problem in computational chemistry: With results hinging on a delicate combination of methods, the interplay of approximate functionals and charge-distribution schemes can lead to drastically different qualitative pictures of ground-state charge transfer.

Functionals with an admixture of E_x^{HF} are useful in describing charge transfer in the lithium–benzene complex. The HOMO–LUMO gap is widened when the proportion of E_x^{HF} is increased, a consequence of the stabilization of the occupied MOs and the destabilization of the unoccupied MOs.

Despite the existence of a state crossing that induces charge transfer, the crossing occurs in the repulsive region of the interaction curve, leaving the equilibrium region unaffected in hybrid functionals and HF. However, the equilibrium region is incorrectly described by pure functionals PBE and BLYP because of a crossing with an artificial state. Ground-state charge distributions display sharp features when state crossings occur, as is clear from Figures 2 and 5.

While modeling the state crossing is prone to errors when using single-reference methods, high computational cost might hinder the use of multireference or excited-state methods for larger systems relevant in materials science. In those situations, rigorous functionals capable of describing charge-transfer phenomena, or alternative computational schemes, are needed.

■ ASSOCIATED CONTENT

Supporting Information

The Supporting Information is available free of charge on the ACS Publications website at DOI: [10.1021/acs.jpca.6b09014](https://doi.org/10.1021/acs.jpca.6b09014).

Plots of the contributions from s and p_z atomic orbitals on lithium to the HOMO of lithium–benzene as a function of the separation between fragments. ([PDF](#))

■ AUTHOR INFORMATION

Corresponding Authors

*L.V.S.: E-mail: lslipchenko@purdue.edu.
*A.W.: E-mail: awasser@purdue.edu.

Notes

The authors declare no competing financial interest.

■ ACKNOWLEDGMENTS

We thank Martín A. Mosquera and Benjamin T. Nebgen. A.W. acknowledges support from the Office of Basic Energy Sciences, U.S. Department of Energy, under grant no. DEFG02-10ER16196. L.V.S. acknowledges support of the National Science Foundation, grant no. CHE-1465154 and Purdue University. This research was supported in part through computational resources provided by Information Technology at Purdue University.

■ REFERENCES

- (1) Conway, B. E. *Electrochemical Supercapacitors: Scientific Fundamentals and Technological Applications* (POD); Kluwer Academic/Plenum: New York, 1999; pp 193–195.
- (2) An, K. H.; Kim, W. S.; Park, Y. S.; Moon, J.-M.; Bae, D. J.; Lim, S. C.; Lee, Y. S.; Lee, Y. H. Electrochemical Properties of High-power Supercapacitors Using Single-walled Carbon Nanotube Electrodes. *Adv. Funct. Mater.* **2001**, *11*, 387–392.
- (3) Goodenough, J. B.; Abruña, H. D.; Buchanan, M. V. *Basic Research Needs for Electrical Energy Storage: Report of the Basic Energy Sciences Workshop for Electric Energy Storage*; U.S. Department of Energy, Office of Basic Energy Science, 2007.
- (4) Kalugin, O. N.; Chaban, V. V.; Loskutov, V. V.; Prezhdo, O. V. Uniform Diffusion of Acetonitrile Inside Carbon Nanotubes Favors Supercapacitor Performance. *Nano Lett.* **2008**, *8*, 2126–2130.
- (5) Shim, Y.; Kim, H. J. Nanoporous Carbon Supercapacitors in an Ionic Liquid: A Computer Simulation Study. *ACS Nano* **2010**, *4*, 2345–2355.
- (6) Shim, Y.; Jung, Y. J.; Kim, H. J. Graphene-based Supercapacitors: A Computer Simulation Study. *J. Phys. Chem. C* **2011**, *115*, 23574–23583.
- (7) Feng, G.; Cummings, P. T. Supercapacitor Capacitance Exhibits Oscillatory Behavior as a Function of Nanopore Size. *J. Phys. Chem. Lett.* **2011**, *2*, 2859–2864.
- (8) Lewars, E. *Computational Chemistry*; Springer, 2010.
- (9) Hohenberg, P.; Kohn, W. Inhomogeneous Electron Gas. *Phys. Rev.* **1964**, *136*, B864.
- (10) Kohn, W.; Sham, L. J. Self-consistent Equations Including Exchange and Correlation Effects. *Phys. Rev.* **1965**, *140*, A1133.
- (11) Jensen, F. *Introduction to Computational Chemistry*; Wiley, 2007.
- (12) Thackeray, M. M.; Wolverton, C.; Isaacs, E. D. Electrical Energy Storage for Transportation - Approaching the Limits of, and Going Beyond, Lithium-ion Batteries. *Energy Environ. Sci.* **2012**, *5*, 7854–7863.
- (13) Perdew, J. P. Climbing the Ladder of Density Functional Approximations. *MRS Bull.* **2013**, *38*, 743–750.
- (14) Burke, K. Perspective on Density Functional Theory. *J. Chem. Phys.* **2012**, *136*, 150901.
- (15) Cohen, A. J.; Mori-Sánchez, P.; Yang, W. Insights into Current Limitations of Density Functional Theory. *Science* **2008**, *321*, 792–794.
- (16) Roy, L. E.; Jakubikova, E.; Guthrie, M. G.; Batista, E. R. Calculation of One-electron Redox Potentials Revisited. Is It Possible to Calculate Accurate Potentials with Density Functional Methods? *J. Phys. Chem. A* **2009**, *113*, 6745–6750.
- (17) Mori-Sánchez, P.; Cohen, A. J.; Yang, W. Localization and Delocalization Errors in Density Functional Theory and Implications for Band-gap Prediction. *Phys. Rev. Lett.* **2008**, *100*, 146401.
- (18) Cohen, A. J.; Mori-Sánchez, P.; Yang, W. Fractional Charge Perspective on the Band Gap in Density-functional Theory. *Phys. Rev. B: Condens. Matter Mater. Phys.* **2008**, *77*, 115123.
- (19) Zhengyu, Z.; Jian, X.; Chuansong, Z.; Xingming, Z.; Dongmei, D.; Kezhong, Z. Theoretical Study of Inner-sphere Reorganization Energy of the Electron Transfer Reactions Between M-C₆H₆ and M⁺-C₆H₆ Complexes in the Gas Phase: An *Ab Initio* Computation. *J. Mol. Struct.: THEOCHEM* **1999**, *469*, 1–6.
- (20) Vollmer, J. M.; Kandalam, A. K.; Curtiss, L. A. Lithium-benzene Sandwich Compounds: A Quantum Chemical Study. *J. Phys. Chem. A* **2002**, *106*, 9533–9537.
- (21) Kang, H. S. Density Functional Study of Lithium-aromatic Sandwich Compounds and Their Crystals. *J. Phys. Chem. A* **2005**, *109*, 478–483.
- (22) Ferre-Vilaplana, A. Storage of Hydrogen Adsorbed on Alkali Metal Doped Single-layer All-carbon Materials. *J. Phys. Chem. C* **2008**, *112*, 3998–4004.
- (23) Martinez, J. I.; Cabria, I.; López, M. J.; Alonso, J. A. Adsorption of Lithium on Finite Graphitic Clusters. *J. Phys. Chem. C* **2009**, *113*, 939–941.
- (24) Marshall, M. S.; Steele, R. P.; Thanthiripattie, K. S.; Sherrill, C. D. Potential Energy Curves for Cation-π Interactions: Off-Axis Configurations Are Also Attractive. *J. Phys. Chem. A* **2009**, *113*, 13628–13632.
- (25) Olivares-Amaya, R.; Stopa, M.; Andrade, X.; Watson, M. A.; Aspuru-Guzik, A. Anion Stabilization in Electrostatic Environments. *J. Phys. Chem. Lett.* **2011**, *2*, 682–688.
- (26) Varganov, S. A.; Avramov, P. V.; Ovchinnikov, S. G. Ab Initio Calculations of Endo-and Exohedral C₆₀ Fullerene Complexes with Li

- + Ion and the Endohedral C₆₀ Fullerene Complex with Li₂ Dimer. *Phys. Solid State* **2000**, *42*, 388–392.
- (27) Baker, T. A.; Head-Gordon, M. Modeling the Charge Transfer Between Alkali Metals and Polycyclic Aromatic Hydrocarbons Using Electronic Structure Methods. *J. Phys. Chem. A* **2010**, *114*, 10326–10333.
- (28) Denis, P. A.; Iribarne, F. C_{2v} or C_{6v}: Which Is the Most Stable Structure of the Benzene-lithium Complex? *Chem. Phys. Lett.* **2013**, *573*, 15–18.
- (29) Foresman, J. B.; Frisch, A. E. *Exploring Chemistry with Electronic Structure Methods*; Gaussian, Inc.: Pittsburgh, PA, 1996; pp 171–172.
- (30) Shao, Y.; Molnar, L. F.; Jung, Y.; Kussmann, J.; Ochsenfeld, C.; Brown, S. T.; Gilbert, A. T.; Slipchenko, L. V.; Levchenko, S. V.; O'Neill, D. P.; et al. Advances in Methods and Algorithms in a Modern Quantum Chemistry Program Package. *Phys. Chem. Chem. Phys.* **2006**, *8*, 3172–3191.
- (31) Shao, Y.; Gan, Z.; Epifanovsky, E.; Gilbert, A. T.; Wormit, M.; Kussmann, J.; Lange, A. W.; Behn, A.; Deng, J.; Feng, X.; et al. Advances in Molecular Quantum Chemistry Contained in the Q-chem 4 Program Package. *Mol. Phys.* **2015**, *113*, 184–215.
- (32) Krylov, A. I.; Gill, P. M. W. Q-Chem: An Engine for Innovation. *Wiley Interdiscip. Rev. Comput. Mol. Sci.* **2013**, *3*, 317–326.
- (33) Gilbert, A. T. B.; Besley, N. A.; Gill, P. M. W. Self-Consistent Field Calculations of Excited States Using the Maximum Overlap Method (MOM). *J. Phys. Chem. A* **2008**, *112*, 13164–13171.
- (34) Perdew, J. P.; Burke, K.; Ernzerhof, M. Generalized Gradient Approximation Made Simple. *Phys. Rev. Lett.* **1996**, *77*, 3865–3868.
- (35) Adamo, C.; Scuseria, G. E.; Barone, V. Accurate Excitation Energies from Time-dependent Density Functional Theory: Assessing the PBE0 Model. *J. Chem. Phys.* **1999**, *111*, 2889–2899.
- (36) Bernard, Y. A.; Shao, Y.; Krylov, A. I. General Formulation of Spin-flip Time-dependent Density Functional Theory Using Non-collinear Kernels: Theory, Implementation, and Benchmarks. *J. Chem. Phys.* **2012**, *136*, 204103.
- (37) Henderson, T. M.; Janesko, B. G.; Scuseria, G. E. Generalized Gradient Approximation Model Exchange Holes for Range-separated Hybrids. *J. Chem. Phys.* **2008**, *128*, 194105.
- (38) Perdew, J. P.; Ernzerhof, M.; Burke, K. Rationale for Mixing Exact Exchange with Density Functional Approximations. *J. Chem. Phys.* **1996**, *105*, 9982–9985.
- (39) Liu, F.; Proynov, E.; Yu, J.-G.; Furlani, T. R.; Kong, J. Comparison of the Performance of Exact-exchange-based Density Functional Methods. *J. Chem. Phys.* **2012**, *137*, 114104.
- (40) Miehlich, B.; Savin, A.; Stoll, H.; Preuss, H. Results Obtained with the Correlation Energy Density Functionals of Becke and Lee, Yang and Parr. *Chem. Phys. Lett.* **1989**, *157*, 200–206.
- (41) Becke, A. D. Density-functional Thermochemistry. III. The Role of Exact Exchange. *J. Chem. Phys.* **1993**, *98*, 5648–5652.
- (42) Yanai, T.; Tew, D. P.; Handy, N. C. A New Hybrid Exchange-correlation Functional Using the Coulomb-attenuating Method (CAM-B3LYP). *Chem. Phys. Lett.* **2004**, *393*, 51–57.
- (43) Becke, A. D. Density-functional Exchange-energy Approximation with Correct Asymptotic Behavior. *Phys. Rev. A: At., Mol., Opt. Phys.* **1988**, *38*, 3098.
- (44) Lee, C.; Yang, W.; Parr, R. G. Development of the Colle-Salvetti Correlation-energy Formula into a Functional of the Electron Density. *Phys. Rev. B: Condens. Matter Mater. Phys.* **1988**, *37*, 785.
- (45) Slater, J. C. *The Self-Consistent Field for Molecules and Solids*; McGraw-Hill: New York, 1974; Vol. 4.
- (46) Vosko, S. H.; Wilk, L.; Nusair, M. Accurate Spin-dependent Electron Liquid Correlation Energies for Local Spin Density Calculations: A Critical Analysis. *Can. J. Phys.* **1980**, *58*, 1200–1211.
- (47) Møller, C.; Plesset, M. S. Note on an Approximation Treatment for Many-electron Systems. *Phys. Rev.* **1934**, *46*, 618.
- (48) Pople, J. A.; Krishnan, R.; Schlegel, H. B.; Binkley, J. S. Electron Correlation Theories and Their Application to the Study of Simple Reaction Potential Surfaces. *Int. J. Quantum Chem.* **1978**, *14*, 545–560.
- (49) Bartlett, R. J.; Purvis, G. D. Many-body Perturbation Theory, Coupled-pair Many-electron Theory, and the Importance of Quadruple Excitations for the Correlation Problem. *Int. J. Quantum Chem.* **1978**, *14*, 561–581.
- (50) Stanton, J. F.; Bartlett, R. J. The Equation of Motion Coupled-cluster Method. A Systematic Biorthogonal Approach to Molecular Excitation Energies, Transition Probabilities, and Excited State Properties. *J. Chem. Phys.* **1993**, *98*, 7029–7039.
- (51) Nooijen, M.; Bartlett, R. J. Equation of Motion Coupled Cluster Method for Electron Attachment. *J. Chem. Phys.* **1995**, *102*, 3629–3647.
- (52) Krylov, A. I. Equation-of-motion Coupled-cluster Methods for Open-shell and Electronically Excited Species: The Hitchhiker's Guide to Fock Space. *Annu. Rev. Phys. Chem.* **2008**, *59*, 433–462.
- (53) Mulliken, R. S. Electronic Population Analysis on LCAO [Single Bond] Mo Molecular Wave Functions. I. *J. Chem. Phys.* **1955**, *23*, 1833.
- (54) Reed, A. E.; Weinstock, R. B.; Weinhold, F. Natural Population Analysis. *J. Chem. Phys.* **1985**, *83*, 735.
- (55) Breneman, C. M.; Wiberg, K. B. Determining Atom-centered Monopoles from Molecular Electrostatic Potentials. The Need for High Sampling Density in Formamide Conformational Analysis. *J. Comput. Chem.* **1990**, *11*, 361–373.
- (56) Reed, A. E.; Curtiss, L. A.; Weinhold, F. Intermolecular Interactions from a Natural Bond Orbital, Donor-acceptor Viewpoint. *Chem. Rev.* **1988**, *88*, 899–926.
- (57) Kim, D.; Hu, S.; Tarakeshwar, P.; Kim, K. S.; Lisy, J. M. Cation-π Interactions: A Theoretical Investigation of the Interaction of Metallic and Organic Cations with Alkenes, Arenes, and Heteroarenes. *J. Phys. Chem. A* **2003**, *107*, 1228–1238.
- (58) Paldus, J.; Čížek, J. Stability Conditions for the Solutions of the Hartree-Fock Equations for Atomic and Molecular Systems. Application to the Pi electron Model of Cyclic Polyenes. *J. Chem. Phys.* **1967**, *47*, 3976–3985.
- (59) Wu, Q.; Van Voorhis, T. Constrained Density Functional Theory and Its Application in Long-range Electron Transfer. *J. Chem. Theory Comput.* **2006**, *2*, 765–774.
- (60) Van Voorhis, T.; Kowalczyk, T.; Kaduk, B.; Wang, L.-P.; Cheng, C.-L.; Wu, Q. The Diabatic Picture of Electron Transfer, Reaction Barriers, and Molecular Dynamics. *Annu. Rev. Phys. Chem.* **2010**, *61*, 149–170.
- (61) Hirao, K. *Recent Advances in Multireference Methods*; World Scientific, 1999; Vol. 4.
- (62) Manceron, L.; Andrews, L. Infrared Spectra and Structures of Lithium-benzene and Lithium-dibenzene Complexes in Solid Argon. *J. Am. Chem. Soc.* **1988**, *110*, 3840–3846.
- (63) Curtiss, L. A.; Redfern, P. C.; Raghavachari, K.; Rassolov, V.; Pople, J. A. Gaussian-3 Theory Using Reduced Møller-Plesset Order. *J. Chem. Phys.* **1999**, *110*, 4703–4709.

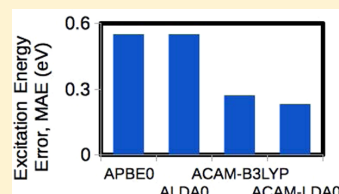
Connection between Hybrid Functionals and Importance of the Local Density Approximation

Martin A. Mosquera,[†] Carlos H. Borca,[‡] Mark A. Ratner,[†] and George C. Schatz*,[†]

[†]Department of Chemistry, Northwestern University, 2145 Sheridan Road, Evanston, Illinois 60208, United States

[‡]Department of Chemistry, Purdue University, 560 Oval Drive, West Lafayette, Indiana 47907, United States

ABSTRACT: The exchange–correlation (XC) local density approximation (LDA) is the original density functional used to investigate the electronic structure of molecules and solids within the formulation of Kohn and Sham. The LDA is fundamental for the development of density-functional approximations. In this work we consider the generalized Kohn–Sham (GKS) theory of hybrid functionals. The GKS formalism is an extension of the Kohn–Sham theory for electronic ground states and leads to a vast set of alternative density functionals, which can be estimated by the LDA and related methods. Herein we study auxiliary electronic systems with parametrized interactions and derive (i) a set of exact equations relating the GKS XC energies in the parameter space and (ii) a formal relation between the parameters and the standard XC derivative discontinuity. In view of the new results and previously reported findings, we discuss why the inclusion of Fock exchange, and its long-range-corrected form (in the ground-state calculations and in linear-response Kohn–Sham equations), dominate over the generalized gradient corrections to enhance the quality of the fundamental gap and to enhance excitation-energy estimations. As an example, we show that the adiabatic CAM-LDA0 (a functional with 1/4 global and 1/2 long-range Hartree–Fock interaction, respectively, a range separation factor of 1/3, and pure LDA exchange and correlation) works for electronic excitations as well as the adiabatic CAM-B3LYP functional.



INTRODUCTION

Calculations based on the theory of density functionals are customary in the study of electronic properties of materials. Unfortunately, the number of density-functional approximations grows, and grows, up to the point where the user (including the authors of this work) might be unsure about which functional should be used and why. Modern functionals are usually parametrized combinations of various objects including orbitals, gradients of the electronic and orbital densities, attenuated electron–electron interactions, etc. One can make matters more intricate by recombining already parametrized density functionals to propose a new approximation.

The work of Kohn and collaborators establishes the electronic density as a variable that can be used to determine *all* the properties of the system. The useful formalism of Kohn and Sham employs a single Slater determinant, where its orbitals, when subject to the exact exchange–correlation potential, yield the ground-state energy and electronic density of the system. Nowadays, many variations of the Kohn–Sham (KS) method are available, making accessible the calculations for molecular dynamics, thermodynamical statistics, and spectroscopy, among others.

The first density-functional approximation (DFA) within KS density-functional theory (DFT) includes correlation and is able to reproduce the ground-state properties of the homogeneous electron gas: a system where many electrons lie in a large periodic box, in such a way that they are properly described by plane waves and a continuum energy spectrum.

Such a functional is known as the local density approximation (LDA), and it is decomposed into kinetic, Hartree, and exchange–correlation (XC) contributions. To study molecules, the XC contribution is used within a set of single-particle Schrödinger equations. The XC LDA energy functional yields a local, multiplicative effective potential that the noninteracting electrons are subject to. This XC functional depends only on the electronic density.

The inclusion of a fraction of the Hartree–Fock orbital-exchange operator in the approximated KS equations helps to improve the estimation of binding energies,¹ lattice constants,² fundamental gaps,³ and excitation energies.⁴ The justification for addition of nonlocal exchange to improve the electronic structure calculations derives from the adiabatic connection formula¹ and density-functional perturbation theory.⁵ An application of this justification is the famous recipe by Perdew et al.⁶ to include 25% of Hartree–Fock exchange in the generalized gradient approximation (GGA) XC energy. If the GGA functional is the popular PBE,⁷ then one obtains the PBE0 approximation,^{8,9} an XC functional with only one parameter. In contrast, the most successful functionals are hybrids with more than three empirical parameters. The hybridization typically consists of combining different types of exchange and correlation functionals, leading to approximations like CAM-B3LYP.¹⁰

Received: November 6, 2015

Revised: February 15, 2016

Published: February 22, 2016

The formulation of Kohn and Sham, strictly speaking, demands employing a local, multiplicative, XC potential, in other words, that all the orbitals (virtual and occupied) are subject to the same XC potential. We will refer to this formalism as *standard KS theory*. An alternative formal theoretical framework to incorporate Hartree–Fock (HF) exchange, or a fraction of it, in the single-particle Schrödinger equation is known as the generalized Kohn–Sham (GKS) method.¹¹ Instead of using an auxiliary model of noninteracting electrons, as in KS DFT, Seidl et al.¹¹ introduced a system of interacting electrons, where the interaction is described by means of a simplified functional of the orbitals, which can depend on parameters. An example of such a tractable interaction is the HF repulsion, often seen as “ $2J-K$ ”. Then, the premise in GKS DFT is that one can approximate a residual functional, similar to the XC energy functional, that corrects the energy and density of the auxiliary system of interacting electrons in such a way that they are close to the corresponding true ground-state values. There is an uncountably infinite number of possible auxiliary systems of electrons, the KS electron system is one of them.

Within the generalization of KS DFT,¹¹ if a fraction of HF exchange is used, then the rest of the exchange energy is calculated using a fraction of the LDA exchange. In general, the GKS method allows us to split the energy into a residual and a nonlocal, parametrized energy. The LDA can be used to estimate the former. In other words, the residual energy is approximated using only an integral over a local function of the density. In the homogeneous electron gas limit, the parameters defining the nonlocal exchange are free. These parameters are related to the addition of nonlocal interactions, their splitting into long- and short-range contributions, and the mixings of different correlation functionals.

The GKS formalism is very broad, and its explicit formulas for the residual energies shown in this study for functionals like PBE0, or CAM-B3LYP, have not been highlighted elsewhere. The residual energies are weighted sums of exchange and correlation energy functionals. These functionals are different from those defined in standard KS theory. We derive a Koopmans’ theorem, and an exact relation between the parameters and the XC derivative discontinuity from standard KS theory. We show how the Coulomb-attenuated method (CAM) can be approached in the GKS framework. A new equation relating the exact XC energies in the parameter space is presented in this work. We suggest that, with respect to the generalized gradient corrections, the inclusion of a fraction of nonlocal exchange in the single-particle Schrödinger equations tends to be an overweighing factor to obtain improved excitation energies. In view of this, here we study: (i) A one-parameter method, consisting in mixing Dirac exchange with HF exchange, while using a 100% LDA correlation. The resulting functional is LDA0,^{12,13} in essence PBE0 without gradient-dependent terms. (ii) A three-parameter method, i.e., the one-parameter method with Coulomb attenuation. We propose that the adiabatic CAM-LDA0 functional (exact for the homogeneous electron gas) can be used as a slightly less expensive alternative to the adiabatic CAM-B3LYP for linear-response calculations. A cautionary remark, the percentage of HF exchange is not *universal*, it varies depending of the type of application.^{14,15} Thus, careful judgment and tuning of parameters are advised, as in the application of any other DFA.

The LDA0 is a functional with little use reported in the literature. We note that it has been used to study vacancies in

magnesium oxide¹² and irradiated silicon carbide.¹³ On the contrary, the functional (adiabatic) CAM-LDA0 has not been considered previously.

■ BACKGROUND THEORY

Suppose n is a given electronic density. It can correspond to that of the true ground state, or a superposition of excited states. Define the energy (G_λ) of a system of electrons, described by a single Slater determinant, which interact through a partial Coulomb interaction:¹⁶

$$G_\lambda[n] = \min_{\Phi \rightarrow n} \langle \Phi | \hat{T} + \lambda \hat{W} | \Phi \rangle \quad (1)$$

where $\lambda > 0$ and \hat{T} and \hat{W} are the kinetic and repulsion energy operators, respectively. In second quantization, \hat{T} reads $1/2 \int d^3r \nabla \hat{\psi}^\dagger(\mathbf{r}) \cdot \nabla \hat{\psi}(\mathbf{r})$, and $\hat{W} = 1/2 \int d^3r d^3r' \hat{\psi}^\dagger(\mathbf{r}') \hat{\psi}^\dagger(\mathbf{r}) w(|\mathbf{r}-\mathbf{r}'|) \hat{\psi}(\mathbf{r}) \hat{\psi}(\mathbf{r}')$. The function w is the Coulomb repulsion potential. The value of the functional G_λ at n is obtained by a constrained minimization over single Slater determinants giving the density n . This minimization problem is solved using Lagrange multipliers and leads to a local potential u_s^λ and a set of orbital energies $\{\epsilon_a^\lambda\}$. The orbitals used to form the Slater determinant satisfy the following equation:

$$\left[-\frac{1}{2} \nabla^2 + \lambda (\hat{j}(\mathbf{r}) + \hat{v}_{x,\lambda}(\mathbf{r})) + u_s^\lambda(\mathbf{r}) \right] \phi_a^\lambda(\mathbf{r}) = \epsilon_a^\lambda \phi_a^\lambda(\mathbf{r}) \quad (2)$$

where $\hat{j}(\mathbf{r})$ and $\hat{v}_{x,\lambda}(\mathbf{r})$ are the local Coulomb and HF exchange potential operators. The potential u_s^λ forces the orbital densities to satisfy $\sum_a \nu_a |\phi_a^\lambda(\mathbf{r})|^2 = n(\mathbf{r})$, for all \mathbf{r} ; $\{\nu_a\}$ are the occupation numbers. We will denote the term enclosed by square brackets in the above equation as f_λ , a Fock operator. The total number of electrons, N , satisfies $N \geq 2$; otherwise, $G_\lambda = G_0$.

The electronic energy density functional is written as $E_v[n] = F[n] + \int d^3r v(\mathbf{r}) n(\mathbf{r})$, where v is the one-body external potential. F is the Levy¹⁷ constrained-search functional, $F[n] = \min \{ \langle \Psi | \hat{T} + \hat{W} | \Psi \rangle | \Psi \rightarrow n \}$. This search is performed over the Hilbert space of fully correlated wave functions.

Denote $\tilde{\Phi}_\lambda[n]$ as the optimal single Slater determinant that is the solution to the minimization problem shown in the right-hand side of eq 1. We can define a partial Hartree–XC (HXC) energy as follows:

$$E_{\text{HXC}}^\lambda[n] = (1 - \lambda) \langle \tilde{\Phi}_\lambda | \hat{W} | \tilde{\Phi}_\lambda \rangle + E_c^\lambda[n] \quad (3)$$

The interaction term $\langle \tilde{\Phi}_\lambda | \hat{W} | \tilde{\Phi}_\lambda \rangle$ is a density functional, and it can be expanded as $E_X^\lambda[n] + E_H[n]$, where $E_H[n]$ is the (usual) Hartree repulsion energy, $1/2 \int d^3r' d^3r n(\mathbf{r}) n(\mathbf{r}') w(|\mathbf{r}-\mathbf{r}'|)$. The exact exchange energy functional, E_X^λ , is thus given by the difference $\langle \tilde{\Phi}_\lambda | \hat{W} | \tilde{\Phi}_\lambda \rangle - E_H[n]$. Under these definitions, if we expand the Levy energy F as $G_\lambda + E_{\text{HXC}}^\lambda$, we find that the correlation energy reads^a

$$E_c^\lambda[n] = \langle \tilde{\Psi} | \hat{T} + \hat{W} | \tilde{\Psi} \rangle - \langle \tilde{\Phi}_\lambda | \hat{T} + \hat{W} | \tilde{\Phi}_\lambda \rangle \quad (4)$$

Here $\tilde{\Psi}$ is the optimal correlated wave function required to compute the F functional at n . The above expression is similar to the correlation energy defined in KS-DFT. E_c^λ corresponds to the usual correlation energy of KS-DFT if $\lambda = 0$. In general, within the exact framework, $E_X^\lambda \neq E_X^0$ and $E_c^\lambda \neq E_c^0$ for $\lambda > 0$.

The LDA is exact for the uniform electron gas (UEG). In the UEG limit, the calculation of G_λ requires solution of the Hartree–Fock problem, where the charge of the electron is scaled by a factor of $\sqrt{\lambda}$. The functional $G_\lambda[n]$ reads $T^{\text{TF}}[n] + \lambda E_{\text{HX}}^{\text{LDA}}[n]$, where T^{TF} is the Thomas–Fermi kinetic energy

functional, and $n = N/V$ (V is the UEG volume). The partial LDA for the HXC energy is

$$E_{\text{HXC}}^{\text{LDA},\lambda}[n] = (1 - \lambda)(E_{\text{H}}[n] + E_{\text{X}}^{\text{LDA}}[n]) + E_{\text{c}}^{\text{LDA}}[n] \quad (5)$$

By adding G_λ and $E_{\text{HXC}}^{\text{LDA},\lambda}$ together, we then recover the exact energy functional for the UEG limit for *any* value of λ .⁶ Hence, $E^{\text{LDA}}[n] = T^{\text{TF}}[n] + E_{\text{HXC}}^{\text{LDA}}[n]$.

■ COULOMB-ATTENUATED METHOD

Further parametrizations can be introduced for the auxiliary system of electrons. One can split the Coulomb interaction between two electrons using long- (lr) and short-range (sr) contributions. Such splitting requires an additional parameter, μ . In general, one can write $w(x) = w_\mu^{\text{lr}}(x) + w_\mu^{\text{sr}}(x)$. If the error function is used to separate the Coulomb interaction, then $w_\mu^{\text{lr}}(x) = \text{erf}(\mu x)/x$, and $w_\mu^{\text{sr}}(x) = \text{erfc}(\mu x)/x$. To include a fraction of long-range Fock exchange, let us define the functional

$$G_{\lambda,\zeta}[n] = \min_{\Phi \rightarrow n} \langle \Phi | \hat{T} + \lambda \hat{W} + \zeta \hat{W}_\mu^{\text{lr}} | \Phi \rangle \quad (6)$$

\hat{W}_μ^{lr} is the lr electron–electron repulsion operator; this operator is obtained by replacing w by w_μ^{lr} in the definition of \hat{W} . In this case, the constrained search is also carried out over the space of single Slater determinants. The corresponding partial HXC energy functional can be shown to be of the form

$$E_{\text{HXC}}^{\lambda,\zeta}[n] = E_{\text{c}}^{\lambda,\zeta}[n] + (1 - \lambda - \zeta)E_{\text{H}}^{\lambda,\zeta}[n] + \zeta E_{\text{H}}^{\text{sr},\lambda,\zeta}[n] \quad (7)$$

The definition of the functionals involved is as follows: $E_{\text{c}}^{\lambda,\zeta}[n] = F[n] - \langle \tilde{\Phi}_{\lambda,\zeta} | \hat{T} + \hat{W} | \tilde{\Phi}_{\lambda,\zeta} \rangle$, $E_{\text{H}}^{\text{sr},\lambda,\zeta}[n] = \langle \tilde{\Phi}_{\lambda,\zeta} | \hat{W}_\mu^{\text{sr}} | \tilde{\Phi}_{\lambda,\zeta} \rangle$, $E_{\text{H}}^{\lambda,\zeta}[n] = \langle \tilde{\Phi}_{\lambda,\zeta} | \hat{W} | \tilde{\Phi}_{\lambda,\zeta} \rangle$. The function $\tilde{\Phi}_{\lambda,\zeta}$ is that which minimizes the expectation value required to calculate $G_{\lambda,\zeta}$ at n .

Equation 7 is a weighted sum of exchange energies and 100% correlation. In general, if one accounts partially for exchange and/or correlation including orbital-dependent forms (in the calculation of a functional like $G_{\lambda,\zeta}$), then the remaining portions of XC energy can be quantified using an explicitly density-dependent approximation, such as an LDA, or GGA. A remark: Definition of the auxiliary system is required prior to assigning the residual energy to be estimated with the LDA/GGA. For example, after setting λ , ζ , and μ , one can apply the LDA/GGA to estimate $E_{\text{HXC}}^{\lambda,\zeta}$. But enhancing this approximation requires a new methodology because $\tilde{\Phi}_{\lambda,\zeta}$, in contrast to $\tilde{\Phi}_{0,0}$ (from standard KS theory), describes the auxiliary system of electrons.

The use of parametrized interactions is an alternative to using standard KS orbitals as density functionals to calculate very accurate, and somewhat expensive, XC potentials, for instance, as in the exact exchange¹⁸ and *ab initio* DFT methodologies.¹⁹

The above definitions encompass the Coulomb-attenuated method, formalized here within GKS theory. The parameters can be identified as $\alpha = \lambda$ and $\beta = \zeta$. The long-range-corrected (LRC) method is obtained by simply setting $\lambda = 0$ and $\zeta = 1$; the only parameter is the separation factor μ . In addition, extra parameters can be introduced to split the different functionals involved in eq 7 while obeying the UEG limit. For example, one can mix the LDA and GGA functionals: $E_Y[n] = a_0 E_Y^{\text{LDA}}[n] + (1 - a_0) E_Y^{\text{GGA}}[n]$, where Y is either “X” or “c”; the expansion is applicable to any of the different energy forms, sr, lr, λ , and/or μ dependent. These types of mixed functionals are well studied with respect to training sets. Deciding which functional should be used can be challenging.²⁰

The energy functional, $E_v[n]$, reads

$$E_v[n] = G_{\lambda,\zeta}[n] + E_{\text{HXC}}^{\lambda,\zeta}[n] + \int d^3r v(r) n(r) \quad (8)$$

The total electronic energy is independent of the parameters λ , ζ , and μ . For instance, suppose that the density is fixed. Differentiation of both sides of the above equation with respect to λ leads to

$$\frac{\partial G_{\lambda,\zeta}}{\partial \lambda} = - \frac{\partial E_{\text{HXC}}^{\lambda,\zeta}}{\partial \lambda} \quad (9)$$

In a similar fashion one obtains $\partial G_{\lambda,\zeta}/\partial \zeta = -\partial E_{\text{HXC}}^{\lambda,\zeta}/\partial \zeta$.

Define the energy operator as

$$\hat{H}_{\lambda,\zeta}[n] = \hat{T} + \lambda \hat{W} + \zeta \hat{W}_\mu^{\text{lr}} + \int d^3r u_s^{\lambda,\zeta}[n](r) \hat{n}(r) \quad (10)$$

where $\hat{n}(r)$ is the density operator and $u_s^{\lambda,\zeta}[n]$ is the Lagrange multiplier required to solve the constrained search defining $G_{\lambda,\zeta}[n]$. Consider the following auxiliary energy functional:

$$\begin{aligned} \hat{H}_{\lambda,\zeta}[n] &= \langle \tilde{\Phi}_{\lambda,\zeta} | \hat{H}_{\lambda,\zeta}[n] | \tilde{\Phi}_{\lambda,\zeta} \rangle \\ &= G_{\lambda,\zeta}[n] + \int d^3r u_s^{\lambda,\zeta}[n](r) n(r) \end{aligned} \quad (11)$$

The wave function $\tilde{\Phi}_{\lambda,\zeta}$ minimizes the expectation value of $\hat{H}_{\lambda,\zeta}[n]$ over the space of single Slater determinants (this minimization gives rise to the GKS equations, e.g., eq 2). Hence, invoking the Hellmann–Feynman theorem, we arrive at

$$\frac{\partial E_{\lambda,\zeta}}{\partial \lambda} = \langle \tilde{\Phi}_{\lambda,\zeta} | \frac{\partial \hat{H}_{\lambda,\zeta}[n]}{\partial \lambda} | \tilde{\Phi}_{\lambda,\zeta} \rangle \quad (12)$$

Expand both sides of this equation using eqs 10 and 11 and observe that

$$\frac{\partial G_{\lambda,\zeta}}{\partial \lambda} = \langle \tilde{\Phi}_{\lambda,\zeta} | \hat{W} | \tilde{\Phi}_{\lambda,\zeta} \rangle \quad (13)$$

If we set $\zeta = 0$, use the above result to integrate both sides of eq 9, and rearrange the result, we obtain

$$E_{\text{HXC}}^{\lambda,0}[n] = E_{\text{HXC}}[n] - \int_0^\lambda d\lambda' \langle \tilde{\Phi}_{\lambda',0} | \hat{W} | \tilde{\Phi}_{\lambda',0} \rangle \quad (14)$$

where $E_{\text{HXC}} = E_{\text{HXC}}^{0,0}$ is the HXC energy of standard KS theory.

After applying the above analysis to the parameter ζ , we can express $E_{\text{HXC}}^{\lambda,0}$ in terms of ζ . This yields

$$\begin{aligned} E_{\text{HXC}}^{\lambda,\zeta}[n] &= E_{\text{HXC}}[n] - \int_0^\lambda d\lambda' \langle \tilde{\Phi}_{\lambda',0} | \hat{W} | \tilde{\Phi}_{\lambda',0} \rangle \\ &\quad - \int_0^\zeta d\zeta' \langle \tilde{\Phi}_{\lambda,\zeta'} | \hat{W}_\mu^{\text{lr}} | \tilde{\Phi}_{\lambda,\zeta'} \rangle \end{aligned} \quad (15)$$

This equation can be further simplified by elimination of the Hartree energies, which are independent of λ and ζ . The final result is

$$E_{\text{XC}}^{\lambda,\zeta}[n] = E_{\text{XC}}[n] - \int_0^\lambda d\lambda' E_X^{\lambda',0}[n] - \int_0^\zeta d\zeta' E_X^{\text{lr},\lambda,\zeta}[n] \quad (16)$$

where $E_X^{\text{lr},\lambda,\zeta}[n] = \langle \tilde{\Phi}_{\lambda,\zeta} | \hat{W}_\mu^{\text{lr}} | \tilde{\Phi}_{\lambda,\zeta} \rangle - E_{\text{H}}^{\text{lr}}[n]$; the lr Hartree energy is obtained after replacing w by w_μ^{lr} in its definition formula. The above equation is an exact relation between XC energies in the parameter space. If the standard XC energy is known, then

subtracting from it the integrated, nonattenuated, and long-range exchange energies gives the XC energy for the auxiliary system defined by λ and ζ .

Generally, if a functional G_z is defined, where the electron–electron interaction is parametrized in terms of a vector of parameters, z , then G_z is related to the corresponding HXC energy by the equation $\nabla E_{\text{HXC}}^z = -\nabla G_z$ (the gradient is taken with respect to the parameters). The integrated form of this relation is

$$E_{\text{HXC}}^{z_1} - E_{\text{HXC}}^{z_0} = - \int_{\gamma} dz \cdot \nabla G_z \quad (17)$$

where γ is a trajectory in the parameter space connecting the points z_0 and z_1 . The difference between HXC energies is independent of the path because the integrand field is conservative: $\oint dz \cdot \nabla G_z = 0$.

Equation 17 expresses the equivalence between different auxiliary electronic systems to calculate the exact ground-state electronic energy (regardless of the parametrization, the functional E_v is always the same). However, the electronic energy approximated by any hybrid DFA does indeed depend on the parametrization of the auxiliary system. Because of this, all the current, hybrid DFAs do not satisfy the condition shown in eq 17.

■ KOOPMANS' THEOREM AND THE FUNDAMENTAL GAP

Let us consider a system where the number of electrons is N , a positive even integer. The ground-state energy of the system is obtained by minimizing the energy functional E_v over densities that yield N electrons. For the ground-state density, n_N^g , suppose that the local potential representing the density of the system is \tilde{u}_s^λ , and the auxiliary Slater determinant is $\tilde{\Phi}_{N,\lambda}$. It can be shown that this potential is given by $\delta E_{\text{HXC}}^\lambda / \delta n(\mathbf{r}) + v(\mathbf{r})$, where the functional derivative is evaluated at n_N^g . The Lagrange multiplier, \tilde{u}_s^λ , has contributions from the partial Hartree-XC, and the one-body external potentials; the latter could be of the form $-\sum_a Z_a / |\mathbf{r} - \mathbf{R}_a|$. Let us define the following electronic energy operator:

$$\hat{\mathcal{H}}_\lambda = \hat{T} + \lambda \hat{W} + \int d^3\mathbf{r} \tilde{u}_s^\lambda(\mathbf{r}) \hat{n}(\mathbf{r}) \quad (18)$$

Suppose that \tilde{u}_s^λ is frozen. It is straightforward to derive a Koopmans' theorem for the LUMO energy. This reads

$$e_L^\lambda = \langle \Phi'_{N+1,\lambda} | \hat{\mathcal{H}}_\lambda | \Phi'_{N+1,\lambda} \rangle - \langle \tilde{\Phi}_{N,\lambda} | \hat{\mathcal{H}}_\lambda | \tilde{\Phi}_{N,\lambda} \rangle \quad (19)$$

where $\Phi'_{N+1,\lambda}$ is the single Slater determinant describing the auxiliary system where the LUMO (of the N -electron system in its ground state) is fully occupied.

A relevant result for the present, *exact* formulation is that the HOMO energy e_H^λ equals the negative of the vertical ionization energy.^{16,21,22} This derives from the definition of the energy G_λ , which demands that the orbitals yield the ground-state density. In the asymptotic region of the real system of electrons, the exponential decreasing rate of the ground-state density is governed by the ionization energy.²¹ For the auxiliary system of partially interacting electrons, the decreasing rate of the density is determined by the HOMO energy.^{23,24} Therefore,¹⁶ $e_H^\lambda = -I$.

In Hartree–Fock theory there is no correlation energy functional, and the Hartree–Fock HOMO–LUMO gap is larger than the fundamental one. Thus, an interaction strength $0 < \lambda \leq 1$ could be appropriate to improve the gap estimation.

Although, strictly speaking, any positive real value of λ can be considered. Perhaps, large values of λ can be useful to study strongly correlated systems.

The LUMO energy is a function of the parameter λ . In standard KS-DFT $\lambda = 0$; all the KS electrons are subject to the same local potential. Furthermore, practical calculations indicate that the KS HOMO–LUMO gap underestimates the fundamental gap of the system.²⁵ In the asymptotic region, for example, the exact HXC potential decays as $(N - 1)/|\mathbf{r}|$, this potential is felt by the LUMO level as well. On the contrary, if $\lambda = 1$ the system displays a full dependency on the two-body interaction operator, which assigns different orbitals different interaction fields. The LUMO is screened by N electrons. Therefore, the LUMO energy with respect to the ionization energy is raised. For an in-depth discussion, see ref 26.

An analysis of the process of removal and addition of a very small amount of electron charge (using the grand canonical ensemble statistics) reveals that the affinity (A) of the molecule is related to the LUMO energy ($\lambda = 0$), and the XC potential, through the expression²⁷ $(-A) = e_L^0 + \Delta_{\text{XC}}$. The discontinuity of the XC potential, Δ_{XC} , is $\lim_{\Delta N \rightarrow 0^+} \nu_{\text{XC}}(N + \Delta N) - \nu_{\text{XC}}(N - \Delta N)$. This quantity is required to widen the KS HOMO–LUMO gap, so it matches the fundamental gap of the system. Within the exact GKS formulation, one can find the best value of the mixing parameter (λ^*) such that the GKS HOMO–LUMO gap matches the fundamental gap of the system.

Assuming Δ_{XC} is given, λ^* is calculated by solving the root-finding problem:

$$\begin{aligned} \Delta_{\text{XC}} &= [e_L^{\lambda^*} - e_H^{\lambda^*}] - [e_L^0 - e_H^0] \\ &= \int_0^{\lambda^*} d\lambda \frac{d}{d\lambda} [e_L^\lambda - e_H^\lambda] \end{aligned} \quad (20)$$

The ionization theorem ($e_L^\lambda = -I$) simplifies the root-finding problem as $\Delta_{\text{XC}} = \int_0^{\lambda^*} d\lambda \frac{d e_L^\lambda}{d\lambda}$. The LUMO energy, e_L^λ can be expressed as the expectation value $\langle \phi_L^\lambda | \hat{f}_\lambda | \phi_L^\lambda \rangle$. Now, we have that (the Fock operator is hermitian)

$$\frac{d e_L^\lambda}{d\lambda} = \langle \phi_L^\lambda | \frac{d \hat{f}_\lambda}{d\lambda} | \phi_L^\lambda \rangle + \left[\langle \frac{d \phi_L^\lambda}{d\lambda} | \hat{f}_\lambda | \phi_L^\lambda \rangle + \text{H.c.} \right] \quad (21)$$

Given that $\hat{f}_\lambda | \phi_L^\lambda \rangle = e_L^\lambda | \phi_L^\lambda \rangle$, the terms in square brackets in the above equation can be written as $e_L^\lambda d \langle \phi_L^\lambda | \phi_L^\lambda \rangle / d\lambda$, which is null because the LUMO is normalized. Hence, we obtain the following relation:

$$\Delta_{\text{XC}} = \int_0^{\lambda^*} d\lambda \langle \phi_L^\lambda | \hat{u}_x^\lambda - u_x^\lambda + \hat{o}_\lambda | \phi_L^\lambda \rangle \quad (22)$$

where \hat{o}_λ is a residual operator. It reads

$$\hat{o}_\lambda = (1 - \lambda) \frac{du_x^\lambda}{d\lambda} + \lambda \frac{d\hat{u}_x^\lambda}{d\lambda} + \frac{du_c^\lambda}{d\lambda} \quad (23)$$

here $u_x^\lambda = \delta E_X^\lambda / \delta n$ and $u_c^\lambda = \delta E_c^\lambda / \delta n$. Equation 22 is exact. It extends the first-order approximation of Seidl et al.,¹¹ which shows that the discontinuity depends on the difference between the orbital averages of the local and nonlocal exchange potentials.¹¹ Equation 22 suggests that the correlation effects manifest, implicitly, through the dependency on λ of the LUMO, correlation, and exchange potentials.

The LDA exchange and correlation potentials are independent of λ , then $\hat{o}_\lambda = 0$. Setting $\lambda = 0$ in the integrand of the right-

hand side of eq 22 leads to the gross estimator $\lambda^* \approx \Delta_{XC}/\langle \phi_L^0 | \hat{v}_{x,0} - u_x^{LDA} | \phi_L^0 \rangle$. In general, the value of λ^* used to reproduce the discontinuity is a *function* of the system because Δ_{XC} and the ground-state orbitals are determined by the external potential and the number of electrons of the system. In practice, for solid structures it was found that the optimal amount of HF exchange correlates with the inverse of the dielectric constant, estimated by using a standard DFA such as PBE.^{28,29}

Equation 20 is valid for any DFA, where the discontinuity reads³⁰ $I^{PP} - A^{PP} - [\epsilon_L^0 - \epsilon_H^0]$. The superscript “app” is used to indicate that the ionization, or affinity, potential is obtained from explicit calculations with the selected DFA; three self-consistent calculations are performed, each one for $N - 1$, N , and $N + 1$ electrons. In molecules, one can estimate the energy gap using any DFA by simply minimizing the ground-state energy of the molecule for different number of electrons. Within this approach there are errors in the ground-state energies associated with the size of the basis set and the self-interaction error (which is critical when the number of electrons changes). In solids, however, a direct calculation of the gap by changing the number of electrons, which does require adding/removing a very small charge to/from the unit cell, is very challenging because of the delocalization of charge. Unfortunately, due to the continuous differentiability of the LDA, and GGA, XC energies, the quasiparticle gap is underestimated, hence the need for Δ_{XC} .

The relation between the parameters and the derivative discontinuity can also be generalized to the many-parameter case (assuming that the ionization theorem holds). Equation 20 can be written as

$$\Delta_{XC} = \int_{\gamma^*} dz \cdot \langle \phi_L^z | \nabla_z \hat{f}_z | \phi_L^z \rangle \quad (24)$$

where γ^* is a trajectory between the point where the interaction is absent ($z = 0$) and the point (z^*) that reproduces the discontinuity. The quantities on the right-hand side are functions of the auxiliary interaction. The specific evaluation of the Fock operator \hat{f}_z depends on the explicit form of the parametrization. It is possible that there is a large set of parameters satisfying the above equation, and that there are points in the parameter space where the LUMO energy is a nonanalytic function, which could be the case if there is orbital crossing (a situation where the integration can be trajectory-dependent).

DYNAMICS AND LINEAR RESPONSE

Suppose a local time-dependent (td) potential, $u_s^\lambda(\mathbf{r},t)$ is given. The Hamiltonian describing the auxiliary system of electrons is

$$\hat{\mathcal{H}}_\lambda[u_s^\lambda](t) = \hat{T} + \lambda \hat{W} + \int d^3r u_s^\lambda(\mathbf{r},t) \hat{n}(\mathbf{r}) \quad (25)$$

The evolution equations can be derived by stationarizing the action

$$\mathcal{A}[\Phi_N, u_s^\lambda] = \int_0^T dt \langle \Phi_N(t) | i\partial_t - \hat{\mathcal{H}}_\lambda[u_s^\lambda](t) | \Phi_N(t) \rangle \quad (26)$$

under the constraint that the state of the system is described at all times by a single td Slater determinant. The evolution equations for the orbitals are then of the form $i\partial_t \phi_a(t) = \hat{f}_k(t) \phi_a(t)$, where $\hat{f}_k(t) = -1/2\nabla^2 + \lambda(j(t) + \hat{v}_{x,i}(t)) + u_s^\lambda(t)$,

For a given interaction strength, λ , and initial state, $\Phi_N(0)$, as a simple extension of the Runge–Gross theorem,³¹ there is a one-to-one correspondence between the space of local, auxiliary td potentials and the space of electronic densities.³² To reproduce the td electronic density of the real system of electrons, the orbitals are propagated self-consistently using a td potential $\tilde{u}_s^\lambda(t) = u_s^\lambda(t) + v(t)$, where $v(t)$ is the total td one-body external potential of the system, which might include the driving scalar field, i.e., a laser field. One can introduce a proper XC action functional in such a way that

$$u_{XC}^\lambda(\mathbf{r},t) = (1 - \lambda) \frac{\delta \mathcal{A}_X}{\delta n(\mathbf{r},t)} + \frac{\delta \mathcal{A}_c}{\delta n(\mathbf{r},t)} + g_{XC}(\mathbf{r},t) \quad (27)$$

where g_{XC} is a memory term that vanishes in adiabatic approximations. The functional derivative symbol is defined as a symmetry operation in the Keldysh space that avoids a causality paradox.³³ The adiabatic approximation is obtained by replacing the actions in the above equation by the corresponding ground-state analogues. The resulting adiabatic, partial HXC potential is $u_{HXC}^{\lambda,ad}(\mathbf{r},t) = (1 - \lambda)u_{HXC}^{gs}[n(\mathbf{r},t)] + u_{xc}^{gs}[n(\mathbf{r},t)]$. For example, if Dirac exchange³⁴ is used, we find $u_{xc}^{gs}(\mathbf{r},t) = -4/3C_X n^{1/3}(\mathbf{r},t)$; the Hartree potential is adiabatic.

Equations 16 and 22 indicate that local and nonlocal exchange energies, and potentials, are quite relevant quantities to explore the relationship between the ground-state GKS XC energies, the XC derivative discontinuity, and the space of parameters. In addition, there is a close connection between the ground-state parametrized methods and their linear-response extensions. In a zero-order electronic transition, an electron is promoted from an occupied orbital to a virtual one. The linear-response formalism, roughly speaking, leads to the *correction* of this type of excitation, where the zero-order transition is shifted in the energy scale by the kernel. The approximated adiabatic kernels in general provide a small shift, usually insufficient to estimate electronic excitations in molecules: It is known that a purely local XC kernel in standard KS theory, like the adiabatic LDA, often produces an unsatisfactory optical gap. In both the td and ground-state cases, with respect to pure HF calculations, the relaxation and compression of the orbital levels caused by the XC LDA potential is excessive. The addition of an appropriate fraction of orbital exchange reduces these effects by inducing orbital-specific screening. Nonetheless, the gradient-based corrections to the XC LDA, present in functionals like PBE, do not seem to produce a significant change on this widening of orbital levels, as we report in the next section.

DISCUSSION

To study the effect of λ , and ζ , we chose a subgroup of the benchmarking set previously reported by Peach et al.⁴ The subset maintains an even balance between the number of charge-transfer and local excitations. Here we analyze the excitation energies of the following molecules: HCl, CO, 4-(*N,N*-dimethylamino)benzonitrile (DMABN), dipeptide, β -dipeptide, *N*-phenylpyrrole (PP), anthracene, and some polyacetylene (PA) oligomers. To refer to td functionals, we affix an “A” to the acronym of their respective ground-state approximation. We compare the performance of the adiabatic functionals: APBEO ($\lambda = 0.25$), ALDA0 ($\lambda = 0.25$), ALDA1 ($\lambda = 0.3$), and ACAM-LDA0. Additionally, we include the data corresponding to AB3LYP and ACAM-B3LYP, calculated by Peach et al.⁴

First, we optimized all the molecular geometries employing the basis set 6-31G* for each functional, PBE0, LDA0, and LDA1. In most cases, the excitation-energy calculations with a certain adiabatic DFA were performed at the molecular geometry obtained with its ground-state equivalent functional. For the calculations with ACAM-LDA0 we use the LDA0 geometry. And, for β -dipeptide the LDA0 optimal geometry was employed for all the excitation calculations. The linear-response TDDFT computations were carried out with the correlation-consistent, polarized, triple- ζ (cc-pVTZ) basis set, except for CO, for which we used d-aug-cc-pVTZ (as suggested in ref 4). Our calculations were run using the NWChem suite.³⁵

We observed that convergence of the linear-response calculations with the adiabatic LDA0 functional is *twice as fast* as with APBE0; both functionals display very close mean absolute errors, Figure 1. The excitation energies from ALDA0

CAM-B3LYP to CAM-LDA0. This latter functional consists in setting $\lambda = 1/4$, $\zeta = 1/2$, and $\mu = 1/3$, whereas the residual parts of exchange and correlation are treated with LDA only. The factor $\mu = 1/3$ comes from the study of Tsuneda et al.,³⁷ and $\zeta = 1/2$ derives from the work of Yanai et al.¹⁰ The performance of ACAM-LDA0 agrees with that of ACAM-B3LYP, Figure 1. The former functional leads to computer times reduced by about 30% with respect to ACAM-B3LYP. The cost cannot be reduced further due to the use of the error function. In settings where computational resources are limited or need to be shared among many users, some reduction of power demands might be desired. Approximation and speed-up of exchange integrals is an ongoing field.^{39,40} If a boosting algorithm can be applied to a functional like the adiabatic CAM-LDA0, then the savings could be increased.

The tendency of gradient-dependent terms to produce small contributions to the excitation energies, for the standard theory (no parameters, $\lambda = 0$), can also be inferred from earlier studies. For instance, the data reported in refs 41–43 suggest that for low-lying excitation energies the results change by small amounts when switching from the adiabatic XC PBE functional to ALDA.

The purpose of the gradient corrections to the LDA XC energy is mainly to extend the LDA functional to the inhomogeneous electron gas case. To investigate atoms and molecules, the gradient-corrected functionals give slightly more accurate ground-state properties than the LDA. In a dissociation process, for example, the curvature of the density increases due to the reduction of the density in the bonding regions. Because the GGAs somewhat account for this, the binding energies are improved. In contrast, the LDA0, or CAM-LDA0, is less suited for describing binding energies.

A question that might come to mind is, “Should the ground-state XC potential be the same as the td one?” The answer depends on the type of application, the user needs, the hardware available, etc. For example, there are molecules for which combining LDA0 ground-state calculations with an excitation-energy analysis based on the ALDA0 XC potential could be enough. In addition, for calculation of forces and atomic motions, it can be convenient to use the same functionals with gradient corrections. On the contrary, there might be cases where one needs an accurate geometry from a different methodology and could simply use a functional like ALDA0, or its CAM version. From the perspective of rigorous TDDFT, however, it must be remarked that the improved, td XC potential should feature dependence on the initial state and the evolution of the electronic density, i.e., memory dependence. Thus, an improved, td XC potential should extend its ground-state counterpart and display a different algebraic structure.

The errors shown in Figure 1 indicate that introduction of the parameters λ , ζ , and μ (alternatively, α , β , and μ) is useful to improve optical properties. Interestingly, the GKS formalism allows for inclusion of *many* types of auxiliary interactions between the auxiliary electrons to enhance the approximations in standard KS theory. It would be desirable to have a reference system where the value of the parameters λ , ζ , μ could be estimated. The concept of the electron gas, which offers a vast set of physical gapless systems, has been originally used to obtain local and semilocal approximations. The way it was traditionally used might discourage employing these systems to estimate parameters like λ , ζ , and μ . However, downscaling the electron gas model to small volumes leads to non-negligible

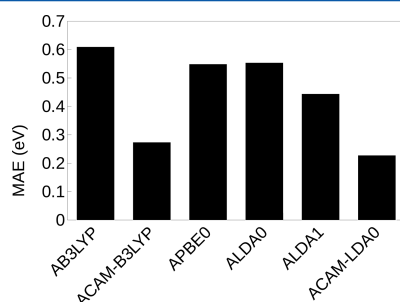


Figure 1. Performance comparison of DFAs in terms of mean absolute error, calculated using the reference values of Table 1.

are around 0.1 eV less than those obtained using APBE0. Also, for this set of excitation energies, both APBE0 and ALDA0 yield similar numbers as AB3LYP. Increasing the amount of Fock exchange raises the excitation energies with respect to APBE0. Consider, for example, LDA with $\lambda = 0.3$, which we denote^b LDA1 (Table 1). ALDA1 gives a slightly better accuracy than ALDA0 (Figure 1). Note, however, that APBE0, ALDA0, and ALDA1 are unable to describe properly the charge-transfer (CT) excitation energies as the ACAM-B3LYP functional does. The solution to improve the description of such processes is the addition of the *long-range* HF exchange contribution. Why does this work? The addition of nonlocal exchange increases the excitation energies but does not raise the CT values high enough. One might try to further increase λ , but this would cause errors in the non-CT excitations. Long-range Fock exchange raises effectively the energy of the long-range excitations, which are essentially of the CT type. For local excitations, the long-range HF exchange has little effect.

The method of Yanai et al.¹⁰ (the creators of CAM) is an extension of the work of Tsuneda et al.,³⁷ who showed that partitioning of the Coulombic interaction and use of Fock exchange for the Ir interactions were of practical utility. These studies focus *only* on exchange interactions. The effect of nonlocal correlations is rather unexplored. Recently, hybrid functionals combining MP2 and local functionals have been proposed (we refer the reader to ref 38 for more information). The inclusion of MP2 can also be analyzed within the GKS framework.

The gradient corrections to the adiabatic LDA0 functional have little effect on the excitation energies. For example, we reduced

Table 1. Calculated Excitation Energies by Using Several Adiabatic DFAs, Reference Values Included^a

system	transition	type	B3LYP	CAM-B3LYP	PBE0	LDA0	LDA1	CAM-LDA0	ref
HCl	Π	CT	7.65	7.79	7.84	7.70	7.90	7.83	8.23
CO	Σ^+	R	10.97	11.79	11.23	11.40	11.60	12.37	12.40
	Π	R	10.19	10.90	10.53	10.69	10.87	11.45	11.53
	Σ^+	R	10.13	10.80	10.46	10.62	10.80	11.34	11.40
	Σ^+	R	9.80	10.37	10.10	10.26	10.42	10.87	10.78
	Δ	L	10.03	10.08	10.05	10.00	10.23	9.98	10.23
	Σ^-	L	9.72	9.71	9.65	9.52	9.74	9.47	9.88
PA $m = 2$	Π	L	8.39	8.47	8.36	8.26	8.41	8.35	8.51
	B_u	L	5.88	6.04	5.89	5.83	5.97	5.99	5.92
	B_u	L	4.81	5.03	4.80	4.74	4.88	4.97	4.95
	B_u	L	4.13	4.39	4.67	4.63	4.19	4.63	4.41
	B_u	L	3.66	3.94	3.62	3.56	3.70	3.86	4.27
	DMABN	B_2	L	4.44	4.72	4.43	4.35	4.52	4.70
PP	A_2	CT	4.64	4.91	4.74	4.67	4.83	4.96	4.56
	B_2	L	4.76	5.06	4.79	4.72	4.95	5.12	4.85
	A_1	L	4.96	5.12	4.86	4.79	5.00	5.19	5.13
	B_2	CT	4.58	5.27	4.91	4.83	5.04	5.46	5.47
	A_1	CT	4.64	5.92	5.15	5.08	5.34	6.28	5.94
	B_{2u}	L	4.38	4.67	4.46	4.40	4.56	4.71	4.88
β -dipeptide	B_{3u}	L	4.47	4.62	4.55	4.48	4.64	4.63	4.46
	$n_1 \rightarrow \pi_2^*$	CT	7.26	8.38	6.96	6.92	7.33	9.05	9.13
	$\pi_1 \rightarrow \pi_2^*$	CT	7.20	8.01	6.73	6.66	6.92	8.37	7.99
	$n_1 \rightarrow \pi_1^*$	L	5.66	5.67	5.61	5.59	5.65	5.72	5.40
	$n_2 \rightarrow \pi_2^*$	L	5.56	5.76	5.69	5.67	5.73	5.79	5.10
	dipeptide	$n_1 \rightarrow \pi_2^*$	CT	6.31	7.84	6.74	6.64	7.12	8.41
	$\pi_1 \rightarrow \pi_2^*$	CT	6.15	7.00	6.50	6.32	6.72	7.23	7.18
	$n_1 \rightarrow \pi_1^*$	L	5.55	5.69	5.76	5.64	5.88	5.78	5.63
	$n_2 \rightarrow \pi_2^*$	L	5.77	5.92	6.03	5.94	6.16	6.10	5.79
	MAE		0.61	0.27	0.55	0.55	0.44	0.23	

^aExcitation types: CT, charge transfer; L, local; R, Rydberg; MAE, mean absolute error. For the dipeptide molecules the subindexes 1 and 2 refer to the first and second carbonyl groups, respectively. The variable m is the number of units in the oligomer.

energy spacings in the spectrum. And, perhaps, at these scales the estimation of the parameters can be performed.

CONCLUDING REMARKS

The GKS formalism allows us to regard XC functionals like PBE0, and LDA0, as part of a different flavor of KS theory that includes at least one parameter. In light of the GKS framework, we studied hybrid functionals and their associated, auxiliary, electronic systems. Also, some formal conditions that hybrid functionals should satisfy were shown. In principle, different systems require different amounts of nonlocal Fock exchange, which can motivate further work on transforming the parameters into purely *ab initio* quantities. Nonlocal exchange corrections in combination with the adiabatic LDA, e.g., the CAM-LDA0 form, can produce better charge-transfer excitation energies with respect to functionals like AB3LYP, and APBE0. This suggests that a portion of nonlocal exchange is a dominant factor for the enhancement of excitation energies. Nonetheless, we remark, discretion and insight by the user is required to properly set up the correct amount of orbital exchange, and related quantities. Knowledge deduced from reliable *ab initio* calculations and experimental measurements might assist in this matter.

AUTHOR INFORMATION

Corresponding Author

*G. C. Schatz. E-mail: g-schatz@northwestern.edu. Phone: +1 847 491 5657.

Notes

The authors declare no competing financial interest.

ACKNOWLEDGMENTS

The research at Northwestern University was supported by the Department of Energy, Basic Energy Sciences, under grant DE-FG02-10ER16153.

ADDITIONAL NOTES

^aA similar expression for the GKS correlation energy was defined by Görling and Levy.¹⁶ Their formula, however, is different from eq 4 because their expansion of the partial HXC energy depends on the exchange energy of standard KS theory.

^bThe GGA version of the XC LDA1 is in essence the PBE0-1/3 functional; see ref 36 for details.

REFERENCES

- (1) Becke, A. D. A New Mixing of Hartree-Fock and Local Density-functional Theories. *J. Chem. Phys.* **1993**, *98*, 1372–1377.
- (2) Heyd, J.; Peralta, J. E.; Scuseria, G. E.; Martin, R. L. Energy Band Gaps and Lattice Parameters Evaluated with the Heyd-Scuseria-Ernzerhof Screened Hybrid Functional. *J. Chem. Phys.* **2005**, *123*, 174101.
- (3) Muscat, J.; Wander, A.; Harrison, N. On the Prediction of Band Gaps from Hybrid Functional Theory. *Chem. Phys. Lett.* **2001**, *342*, 397–401.
- (4) Peach, M. J.; Benfield, P.; Helgaker, T.; Tozer, D. J. Excitation Energies in Density Functional Theory: An Evaluation and a Diagnostic Test. *J. Chem. Phys.* **2008**, *128*, 044118.

- (5) Görling, A.; Levy, M. Exact Kohn-Sham Scheme Based on Perturbation Theory. *Phys. Rev. A: At., Mol., Opt. Phys.* **1994**, *50*, 196–204.
- (6) Perdew, J. P.; Ernzerhof, M.; Burke, K. Rationale for Mixing Exact Exchange with Density Functional Approximations. *J. Chem. Phys.* **1996**, *105*, 9982–9985.
- (7) Perdew, J. P.; Burke, K.; Ernzerhof, M. Generalized Gradient Approximation made Simple. *Phys. Rev. Lett.* **1996**, *77*, 3865–3868.
- (8) Adamo, C.; Scuseria, G. E.; Barone, V. Accurate Excitation Energies from Time-dependent Density Functional Theory: Assessing the PBE0 Model. *J. Chem. Phys.* **1999**, *111*, 2889–2899.
- (9) Adamo, C.; Barone, V. Inexpensive and Accurate Predictions of Optical Excitations in Transition-metal Complexes: The TDDFT/PBE0 Route. *Theor. Chem. Acc.* **2000**, *105*, 169–172.
- (10) Yanai, T.; Tew, D. P.; Handy, N. C. A New Hybrid Exchange-correlation Functional Using the Coulomb-attenuating Method (CAM-B3LYP). *Chem. Phys. Lett.* **2004**, *393*, 51–57.
- (11) Seidl, A.; Görling, A.; Vogl, P.; Majewski, J.; Levy, M. Generalized Kohn-Sham Schemes and the Band-gap Problem. *Phys. Rev. B: Condens. Matter Mater. Phys.* **1996**, *53*, 3764–3774.
- (12) Rinke, P.; Schleife, A.; Kioupakis, E.; Janotti, A.; Rödl, C.; Bechstedt, F.; Scheffler, M.; Van de Walle, C. G. First-principles Optical Spectra for F Centers in MgO. *Phys. Rev. Lett.* **2012**, *108*, 126404.
- (13) Liao, T.; Roma, G. First Principles Defect Energetics for Simulations of Silicon Carbide Under Irradiation: Kinetic Mechanisms of Silicon Di-interstitials. *Nucl. Instrum. Methods Phys. Res., Sect. B* **2014**, *327*, 52–58.
- (14) Magyar, R. J.; Tretiak, S. Dependence of Spurious Charge-transfer Excited States on Orbital Exchange in TDDFT: Large Molecules and Clusters. *J. Chem. Theory Comput.* **2007**, *3*, 976–987.
- (15) Kronik, L.; Stein, T.; Refaelly-Abramson, S.; Baer, R. Excitation Gaps of Finite-sized Systems from Optimally Tuned Range-separated Hybrid Functionals. *J. Chem. Theory Comput.* **2012**, *8*, 1515–1531.
- (16) Görling, A.; Levy, M. Hybrid Schemes Combining the Hartree-Fock Method and Density-functional Theory: Underlying Formalism and Properties of Correlation Functionals. *J. Chem. Phys.* **1997**, *106*, 2675–2680.
- (17) Levy, M. Universal Variational Functionals of Electron densities, First-order Density matrices, and Natural Spin-orbitals and Solution of the v-representability Problem. *Proc. Natl. Acad. Sci. U. S. A.* **1979**, *76*, 6062–6065.
- (18) Kümmel, S.; Kronik, L. Orbital-dependent Density Functionals: Theory and Applications. *Rev. Mod. Phys.* **2008**, *80*, 3–60.
- (19) Grabowski, I.; Lotrich, V.; Hirata, S. Ab Initio DFT-The Seamless Connection Between WFT and DFT. *Mol. Phys.* **2010**, *108*, 3313–3322.
- (20) Rappoport, D.; Crawford, N. R. M.; Furche, F.; Burke, K. In *Encyclopedia of Inorganic Chemistry. Computational Inorganic and Bioinorganic Chemistry*; Salomon, E. I., King, R. B., Scott, R. A., Eds.; Wiley: Chichester, U.K., 2009; pp 159–172.
- (21) Almbladh, C.-O.; Von Barth, U. Exact Results for the Charge and Spin densities, Exchange-correlation Potentials, and Density-functional Eigenvalues. *Phys. Rev. B: Condens. Matter Mater. Phys.* **1985**, *31*, 3231–3244.
- (22) Wu, Q.; Ayers, P. W.; Yang, W. Density-functional Theory Calculations with Correct Long-range Potentials. *J. Chem. Phys.* **2003**, *119*, 2978–2990.
- (23) Handler, G. S.; Smith, D. W.; Silverstone, H. J. Asymptotic Behavior of Atomic Hartree-Fock Orbitals. *J. Chem. Phys.* **1980**, *73*, 3936–3938.
- (24) Handy, N. C.; Marron, M. T.; Silverstone, H. J. Long-range Behavior of Hartree-Fock Orbitals. *Phys. Rev.* **1969**, *180*, 45–48.
- (25) Refaelly-Abramson, S.; Baer, R.; Kronik, L. Fundamental and Excitation Gaps in Molecules of Relevance for Organic Photovoltaics from an Optimally Tuned Range-separated Hybrid Functional. *Phys. Rev. B: Condens. Matter Mater. Phys.* **2011**, *84*, 075144.
- (26) Baerends, E. J.; Gritsenko, O. V.; Van Meer, R. The Kohn-Sham Gap, the Fundamental Gap and the Optical Gap: The Physical Meaning of Occupied and Virtual Kohn-Sham Orbital Energies. *Phys. Chem. Chem. Phys.* **2013**, *15*, 16408–16425.
- (27) Perdew, J. P.; Parr, R. G.; Levy, M.; Balduz, J. L., Jr Density-functional Theory for Fractional Particle Number: Derivative Discontinuities of the Energy. *Phys. Rev. Lett.* **1982**, *49*, 1691–1694.
- (28) Marques, M. A. L.; Vidal, J.; Oliveira, M. J. T.; Reining, L.; Botti, S. Density-based Mixing Parameter for Hybrid Functionals. *Phys. Rev. B: Condens. Matter Mater. Phys.* **2011**, *83*, 035119.
- (29) Koller, D.; Blaha, P.; Tran, F. Hybrid Functionals for Solids with an Optimized Hartree-Fock Mixing Parameter. *J. Phys.: Condens. Matter* **2013**, *25*, 435503.
- (30) Mosquera, M. A.; Wasserman, A. Integer Discontinuity of Density Functional Theory. *Phys. Rev. A: At., Mol., Opt. Phys.* **2014**, *89*, 052506.
- (31) Runge, E.; Gross, E. K. U. Density-functional Theory for Time-dependent Systems. *Phys. Rev. Lett.* **1984**, *52*, 997–1000.
- (32) Baer, R.; Livshits, E.; Salzner, U. Tuned Range-separated Hybrids in Density Functional Theory. *Annu. Rev. Phys. Chem.* **2010**, *61*, 85–109.
- (33) Mosquera, M. A. Action Formalism of Time-dependent Density-functional Theory. *Phys. Rev. A: At., Mol., Opt. Phys.* **2013**, *88*, 022515.
- (34) Dirac, P. A. Note on Exchange Phenomena in the Thomas Atom. *Math. Proc. Cambridge Philos. Soc.* **1930**, *26*, 376–385.
- (35) Valiev, M.; Bylaska, E. J.; Govind, N.; Kowalski, K.; Straatsma, T. P.; Van Dam, H. J. J.; Wang, D.; Nieplocha, J.; Apra, E.; Windus, T. L.; Jong, W. A. NWChem: A Comprehensive and Scalable Open-source Solution for Large Scale Molecular Simulations. *Comput. Phys. Commun.* **2010**, *181*, 1477–1489.
- (36) Guido, C. A.; Brémond, E.; Adamo, C.; Cortona, P. Communication: One third: A New Recipe for the PBE0 Paradigm. *J. Chem. Phys.* **2013**, *138*, 021104.
- (37) Tsuneda, T.; Song, J. W.; Suzuki, S.; Hirao, K. On Koopmans' Theorem in Density Functional Theory. *J. Chem. Phys.* **2010**, *133*, 174101.
- (38) Chai, J.-D.; Mao, S.-P. Seeking for Reliable Double-hybrid Density Functionals without Fitting Parameters: The PBE0–2 Functional. *Chem. Phys. Lett.* **2012**, *538*, 121–125.
- (39) Neese, F.; Wennmohs, F.; Hansen, A.; Becker, U. Efficient, Approximate and Parallel Hartree-Fock and Hybrid DFT Calculations. A ‘Chain-of-spheres’ Algorithm for the Hartree-Fock Exchange. *Chem. Phys.* **2009**, *356*, 98–109.
- (40) Mejía-Rodríguez, D.; Huang, X.; del Campo, J. M.; Köster, A. M. Chapter Four-hybrid Functionals with Variationally Fitted Exact Exchange. *Adv. Quantum Chem.* **2015**, *71*, 41–67.
- (41) Hirata, S.; Head-Gordon, M. Time-dependent Density Functional Theory for Radicals: An Improved Description of Excited States with Substantial Double Excitation Character. *Chem. Phys. Lett.* **1999**, *302*, 375–382.
- (42) Hirata, S.; Head-Gordon, M. Time-dependent Density Functional Theory within the Tamm-Dancoff Approximation. *Chem. Phys. Lett.* **1999**, *314*, 291–299.
- (43) Furche, F.; Ahlrichs, R. Adiabatic Time-dependent Density Functional Methods for Excited State Properties. *J. Chem. Phys.* **2002**, *117*, 7433–7447.